PREDICTION AND OPTIMIZATION OF RESIDUAL STRESSES, WELD-BEAD PROFILE AND MECHANICAL PROPERTIES OF LASER WELDED COMPONENTS

By

K. Y. BENYOUNIS, B. Sc., M. Sc.

A Thesis Submitted in Fulfilment of the Requirements for the Degree of Doctor of Philosophy (PhD)

Supervisor

Dr. Abdul-Ghani Olabi

School of Mechanical and Manufacturing Engineering

Dublin City University

December 2006

DECLARATION

I hereby certify that this material, which I now submit for assessment on the programme of study leading to the award of PhD in Engineering is entirely my own work and has not been taken from the work of others save and to the extent that such work has been cited and acknowledged within the text of my work.

Signed: 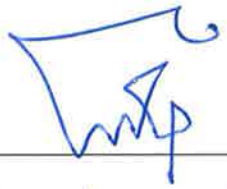 ID: **51178559**

Date: 31/01/2007

ACKNOWLEDGEMENTS

First of all I would like to express my sincere thanks and gratitude to Almighty Allah, who helped and blessed me during the course of my studies.

Also, I am really grateful to my supervisor Dr. Abdul Ghani Olabi. Without his continuous help and advice this work would not have been made possible.

I am thankful to my, Wife and my kids, whose have given me the chance of discovering what I like, and of devoting myself to it.

I also would like to gratefully acknowledge the Libyan government for the financing of this research.

I also would like to take this opportunity to extend my thanks to Mr. Martin Johnson for his expert work during laser welding.

I also would like to take this opportunity to extend my thanks to Mr. Ali El-Tamimi for valuable help.

I would like to thank the technical staff of the School of Mechanical & Manufacturing Engineering, especially Mr. Liam Domican, Mr. Michael May and Mr. Chris Crouch.

Last but not least I would like to take this opportunity to extend my thanks to each one of my friends, here in Ireland and back home, for their honest and sincere concerns about my study and myself.

Prediction and Optimization of Residual Stresses, Weld-Bead Profile and Mechanical Properties of Laser Welded Components

K. Y. Benyounis, B. Sc., M. Sc.

ABSTRACT

Recently, laser welding has become a leading industrial joining process. Mainly because it has become highly automated using sophisticated robotic systems. However, to make effective use of automated laser welding it is essential to have a high degree of confidence in predicting the welding outcome. To achieve a desired weld quality, the weldments are normally examined and related to the weld input parameters. This input-output relationship can be in the form of mathematical models that can be programmed and fed to the robotic control system.

This work aims to introduce experimentally based mathematical models developed by applying Response Surface Methodology (RSM) using Design-Expert software V7 to relate the residual stress distribution, weld bead parameters, mechanical properties and operating cost to the laser welding input parameters, namely: laser power, welding speed and focal point position. Also, the desirability approach was used in conjunction with RSM to find out the optimal combination of the welding parameters to achieve the required weld quality. In addition to this, microstructural investigation of the welded joints was carried out to study the effect of varying the welding conditions on the microstructure of the Weld zone (WZ) and Heat affected zone (HAZ). Common materials were investigated in this work (i.e.AISI1016, AISI1045 and AISI304) with different thicknesses and joint configurations using a 1.5 kW CW CO_2 Rofin laser as a welding source and two focusing lenses with focal lengths of 127 and 190 mm.

Many models were developed to predict the responses of interest for similar and dissimilar welding. Also, the main effects and the interaction effects of the process parameters on the responses were discussed and presented graphically for all materials and joint configurations. Moreover, by using the developed models the welding process was optimized by determining the optimal combination of the process input parameters at which the desired weld quality can be achieved for each material. Finally, the size and orientation of the solidified structures were related to the welding conditions. It was observed that when the heat input increases the weld-bead geometry and the microstructures become bigger and coarser respectively.

TABLE OF CONTENTS

LIST OF FIGURES

LIST OF TABLES

CHAPTER I
INTRODUCTION

1. INTRODUCTION

Welding is the most economical and efficient way to joint metals permanently. It plays an important role in steel fabrication and repair. It is also used in the fabrication of spacecraft, fighter planes, submarines, and atomic power plants. Welding ranks highly among industrial processes and involves more scientific principles and variables than those involved in any other industrial process. There are many different kinds of welds. Some processes cause sparks and others do not even require extra heat. Welding can be done anywhere, outdoors or indoors, underwater, and in outer space. Numerous welding methods or techniques are in common use for a wide range of applications [1 - 2].

Laser welding is one of the newest welding techniques. The laser was originally developed in the 1960s at the Bell Telephone Laboratories as a communication device. The present welding lasers use active mediums, which are either in the form of a solid or a gas. There are three main types of solid-state laser: the ruby, neodymium glass and the neodymium yttrium aluminium garnet (Nd-YAG). In fact, the Nd-YAG laser has practically replaced the other two types. The gas lasers used for welding are currently all CO_2 lasers since they have proved to be the most efficient and produce the highest power. However, carbon monoxide CO lasers, which have a shorter wavelength, are under development and evaluation [3-4].

Fabrication by laser welding in general is an effective way to reduce production and fabrication costs. This is due to the advantage of high production rates as well as the fact that lasers can be mechanised, computer controlled and integrated into assembly lines. As a high quality low distortion welding process, it has revolutionized many industries by using this application in their fabrication processes. It has also the advantages of deep penetration with low heat input and a narrow weld width. With all these advantages, some distortion is still introduced, which can cause problems for high precision welding of critical components [4 - 5].

Laser welding involves highly localized heating of the metal components being joined together. Therefore, the temperature distribution in the weldment is not uniform. In the melted weld pool, stresses are released. Upon cooling, the weld pool solidifies and starts to shrink; exerting stresses on the surrounding weld metal and the heat affected zone (HAZ). These stresses remain in the welded metal and cause

unwanted distortion [5]. As a result of varying the welding process input parameters the localized heat input will differ. Thus, the weld quality in terms of residual stresses, weld bead geometry, and mechanical properties of the welded joint will vary.

Recently, laser welding has become a leading industrial joining process. Mainly because it has become highly automated using sophisticated robotic systems controlled by computers, which can achieve higher weld precision and repeatability. However, to make effective use of automated laser welding it is essential to have a high degree of confidence in predicting the welding results. To achieve a desired weld quality, the weld bead geometry and the mechanical properties are normally examined and related to the weld input parameters. This input-output relation can be in the form of operational mathematical models, or databases, that can be programmed and fed to the robotic control system [3 - 4] enabling the desired results to be automatically achieved.

For welding a new component, there are certain weld-joint specifications to be met. This can be only achieved by (coarse or fine) tuning the welding process's input parameters and inspecting, whether or not, the results comply with the desired specifications. Such a task is usually carried out by skilled personnel or an engineer. However, this parameter selection process is based on trial and error and is always time consuming. Moreover, this traditional method is non-systematic and usually does not produce an optimised welding parameters combination, which can be used for different outcomes. This is due to the fact that the welding process is affected by different input and output parameters. A systematic study, such as Design of Experiment (DOE) and analysis of the results using Response Surface Methodology (RSM), would allow calculation and visualisation of the interactive effects of the input parameters on the results. Once a study of this nature has been done, the ideal or the optimum welding parameters combinations can be examined or used to produce the desired weld specifications within the parameters ranges considered in the study.

1.1 Thesis Objective

The goal of this work is to apply Response Surface Methodology (RSM) to develop mathematical models, in terms of the laser welding input parameters. These models will assist engineers and technologists to achieve desirable weld properties. This approach assures the highest reliability in welded components, lowers process start-up costs and improves weld quality. Furthermore, RSM reduces the numbers of experiments without any significant loss in the accuracy of the models developed [6].

In addition to that, the developed models are useful to predict a given response and also allow the engineers to select the optimal combination of the process input parameters to maximise or minimise certain responses. The response could be maximum principal stress, a certain weld-bead geometry parameter or a certain mechanical property of the welded joint … etc.

The main objectives of the present research can be summarized in the following points:

1. To develop mathematical models using RSM with the aid of Design-Expert version-7 statistical software to predict the following responses:
    a) Distribution of maximum principal residual stresses through the depth and along the x-axis.
    b) Welded zone width and penetration.
    c) Width of HAZ.
    d) Heat input.
    e) Impact strength.
    f) Tensile strength and notched tensile strength.
    g) Tensile-shear strength for lap joint.
    h) Operating cost per meter.
2. To present the developed models in 3D plots and contour graphs etc. These plots and graphs will explain the effect of the welding variables and their interactions on the above-mentioned responses.
3. To demonstrate the individual affect of a certain parameter on a given response at set values of the remaining parameters.

4. To determine the optimal combination of the process input variables, based on the developed models and numerical optimisation, to achieve the desired criterion. As an example; increasing the welding speed and decreasing the laser power, which would result in lower operation costs and improved welding productivity. Then, the working ranges could be extracted to determine the precise factors ranges at which the process can be considered safe, efficient and economic.
5. To study the microstructure of the welded joints, by investigating the effect of varying the heat input on the microstructure and microhardness of the WZ and HAZ.

Different materials are to be investigated in this work namely; low carbon steel, AISI1016, medium carbon steel, AISI1045, and stainless steel, AISI304, using a 1.5 kW CW CO_2 Rofin laser as a welding source, with different joint configurations. The process input parameters that were under control are laser power (P), welding speed (S) and focus point position (F).

1.2. Thesis Outline

Chapter 1 outlines a general introduction on welding and laser welding as well as an opening introduction about the benefits of applying RSM. This chapter also presents the objective of the current work and the materials to be investigated. Chapter 2 presents a review of the literature related to residual stress, application of optimization techniques in welding and the effect of laser welding parameters on the welds properties and outcomes. Chapter 3 summarizes the design of experiments and some details on the Box-Behnken and central composite designs, as well as the steps followed to build up a mathematical model. Chapter 4 describes the experimental procedures and summarizes the incremental hole-drilling method (IHDM) theory and equations. The equipment and devices used in this work are also presented. Chapter 5 presents the results and discussion achieved for all materials investigated herein. Chapter 6 illustrates the results of the numerical and graphical optimization along with the optimal welding setting for each material and joint configuration for a given criterion. Chapter 7 outlines the conclusions of this study and suggests some recommendations for future work.

CHAPTER II
LITERATURE REVIEW

2. LITERATURE REVIEW

2.1 Residual Stresses

Residual stresses are internal stresses that remain in the component without any external loading. Residual stress exists in practically all mechanical components, whether they are metal or not (Ceramic, glass, polymer, wood etc.). They are self-balanced internal stresses; therefore, the resultant force and moment produced by them must be equal to zero. Residual stresses can be classified as macro stresses and micro stresses. Macro stresses occur over a long range and they are self-equilibrated in the cross-section of the manufactured part. In all welded structures, residual stresses are produced in regions around the weldment. Whereas, micro stresses are of a short range. They are homogenous or inhomogeneous on a micro scale [7].

All manufacturing and fabricating processes introduce residual stresses into the manufactured part. Extreme service loading may also change the state of residual stress in the part. The effect of residual stress may be either beneficial or detrimental, depending upon the sign, magnitude and distribution of the stress. In fact, compressive residual surface stresses are important because notches, scratches, sharp changes in cross-section, etc. concentrate additional applied tensile stresses near the surface and can act to initiate a crack. These additional applied tensile stresses must overcome the residual compressive stresses to initiate the crack. Thus, the presence of surface compressive residual stresses is a highly favourable condition. On the other hand, tensile residual stresses will speed up crack nucleation, which may result in early failure of the welded component. [7, 8].

In welded components there are three phenomena by which the transverse residual stress would be generated, these phenomena are as follows:

a- Variation in shrinkage of the areas which are heated in a different ways

b- Surface quenching.

c- Non-equilibrium transformation of austenite.

In reality, the various stress origins are not independent. At least two or even three different kinds of stress on cooling welded joint are superimposed, leading to a complicated total state of stress [9].

2.1.1 Distortion in weldment.

As previously discussed welding involves highly localized heating. Also, the temperature is non-uniformly distributed. Upon cooling, the weld pool solidifies and shrinks resulting in stresses in WZ and HAZ. If the stresses produced from thermal expansion and contraction exceed the yield strength of the material being welded, localized plastic deformation in the component occurs. Therefore, the component dimensions change and destroy the structure [10]. Three different types of residual stress induced distortion can be found in welded structures. Longitudinal and transverse shrinkage can cause in-plane distortion of the component. Plane or axis-symmetrical angular shrinkage can cause distortion perpendicular to the plane of the welded component. Another distortion is bending due to grids with longitudinal and transverse welds. Examples of distortion that can occur during welding are illustrated in Fig. 2.1 [11].

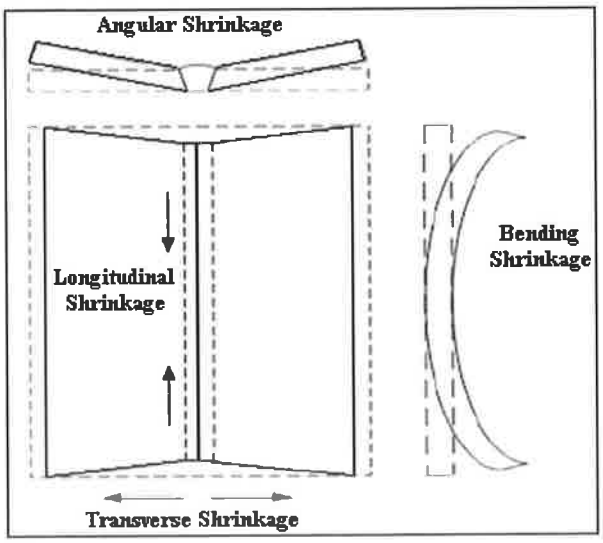

Fig. 2.1: Distortion in weldment [11].

2.1.2 Measurement techniques.

Many methods are widely in use for measuring residual stress in welded components, such as X-ray diffraction, the hole-drilling method and other destructive and non-destructive methods. Mechanical techniques are destructive since they use a strain gauge which requires that the component be drilled or cut. Among the non-destructive techniques, some are based on acoustic or magnetic effects; whereas the

diffraction methods utilize X-ray or neutron beams to evaluate the residual stress. While it is not the aim herein to review the different techniques of measuring residual stress in detail, it is important to describe briefly only the most common techniques currently in use for evaluating residual stress in welded components.

2.1.2.1 Mechanical methods

These techniques are called stress-relaxing methods, which analyze the stress-relaxation produced in a metal part when material is removed. By measuring the deformation caused by the relaxation, the values of the residual stress present in the part before the metal was removed can be determined by analyzing the successive state of equilibrium [12]. The most common mechanical methods are as follows:

a. Sectioning technique.

To determine the residual stress using this method, first of all an electrical strain gauge has to be fixed onto the surface of the welded component. Then, a small portion of metal from the area containing the electrical strain gauge has to be gradually machined. Finally, the magnitude of the strain can be determined by measuring the change in the electrical resistance of the gauge due to the change in the equilibrium state [13]. Although this technique is a destructive method and gives only the average residual stress for the area from which the piece was removed, it is still counted as a simple and accurate method. This technique has been reviewed and suggested by many researchers [14, 15].

b. Hole drilling technique.

Nowadays, the hole drilling method has become the most common technique for measuring residual stress in a component, due to its simplicity, inexpensiveness and flexibility since the technique can be applied either in the laboratory or at the worksite to a wide range of materials, including polymers, in different positions horizontal, vertical and overhead [13, 16]. This method is considered as a semi-destructive technique, since the portion of material removed is relatively small and can be easily repaired. This technique has some limitations, for example, relatively poor strain sensitivity, uncertainties due to inaccuracies when introducing the hole

(i.e. alignment, diameter, profile, depth, etc.), surface roughness and the specimen preparation.

This technique involves drilling a small hole into the component at the centre of a special strain gauge rosette and subsequent measurement of the locally relieved surface strains. By using formulae and calculations derived from experimental and finite element analyses the residual stress and its direction can evaluated [16].

2.1.2.2 Diffraction techniques

Diffraction methods are based on determining the elastic deformation which will cause changes in the interplanar spacing, d, from their stress free value, d_0. Then, the strain could be calculated by using Bragg's law and of course it is necessary to have an accurate measure of stress-free interplanar spacing. The most common diffraction methods are as follows:

a. X-ray diffraction

This technique is one of the most common methods in measuring the surface residual stress in crystalline material non-destructively. Norton et al. [17,18] introduced the use of X-ray diffraction to measure residual stress. Due to its short wavelength, X-rays penetrate a very thin surface layer of material, up to tens of microns, and are then reflected back from the atomic planes they have penetrated. By knowing the wavelength, the change in 2-theta, and the change in the interplanar spacing d, the stress can be calculated from the strain using Hooke's law.

During the last few decades this technique has undergone many improvements and developments due to the introduction of new computerized equipment that has sped up the process involved in evaluating the residual stress in crystalline materials and also the introduction of new software to analyze the data [16,19].

Although this technique requires a relatively long time to measure the residual stress at each point, it has a lot of applications, especially in evaluating the residual stress in complicated shapes and in monitoring the stress residual in a composite. Many investigations have utilized the X-ray diffraction technique to determine the

surface residual stress in different materials including ceramics and composites [20, 21, 22].

b. Neutron diffraction

The principles of this technique are the same as with X-ray diffraction, the greatest advantage over X-ray diffraction is its capability of much higher penetration; up to 100 mm in aluminium or 25 mm in steel. However, in contrast with X-ray diffraction this technique has less resolution, higher cost and much less availability generally only being available at central facilities [16]. Neutron diffraction has been used to evaluate the macro-residual stress in different engineering components fabricated by welding [23, 24, 25].

2.1.2.3 Other non-destructive techniques

These methods are based on measurements of electromagnetic, optical and other physical phenomena in the residual stress zone. The common methods among this category are as follows:

a. Magnetic method

The principle of this method is that when a ferromagnetic component is subjected to a magnetic field it becomes magnetized; the magnetisation will orientate with the crystalline directions. A change in the stress level will result in discontinuous changes in magnetization. These changes can be monitored by an electromagnetic detector. The recorded signals, called Barkhausen noise, are affected by the residual stress. The magnetic or barkhausen noise method is a completely non-destructive method, cheap, easy and quick. On the other hand, this method is limited only to ferromagnetic materials. In this method the magnetic parameters are dependent on the residual stress present, but some other factors also affect the measurements, such as hardness, grain alignment and grain size. [13, 16].

b. Ultrasonic method

The principle of this method is that the velocity of ultrasound waves in a material is directly affected by the stress level and direction. The changes in the wave's velocity provide the average macro-stress along the wave path. Although this method is completely portable and cheap to perform, the wave's velocities depend on microstructural in-homogeneities and there are difficulties in separating the effects of

multi-axial stresses. This method is suitable for routine inspection procedures for large components such as steam turbine discs [16, 26].

In contrast, the X-ray diffraction method gives accurate measurement of the surface residual stress; on the other hand it is not able to provide the distribution of the residual stress through the depth. The other non-destructive methods are not available in the school and are also not accurate because lots of factors affect the measurements. In addition to this, destructive methods are inappropriate because the specimen must be sectioned and it becomes impossible to use it again. The hole drilling method has been selected as the best choice herein, because it is available, accurate, simple and, if the incremental hole drilling method is used gives the residual stress distribution over the depth. This method will be used to measure the maximum residual stress distribution in this work. Therefore, a detailed review, including recent developments and applications of this technique, is important.

2.1.3 Development of the hole drilling method

The first proposal of this method was in 1934, when J. Mathar [27] utilized a mechanical extensometer to determine the residual stresses in structural components by disturbing their stress equilibrium. In 1950, Soete et al. [28] suggested the use of strain gauges to replace the mechanical extensometer in order to improve the accuracy of measurements. They carried out through thickness measurements for thin plates, with the assumption that residual stress is uniformly distributed through the thickness.

The early applications of this technique used a full depth hole which gives a single figure of residual stress. Kelsey [29], in 1956, studied the variation of residual stress with the hole depth. In 1966, Rendler and Vigness [30], suggested a further development in the hole drilling method by introducing a regular and reproducible procedure, and the current application of this method for measuring uniform stress started with this work. Also, they defined the geometry of the ASTM E837 standard rosette.

Bynum [31] has discussed the influence of a number of factors on the accuracy of this technique, including the method of drilling the hole. He suggested the use of air-abrasive hole-drilling with a 0.062" nozzle, which gives the most reproducible

and accurate results. He demonstrated equations to calculate the principal stresses and their direction.

Redner and Beaney [32] have investigated the different factors that affect the accuracy of residual stress measurements using the blind hole drilling method. They have concluded that the hole drilling method is now a mature, well-documented procedure and is capable of producing consistently reliable results.

Ajovalasit [33] has investigated the effect of hole eccentricity or misalignment between the hole and the rosette centres, on the experimentally determined calibration coefficients of the standard rosettes. He proposed a theory by which the correct determination of the constants and the maximum error can be evaluated providing that some parameters are known.

Procter and Beaney [34] have designed and developed a portable system, using air abrasion machining for stress-free hole-drilling. They faced some problems, such as the wear in the nozzle, which did not maintain hole circularity with varying hole depth, they suggested a rotating nozzle to overcome these problems.

In 1982, Flaman [35] introduced the use of an air turbine for ultra speed drilling. He compared low speed end milling and ultra high speed end milling. He found that the ultra high speed drill is superior to the traditional low speed.

Schajer [36], in 1981, successfully employed the finite element method for the measurement of residual stress. As a result of this study he calculated the calibration constants for uniform stress fields, also providing tabulations of these non-dimensional constants. A comparison has been made between the theoretical results he obtained and other experimental results found by other investigators. He found that the results were in good agreement, with differences of 5% in some cases. Other authors have employed different finite element approaches to calculate the calibration coefficients for uniform stress fields and to study the accuracy and reliability of this method [37, 38].

Chow and Cundiff [39] have studied the accuracy of the method in terms of drilling speed, cutter wear, drilling mode and applied drilling force. Their results revealed that the accuracy can be improved by using a new milling cutter, intermittent milling and applying a lower force during milling.

Nawwar et al. [40] modified the hole drilling technique to determine the residual stress in thin plates. The results indicated that the accuracy of this technique in this case is within ± 5%.

Recently, the measurements of the variation in residual stress with depth, by using the incremental hole drilling method or the step-by-step hole drilling method, has received much attention in order to develop solutions for non-uniform stress fields. In 1978, Zochowski [41] was the first to propose a technique to calculate non-uniform stress distribution over the depth.

Niku-lari et al. [42] have discussed different theoretical approaches that already exist in the literature and the use of FAM to develop a simple equation for calculating the calibration coefficients. According to their assumption, they also suggested this method to be used in cases where isotropic stresses are introduced by surface treatment. They found that the drilling method used did not induce any significant residual stresses. Furthermore, they have tested this method on different materials, a very good agreement has been obtained by comparing the results with those obtained by bending-deflection and the X-ray diffraction method.

Another study was carried out by Schajer [43] to develop appropriate calibration coefficients. He examined four different procedures for determining non-uniform residual stress fields. It was found that the incremental strain and the average stress methods are the simplest to apply because these procedures use experimentally measured calibration data. In 1988, Schajer [44] again applied the integral method for calculating non-uniform residual stress. He also successfully used the finite element calculation to evaluate the calibration coefficients which are required to determine residual stresses in practice. He presented these calibrating coefficients in tables for a range of hole sizes and depths. Moreover, he found that the practical depth limit is in the range of $0.3\text{-}0.4r_m$.

Shaw and Chen [45] have presented a finite element technique to analyze the data obtained by hole drilling. They assumed the residual stresses to be the initial stresses existing in the component. It is also assumed that the measured strains are affected by the elimination of the initial stresses. Their results showed a good

agreement with previous studies. It was concluded that the use of this analytical method allows great flexibility in the choice of specimen shape and material.

Lu and Flavenot [46] have described a procedure for measuring the residual stress profile over the depth using a step-by-step hole-drilling method. They demonstrated that the variation in surface strain for each increment is not only due to material removal, but also depends on the geometrical development of the hole. Their study of the method's sensitivity demonstrated that this method can be correctly used only for depths of less than one half of the cutter diameter. They select several examples to define the method's field of application; however, it may be used on multilayer and non-metal materials.

During the 1990's a large number of studies were carried out to review and improve the incremental hole drilling method. Schajer [47] has described an averaging procedure to minimize the effect of the random experimental errors.

Lin and Chon [48] have studied the method accuracy by analysing the error caused by the local yielding around the hole for different materials. They demonstrated that this type of error is negligible when the residual stresses measured are less than 65% of the yield stress.

Flaman and Boag [49] have compared three different stress fields, uniaxial stress, bending stress and subsurface stress, based on a finite element technique. Their data-analysis techniques showed excellent agreement for the uniaxial stress, whereas significant discrepancies were apparent for the other two stress fields.

Beghini and Bertini [50] have presented recent results in order to improve the hole-drilling method. Their work was concerned with two main topics. Firstly, in regard to the effect of plasticity, they managed to write simple empirical relationships, which allow the estimation of uniform stress higher than one half of the material yield strength. Secondly, in regard to through thickness residual stress evaluation, analytical expressions for the influence functions have been proposed, which appear to give some advantages in variable residual stress analysis, compared to currently employed methods.

Zuccarello [51] has investigated the optimum step distribution that minimizes the error sensitivity at a given maximum hole depth and total number of steps. Also,

he proposed a reliable statistical estimation of the uncertainty on the computed stresses.

In 1994 Lu et al. [22] compared the X-ray diffraction and the step-by-step hole drilling method in measuring the residual stress distribution for components produced by different welding processes. The comparison results showed them to be complementary. They also combined the two methods in order to obtain a general view of the state of residual stresses in the plane and through the thickness of the component.

In the step-by-step hole drilling method the strain gauges are read at each increment, residual stresses corresponding to incremental depths are calculated and the stress gradient over the thickness is determined. The incremental hole drilling method has become a widely accepted technique for measuring residual stress distribution over the depth of the component. ASTM E837 Standard and Measurement Group TN-503-5 [52, 53] describe the procedure for this technique with the assumption that residual stresses are uniform throughout the thickness. A recent publication [54] points out some of the practical aspects in more detail and gives advice on the recommended analysis and procedures.

Currently, the focus is on developing a technique that can obtain surface residual stress by the application of fine hole drilling which uses depth increments as small as 20 μm to improve the measurement resolution. Only a few researchers have studied this approach. Gadow et al. [55, 56] and Buchmann et al. [57] have investigated residual stress in coatings and composites; they used increments as small as 10 μm. In 2005, Grant et al. [58] used this approach for measuring the induced residual stress that might develop during machining.

2.2 Application of Different Optimization Techniques in the Welding Field

Generally, the quality of a weld joint, in terms of different features, is directly influenced by welding input parameters during the welding process; therefore, welding can be considered as a multi-input, multi-output process. Conventionally, to achieve the desired weld quality a great deal of time and cost are expended using a trial-and-error method to obtain optimal welding conditions through a combination

of the various welding process input parameters. In order to overcome this problem, various methods have been used to obtain the desired output variables, by developing models to specify the relationship between the input parameters and output variables. In the last two decades, the use of Design of Experiment (DoE), evolutionary algorithms and computational networks have grown rapidly and been adapted for many applications in different processes.

One process that is currently being optimized by the above mentioned techniques is the welding process. The following is a comprehensive literature review of the application of these techniques in order to correlate the input parameters to the output variables and to optimize the welding process through use of the developed models. The literature is reviewed according to the weld joint features.

2.2.1 Weld-bead geometry

Theoretically, an extremely thin fused layer might be sufficient for connecting the parts to be joined. The fusion layer should also not be thicker than necessary in order to avoid wasting of energy, edge burn-off, sagging of the weld pool and deep weld end craters [59]. Control of weld bead shape is essential as the mechanical properties of welds are affected by the weld bead shape [60]. Therefore, it is clear that precise selection of the process parameters is necessary.

Raveendra and Parmar [61] have built mathematical models using the fractional factorial technique to predict the weld bead geometry and shape relations (penetration, width, reinforcement height, width to penetration ratio and percentage dilution). The base metal was a 13-mm thick low carbon structural steel plate. The parameters of the FCAW process considered in this work were: arc voltage, welding current, welding speed, gun angle and nozzle-to-plate distance. They have developed models which can be used either to predict the bead geometry or to determine a combination or a range of parameters to obtain the desired bead geometry dimensions within the factors domain. Furthermore, these models can also be used in a production system for automatic control of welding conditions.

Gupta and Parmar [62] have used the fractional factorial technique (FFT) 2^{5-1} to develop mathematical models to predict the weld bead geometry and shape relationships for the SAW of microalloyed steel; the thickness ranged between 10

and 16 mm. They investigated bead penetration, weld width, reinforcement, dilution, width/penetration, and width/reinforcement as affected by wire feed rate, open circuit voltage, nozzle-to-plate distance, welding speed and workpiece thickness. It was found that the FFT was convenient for the prediction of the main effects and the interaction effects of different combinations of welding parameters. Mathematical models were developed which can be used effectively to predict the weld zone dimensions. Moreover, they mentioned that, if a specific set of requirements for weld bead dimensions is given, these models can be used in a computer program to determine a combination of parameters which will meet the requirements.

Yang et al. [63] have used linear regression equations for computing the weld features (melting rates, total fusion area, penetration, deposit area, bead height and bead width) from SAW process variables (electrode extensions range, welding voltage, welding current, welding speed and electrode diameter) using both positive and negative electrode polarity. The base material was a 19 mm thick ASTM A36 steel plate. They managed to develop regression equations for each weld feature in both polarity conditions. Their results indicated that the linear regression equations were equally useful for computing the various features of the SAW process.

The development of the mathematical models using the five level factorial technique to predict the weld bead geometry for depositing 316L stainless steel onto structural steel IS 2062 in single wire surfacing using the SAW process was studied by Murugan et al. [64]. They investigated the following weld bead parameters (penetration, reinforcement, width and dilution) as affected by the following SAW process variables (open-circuit voltage, wire feed-rate, welding speed and nozzle-to-plate distance). It was shown that the developed models can be employed easily in automated or robotic welding, in the form of a program, for obtaining the desired high quality welds. The results demonstrated that the bead penetration is not affected significantly by the voltage and nozzle-to-plate distance and the width is not affected by the latter. Furthermore, it was proven that the dilution increased when voltage and welding speed are increased from its lowest level to its centre level, but dilution is not affected by changes in voltage when welding speed is at its centre level. They found that the dilution decreased with increasing voltage when welding speed is increased from its centre level to its highest level.

Murugan and Parmar [65] used a four-factors 5-levels factorial technique to predict the weld bead geometry (penetration, reinforcement, width and dilution %) in the deposition of 316L stainless steel onto structural steel IS2062 using the MIG welding process. The following process parameters were controlled; open-circuit voltage, feed rate, welding speed and nozzle-to-plate distance. It was demonstrated that this factorial technique can be employed easily for developing mathematical models to predict the weld bead geometry within the factors ranges and these models can be fed into automatic robotic surfacing in a form of program to obtain the desired high quality. In addition to this, the effect of each factors on the weld features were determined and presented graphically.

The effect of process parameters (welding current, travel speed, gap width, bead height and arc deflection current) on the bead shape in a narrow gap-GTAW process with magnetic arc oscillation was studied by Starling et al [66]. Two AISI 304L stainless steel plates (9.5 and 6 mm thick) were employed to prepare the narrow gap joints and an AWS ER308L wire of 0.96 mm diameter was used as a filler metal. Statistical experimental design and linear-regression modelling were used in this investigation to develop the model. It was shown that the arc oscillation has little effect on the lateral fusion of the joint, however, this oscillation does improve bead shape by increasing its concavity. It was reported that when the gap width was reduced, the undercutting level tended to increase remarkably. Also, the effects of other welding parameters were in good agreement with the results of previous works.

Murugan and Parmar [67] developed mathematical models using RSM to study the direct and interaction effects of SAW parameters (open circuit voltage, wire feed rate, welding speed and nozzle-to-workpiece distance) on the cladding geometry (depth of penetration, height of reinforcement, weld width and dilution %). The process parameters obtained from the developed models were employed to clad IS2062 structural steel plate of 20-mm thickness using 316L stainless steel wire of 3.15 mm diameter. They concluded that a low dilution of 22.57% can be produced by both high voltage and high welding speed or by low voltage and low welding speed. It was reported that the hardness of the existing martensitic structures at the

intermediate mixed zones in overlays was below 400 VHN, due to low carbon content in the cladding.

Gunaraj and Murugan [68] have highlighted the use of response surface methodology (RSM) to develop mathematical models and plot contour graphs relating important input parameters namely the open-circuit voltage, wire feed rate, welding speed and nozzle-to-plate distance to some responses namely, the penetration, reinforcement, width and percentage dilution of the weld bead in SAW of pipes. They demonstrated that all responses decrease with increasing welding speed. Also, when the nozzle-to-plate distance increases all responses decrease, but reinforcement increases. Moreover, an increase in the wire feed rate results in an increase in all responses but the width remains unchanged.

In 1999, Gunaraj and Murugan [69] also studied the effect of SAW parameters on the heat input and the area of HAZ for low carbon steel with two joint types, bead-on-plate and bead-on-joint, using mathematical models developed by RSM. They found that for the same heat input, the area of the HAZ is greater for the bead-on-plate than that for bead-on-joint. They found that the effect of SAW parameters on the area of HAZ in both cases follows the same trend.

Koleva [70] has developed models to investigate the influence of EBW parameters namely electro beam power, welding velocity, distance from the main surface of the magnetic lens to the focus point and the distance between the magnetic lens and the sample surface on the welding depth and width. The experiment was performed with samples of austenitic steel, type 1H18NT. Also, the desirability approach was used to find the optimal welding conditions which would lead to the desired depth and width. The author has suggested the use of the developed models for on-line control of the process. This allows the selection of the optimal levels, eliminates the time required for testing and prevent losses of components.

Gunaraj and Murugan have divided their study into two parts, in the first part [71] they developed a model to relate the weld bead volume to SAW parameters with slightly changed open-circuit voltage limits from those used in their previous work [68]. This change is reflected in the development of new models to correlate the rest of the responses mentioned earlier to the process. Their results revealed that the penetration reduces, and the bead width and dilution increase considerably as

welding voltage increases. Also, they proved that the reinforcement is least when all SAW parameters are at their upper limits and the wire feed rate is at its lower limit. In the second part [72] the total volume of the weld bead was optimized (minimized) by keeping the other bead parameters as constrains to obtain sound welded pipes. Also, sensitivity analysis was carried out to predict the effect of the other bead parameters on the total volume.

Gunaraj and Murugan [73] continued their previous study and successfully investigated the effect of SAW parameters on HAZ characteristics. They pointed out that the heat input and wire-feed rate has a positive effect, but welding speed has a negative effect on all HAZ characteristics. They also concluded that the width of HAZ is of a maximum (about 2.2 mm) when the wire-feed rate and the welding speed are at their minimum limits.

The effect of the laser welding parameters on the bead geometry of 2.5 mm thick AISI304 stainless steel has been investigated by Manonmani et al. [74]. In this study the relationship between the process parameters (beam power, welding speed and beam incidence angle) and the weld bead parameters (penetration, bead width and area of penetration) has been developed using RSM. To verify the developed models a conformity test run were carried out using intermediate values of the process parameters. It was confirmed that the model developed were accurate since the error percentages were between -4.317% and 3.914%. It was demonstrated that the depth of penetration and penetration area increase as the beam power and the beam angle increase. Also, as the welding speed increases, the width decreases, whereas the penetration depth and area increase to an optimum value and then decrease with further increases in welding speed. This is due to the fact that the effect of keyholing is predominant at lower speed and as the welding speed is increased the mode of heat transfer changes from keyholing to conduction type of welding. It was reported that the variation in the bead width is slightly affected by the process parameters.

In 2005, Gunaraj and Murugan [75] extended their study and managed to establish mathematical expressions to predict the penetration size ratio 'PSR' (the ratio of bead width to the height of penetration) and the reinforcement form factor 'RFF' (the ratio of bead width to the height of reinforcement). These expressions and

the others developed earlier can be fed into a computer, relating the weld bead dimensions to the important SAW parameters, in order to optimize the process to obtain the required bead shape and weld quality.

Kim et al. [76] have used genetic algorithm (GA) and RSM to determine the optimal welding conditions in GMAW process, the base metal was mild steel with a thickness of 5.8 mm. First, the near-optimal conditions were determined through a GA, and then the optimal conditions were determined over a relatively small region by using RSM. The desirability function approach was used to find the optimal conditions. They correlated the following parameters; wire-feed rate, welding voltage and welding speed to some responses, namely, bead width, penetration and height. They concluded that by combining these two techniques, a good result for finding the optimal welding conditions can be obtained.

Koleva [77] has carried out another work by applying RSM to establish the relationship between performance characteristics (weld depth, weld width and thermal efficiency) and its influencing factors (beam power, welding velocity, focus position, focusing current of the beam and the distance to the sample surface) for EBW of austenitic stainless steel. Optimal welding regimes were found through the thermal efficiency optimization. New statistical approaches were proposed to choose the focus position at a condition of maximum thermal efficiency and welding depth.

A comparison between GA and RSM in the optimization of the GMAW process when welding of 9.5 mm thick mild steel with a square-groove butt joint was carried out by Correia et al. [78]. The criterion was to choose the best values of three parameters (reference voltage, wire feed rate and welding speed) based on four quality responses (deposition efficiency, bead width, depth of penetration and reinforcement). Their results indicated that both methods are capable of finding the optimum conditions. Also, they found that GA is a powerful tool for optimization, especially in irregular experimental regions, because there is no need to generate models. A selection of the correct settings of the GA tool parameters, such as, population number, number of generations, etc. was required. On the other hand, the RSM technique found a better compromise between the evaluated responses than the GA, but RSM is not able to build a model to fit the data over irregular experimental regions.

Koleva and Vuchkov [79] have established the relationship between EBW parameters (beam power, welding velocity and focus position) and weld-depth and weld-width using RSM in order to improve the quality of the process in mass production. They reported that the optimal process parameters values when welding stainless steel are: power 6.5-8 kW, welding velocity 11.667-1.333 mm/s and focus position 78 mm below the sample surface.

Kannan and Murugan [80] have studied the effect of flux cored arc welding process parameters (welding current, welding speed, nozzle-to-plate distance and welding torch angle with reference to vertical) on the duplex stainless steel clad quality in terms of penetration, width, reinforcement and percentage dilution. It was demonstrated that the process parameters have a significant effect on the bead geometry of the clad. The effect of the input process parameters on the clad quality parameters have been presented in graphical form, which assist in finding the welding parameters combination that would lead to the desired clad quality quickly.

Kim et al. [81] have studied the interrelationship between robotic CO_2 arc welding parameters and bead penetration by developing mathematical models using factorial techniques to predict the desired bead penetration. Partial-penetration and single-pass welds were fabricated in 12 mm SS400 plates based on controlling four different process parameters (arc voltage, welding current, welding speed and welding angle). They found that all the investigated parameters affect the bead penetration. They suggested extending the empirical formulae to plates of varying thickness and many other parameters which were not included in their research.

Kim et al. [82] have employed factorial design (FD) to correlate the robotic GMAW process parameters (welding voltage, welding speed and arc current) to three responses (bead width, bead height and penetration) for optimization purposes. The material used was plates of AS 1204 mild steel adopting the bead-on-plate technique. Electrode wire with a diameter of 1.2 mm with the same mechanical and physical properties of the base metal was used. Their results showed that all process parameters influenced the responses and the models developed are able to predict the responses with 0-25% accuracy.

D. Kim et al. [83] have proposed a method for determining the near-optimal setting of GMAW process parameters (wire feed rate, welding voltage and welding

speed) in welding plates made of mild steel with a thickness of 0.4 mm using a controlled random search (CRS). The CRS was used to determine the welding process parameters by which the desired weld bead (front bead height, back bead width and penetration) can be formed. They managed to determine the optimal welding conditions that lead to the desired weld beads.

Andersen et al. [84] have explained some concepts related to Neural networks (NNs) and how they can be used to model weld bead geometry, in terms of equipment parameters, in order to evaluate the accuracy of NN for weld modelling. They carried out a number of simulations and they used actual GTAW data for this purpose. The data consisted of values for voltage, current, electrode travel speed and wire feed speed and the corresponding bead width, penetration, reinforcement height and bead cross-sectional area. The performance of NNs for weld modelling was presented and evaluated using actual welding data. It was concluded that the accuracy of NN modelling is fully comparable with the accuracy achieved by more traditional modelling schemes.

Evaluation of ANN for monitoring and control of the plasma arc welding process was carried out by Cook et al. [85]. Three areas of welding application were investigated in this work: weld process modelling, weld process control and weld bead profile analysis for quality control. A network was constructed to determine the torch standoff, forward current, reverse current and travel speed for desired crown width and root width. The base material was 2219 aluminium alloy in the form of plates 6.35 mm thick; the joint type was bead-on-plate. It was confirmed that ANNs are powerful tools for analysis, modelling and control of such applications. Also, the results obtained when analyzing weld profile data suggested that ANNs can yield real-time results of equal or better accuracy and reliability than previously used data analysis algorithms.

Vitek et al. [86] have developed a model to predict the weld pool shape parameters (penetration, width, width at half-penetration and cross-section area) in pulsed Nd-YAG laser welds of Al-alloy 5754 using neural network (NN). They have considered the following process parameters; travel speed, average power, pulse energy and pulse duration. They developed a routine to convert the shape parameters into a predicted weld profile which was based on the actual experimental weld

profile data. The accuracy of the model was excellent. They concluded that this approach allows for instantaneous results and therefore, offers advantages in applications where real-time predictions are needed and computationally intensive predictions are too slow.

A comparison between back-propagation and counter-propagation networks in the modelling of the TIG welding process was made by Juang et al [87]. The complicated relationships between the welding process parameters and the weld pool features were considered. The input process parameters were: welding speed, wire feed speed, cleaning percentage, arc gap and welding current, while the output features were: front height, front width, back height and back width. The base metal was pure 1100 aluminium with a plate thickness of 1.6 mm. The experimental results, for the TIG welding process, showed that the counter-propagation network has a better learning ability than the back-propagation network. However, the back-propagation network has better generalization ability than the counter-propagation network.

Park and Rhee [88] have analyzed the signal of the plasma, or spatter, and bead size, to develop a bead size estimation system using the regression method and a NN method. It was found that the relationship is a nonlinear function caused by the penetration state. In contrast, the authors concluded that the regression models were appropriate for estimation when classifying the penetration state as partial penetration and full penetration, whereas, the NN was a very accurate estimation approach for bead size.

Chan et al. [89] have proposed a model to predict the bead-on-plate weld geometry (bead width, height, penetration and bag length at 22.5°) in GMAW of low alloy steel with C25 shielding gas. The process parameters were current, voltage, wire travel speed and workpiece thickness. Back propagation network (BPN) was used. Their results revealed that the weld bead geometry problem can be accurately modelled by using BPN. A new weld bead parameter $l_{22.5}$ (length from the origin to periphery at 22.5° from the work piece surface) has been defined.

Tarng et al. [90] have constructed the relationship between TIG welding process parameters (gap, gas flow rate, current, welding speed and cleaning) and weld bead geometry parameters (front depth, back height, back width and cluster

number). To search for the process parameters with the optimal weld pool geometry, an optimization algorithm called simulated annealing (SA) was applied to the network. Finally, the quality of the aluminium welds based on the output variables was classified and verified by a fuzzy clustering technique. The membership gradings corresponding to categories, good, fair and poor, were listed, and the results showed that the membership gradings for the category 'good' was much higher. Therefore, good weld quality can be obtained by using the optimal welding process parameters.

A comparison of back-bead prediction (width and depth) of the GMAW process using multiple regression analysis (MRA) and artificial neural network (ANN) analysis have been carried out by Lee and Um [91]. The controlled process parameters were: Gap, current, voltage and speed. The workpiece material was SS41 mild steel. It was found that the error rate predicted by the ANN was smaller than that predicted by MRA, in terms of the width and depth of the back-bead. It was also found that between the two predictions, the prediction of the width was superior to the prediction of the depth in both methods. Moreover it was concluded that the welding speed was the most important factor in the geometry of the back-bead, followed by welding current, gap and arc voltage.

Jeng et al. [92] have used BPN and learning vector quantization neural networks to predict the laser welding (LW) parameters for butt joints. The input parameters included were workpiece thickness and welding gap, while the output parameters 'responses' were optimal focus position, acceptable welding parameters of laser power, welding speed and weld quality, including weld width, undercut and distortion. They managed to integrate all the networks together to make an accurate prediction model of the laser welding parameters. Therefore, the limitation in the industrial application of LW for butt joints can be reduced through the use of this well established model.

Usage of ANN to model the GMAW process was reported by Nagesh and Datta [93]. BPN was used to associate the welding process parameters (electrode feed rate, arc power, arc voltage, arc current and arc length) with output features of bead geometry (bead height and width, penetration depth and area). The workpiece material was grey cast iron and a mild steel electrode was used. It was showed that

there was a small error percentage difference between the estimated and experimental values, which indicates that the NN can yield fairly accurate results.

Ridiings et al. [94] have applied NN technique to predict the outer diameter of the weld bead shape for three wire, single pass per side, submerged arc, line-pipe seam welds using the following welding process parameters: current, voltage and angle for the three wires as well as the welding speed, stickout and spacing of wires. The plates welded were of various thicknesses from 15.9 to 25.4 mm and they were varied in strength from X52 to X65. The welding was carried out using alloyed wires with a 4 mm diameter. It was shown that NNT can predict a weld bead shape with a high degree of confidence. The contribution of each factor to the variation in the final weld bead shape was determined. Furthermore, it was mentioned that an efficient model can be built using different NNs to predict the bead shape when using a smaller number of measurements for separate areas. However, the higher the number of measurements the better the accuracy of the technique.

Kim et al. [95] have presented an intelligent algorithm to establish the relationship between GMA CO_2 welding process parameters; (number of passes, arc current, welding voltage and welding speed and bead height), in order to predict the bead height using a NN and MRA for the robotic multi pass butt welding process of BV-AH32 steel with 12 mm in thickness. Their results showed that all the process parameters would influence the bead height. Also, the developed models were able to determine the welding condition required to achieve the desired bead height, which helped to develop an automatic control system and to establish guidelines and criteria for the most effective joint design.

The effect of energy input per unit length of weld from the travelling heat source on the laser efficiency and weld quality have been investigated by Casalino et al. [96]. A number of austenitic stainless steel butt joints were produced by CO_2 laser welding irradiation. The welding efficiency was calculated as the melted area to energy input per unit length ratio. Moreover, the weld crown and depth were measured in order to evaluate the quality of the joint. ANN was used to correlate the collected data to the process parameters (laser power, speed and material thickness), then these parameters were clustered using a fuzzy C-means algorithm. In order to select the optimum network parameters a 24-factorial design was used. Finally, a

model was built to choose the most suitable laser welding process for producing high efficiency and superior quality. It was recommended to consider more input factors such as laser focus, different materials and different weld beads.

Christensen et al. [97] have developed a multilayer feed forward network for modelling and online adjustment of GMAW process parameters to guarantee a certain degree of quality. In this study, butt joint welding with full penetration of standard steel S135 with 3 mm thickness was carried out. The process parameters were; wire feed speed, voltage, welding speed and gap width while the network inputs were back bead width and back bead height. In open loop control strategy, it has been demonstrated that use of the model to provide high quality welding is feasible and the network training was straightforward and effective. Whereas, in the closed loop experiments a single input and single output control scheme was investigated, it was shown that it was applicable for adaptive control of GMAW with some limitations.

Juang and Tarng [98] have adopted a modified Taguchi method (TM) to analyze the effect of each welding process parameter (arc gap, flow rate, welding current and speed) on the weld pool geometry (front and back height, front and back width) and then to determine the TIG welding process parameters combination associated with the optimal weld pool geometry. It was experimentally reported that, the four smaller-the-better quality characteristics, 'four responses' of the weld pool in the TIG welding of S304 stainless steel of 1.5 mm in thickness are greatly improved by using this approach.

Lee et al. [99] have used the Taguchi method and regression analysis in order to optimize Nd-YAG laser welding parameters (nozzle type, rotating speed, title angle, focal position, pumping voltage, pulse frequency and pulse width) to seal an iodine-125 radioisotope seed into a titanium capsule. The accurate control of the melted length of the tube end was the most important to obtain a sound sealed state. It was demonstrated that the laser pulse width and focal position were the laser welding parameters that had the greatest effects on the S/N ratios of the melted length. The optimal welding conditions were obtained at a pulse width of 0.86 ms and a focal position of 3.18 to 3.35 mm. Furthermore, confirmation experiments were conducted

at the optimal welding conditions, it can be said that the titanium tube ends were sealed perfectly.

2.2.2 Mechanical properties

In any welding process, the input parameters have a significance influence on the joint mechanical properties. By varying the input process parameters combination the output would be different welded joints with significant variation in their mechanical properties. Accordingly, welding is usually done with the aim of getting a welded joint with excellent mechanical properties. To determine these welding condition combinations that would lead to excellent mechanical properties. Different methods and approaches have been used to achieve this aim. The following is a review of some articles that utilize these techniques for the purpose of optimizing the mechanical properties of the welded joint.

Wang and Rasmussen [100] have investigated the inertia welding process of low carbon steels using RSM, with the purpose of establishing an empirical functional relationship between the process parameters (the axial pressure, the initial rubbing velocity and the total moment of inertia) and the breaking strength of the joint. It was concluded that a relatively wide range of operating conditions would produce successful welds. Also, they observed that the average microhardness at the weld was about 27 percent higher than the base material and the ideal weld should be made with the least possible amount of kinetic energy as long as full penetration at the interface is achieved.

Application of the factorial technique for weld quality prediction for the plasma transferred arc (PTA) weld cladding process on mild steel was investigated by Harris and Smith [101]. The process variables considered were current, powder feed rate, torch travel speed, oscillation width and torch stand-off distance. Four deposit quality features were measured, namely; deposit height, width, hardness and dilution. It was confirmed that all the process variables were acting as main process parameters in controlling the deposit quality. Also, it was reported that the PTA process is an excellent choice for depositing high quality hard-facing deposits at low controlled dilution.

Optimization of friction welding of dissimilar materials using factorial design was studied by Murti and Sundaresan [102]. They studied the friction welding of three industrially useful dissimilar materials: low alloy steel to austenitic stainless steel; medium carbon steel to high speed steel and aluminium to stainless steel. The main aim was to determine the metallurgical and mechanical behaviour of the friction welded joints produced using optimum welding conditions. Three mathematical models were developed to relate the NTS and shear energy to the process parameters, namely: friction pressure, friction time and forging pressure with different levels according to the two materials which formed the joint. It was reported that the statistical experimental design was useful for reducing the number of trials necessary to optimize the welding conditions for friction welding. Also, the strength of the joint which was produced by using the optimized condition was in fair agreement with the predicted results. Moreover, in all cases, the joint strength was at least as high as those of the softer of the two materials that formed the joint.

Control of distortion in robotic CO_2-shielded FCAW was investigated by Arya and Parmar [103]. A three level fractional factorial technique was used to develop mathematical models to predict the angular distortion in 10 mm thick low carbon steel. The effect of arc voltage, wire feed rate, welding speed and groove angle on the angular distortion in single vee butt welds was investigated with and without sealing run. It was concluded that the models developed were fairly accurate and can be usefully employed for controlling the angular distortion in automated welding lines using the FCAW process.

Yamaguchi et al. [104] have investigated the friction welding process of 5056 aluminium alloy using RSM. Their aim was to find the optimal welding conditions that would yield maximum tensile strength at the weld. The process input parameters were friction pressure, up-set pressure, friction time, rotating speed and braking time. It was reported that the successful welds showed 89.2% joint efficiency in tensile strength. It was also observed that the friction layer formed at the friction interface disappeared in these successful weld runs.

Koichi et al. [105] have studied the combination of welding conditions that produce maximum notched tensile strength of friction welded joints of S4 5C carbon steel using RSM. They managed to correlate the process parameters (friction

pressure, upset pressure, friction time, rotation speed and braking time) to the tensile strength of the weld joint. Successful weld strength was obtained using the optimal welding condition predicted by the empirical equation.

Benyounis et al. [106] have proposed models using RSM to investigate the effect of welding parameters in SAW (welding current, arc voltage and welding speed) on the impact strength at two testing temperatures of 50 °C and 27 °C. The aim was to predict and optimise the impact strength of the spiral-welded joints with respect to the process parameters. It was observed that the welding current was the most significant factor associated with the impact strength, then the welding speed, whereas the welding voltage has no significant effect within the factors domain investigated. They listed the optimal welding conditions that would lead to acceptable impact strength with improving the process productivity.

Zhou et al. [107] have utilized factorial experimentation to investigate the influence of joining parameters (rotational speed, frictional time and pressure) on the notched tensile strength (NTS) of dissimilar aluminium-based metal matrix composite MMC/AISI304 stainless steel friction joints. It was observed that frictional pressure and rotational speed have a statistically-significant effect on the NTS values. Moreover, they reported that the highest NTS occurs in joints produced at a high frictional pressure of 120 MPa.

The production of strong and stiff, aluminium-titanium, multi-layered composites (laminates) by explosive welding was undertaken by Ege et al. [108]. The study was performed using RSM to investigate the mechanical behaviour of the laminates with changes in two characteristic variables; abundance of interfaces and volume percentage of the more ductile component. Eighteen laminates were produced and then one-step welding of these laminates was carried out by explosive-introduced pressuring. Yield strength, ultimate tensile strength and elongation were the responses under consideration. A second-order model was fitted to define the relationship between the yield strength and the two variables. It was reported that the mechanical properties of the laminates depend strongly on the relative amounts of the components, but only weakly on the abundance of the interface within the selected operability region. It was also mentioned, that with the aid of the developed

model it is possible to fabricate laminates that are tailored to strength, density and load specifications.

Fatigue endurance of flux cored arc welded (FCAW) cruciform joints containing lack of penetration (LoP) using Design of Experiment (DoE) was studied by Balasubramanian and Guha [109]. The aim was to optimise some dimensional factors that affected the fatigue life of cruciform joints made of quenched and tempered steel (ASTM 517 F grade). It was mentioned that the techniques described in this work were fairly simple and economical to optimise the time consuming fatigue tests. It was also reported that some factors affecting the fatigue endurance were optimised to attain a maximum fatigue life, but the validity of the procedure is limited to the factors domain considered for the investigation. It was noted that the ANOVA technique is the most convenient to identify the significance of the main effects and interaction effects of joint dimensions. The same authors [110] continued their investigation by developing mathematical models using DoE to predict the fatigue life of shielded metal arc welding SMAW and FCAW cruciform joints failing from root and toe regions. Using the developed models the fatigue life of SMAW and FCAW cruciform joint can be predicted at a 95% confidence level, however, the validity of the models is limited to the factors domain. It was found that the factorial experimentation technique DoE is more economical for predicting the effect of various factors on fatigue life through conducting a minimum number of experiments.

Allen et al. [111] have proposed a model based on central composite design (CCD) with the alpha parameter set equal to 2, for robotic gas metal arc welding of sheet metal of 409-gauge, stainless steel. The six factors controlled in this study were: wire feed speed, weld travel speed, arc voltage, contact-tube-to-work distance, root opening and offset. The objective was to minimize the weld cycle time by maximizing welding speed, while maintaining predictable weld quality over a range of worst-case processing conditions. The optimal welding conditions for this type of material with a lap joint were reported and confirmed by experimental tests. The effect of the process parameters was presented graphically.

Raghukandan [112] has conducted experiments to clad low carbon steel and copper plates using nitroglycerine explosive (2500 m/s detonation velocity). The aim

was to adopt RSM to relate the bond and shear strength of the clad to four process factors (flyer thickness, loading ratio, angle of inclination and stand-off distance). Mathematical models were developed and the effect of process parameters on the responses was discussed. It was found that the flyer thickness, the loading ratio and the angle of inclination have significant contribution to the interfacial morphology of explosive clad.

V. Murugan and Gunaraj [113] have implemented RSM to correlate the angular distortion in GMAW of structural steel plate (IS: 2062) to the process parameters, namely: time gap between successive passes, number of passes and wire feed rate. The main and interaction effects of the process parameters were analyzed and presented. It was found that the number of passes had a strong effect on the response, therefore, to control the angular distortion in practice the number of passes has to be monitored carefully. Moreover, it was demonstrated that all the process parameters have a negative effect on the angular distortion.

Koganti et al. [114] have employed a full factorial design to define the optimum weld MIG process parameters for non-treatable 5754 aluminium alloys. The effects of weld process parameters on the lap joint failure load (tensile-shear strength) and weld penetration were investigated. The process parameters were: power input (torch speed, voltage, current, wire feed rate), pulse frequency and gas flow rate. The joint strengths and weld penetration were measured for various operating ranges of weld factors. It was indicated that the power input and the gas flow rate were the two significant factors based on lap shear load to failure and weld penetration data. It was reported also, that the lower the power input, the lower the shear load to failure and depth of penetration and vice versa. The optimum factor settings for higher joint strength were high power input and high gas flow rate.

Sampath [115] has presented an innovative constrains-based approach that proved quite efficient in developing a specification for consumable solid-wire electrodes for GMAW of HSLA-80 and HSLA-100 steels that meet or exceed the US Navy requirements. Initially, he converted the US Navy requirements into a set of constraints which related the chemical composition of steels to certain metallurgical characteristics. Subsequently, a 2^3 factorial design was used to develop a batch of welding electrodes in order to evaluate their performance. Among the eight

electrodes used, it was shown that two electrodes met or exceeded ER-100s requirements, while one electrode met or exceeded ER-120s requirements. It was concluded that the use of this approach greatly reduced the risk inherent in developing electrode specifications.

Canyurt [116] has extended the GA approach to the estimation of mechanical properties of the joints of brass material. He developed non-linear models to specify the effect of GTAW process parameters (gap between plates, torch angle, quantity of shielding gas, pulse frequencies and electrode tip angle) on the tensile strength of the welded joint. He examined the effect of the five welding parameters on the strength value using the genetic algorithm welding strength estimation model (GAWSEM). Also, he indicated that the changes in the gap between the joint parts from 0 to 0.5 mm leads to a 4.4 times decrease in the joint strength and changes in the torch angle from 60° to 90° leads to a 1.9 times increase in the joint strength. Furthermore, he reported that the optimum quantity of the shielding gas and the pulse frequencies were 16.5 l/min and 30 Hz.

Pine et al. [117] have presented an experimental and numerical study to determine the torsional stiffness, elastic limit and ultimate strength of spot welded, adhesively bonded and weld-bonded box sections. They investigated a variety of factors, namely: joining technique, sheet thickness, steel strength, section area, section design and end weld using factorial design techniques to determine their effects on the torsional properties of box sections. The authors have concluded that the joining technique, section area and section thickness were the main factors which have the greatest effect on the torsional stiffness of the box sections. It was found that the torsional stiffness can be improved without substantial weight gain by changing the joining technique from 50 mm pitch spot welds to adhesive bonding, increasing the section area and to a lesser extent, changing the section design. Furthermore, the steel strength was the most important factor in determining the elastic limit and ultimate strength.

Control of distortion and overall quality of welds were investigated by Casalino et al. [118] in order to select the GMAW process parameters that minimize thermal deformation and evaluate weld quality. They integrated the artificial intelligence (AI) techniques and FEM with the aid of experimental trials of bead-on-plate welds. The

base metal was 1.6 mm thick low-carbon steel, a 0.9 mm diameter copper-coated wire was used as an electrode with a shielding gas consisting of a 75% Ar – 25% CO_2 mixture with flow rate of 10-15 ft^3/h. ANN was used at first to link the process parameters to the geometry of the molten zone, which allowed the geometries throughout a range of process parameters to be calculated. Then FEM was applied to predict the residual stress value and distortion in the welded joint. Finally, fuzzy C-means clustering algorithm was applied to evaluate the quality joints. Mathematical models for GMAW were constructed. Experimentally butt welded joint were validated. It was concluded that the experimental result are in good agreement with the mathematical model.

ANN and Taguchi methods were used to predict the bead geometry parameters (front width, back width and depth of penetration) by Seshank et al. [119]. Aluminium plates were bead-on-plate welded using pulsed current GTAW, the controlled parameters were: peak current, base to peak current ratio, % time at peak current, frequency and welding speed. Taguchi's orthogonal array was used to set the welding conditions to be studied. Different ANNs were built to predict the responses. The results they achieved were found to be of good accuracy. An online relationship has been built to make the prediction of the depth of penetration possible if the top bead width is known. Moreover, it was found that a simple MLP with a single hidden layer with a Tanh transfer function and momentum learning is more effective than the networks that have two or three hidden layers.

Li-Ming et al. [120] have established a static model for SiC_w/6061 Al metal matrix composites in diffusion welding using ANN. The relationship between welded joint strength and welding parameters, such as, welding temperature, welding pressure and welding time was presented. The effect of process parameters on the joint strength was demonstrated and optimal technical parameters were obtained. It was proven that the developed static model was in good agreement with the actual data.

Sterjovski et al. [121] introduced ANN modelling as an alternative technique to those currently in the literature to predict the hardness of HAZ, and hence, trying to control it to minimize the risk of hydrogen assisted cold cracking in welding in-service pipelines by the hot tapping technique. The model developed included

materials characteristics; chemical composition and hardness (as inputs), the peak temperature, holding time and cooling rate of the HAZ thermal cycle simulation were also used as key inputs in the model to predict the HAZ hardness. It was reported that the hardness of HAZ increases with increasing the following: carbon content, original hardness of pipe or fitting material and more rapid cooling. They compared the predictive capabilities of the models developed with other published works to the neural network model they developed. It was clear that the NN model produced a much lower error across a broader range of HAZ hardness values.

Lightfoot et al. [122] have used ANN to develop a model to study the FCAW process factors affecting the distortion of 6 – 8 mm thick D and DH grade steel plates. A sensitivity analysis was carried out, which highlighted a number of apparently key factors that influenced distortion. It was proven that the carbon content played a key role in the amount of distortion produced by the welding process. They found that an increase in the carbon content was beneficial in reducing thin plate distortion caused by welding. Also, they identified a number of distortion-related factors, such as carbon content, YS/TS ratio and rolling treatment. It was concluded that these factors can be controlled to reduce the distortion in 6-8 mm thick plates.

Sterjovski et al. [123] have applied the ANN models to predict the mechanical properties of steels in various applications, namely: impact strength of quenched and tempered pressure vessel steel exposed to multiple postweld heat treatment cycles, the hardness of the simulated HAZ in pipeline and lap fitting steel after in-service welding and the hot ductility and hot strength of various microalloyed steel over the temperature range for stand or slab straightening in continuous casting process. It was found that the three ANN models successfully predicted the mechanical properties. It was also shown that ANNs could successfully predict multiple mechanical properties and the result of the sensitivity analysis were in agreement with both findings of the experimental investigation and reported results in the literature. Furthermore, it was mentioned that the use of ANNs resulted in large economic benefits for organisations through minimizing the need for expensive experimental investigation and/or inspection of steels used in various applications.

Okuyucu et al. [124] developed a model using ANN for the analysis and simulation of the correlation between friction stir welding (FSW) parameters of aluminium plates and mechanical properties of the welded joint. The process parameters consist of weld speed and tool rotation speed verses the output mechanical properties of weld joint, namely: tensile strength, yield strength, elongation, hardness of WZ and hardness of HAZ. Good performance of the ANN model was achieved and the model can be used to calculate mechanical properties of the welded plates as a function of process parameters. Also, it was found that the correlation between the measured and predicted values of tensile strength, hardness of HAZ and hardness of weld metal were better than those of elongation and yield strength.

Laser butt-welding of a thin plate of magnesium alloy using the Taguchi method has been optimized by Pan et al. [125]. They studied the effect of Nd-YAG laser welding parameters (shielding gas type, laser energy, conveying speed, laser focus, pulse frequency and pulse shape) on the ultimate tensile stress. Their result indicated that the pulse shape and energy of the laser contributed most to thin plate butt-welding. It was found that the optimal combination of welding parameters for laser welding were argon as a shielding gas, a 360 W laser energy, a workpiece speed of 25 mm/s, a focus distance of 0 mm, a pulse frequency of 160 Hz and type III pulse shape. It was also found that the superior ultimate tension stress was 169 MPa at an overlap of the welding zone of approximately 75%.

Murugananth et al. [126] have coupled ANN model with optimization software, which utilize linear and nonlinear techniques to explore possible combination of carbon, manganese and nickel concentrations for a given set of welding parameters, to predict the weld metal composition that would maximise the toughness at – 60 °C. The predicted weld metal composition was Fe-0.034C-0Mn-7.6Ni-0.65Si-0.038O-0.018N-0.013P-0.006S (wt. %) and toughness of 87 J ±20 J at 60 °C.

Factors that affect weld mechanical properties (oxygen, nitrogen, carbon, hydrogen and iron contents in the weld joint as well as the cooling rate) of commercially pure titanium have been investigated by Wei et al. [127]. ANNs techniques were used, to predict the ultimate tensile strength, yield strength, elongation, reduction of area, Vickers hardness and Rockwell B hardness. The input

data was obtained from mechanical testing of single-pass autogenous welds. The ANN models were developed. An oxygen equivalent equation (OEE) was also used to predict the mechanical properties of CP titanium welds; a good agreement was found between both ANN and OEE. The obtained results indicated that both oxygen and nitrogen have the most significant effect on the strength while hydrogen has the least effect. Also, it was reported that cooling rate is more important than the carbon and iron content in the UTS model, and more important than oxygen and the iron content and equally important as the carbon content in the yield strength model.

Anawa et al. [128] have applied the Taguchi approach to optimize the laser welding process of dissimilar materials, namely: plain carbon steel and AISI316 with the same thickness of 1.5 mm. The process parameters were laser power, welding speed and focus position against one response (notched tensile strength). The experimental results indicated that the process could be optimized using the Taguchi method in order to obtain superior welded joints. Anawa et al. [129] have continued their investigation and studied the effect of the laser welding parameters mentioned above on the impact strength of the same joint at room temperature using the same optimizing technique. The results indicated that the laser power has the most significant effect on the impact strength. Also, it was mentioned that the optimal settings to obtain excellent impact strength were the highest laser power, a welding speed of 750 mm/min and a focus position of -0.5 mm.

Joining steel with aluminium by means of laser welding and zinc-based filler wire has been investigated by Mathieu [130]. In order to optimize the process a series of samples has been carried out in accordance with the Taguchi method. The chosen process parameters were: laser power, defocusing length, tilt angle of the assembly with respect to the laser beam axis, braze welding speed, filler wire speed, diameter of the fibre and laser beam shaping. The effect of these parameters on the tensile strength and microstructure of the weld has been studied. It was found that by using the Taguchi approach, it is possible to find out the best operating conditions. By using these operating conditions the mechanical performance of the steel/aluminium assemblies reach fracture strengths greater than 20 N/mm.

2.2.3 Comparison between the optimization techniques

Derived from the above literature review some insight has been gained into the use of DoE, ANN, GA, Taguchi method and other techniques for modelling and optimizing different welding processes. It was noted that RSM performs better than other techniques, especially ANN and GA, when a large number of experiments are not affordable. The trend in the modelling using RSM has a low order nonlinear behaviour with a regular experimental domain and relatively small factors region, due to its limitation in building a model to fit the data over an irregular experimental region. Moreover, the main advantage of RSM is its ability to exhibit the factor contributions from the coefficients in the regression model. This ability is powerful in identifying the insignificant factors main effect, insignificant interactions or insignificant quadratic terms in the model and thereby can reduce the complexity of the problem. On the other hand, this technique required good definition of ranges for each factor to ensure that the response(s) under consideration is changing in a regular manner within this range. The most popular designs within RSM designs are the central composite design (CCD) and Box-Behnken design. In regard to ANNs, it noted that ANNs perform better than the other techniques, especially RSM when highly nonlinear behaviour is the case. Also, this technique can build an efficient model using a small number of experiments; however the technique accuracy would be better when a larger number of experiments are used to develop a model. On the other hand, the ANN model itself provides little information about the design factors and their contribution to the response if further analysis has not been done. The most popular ANNs are learning vector quantization neural networks, back-propagation and counter-propagation networks. In the case of GA, it is a powerful optimization tool especially in irregular experimental regions. The main characteristic of GAs over the other optimization techniques is that they operate simultaneously with a huge set of search space points to find the optimal welding condition instead of a single point. On the other hand, this technique required a good setting of its parameters and uses a large computational effort, and therefore a long run time. Also this technique does not develop mathematical models. The Taguchi method is also one of the powerful optimization techniques which characterize with improving the product quality and reliability at low cost. The optimization algorithm works by

calculating signal-to-noise (SN) ratios for each combination and then the combination having a maximum SN ratio is defined as the optimal setting. However, Taguchi's analysis approach of SN may lead to non-optimal solutions, less flexibility and the conduction of needless experiments. Table 2.1 presents a comparison between the above mentioned common modelling/optimizing algorithms methods based on this literature review.

Table 2.1: Comparison between the common modelling/optimizing techniques

Technique / Comparison	ANNs	GA	RSM	Taguchi	Factorial Designs
Computational time	Long	Very long	Short	Medium	Short
Experimental domain	Regular or irregular	Regular or irregular	Regular only	Regular or irregular	Regular only
Model developing	Yes*	No	Yes	No	Yes†
Optimization	Through model	Straight	Through model	Straight	Through model
Understanding	Moderate	Difficult	Easy	Normal	Easy
Availability in software	Available	Available	Available	Available	Available
Optimization Accuracy level	High	High	Very high	Normal	Very high
Application	Frequently	Rarely	Frequently	Rarely	Occasionally

*) No factors interaction effects. †) No factors quadratic effects.

The optimization methods covered in this survey are appropriate for modelling, controlling and optimizing the different welding processes. The survey reveals the high level of interest in the adaptation of RSM and ANNs to predict response(s) and optimize the welding process. Generally, there is a lack of comparative study regarding the performance of the optimization methods. In other words, for a given optimization problem which method is best suited. Combining two optimization techniques, such as GA and RSM, would reveal good results for finding out the optimal welding conditions. Future work should focus on the application of these modelling and optimization techniques to find out the optimal welding combinations for a certain welding process at which the process could be considered safe, environment friendly and economical.

2.3 Review of Some Previous Studies on Laser Welding of Different Materials.

A rapid growth has been now achieved in the development of automated material processing systems using industrial lasers as the processing tool. The fraction of welding in all industrial applications of lasers is about 15-25%. This percentage may vary from country to country. This rapid growth came into effect because of the advantages of the laser over the conventional material processing method. The laser welding process is a non-reactive process and it has the ability to be adapted to most types of processing tasks. Moreover, laser welding has the ability to provide deep, narrow welds at high welding speed with minimal heat input. These advantages make it a most powerful candidate for automobile production, especially with the increased requirements concerning precision, flexibility and degree of automation [131].

Kim [132] has reported that the ability to absorb the laser power depends on the wavelength of the laser beam and the optical properties of the workpiece material. Also, he mentioned that the principal variables of laser beam welding are the laser power, travel speed and spot size. Carlson [133] has mentioned that the data obtained in one investigation often is not directly transferable to another machine or optics, due to the differences in the laser machines designs and even differences in the focusing optics on the same machine. However, most characteristic trends in parametric behaviour would be expected to be more universal.

Carlson [133] has mentioned also that deep penetration welding can be performed when the power density of the beam exceeds about 10^6 W.cm^{-2}. When the workpiece is exposed to a beam with a power density that exceeds this threshold, the exposed area melts and vaporizes almost instantaneously, creating a cavity or keyhole. When the workpiece moves relatively to the beam, the vapour pressure of the metal sustains the keyhole and, along with the surface tension forces, directs molten metal flow from the front of the keyhole, along the sidewalls of keyhole, to the rear of the keyhole where it rapidly solidifies forming the weld nugget. Therefore, the metal vapour or plasma must be controlled to maintain the keyhole as it is highly absorbent of laser power. As a result of maintaining the keyhole, a steady

state condition could be attained with a characteristic deep penetration weld along with its high aspect ratio (depth/width).

The temperature of the keyhole has been addressed by Kroos et al. [134]. They concluded that the temperature at the keyhole wall exceeds the evaporation temperature by approximately 100 K. It was found that there is a threshold for laser power per workpiece thickness, above which the formation of the keyhole commences. For iron the threshold is 7900 Wcm^{-2}. Denney and Metzbower [135] have shown that the diameter of the keyhole is very close to the diameter of the focused laser beam.

Nath et al. [136] have estimated the utilized laser power in welding processes using experimental results and a dimensionless parameter model. It was reported that the estimated laser coupling efficiency, absorption of CO_2 laser beam, in conduction and keyhole welding were about 16% and 65% respectively for bead-on plate welding of AISI304 stainless steel. It was mentioned that the conduction loss is small at high welding speed and in keyhole welding.

Duhamel and Banas [137] have plotted the depth of penetration as a function of heat input for different steel alloys; their data for stainless steel is shown in Fig. 2.2. The data shows a tendency to be randomly scattered with a general trend of increasing penetration with increasing heat input. They attributed the scatter to plasma control effectiveness and incident beam spot size. Furthermore, they proposed a curve through the data points which represent the minimum energy required to fabricate the weld. This is the "minimum energy envelope" shown in Fig. 2.2 and represents the optimized welding conditions.

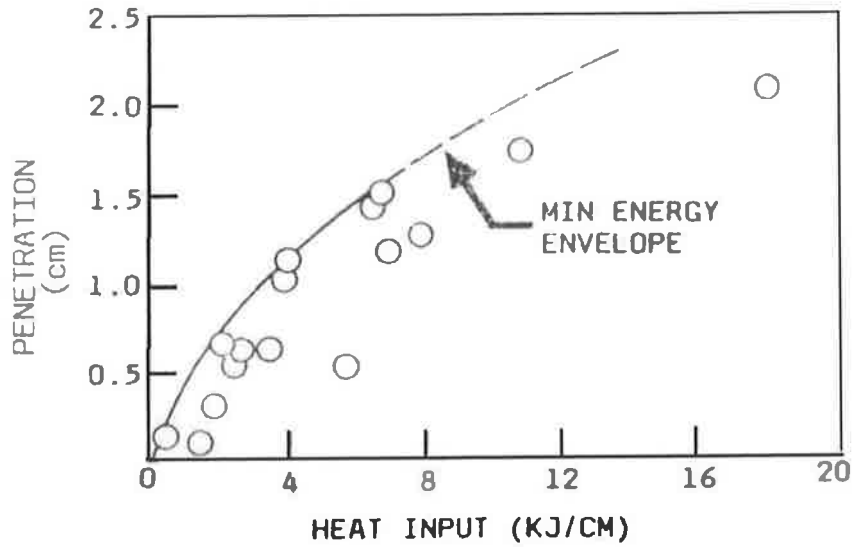

Fig. 2.2: Effect of heat input on weld penetration for AISI304 [137].

Carlson [133] have also investigated different combinations of laser power levels and welding speeds which produce full penetration welds as shown in Fig. 2.3. It was noticed that the welds made up at lower power and slower travel speeds were wider. He demonstrated that as the laser power and the welding speeds increases, the heat input decreases resulting in narrower welds with larger aspect ratio. It was observed that the minimum heat input of 5.73 kJ/cm associated with a laser power of 8 kW and a welding speed of 14 mm/sec, the most efficient combination, produced full penetration with largest aspect ratio. As the laser power and welding speed combination increases above the most efficient, the heat input increases again resulting in wider welds. It was confirmed by Carlson that these are an optimum set of parameters which would produce full penetration with the highest aspect ratio for a particular beam profile, material type, focusing optics and welding procedure.

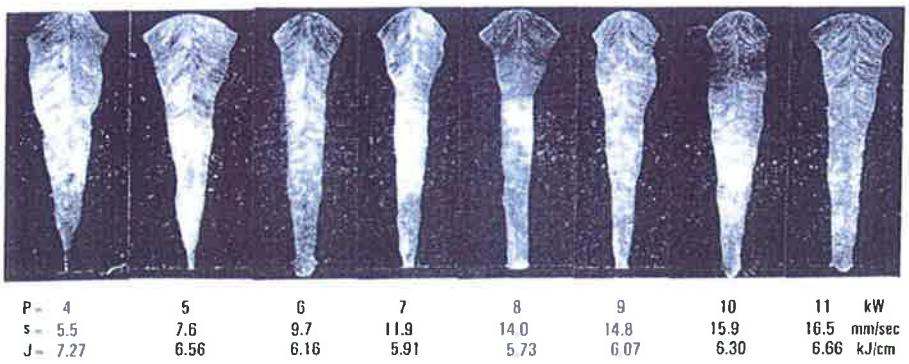

Fig. 2.3: Weld Bead profile for full penetration weldment at different combinations [133].

In laser welding, the weld bead shape, mechanical properties and microstructure of the welded joint are influenced by a number of process parameters such as laser power, welding speed, depth of focus in respect to the substrate surface and shielding gas. These parameters and their effect on the outcome of the laser welding process for common materials will be reviewed in the following subsections.

2.3.1 Laser power

The main effect of the laser power is on the depth of penetration. Generally, the depth of penetration increases in a linear manner with the increase in the laser power as reported in [138]. El-Batahgy [139] has pointed out that laser beam power has a strong effect on the depth of penetration when welding AISI304L, but it has less effect on the other weld bead parameters. Batahgy also concluded that the laser power has slight effect on the microstructure of the welds, however, the higher the laser power, the coarser the dendritic structure. Within the laser power range considered in this study it has been found that the laser power has no significant effect on the mechanical properties of the welded joint at room temperature.

Laser beam welding of SS1147 mild steel has been studied by Huang et al. [131]. It was found that for a given sheet thickness there is a minimum requirement of output power in order to fully penetrate through the sheet. Also, it has been suggested to employ the highest output power possible to improve the production

efficiency by using high welding speed, yet the power can only be increased until the maximum output power achievable by the laser is reached. However, to ensure long life of the laser it was recommended to apply output power of the laser at least 10% below the maximum achievable power.

Kim [132] has reported that at a fixed welding speed, the depth of penetration is proportional to the laser power. Moreover, it was found that if the metal vapour pressure is insufficient to resist the fluid dynamic forces of the molten metal, the deep keyhole collapses. If this is the case and at low travel speed (less than 0.5 m/min), an abrupt decrease in penetration occurs, and a roughly hemispherical fusion zone is obtained.

It was mentioned by Dawes [4] that when using continuous wave (CW) mode CO_2 laser with up to 10 kW for welding steel, a penetration of 1.5 mm for every kilowatt of the power would be achieved at welding speed of 1 m/min. Furthermore, it was stated that the relationship between the laser power and penetration is proportional.

A parametric investigation was conducted by Bruck et al. [140] to evaluate the effect of power, travel speed and focal position on high power laser welding of Inconel 600, AISI304 and AISI1018. These parameters were varied for flat, horizontal and vertical position welding. It was reported that the penetration increases with laser power and decreases with travel speed. The superior penetration was found to be in the vertical welding position. Flat position welds were, in general, of slightly deeper penetration than the horizontal position welds. It was found that the absence of weld defects is evident in all cases. However, porosity was observed near the root of some partial penetration. It was mentioned that such porosity may be eliminated by specific joint preparation such as a gap.

Ng and Watson [141] have investigated the clamping geometry and welding speed effect on the hardness, weld penetration and weld width of a high carbon steel gauge plate of 2 mm thickness welded using CO_2 laser. It was found that the clamped geometry led to lower hardness and a coarse grain structure. Whereas, for the same operating conditions, the unclamped geometry gave deeper weld penetration and wider width. It was reported that the hardness gradients were lower for the clamped geometry by approximately 40%, due to the slower cooling rate achieved in the

clamped geometry, therefore, these welds were less likely to crack under cyclic loading.

2.3.2 Welding speed

Since the depth of penetration is an important weld bead parameter, its relationship with the welding speed should be discussed. It was confirmed in [138] that this relationship is almost inversely proportional as the welding speed is increased up to at least 5 m/min.

In 1980, Mazumder and Steen [142] reported that for a given power, welding can be carried out over a range of thicknesses. Outside that range it is not possible to achieve full penetration. Higher speed may lead to insufficient penetration, whereas, lower speed leads to excessive melting, loss of material and weld perforation. It was found that for acceptable weldment the range of the welding speed decreases with increasing material thickness as shown in Fig. 2.4.

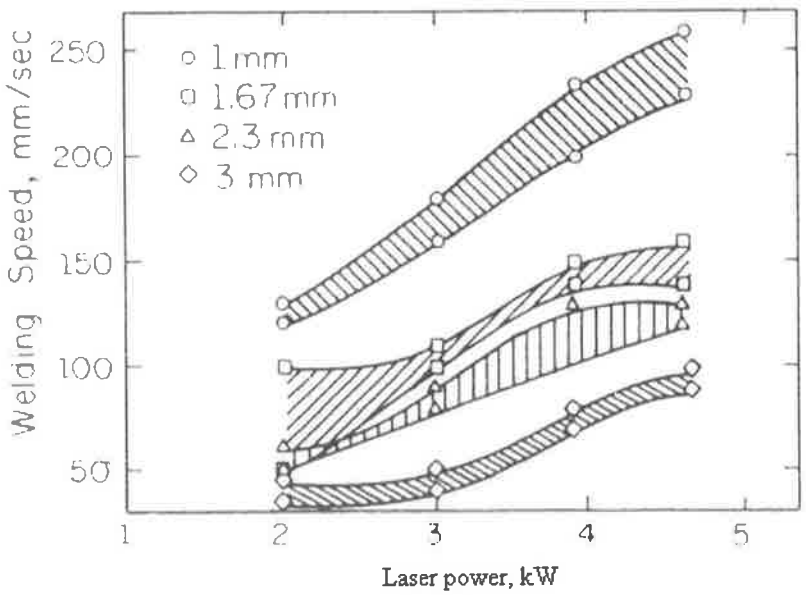

Fig. 2.4: Welding speed vs. power for 5 kW CO2 laser, material Ti-6Al-4V [142].

It has been found by Manonmani et al. [74] that as the welding speed increases the penetration depth increases and then it decreases with further increase in the welding speed. They have related this to the effect of keyholing, since it is predominant at lower welding speed and as the speed is increased the mode of the heat transfer changes from keyholing to conduction type of welding. At low speed

the diffusion of the heat into the base metal is easy and hence penetration increases. Moreover, they have mentioned that the area of the fusion zone has the same trend of the depth of penetration because it is a function of penetration depth and width of the bead.

The second most important bead parameter is the weld pool width. Generally, the bead width decreases as the welding speed increases as reported in [4, 74]. In fact, the ratio of penetration to width is usually investigated and it normally increases with increasing welding speed as stated in [4, 139,132].

2.3.3 Focal point position

The focus spot size has to be carefully selected to guarantee the required power density at which the weld keyhole would be formed. For example, if the focus spot size were doubled for a given laser power, the area would be four times larger and the power density would be only a quarter of that achieved with the original spot size. The question to bear in mind is, 'where should the focus position be?' The answer is the position at which the maximum depth of penetration can be achieved, which usually appears to be at the minimum waist diameter or just to one side of it [4]. Many investigations were carried out to find out the optimal focal position with respect to the substrate. It has been reported in [138] that the optimal position is approximately 1 mm below the surface when welding 6 mm AISI301 with a laser power of 5 kW and welding speed of 16 mm/s. For mild steels, it has been known from general consensus that the optimal position for the focal point is below the surface, but the exact distance is dependent on the material thickness, laser power and welding speed [131].

It was mentioned by Kim [132] that the depth of penetration decreases linearly as the focal position decreases from -1.75 to -3.5 mm. He found that as the depth of focus is less than -1.75 mm, the beam shape tends to be a characteristic of conduction welding. He concluded that the optimal focus position in 3 kW CO_2 laser welding is between 0.5 and 1.5 mm below the surface when a focusing lens with a focal length of 127 mm is used.

The relationship between the defocusing distance and penetration depth of AISI304L and AISI316L has been pointed out in [139]. It was found that the depth of penetration deceased from 1.9 to 1.6 mm as a result of changing the defocusing

distance from zero to either -1 or 1 mm, then the depth of penetration decreased remarkably. He verified that the effective range of defocusing distance at which the maximum penetration and acceptable weld profile can be achieved lies between zero and -1 mm. Furthermore, he reported that the most acceptable weld profile was obtained at a defocusing distance of -0.2 mm. However, in the case of welding a plate of 5 mm thickness the optimal defocusing distance, to attain an acceptable weld profile, was -0.4 mm.

2.3.4 Shielding Gases

During welding, metal vapour ejected from the keyhole absorbs laser power, ionises and forms a plasma cloud just above the weld keyhole. This cloud is partially transparent to the laser beam and if not considerably reduced will expand and scatter the laser beam and the weld depth of penetration will be reduced as a result of the reduction in the power density. A correct shielding gas is used to suppress plasma formation and ensure maximum transmission of the laser beam and its absorption by the workpiece. Other benefits that can be gained by using shielding gas are protection of the keyhole and the solidified molten metal from oxidation consequently avoiding porosity and oxide inclusions which would lead to poor weld quality [4,131].

El-Batahgy [139] has used initially argon gas as a shielding gas, then for comparison he used helium, while other laser parameters were kept constant. He noticed that the weld profile was remarkably improved where fusion zone interfaces are almost parallel to each other. This is due to the effect of plasma cloud being reduced as a result of the higher ionization potential of helium.

Kim [132] has investigated the effect of gas flow rate (helium and argon) when welding AISI316 and low carbon steel. It was reported that when low flow rate (less than 10 l/min and less than 5 l/min for helium and argon respectively) was used the penetration depth was less deep and the bead width was wider. This was due to the fact that a low flow rate does not remove the plasma and this absorbs the laser power. But as the moderate flow rate of 10-30 l/min and 5-15 l/min for helium and argon respectively is used a sound bead and deep penetration was achieved and the depth of penetration increased gradually with increasing flow rate. When the gas flow rate is further increased the humping bead and the big porosity were obtained and the depth

of penetration sharply decreased. This is due to the fact that the high gas pressure would disturb the flow of molten metal around the beam hole and expand the beam hole to reduce the beam focusing effect, thereby decreasing the depth of penetration.

Sibillano et al. [143] have studied the effect of gas conditions (geometry of the gas delivery system, gas flow rate and nozzle stand-off distance NSD) when welding AA5083 aluminium alloy. It was demonstrated that all shielding gas conditions investigated can significantly affect the features of the weld seam. Also, it was found that high gas flow rate, combined with a low NSD, created a narrower and deeper keyhole.

Chung et al. [144] have studied the effect of shielding gas types on CO_2 tailored blank weldability of low carbon automotive galvanized steel. It was found that the weld penetration and the joint strength are strongly dependent on the type of shielding gas used. Also, the maximum travel speed and gas flow rate necessary to form a keyhole weld are dependent upon shielding gas type. It was demonstrated that helium and 50% argon + 50% nitrogen were the best shielding gases from the viewpoint of penetration and keyhole formability when welding this type of material.

In conclusion, helium is better than argon in preventing the weld metal and reducing the plasma as a result of the higher ionization potential of helium as stated in [132,139]. On the other hand, the cost of helium is almost 2.5 times as that of argon [4], also, from the primarily experiments we noticed that sound weld penetration and parallel fusion zone interfaces were obtained by using argon as a shielding gas, this could be related to the focusing system of the laser machine used in this work which has low nozzle stand-off distance which has a significant effect as demonstrated by Sibillano [143]

2.3.5 Microstructure

Laser welding of 0.9 mm thick of AISI304L and AISI12L13 free-cutting steel tubular parts were investigated by Li and Fontana [145]. The experiments were performed in such way as to control solidification cracking and micro-fissuring. It was found that the impurities, such as S, Pb and P, contained in the AISI12L13 were the cause of the solidification cracks. It was mentioned that a 0.12 mm off-set of the

laser beam towards the AISI304L and an impingement angle of 15° with respect to the fit-up face of the butt joint can produce sound welds.

The rapid solidified structure of stainless steel welded by laser beam was examined by Zambon and Bonllo [146]. They have investigated the laser welding parameters effect on the microstructural characterization of both FZ and HAZ of AISI304, 316 and duplex UNS31803 stainless steels. It was concluded that the extremely localized heat input achieved by laser welding results in high cooling rates- consequently formulation of non-equilibrium microstructures may take place. Low amounts of delta ferrite have been found in AISI304, 316 weld beads. It was demonstrated that non-equilibrium microstructures affect the in-service properties and decrease the mechanical and corrosion resistance of the joint. Moreover, it was stated that microstructural optimization is needed and can be achieved by adopting properly selected process parameters.

Farrar [147] has reviewed the solidification microstructure, cracking, effect of precipitation and the factors which control the mechanical and high temperature properties of austenitic stainless steel weldments. It was found that the properties are highly dependent on weld metal chemistry. It was reported that at high temperatures δ-ferrite would transform to various inter-metallic and carbides and it might lead to hot cracking. The author suggested a range for each alloying element. If the composition is controlled within these ranges, this could be effective in controlling inter-metallic phase formation and reduce the remaining δ-ferrite in order to promote adequate resistance to hot cracking.

El-Batahgy [139] has investigated the effect of the welding speed on weld microstructure of AISI304L. He noticed the highly directional nature of the microstructure around the axis of the laser beam. This is due to the high cooling rate achieved. Also, he demonstrated that the higher the welding speed, the finer the dendritic structure, which he attributed to the increase in the solidification and cooling rate. In general, he concluded that the microstructure of all laser welds were always austenite with few percent of delta-ferrite of 2-3 vol.% at the dendritic boundaries.

Tsay et al. [148] have reported that equiaxial austenite grains together with annealed twins were the microstructure of the base metal and the heat affected zone

(HAZ) of a typical laser weld are as shown in Fig.2.5a, while the fusion zone (FZ) consisted of columnar dendrites as shown in Fig. 2.5b. Also, they reported that the microhardness measurements of the laser welds indicted that both FZ and HAZ had a slightly higher hardness (197 ± 5 Hv) than the base metal (181 ± 5 Hv). It was noted that AISI304SS would not form a hardened structure after laser treatment unlike carbon steel and alloy steel.

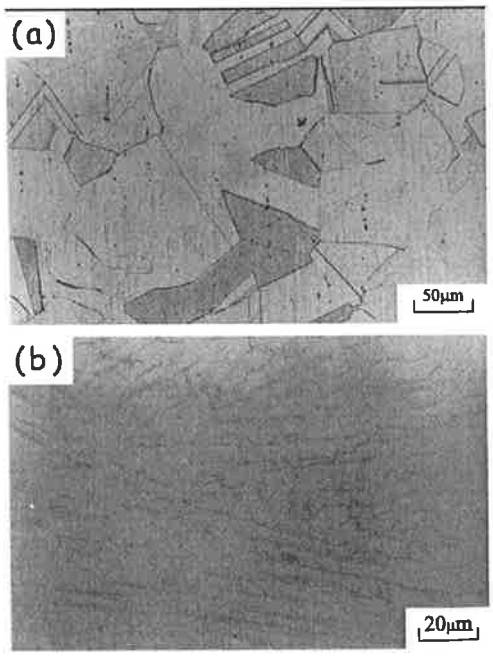

Fig. 2.5: The microstructure of (a) the base metal and (b) the FZ [148].

Bayraktar et al. [149] have investigated welding of different materials by laser, TIG and RSW processes. They have reported that a certain proportion of martensite was observed in the laser welded parts of the non-stabilised grade AISI430 and the amount of martensite is higher than that of TIG and RSW processes, due to high cooling rate. It has been noticed that the amount of the equiaxed zone in the centre of the weld bead increases with the welding speed of the laser process. They mentioned that the hardness value decreases when the welding energy increases for all processes.

Dilthey and Risch [150] have reported that when welding austenitic stainless steels, hot-cracks in the fusion zone are developed in the grain boundary region due to the residual stress. These hot-cracks tend to decrease with a lower energy-per unit length, smaller HAZ and minimum residual stress.

It was reported by Nath et al. [136] that good quality welds can be obtained in AISI304 stainless steel. However, inclined columnar grains, about 45° from the centreline, grow from the opposite sides of the weld pool and a thin region of axial grains at the weld centreline (appear as fine equiaxed grains). It was observed that the fusion zone exhibited a primary ferrite solidification mode. Primary ferrite solidified austenitic stainless steel welds are considered to be more resistant against solidification cracking compared with those associated with primary austenitic modes of solidification.

Katayama and Matsunawa [151] have investigated the microstructure of CO_2 laser welds of austenitic stainless steel of Cr_{eq}= 19.1% and Ni_{eq}= 16.6% with the variation in welding speed from 0.4 to 15 m/min. It was found that the weld metal microstructure was fully austenitic. The average primary dendrite-arm spacings (cell sizes) were measured to estimate cooling rates. The cell sizes varied widely at the slower welding speed, and were smaller as the welding speed increased. It was noted that smaller spacings were presented at the bottom of the weld beads, due to a faster cooling rate. It was mentioned that from the cell sizes of 1 and 2.5 μm of this type of material the cooling rates were extrapolated to be as fast as 10^6 and 10^5 °C/s.

The microstructure of the laser welds is influenced by the welding speed; higher welding speed leads to finer grains, whereas, lower welding speed results in coarser grains. This is due to the fact that the cooling rate increases as the welding speed increases, since the volume of molten metal and the heat input decrease with increasing welding speed at constant laser power [4, 139].

Nevertheless, very few investigations, as far as the author is aware, have been addressed to establish the functional relationship and mathematical models between the laser welding process parameters and the welds mechanical properties, weld-bead geometry and residual stress distribution. Furthermore, fewer articles have tried to explain the complex phenomena relating to the interaction of the process parameters with each other for a certain response. Therefore, and as stated earlier, this work aims to use RSM to develop mathematical models to relate the welds outcomes to the process input parameters.

CHAPTER III

DESIGN OF EXPERIMENTS

3- EXPERIMENTAL DESIGN

3.1 Introduction

In industry, experiments are conducted to enhance the understanding and knowledge of different manufacturing processes with the aim of producing high quality products. To ensure continuous improvements in process quality, it is essential to be aware of the process behaviour, the amount of variability and its effect on the process outputs. In the engineering field, experiments are often carried out to explore, estimate or confirm. Exploration refers to understanding the data from the process. Estimation refers to determining the effect of the process variables on the output performance characteristics (or quality characteristics). Confirmation implies verifying the predicted results obtained from the experiment [152].

One of the conventional common approaches utilized by many engineers in manufacturing companies is one-variable-at-a-time (OVAT), where the engineer varies one variable at a time keeping all other variables involved in the experiment fixed. This approach required large resources to obtain a limited amount of information about the process. OVAT experiments are often unreliable, time consuming, may not yield the optimal condition and do not address the interaction effect between the process variables [152].

Methods that have statistical bases can replace OVAT experimental approach. These methods, usually called Design of Experiment (DOE), play a key role in planning, conducting, analysing and interpreting data from engineering experiments. If a certain quality feature of a product, the response, is being affected by many variables, the best strategy is then to design an experiment in order to achieve valid, reliable and sound conclusions in an effective, efficient and economical manner. It is important to know that some factors may have strong effects on the response, others may have moderate effects and some have no effects at all. Therefore, the aim of a well designed experiment is to specify which set of factors in the process affects the process performance most, and then the best levels for these factors to reach the desired quality level can be found out [151].

Sir R. Fisher introduced DOE in the early 1920s to determine the effect of various fertilizers on a range of land plots. Since then, DOE has been utilized in

many disciplines such as biological, pharmaceutical, engineering etc. In the last two decades, the use of DOE has grown rapidly and been adapted for many processes in industry such as machining, chemical mixing and welding to find out the optimal conditions.

Responses surface methodology (RSM) is the best known type of DoE design; the concept of RSM was introduced in the early 50's by Box and Wilson [153]. Among the RSM designs, two most popular types of experimental designs exist for developing second-order models: central composite design (CCD) and Box-Behnken design (BBD). Since these particular designs are being used in this work, some details about them will be presented in the next sections.

3.2 Response Surface Methodology (RSM)

Engineers often search for the conditions that would optimize the process of interest. In other words, they want to determine the values of the process input parameters at which the responses reach their optimum. The optimum could be either a minimum or a maximum of a particular function in terms of the process input parameters. RSM is one of the optimization techniques currently in widespread usage to describe the performance of the welding process and find the optimum of the responses of interest.

RSM is a set of mathematical and statistical techniques that are useful for modelling and predicting the response of interest affected by several input variables with the aim of optimizing this response [154]. RSM also specifies the relationships among one or more measured responses and the essential controllable input factors [155]. If all independent variables are measurable and can be repeated with negligible error, the response surface can be expressed by:

$$y = f(x_1, x_2, \ldots x_k) \tag{3.1}$$

Where: k is the number of independent variables

To optimize the response "y", it is necessary to find an appropriate approximation for the true functional relationship between the independent variables and the response surface. Usually a second order polynomial Eq.3.2 is used in RSM.

$$y = b_o + \sum b_i \chi_i + \sum b_{ij} \chi_i \chi_j + \sum b_{ii} \chi_{ii}^2 + \varepsilon \qquad (3.2)$$

As mentioned earlier the utilized RSM designs in this work are CCD and BBD. The following are some details on these two designs:

3.2.1 Central composite design (CCD)

The most popular RSM design is CCD. CCD has three groups of design points: (a) two-level factorial or fractional factorial design points, (b) axial points (sometimes called star points) and (c) centre points. CCD's are designed to estimate the coefficients of a quadratic model. All point descriptions will be in terms of coded values of the factors [154,156].

a) Factorial points

The two-level factorial part of the design consists of all possible combinations of the +1 and -1 levels of the factors. For the two factors case there are four design points: (-1, -1) (+1, -1) (-1, +1) (+1, +1). In general, the number of factorial points is equal to 2^k.

b) Star or axial points

The star points have all of the factors set to 0, the midpoint, except one factor, which has the value +/-α. For a two factors case, the star points are: (-α, 0) (α, 0) (0, -α) (0, α). The value for α is calculated in each design for both rotatability and orthogonality of blocks. A design is rotatable if the variance of the predicted response at any point x depends only on the distance of x from the design centre points and a design is orthogonal if the effects of any factor balance out (sum to zero) across the effects of the other factors. The experimenter can choose between these values or enter a different one. The default value is set to the rotatable value and can be calculated by: $\alpha = (2^k)^{1/4}$. The number of star points is equal to 2k.

c) Centre points

Centre points, as implied by the name, are points with all levels set to coded level (0) the midpoint of each factor range: (0, 0). Centre points are usually repeated 4-6 times to get a good estimate of experimental error (pure error). These points are shown in Fig. 3.1 and Fig. 3.2 for two and three factors designs respectively.

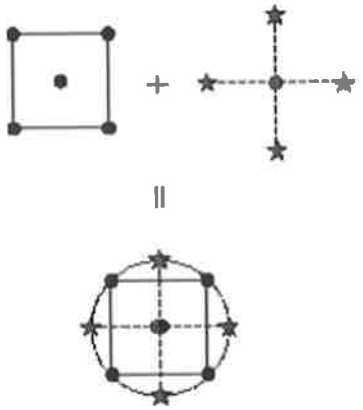

Fig. 3.1: Generation of CCD for two factors [157].

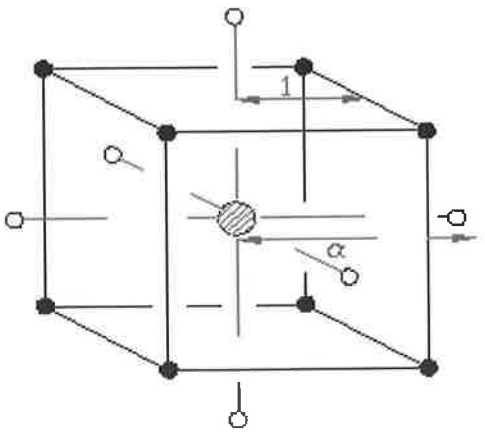

Fig. 3.2: Schematic of a CCD for three factors [158].

3.2.1.1 Analysis for the design

The values of the coefficients b_0, b_i, b_{ii} and b_{ij} can be calculated using regression analysis. For three factor experiments the coefficients are computed by the Eqs. 3.3 to 3.6. The sum of squares of the model and each term is given by Eqs. 3.7 to 3.13 [159,160].

$$b_0 = 0.1663\sum_{i=1}^{20} y_i - 0.0568\sum_{j=1}^{3}\sum_{i=1}^{20} x_{ij}^2 y_i \tag{3.3}$$

$$b_i = 0.0732\sum_{i=1}^{N} x_{ij} y_i \qquad \text{j} = 1,2,3 \tag{3.4}$$

$$b_{uj} = 0.1663\sum_{i=1}^{20} x_{ui} x_{ij} y_i \qquad \text{u} \neq \text{j} \qquad \text{j, u} = 1,2,3 \tag{3.5}$$

$$b_{ii} = 0.0625\sum_{i=1}^{20} x_{ij}^2 y_i + 0.0069\sum_{j=1}^{3}\sum_{i=1}^{20} x_{ij}^2 y_i - 0.0568\sum_{i=1}^{20} y_i \tag{3.6}$$

$$SS_T = \sum_{i=1}^{20} (y_i - \bar{y})^2 \tag{3.7}$$

$$SS_M = \sum_{i=1}^{20} (\hat{y}_i - \bar{y})^2 \tag{3.8}$$

$$SS_R = \sum_{i=1}^{20} (y_i - \hat{y}_i)^2 \tag{3.9}$$

$$SS_{PE} = \sum_{i=1}^{n_o} (y_i - \hat{y}_i)^2, \text{ for centre points only} \tag{3.10a}$$

$$SS_{lof} = SS_R - SS_{PE} \tag{3.10b}$$

$$SS_{b_i} = b_i \sum_{i=1}^{20} x_i y_i \tag{3.11}$$

$$SS_{b_{ij}} = b_{ij} \sum x_i x_j y_i \tag{3.12}$$

$$SS_{b_{ii}} = b_0 \sum_{i=1}^{20} y_i + b_{ii} \sum_{i=1}^{20} x_i^2 y_i - (\sum y_i)^2 / 20 \tag{3.13}$$

3.2.2 Box-Behnken Design (BBD)

The second most popular RSM designs are BBDs, which are based on three levels of each factor. These designs were developed by Box and Behnken in 1960 [161]. They are constructed by first combining two-level factorial designs with

incomplete block designs and then adding a specified number of centre points. For three factors, the total number of points is equal to 12 design points and 5 centre points, making 17 points. Although, the 12 unique combinations represent less than one-half of all possible combinations for three factors with the same number of levels, they offer enough information to fit the 10 coefficients of the polynomial shown in Eq. 3.2 [162]. Fig. 3.3 presents a schematic diagram for BBD for three factors.

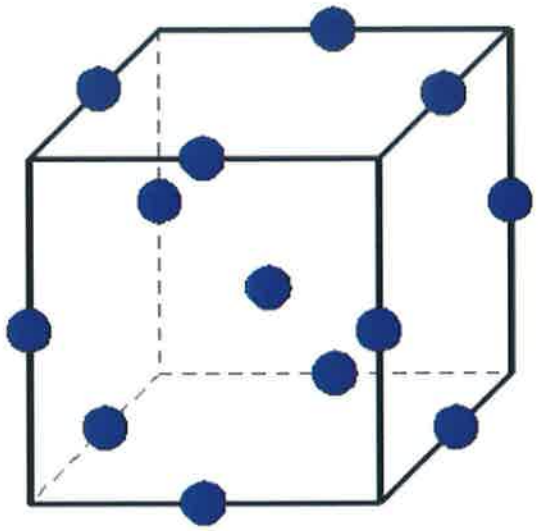

Fig. 3.3: A schematic diagram for BBD of three factors [158].

3.2.2.1 Analysis for the design

To find out the 10 coefficients in the polynomial Eq. 3.2 the following equations can be used Eqs. 3.14 to 3.17. The sum of squares for each term of BBD could be calculated by applying Eq. 3.7 to 3.110b and Eqs. 3.14 to 3.17 for designs with 3 factors. Where A, B, C_1 and D_1 are constants and for three factors design they are equal to 1/8, 1/4, -1/16 and 1/4 respectively [161].

$$b_o = \bar{y}_o \tag{3.14}$$

$$b_i = A\sum_{u=1}^{N} x_{iu} y_u \tag{3.15}$$

$$b_{ii} = B\sum_{u=1}^{N} x_{iu}^2 y_u + C_1 \sum_{i=1}^{N} x_{ii}^2 y - (\bar{y}_o / s) \tag{3.16}$$

$$b_{ij} = D_1 \sum_{u=1}^{N} x_{iu} x_{ju} y_u \tag{3.17}$$

$$SS_{b_i} = A\sum_{i=1}^{N} (x_i y_i)^2 \tag{3.18}$$

$$SS_{b_{ij}} = D_1 \sum_{u=1}^{N} (x_{iu} x_{ju} y_u)^2 \tag{3.19}$$

$$SS_{ii} = b_o \sum_{u=1}^{N} y_u + \sum_{u=1}^{N} b_{ii} x_{iu}^2 \; y_u - \sum_{u=1}^{N} (y_n)^2 / N \tag{3.20}$$

3.3 Comparison between CCD and BBD

Experimenters may be unsure why they should choose one design over another. Below is a comparison between the most common response surface designs - the Central Composite and Box-Behnken [156].

a) Central Composite Design

The main features of this RSM design are:

1. Created from a 2-level factorial design, improved with centre points and axial points.
2. Normally has 5 levels for each factor, this can be modified to a face-centred CCD by choosing α =1.0. The face-centred design has only three levels for each factor.
3. Created for estimating a quadratic model.
4. Rather insensitive to missing data, making them more robust to problems.
5. Replicated centre points provide excellent prediction capability near the centre of the design space.
6. Region of operability must be greater than region of interest to accommodate axial runs.

b) Box-Behnken

The main features of this RSM design are:

1. Has specific positioning of design points.
2. This design has 3 levels for each factor.
3. Created for estimating a quadratic model.
4. Provides strong coefficient estimates near the centre of the design space, but weaker at the corners of the cube, due to the absence of design points.
5. Sensitive to missing data and a bad run.
6. Region of interest and region of operability are nearly the same.

3.4 General Steps in RSM

To carry out any RSM, the problem is usually considered in sequential steps. The following steps are performed in order to develop a mathematical model in the case of laser welding:

1. Identifying the critical process variables (or factors).

The critical factors can be defined from the past literature or by conducting a preliminary study (i.e. screening study) based on factorial design or partial factorial design. In our case the vital process factors were determined from the past literatures. The process input factors are laser power, welding speed and focal position with respect to the substrate surface.

2. Finding the limits of each factor.

To find the limits of each factor, trial weld runs were performed by changing one of the process parameters at a time. The criteria of selecting the working ranges were absence of clear welding defects, a smooth and uniform welded surface with a sound face and root bead and in some experiments a full penetration depth. Although, Design-Expert V7 software was used to code the data, develop the design matrix and analyze the case, the limits for each factor were coded via this relationship; $X_I = 2(2X - (X_{max} + X_{min}))/ (X_{max} - X_{min})$. Where: X_i is the required coded value, X is any value of the factor which wanted to be coded and X_{max}, X_{min} are the upper and lower limit of the factor being coded respectively [154].

3. Design matrix development

The matrix depends on the type of RSM design selected. For CCD and BBD the design matrixes in coded values are shown in Table 3.1 and Table 3.2 respectively. As stated earlier, in the current work the matrix for each experiment was developed using the same statistical software. For three factors the experimental runs for CCD and BBD are 20 and 17 respectively [154, 155]. These experimental runs are sufficient for the estimation of the coefficients in Eq. 3.2.

Table 3.1: Design matrix for CCD, coded values.

Run No.	Order No.	Laser Power	Welding Speed	Focal position
1	8	-1	-1	-1
2	4	1	-1	-1
3	15	-1	1	-1
4	5	1	1	-1
5	13	-1	-1	1
6	11	1	-1	1
7	17	-1	1	1
8	12	1	1	1
9	7	-1.682	0	0
10	18	1.682	0	0
11	10	0	-1.682	0
12	6	0	1.682	0
13	1	0	0	-1.682
14	19	0	0	1.682
15	2	0	0	0
16	3	0	0	0
17	16	0	0	0
18	14	0	0	0
19	9	0	0	0
20	20	0	0	0

Table 3.2: Design matrix for BBD, coded values.

Run No.	Order No.	Laser Power	Welding Speed	Focal position
1	10	-1	-1	0
2	17	1	-1	0
3	1	-1	1	0
4	11	1	1	0
5	13	-1	0	-1
6	14	1	0	-1
7	6	-1	0	1
8	7	1	0	1
9	12	0	-1	-1
10	15	0	1	-1
11	4	0	-1	1
12	2	0	1	1
13	5	0	0	0
14	3	0	0	0
15	16	0	0	0
16	8	0	0	0
17	9	0	0	0

4. Performing the experiment

The welding experiments were carried out according to the design matrix Tables 3.1 and 3.2 and in a random order to avoid any systematic error in the experiment.

5. Recording the responses

All responses, mentioned earlier in chapter one, were measured in sequential order for each experiment following the measuring procedure of each response. Usually, the first response measured is residual stress if it's of interest in the active experiment. If applicable, an average of at least three recorded measurements is calculated and considered for further analysis.

6. Development of the mathematical model

The functional relationship representing any response of interest can be expressed as y = f(P, S, F) and Eq. 3.2 becomes as follows:

$$Y = b_o + b_1 P + b_2 S + b_3 F + b_{11} P^2 + b_{22} S^2 + b_{33} F^2 + b_{12} PS + b_{13} PF + b_{23} SF \qquad (3.21)$$

7. Estimation of the coefficients in the model

Regression analysis is applied to specify the values of the coefficients in Eq. 3.21. Eqs 3.3 to 3.6 were used to evaluate the coefficients for CCD and Eqs. 3.14 to 3.17 were applied to evaluate the coefficients for BBD. The computer software was used to evaluate the coefficients for all responses of each experiment.

8. Testing the adequacy of the models developed

The analysis of variance (ANOVA) was used to test the adequacy of the models developed. The statistical significance of the models developed and each term in the regression equation were examined using the sequential F-test, lack-of-fit test and other adequacy measures (i.e. R^2, Adj- R^2, Pred. R^2 and Adeq. Precision ratio) using the same software to obtain the best fit. The Prob.>F (sometimes called p-value) of the model and of each term in the model can be computed by means of ANOVA. If the Prob.> F of the model and of each term in the model does not exceed the level of significance (say α= 0.05) then the model may be considered adequate within the confidence interval of (1- α). For the lack-of-fit test, the lack of fit could be considered insignificant if the Prob.>F of the lack of fit exceeds the level of significance. Table 3.3 below is a summery of the ANOVA table. The equations by which the adequacy measures can be calculated are shown below, Eqs. 3.22 to 3.26 [154, 156].

Table 3.3: ANOVA table for full model:

Source	SS	df	MS	$F_{cal.}$- Value	p-value or Prob > F
Model	SS_M	p	Each SS divided by its df	Each MS divided by MS_E	From table or software library
P	SS_1	1			
S	SS_2	1			
F	SS_3	1			
PS	SS_{12}	1			
PF	SS_{13}	1			
SF	SS_{23}	1			
P^2	SS_{11}	1			
S^2	SS_{22}	1			
F^2	SS_{33}	1			
Residual	SS_R	N-p-1			-
Lack of Fit	SS_{lof}	$N - p - n_0$			From table
Pure Error	SS_E	n_{0-1}			-
Cor Total	SS_T	N - 1	-	-	-

Where:

P: Number of coefficients in the model.
N: Total number of runs.
n_0: Number of centre points.
SS: Sum of squares.
df: Degree of freedom.
MS: Mean square.

$$R^2 = 1 - \left[\frac{SS_R}{SS_R + SS_M}\right] \tag{3.19}$$

$$AdjR^2 = 1 - \left[\left(\frac{SS_R}{df_R}\right) \times \left(\frac{SS_R + SS_M}{df_R + df_M}\right)^{-1}\right] \tag{3.20}$$

$$\Pr edR^2 = 1 - \left[\frac{PRESS}{SS_R + SS_M}\right] \tag{3.21}$$

$$PRESS = \sum_{i=1}^{n} (y_i - \hat{y}_{i,-i})^2 \tag{3.22}$$

$$Adeq.precision = \left[\frac{Max(\hat{Y}) - Min(\hat{Y})}{\sqrt{\frac{p \times MS_R}{n}}}\right] \tag{3.23}$$

Where:

p: Number of model parameters (including intercept b_0)
n = number of experiments

9. Model reduction

Usually, the full model, Eq. 3.21, consists of insignificant model terms that need to be eliminated, terms that have p-value greater that the level of significance α. This elimination can be done manually or automatically. The three automatic procedures of evaluating all possible regression equations (or selection of variables) are [156,163]:

a) Forward selection procedure: This procedure begins with only the constant term, and the first variable added is the one with the highest simple correlation with y. If the regression coefficient of this variable is significant it will remain in the equation. After y has been adjusted for the effect of the first variable a new search for the second variable with highest correlation with y is begun. The significance of the regression coefficient of the second variable is then tested. If the regression coefficient is significant, a search for a third variable is made in the same way. The procedure is completed when the last variable entered into the equation has an insignificant regression coefficient or when all variables are included. The test statistic for this selection process is the standard t or F-statistic, which is equal to t^2.

b) Backward elimination procedure: In this procedure, the full equation is fitted and the variables are sequentially eliminated one at a time. The variable with the smallest contribution to the reduction of error is eliminated first, or the variable with the smallest t ratio (i.e. the ratio of the regression coefficient to its standard error) and so on. In the case of more than one variable having an insignificant t ratio, the procedure operates by dropping the variable with the smallest insignificant t ratio and the equation with the remaining variables is then fitted and the ratios for the new regression coefficient are tested. The procedure is stopped when all the t ratios are significant or all but one variable has been deleted.

c) Stepwise regression method: This method is basically a forward selection. However, the possibility of eliminating a variable that might be added in an earlier stage, as in the backward procedure, is considered. The calculations used for the inclusion and deletion of variables are the same as for forward and backward

procedures. This procedure has the advantage of assuming different or similar levels of significance for inclusion or deletion of variables from the regression equation.

10. Development of the final reduced model

At this stage the final reduced model can be build up as determined by applying the above steps. This model contains only the significant terms and the terms that are necessary to maintain hierarchy. Also, a reduced quadratic ANOVA table can be produced.

11. Post analysis

When the final model has been tested and checked and found to be adequate, the response at any midpoints can be predicted using this adequate model. Also, producing some important plots, such as 3D graphs, contours and perturbation plots, to present the factors effect and how they contribute to the response. Moreover, it is now possible to employ the developed model to find the welding setting at which the process could be optimized.

3.5 Optimization

3.5.1 Desirability approach

There are many statistical techniques for solving multiple response problems, such as overlaying the contours plot for each response, constrained optimization problem and desirability approach. The common statistical software packages, such as GPSS, NEMROD and Design-Expert, include multiple response optimization techniques. The desirability method is recommended due to its simplicity, availability in the software and it also provides flexibility in weighting and giving importance to individual responses. Solving such multiple response optimization problems using this technique consists of using a technique for combining multiple responses into a dimensionless measure of performance called the overall desirability function. The desirability approach consists of transforming of each estimated response, Y_i, into a dimensionless utility bounded by $0 < d_i < 1$, where a higher d_i value indicates that the response value Y_i is more desirable, if $d_i = 0$ this means a completely undesired response or vice versa when $d_i = 1$ [164]. In the current work the individual desirability for each response d_i was calculated using Eqs. 3.27-3.30.

The shape of the desirability function can be changed for each goal by the weight field 'wt_i'. Weights are used to give added emphasis to the upper/lower bounds or to emphasize the target value. Weights could be ranged between 0.1 and 10; weight greater than one gives more emphasis to the goal, while weight less than one gives less emphasis to the goal. With weight value of one, this will make the d_i's vary from zero to one in a linear mode. In the desirability objective function (D), each response can be assigned an importance (r), relative to the other responses. Importance varies from the least important a value of 1(+), to the most important a value of 5(+++++). If the varying degrees of importance are assigned to the different responses, the overall objective function is shown below Eq. 3.31. Where n is the number of responses in the measure and T_i is the target value of i^{th} response [156].

- For goal of maximum, the desirability will be defined by:

$$d_i = \begin{cases} 0 & , \quad Y_i \le Low_i \\ \left(\dfrac{Y_i - Low_i}{High_i - Low_i} \right)^{wt_i} & , \quad Low_i \langle Y_i \langle High_i \\ 1 & , \quad Y_i \ge High_i \end{cases} \tag{3.27}$$

- *For goal of minimum, the desirability will be defined by:*

$$d_i = \begin{cases} 1 & , \quad Y_i \le Low_i \\ \left(\dfrac{High_i - Y_i}{High_i - Low_i} \right)^{wt_i} & , \quad Low_i \langle Y_i \langle High_i \\ 0 & , \quad Y_i \ge High_i \end{cases} \tag{3.28}$$

- *For goal as a target, the desirability will be defined by:*

$$d_i = \begin{cases} \left(\dfrac{Y_i - Low_i}{T_i - Low_i}\right)^{wt_{1i}} & , \quad Low_i \langle Y_i \langle T_i \\ \left(\dfrac{Y_i - High_i}{T_i - High_i}\right)^{wt_{2i}} & , \quad T_i \langle Y_i \langle High_i \\ 0 & , \quad Otherwise \end{cases} \tag{3.29}$$

- *For goal within range, the desirability will be defined by:*

$$d_i = \begin{cases} 1 & , \quad Low_i \langle Y_i \langle High_i \\ 0 & , \quad Otherwise \end{cases} \tag{3.30}$$

$$D = \left(\prod_{i=1}^{n} d_i^{r_i}\right)^{\frac{1}{\sum r_i}} \tag{3.31}$$

3.5.2 Optimization approach in Design-Expert software

The optimization part in Design-expert software V7 searches for a combination of factor levels that simultaneously satisfy the requirements placed (i.e. optimization criteria) on each one of the responses and process factors (i.e. multiple response optimization). Numerical and graphical optimization methods were used in this work by choosing the desired goals for each factor and response. As mentioned earlier, the numerical optimization process involves combining the goals into an overall desirability function (D). The numerical optimization feature in the design expert software package finds a point or more in the factors domain that would maximize this objective function. In a graphical optimization with multiple responses, the software defines regions where requirements simultaneously meet the proposed criteria by superimposing or overlaying critical response contours on a contour plot. Then, a visual search for the best compromise becomes possible. In the case of

dealing with many responses, it is recommended to do numerical optimization first; otherwise it could be impossible to uncover a feasible region. The graphical optimization displays the area of feasible response values in the factor space. Regions that do not fit the optimization criteria are shaded [156]. Fig.3.1 shows a flow chart of the optimization steps in the design-expert software.

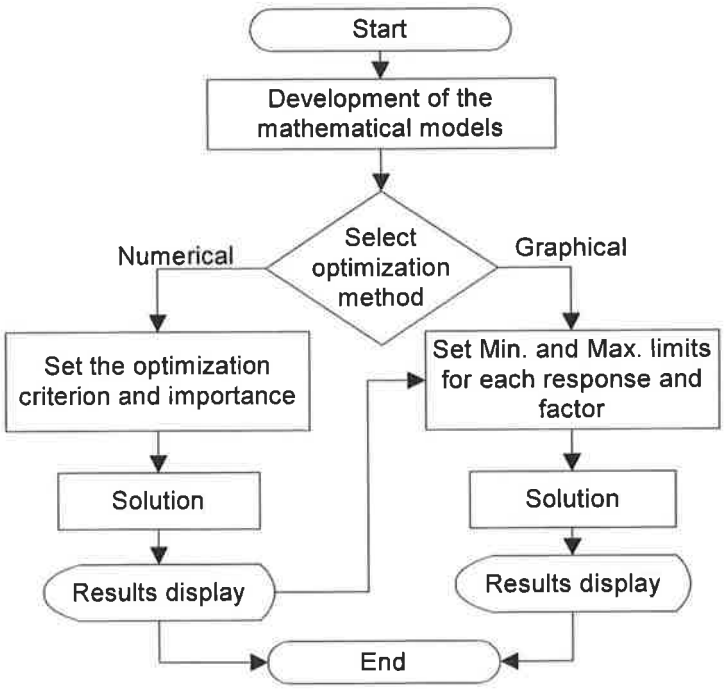

Fig. 3.1: Optimization steps.

CHAPTER IV
EXPERIMENTAL WORK

4. EXPERIMENTAL WORK

In this chapter the materials, equipment, theories and procedures which were used or followed in this work are presented.

4.1 Material

In this research three standard materials have been selected to be welded by means of CO_2 laser welding. The materials were selected due to their wide application and also to provide more knowledge on their welding input and output performance. These materials are: plain carbon steel of standard grade AISI1016, medium carbon steel of standard grade of AISI1045 and stainless steel of standard grade of AISI304. The surface condition of these materials is a smooth surface (Ra values between 0.1 and 0.5 μm). These materials are the most popular for different engineering applications in industry, such as automotive, simple structural components, jigs, fixtures, pharmaceutical equipment, chemical vessels, vacuum vessels, power plant etc. [1,11]. Their standard chemical compositions are shown in Table 4.1 along with their typical chemical composition as analyzed by the Spark analyzer Spectromax shown in Fig. 4.1. The spark analyzer is equipped with spark analyser software DIA 2000SE for data management.

Table 4.1: Chemical compositions of the materials.

Code		Chemical composition								Plates dimensions mm
		C	Mn	Si	Cr	Ni	P	S	Fe	
AISI1016	standard	0.14 - 0.2	0.6 - 0.9	0.35	-	-	Max 0.04	Max 0.05	98.81-99.26	160 x 80 x 3
	Typical	0.161	0.68	0.196	0.044	0.070	0.004	0.008	Bal.	
AISI1045	standard	0.43-0.50	0.60-0.90	0.15-0.35	-	-	Max 0.04	Max 0.05	98.16-98.82	180 x 80 x 5
	Typical	0.44	0.72	0.23	-	-	0.009	0.002	Bal.	
AISI304	standard	Max 0.08	Max 2	Max 1	18 - 20	8 - 10.5	Max 0.045	Max 0.03	66.345-74	160 x 80 x 3
	Typical	0.048	1.66	0.284	20.817	7.81	0.023	0.031	Bal.	
AISI304	standard	Max 0.08	Max 2	Max 1	18 - 20	8 - 10.5	Max 0.045	Max 0.03	66.345 - 74	160 x 80 x 1
	Typical	0.053	1.86	0.423	19.638	8.234	0.017	0.025	Bal.	

Fig. 4.1: Photograph of the Spectromax spark analyzer.

4.2 Joint Type and Preparation

Square butt joints are mostly used for metals that are 10 mm or less in thickness. Preparation of the joint is simple, since it only requires matching the edges of the plates together. However, and especially for laser welding, it is important that the plates are fitted together correctly for the entire length of the joint. Therefore, the plate's edges were machined using CNC milling machine to ensure full contact along the weld line during laser welding. Lap joints are mainly used in sheet fabrication and consumer goods such as cars, households and power plants. Recently, trends toward the economical fabrication of vehicle shells have led to the implementation of the laser welded lap joint instead of resistance spot welding [4, 5]. These two types of commonly used joint configurations were utilized in this work. Square butt joints were used with 5 mm AISI1045 and 3 mm AISI304 as well as in dissimilar welding of 3 mm AISI1016 with AISI304, and lap joints were used with 1 mm AISI304. No special heat treatment was carried out before or after the laser welding. A fixture was designed to clamp the plates during welding to avoid any deformation occurring due to the thermal loading. This fixture is shown in Fig. 4.2. This fixture was designed to accommodate both joint configurations (i.e. butt and lab) used in this work and to hold the welded sample during residual stress measurements.

(a) (b)

Fig. 4.2: Clamping the plates (a) butt-joint and (b) lap joint.

4.3 Laser welding

4.3.1 Laser welding machine

The laser used is a Rofin DC 015 industrial CO_2 slab laser, which operates at 1.5 kW output power with a wavelength of 10.6 μm. This laser is a high frequency excited, diffusion cooled CO_2 gas laser, designed to be used for processing materials on an industrial scale for cutting, welding, hardening, engraving, marking, and cladding. The laser machine, shown in Fig. 4.3, was provided by Mechtronic Industries, who supplied the Rofin laser with motion table and also the control software. The machine type is MTI 0505 Scientific, incorporated with two Mannesman Rexroth precision machine tables with a resolution of 0.00125 mm, to provide XY motion of 50 x 50 cm. A speed control is provided to control the speed from 1 mm/min to 5000 mm/min in 1 mm steps. This laser machine is equipped with a power supply, computer rack, controller terminal, water chiller, air compressor and fume extraction system. The beam delivery system in this machine accepts both 127 and 190 mm FL high pressure lenses. The beam delivery system has a high pressure nozzle assembly with four thumbscrew adjusters to centre the assist gas around the beam, and replaceable copper nozzles which allow a stand-off distance between material and workpiece of 1 mm at 50% shoe height. The lens assembly allows ±10 mm lens focal position, relative to the tip via a micrometer movement operated manually by a rotating drum. The gas used for the operation is a Premix laser gas. It

contains a 94% mixture of Carbon Dioxide, Helium, Nitrogen and Xenon, plus 6% of potentially hazardous Carbon Monoxide. The laser gas bottle contains 1500 Standard Litres. The specifications of this machine are presented in Table 4.2 [165,166].

Fig. 4.3: Photograph of the laser machine and its units.

Table 4.2: Laser machine specifications.

Voltage	3x230/400 V, at 50 or 60 Hz
Max Current Consumption	38-45A
Stability	±2% (cooling water $\Delta T \leq \pm 1K$)
Beam Quality Factor	k>0.9
Width	26 µs-CW
Laser Gas	Rofin-Sinar special-Premix
Consumption	<0.15 l/h
Laser Gas Exchange Intervals	72 h
Mode	semiautomatic
Cooling Water	Demineralized water
Minimal Flow Rate	≥4000 l/h
Supply Pressure	6 bars
Temperature	20 °C
Refrigeration Capacity	≥24 kW
Laser Head	L=1700mm W=800mm H=853mm
Control Cabinet	W=800 D=600 H=1900
Head Weight	500kg
Cabinet Weight	570kg

4.3.2 Laser welding

The laser welding operation was carried out in the school workshop. In order to define the working ranges for each process parameter primarily, screening studies were carried out on each material. Trial weld runs were performed by changing one of the process parameters at a time for each material. The criteria for selecting the working ranges were absence of clear welding defects, a smooth and uniform welded surface with sound face and root bead and full penetration of the weld in some cases. After determining the range of each factor for each material the actual experiment was designed based on RSM, as described in chapter 3. The welding operation was performed according to the design matrix that complies with the RSM designs considered in this work (i.e. CCD or BBD) and in a random order to avoid any systematic error in the experiment. Argon gas was used as a shielding gas with a constant flow rate of 5 l/min [132, 139, and 143]. During the laser welding operation, the plates were clamped rigidly to avoid any deformation caused by the thermal loading, which may affect the results [5, 10]. No special heat treatment was carried out either before or after the laser welding. However, the plate's edges were prepared to ensure full contact along the weld line during the laser welding and cleaned by acetone to remove any remaining cutting fluid, dust or fat [4, 11].

4.4 Measuring Residual Stress

Many methods are widely in use for measuring the residual stress in welded components, for example X-ray diffraction, hole drilling method and other destructive and non-destructive methods. X-ray diffraction gives accurate measurement of the surface residual stress. However, it is unable to describe the distribution of the residual stress through the depth. Destructive methods are inappropriate in the current work, because the specimen must be sectioned and therefore would be unsuitable for reuse for other testing. Thus, the incremental hole-drilling method (IHDM) was the best alternative to measure the maximum residual stress distribution. This technique is one of the stress-relaxing methods that analyse the stress-relaxation produced in a metal part when material is removed. By measuring the deformation caused by the relaxation and analysing the successive

state of equilibrium [12-14] and [42-46 and 54], the values of the residual stress present in the part before removing metal can be determined.

4.4.1 Incremental hole-drilling method (IHDM)

The early application of the hole-drilling technique consists of drilling a hole of a full depth of 0.4D or of about 1.5 times the cutter diameter, where D is the gauge-circle diameter, which for example is equal to 5.13 mm for 062UM and 062UL rosette. When the hole depth reaches the target, the deformations in the three stain gauges are read, and then used along with the calibrating coefficients, taken from the graphs presented in Fig. 4.4 and Eqs 4.1 to 4.4, to determine the principal stresses σ_{Max}, σ_{Min} and the angle between their direction and the datum direction as shown in Fig. 4.5. However, the relationship between the calibrating coefficients of UL and UM can be expressed as in Eqs. 4.5 and 4.6 [167]. Also, the experimental procedure used and the theoretical formulation have limited the application of this technique to the case where the residual stresses are homogeneous through the thickness, as stated by Soete [28], Kelsey [29] and Vigness [30].

$$\sigma_{Min},\sigma_{Max} = \frac{\varepsilon_3 + \varepsilon_1}{4\overline{A}} \pm \frac{\sqrt{(\varepsilon_3 - \varepsilon_1)^2 + (\varepsilon_3 + \varepsilon_1 - 2\varepsilon_2)^2}}{4\overline{B}} \tag{4.1}$$

$$\overline{A} = -\frac{1+v}{2E} \times \overline{a} \tag{4.2}$$

$$\overline{B} = -\frac{1}{2E} \times \overline{b} \tag{4.3}$$

$$\alpha_1 = 0.5 \times \tan^{-1}\left(\frac{\varepsilon_3 + \varepsilon_1 - 2\varepsilon_2}{\varepsilon_3 - \varepsilon_1}\right) \tag{4.4}$$

$$\frac{\overline{a}(UM)}{\overline{a}(UL)} = 1.06 \tag{4.5}$$

$$\frac{\overline{b}(UM)}{\overline{b}(UL)} = 1.17 \tag{4.6}$$

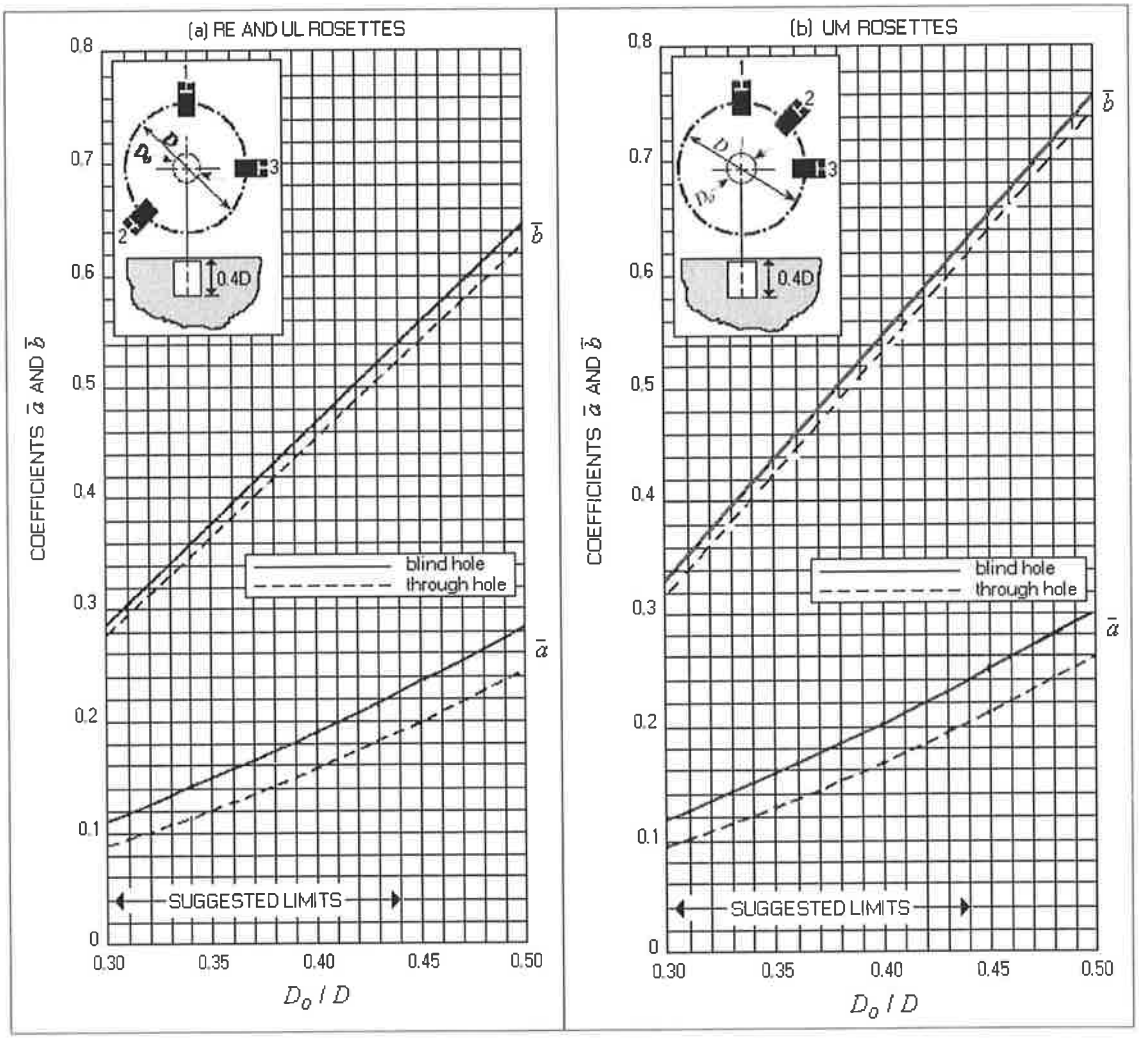

Fig. 4.4: Calibrating coefficients $\bar{a}$ and $\bar{b}$ versus dimensionless hole diameter (typical) for Vishay Measurements Group residual stress rosettes [53].

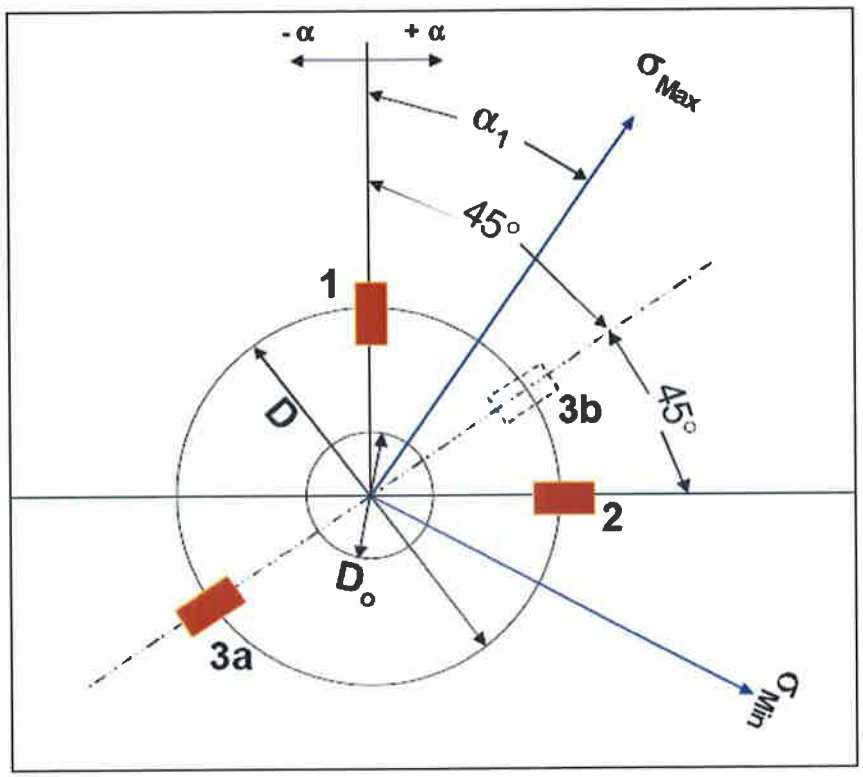

Fig. 4.5: Typical strain gauge rosette.

Recently, there has been a great effort towards the improvement of this technique to allow it to be used for non-homogeneous residual stress, as verified in [41-44]. In order to measure the variation of the residual stress with depth, the drilling operation has to be performed in several increments. Also, the application of FEM was introduced to calculate the calibration coefficients [44-46]. Basically, in the IHDM the hole is drilled step-by-step. During drilling to an increment Z_1, the micro-strain values are read from the strain indicator and then the drilling is continued again towards increment Z_2. When the new depth is reached, the micro-strain values are recorded again and so on until the final increment at a hole depth of 0.4D is reached. When the drilling is finished the principal stresses corresponding to each increment can be determined by applying Eqs 4.1 to 4.3 and the right calibrating coefficients for each increment and strain gauge rosette type from Fig. 4.6 and Fig. 4.7.

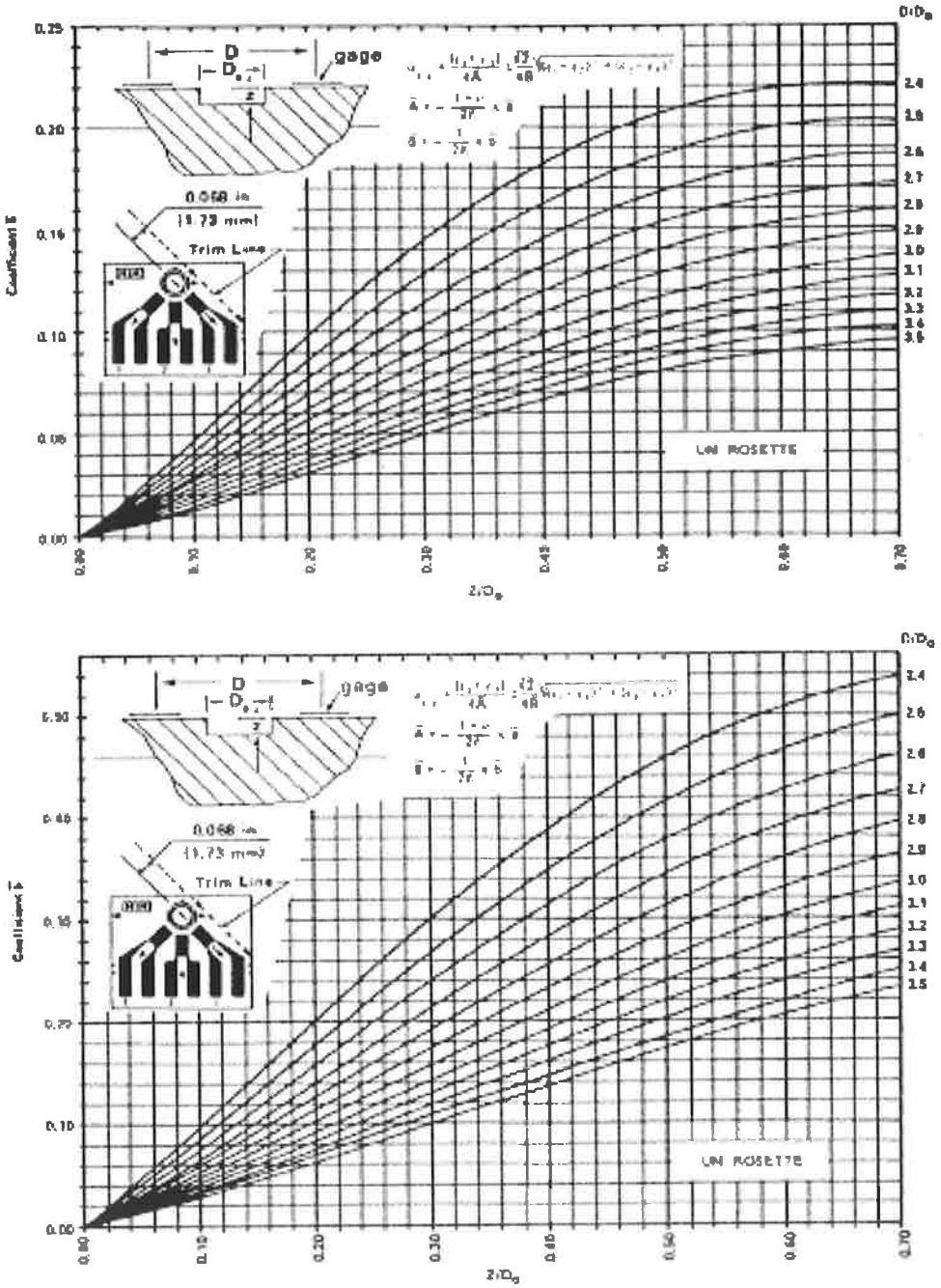

Fig. 4.6: Calibrating coefficients $\bar{a}$ and $\bar{b}$ as a function of hole depth for UM rosettes [167].

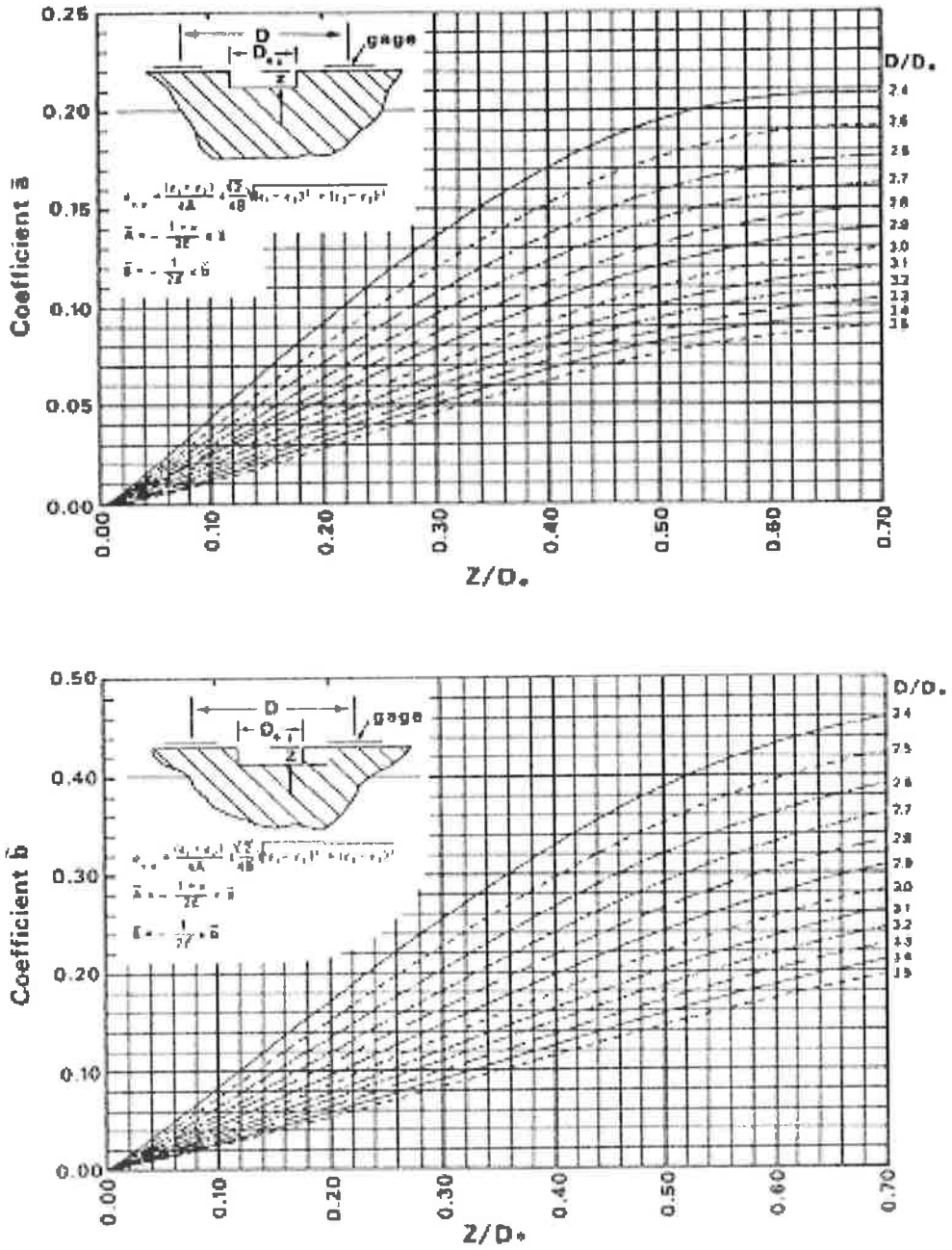

Fig. 4.7: Calibrating coefficients $\bar{a}$ and $\bar{b}$ as a function of hole depth for UL rosettes [167].

4.4.2 Hole-drilling method equipments

4.4.2.1 RS-200 Milling Guide

The commercially available RS-200 Milling Guide shown in Fig. 4.8 is a precision fixture for accurate positioning and drilling of a hole through the centre of a special strain gauge rosette.

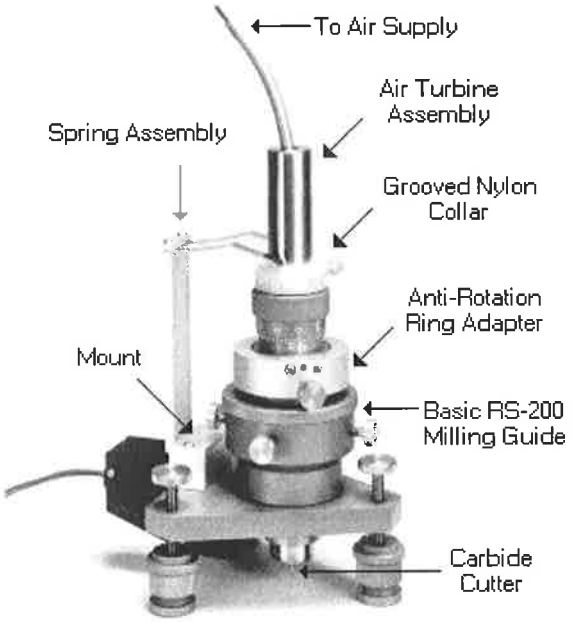

Fig. 4.8: RS-200 Milling Guide [53].

4.2.2.2-Digital strain indicator

Digital strain indicator P-3500 was used in this investigation. This device accepts full, half or quarter bridge inputs and the required bridge completion for 120 or 350 Ω bridges are provided. It has an accuracy of ± 3με for a gauge factor less than 1.00 or of ± 1με for a gauge factor greater than 1.00. This instrument measures up to 199990 με in both sides. A SB-10 switch and balance unit was used in conjunction with the digital strain indicator. This instrument was designed to provide the output reading with ten channels of strain gauge information on one strain indicator. Each channel has to be initially balanced to zero to simplify data interpretation and reduction. Fig. 4.9 shows a photograph of these instruments.

Fig. 4.9: Photograph of the digital strain indicator and the balance unit.

4.4.2.3-Cement Kit

A fast-setting-cement kit type RS-200-CK Cement (Grip cement liquid) is used to tightly attach the guide to the workpiece. As recommended by the producer two measures were mixed with 12 drops of the grip cement liquid. Fig. 4.10 is a photograph of the cement kit.

Fig. 4.10: Photograph of the cement kit.

4.4.2.4-Adhesive

M-Bond 200 is a special adhesive which has been tested and certified for use with bonding strain gauges. It required one minute thumb pressure, followed by a minimum two minutes delay before tape removal. Bond strength increases rapidly during first the five minutes.

4.4.2.5-Other accessories used

Some other accessories were used during the testing. They fall into the following categories: surface preparation and cleaning; including silicon-carbide paper, precision wipes and degreaser type CSM-1A. Installation tools; including cuter, pliers and tapes. Soldering materials; including soldering iron and solder. Connection materials; including different colour electrical wires and a multi-meter for continuity test.

4.4.3 Residual stress determination

The basic test procedure described in Measurement Group TN-502-5 and ASTM 837 was followed [52-54]. Two types of strain gauge rosettes were used; the first type was the CEA-06-062UM-120, shown in Fig. 4.11a, which allows measurement of residual stresses close to the weld-bead, to ensure that the hole is located in the HAZ. The second type was the CEA-06-062UL-120, shown in Fig. 4.11b, which allows measurement of residual stress at other locations at a given distance from the weld centre line. Commercially available milling guide apparatus (model RS-200), shown in Fig. 4.12, with an ultra-high speed air turbine and a carbide cutter of diameter 1.6 mm, were used to drill a hole in the centre of the strain gauge rosette at given increments of 0.127, 0.254, 0.508, 0.762, 1.016, 1.27 and 2.052 mm as recommended in the guides [14, 20]. Calibration coefficients $\bar{a}$, $\bar{b}$ and material properties were used to transform the incremental hole drilling strain data into stress using the blind hole analysis described in [54, 167]. The calibration coefficients were taken from Fig. 4.6 and Fig. 4.7 [167] for both strain gauges. The values of these calibration coefficients are shown in the spreadsheet example page in Appendix A. As the number of calculations is relatively large, the residual stress for

all samples at the different locations and depths were calculated with the aid of Microsoft Excel software 2000. The required equations were built in an Excel file beside the material properties and the required calibrating coefficients for each increment, taking into account the two types of strain gauge rosette [53, 54 and 167] used in this study. In this Excel file, the only inputs required are the experimentally measured micro-strains ε_1, ε_2 and ε_3, determined by the hole drilling method. Also, this Excel file enables us to obtain the final actual responses in the separate sheet for further analysis. The calculated responses rounded to the nearest MPa for all samples at the different locations were then tabulated for further investigation.

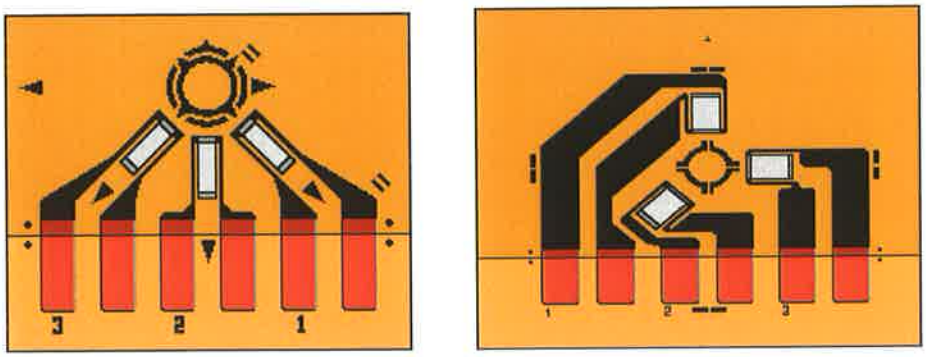

(a) (b)

Fig. 4.11: Photograph of strain gauge rosettes used, (a) 062UM type and (b) 062UL type [53].

Fig. 4.12: Photograph shows the milling guide apparatus and the other kits.

4.5 Bead Geometry Measurements

Transverse specimens were cut from each weldment for all materials. Each transverse specimen was prepared using standard metallographic procedures, including hot-mounting, grinding and polishing. The bead profile parameters, shown in Fig. 4.13, (i.e. depth of penetration, bead width, width of HAZ, width of half penetration and bead area) were measured using a Mitutoyo optical microscope, shown in Fig. 4.14, comprising digital micrometers (with an accuracy of 0.001 mm), which allow measurement in both x and y directions. The bead area was measured using image-analyzer software called Enterprise. The image of the entire weld-pool was captured first by using the MEIJI, EMZ-TR series optical microscope, shown in Fig. 4.15, and then the image was exported to the image-analyzer software for calibrating the image dimensions and area calculation. The average of at least three results of each weld-bead parameter was calculated for each sample for all materials and recorded for further analysis.

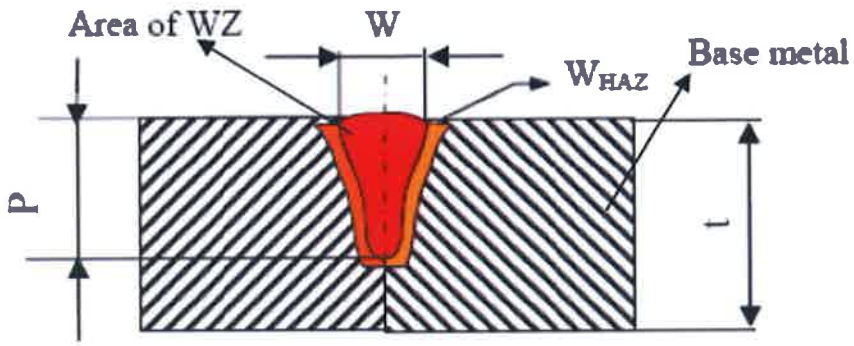

Fig. 4.13: Schematic diagram for transverse cross-section of a butt-joint.

Fig. 4.14: Photograph shows the optical microscope used to measure the bead geometry.

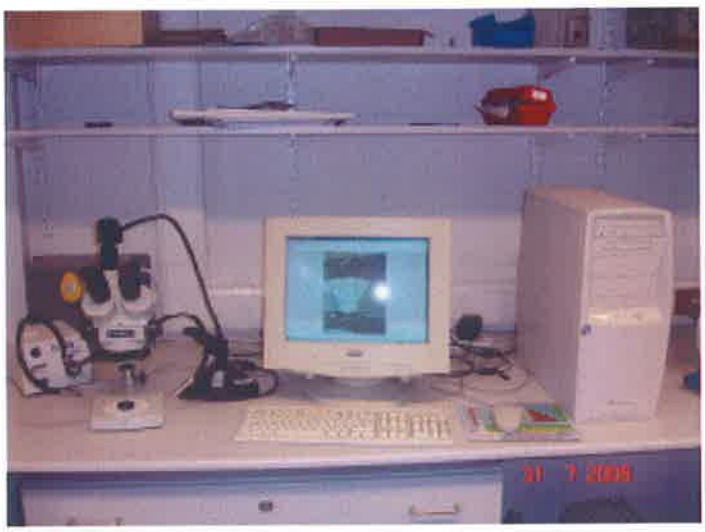

Fig. 4.16: Photograph shows the optical microscope and the software used to capture the entire weld-pool.

4.6 Mechanical Testing

4.6.1 Tensile testing

In this work notched tensile strength (NTS) was investigated for 5 mm butt-joints of AISI1045. Tensile strength was examined for the butt-joints of 3 mm AISI304 and for 3 mm AISI1016 with AISI304 dissimilar welding. Finally, the tensile-shear strength or failure load was investigated for 1 mm AISI304 lab-joints. Tensile tests were performed in air using the Instron universal electromechanical testing machine model 4202 shown in Fig. 4.16. A gauge length of 12.5 mm and a crosshead speed of 5 mm min^{-1} were applied for testing the tensile strength of 3 mm AISI304 butt-joints and 1 mm AISI304 lap-joints. A gauge length of 25 mm and a crosshead speed of 0.75 mm min^{-1} to minimize the strain hardening effect as mentioned in [168] were used for testing NTS of AISI1045 butt-joints. The average of at least three results for each mechanical property was calculated for each sample for all materials. The experimental calculated averages for each response were tabulated for further analysis. The NTS specimens were produced by machining the welded plates from its lower side to the required size of the NTS specimen, as mentioned in [168]. Fig. 4.17 illustrates the dimension of the notched tensile specimen utilized in the test. The tensile tests was conducted in accordance with ASTM E 8M-01^{E2} [169] and tensile-shear specimens were cut off from the welded plates by means of laser cutting to their required standard sizes. Fig. 4.18 shows the dimension of the standard tensile test specimen utilized in this work [170]. Fig. 4.19 presents the centre-line welding lap joint and the dimension of tensile-shear specimen utilized in this work. In all weld plates, the rolling direction is kept perpendicular to the welding direction and in all tensile test specimens the weld pool was guaranteed to be in the centre of specimen gauge length, as shown in Fig. 4.20. Fig. 4.21 is a photograph of the different tensile specimens used in this work.

Fig. 4.16: Photograph shows the Instron testing machine.

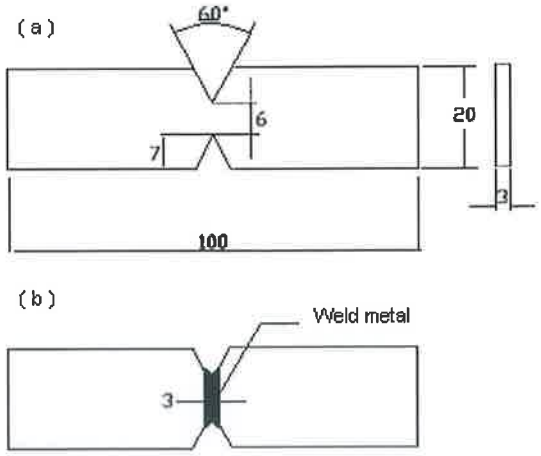

Fig. 4.17: Schematic diagrams showing the dimensions of notched tensile specimens for (a) the steel plate (b) the laser weld, dimensions in mm [168].

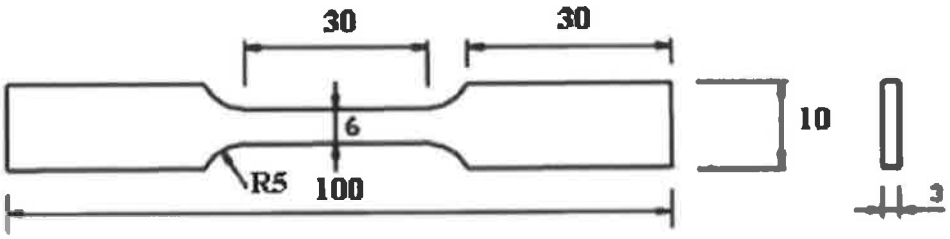

Fig. 4.18: Schematic diagram showing the dimensions of the standard subsize tensile specimen [169].

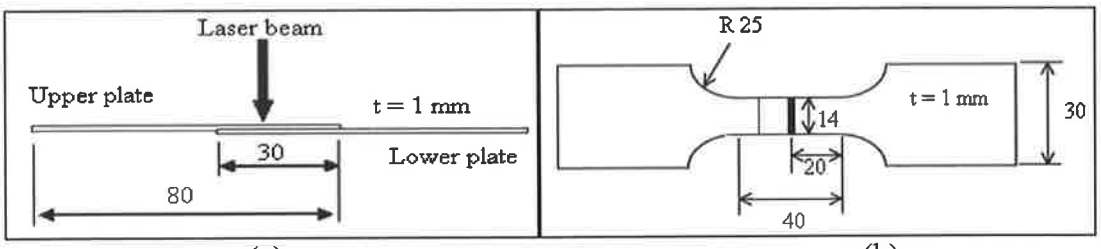

(a) (b)

Fig. 4.19: Schematic diagrams showing the (a) Centre-line welding lap joint, (b) Tensile-shear specimen [170].

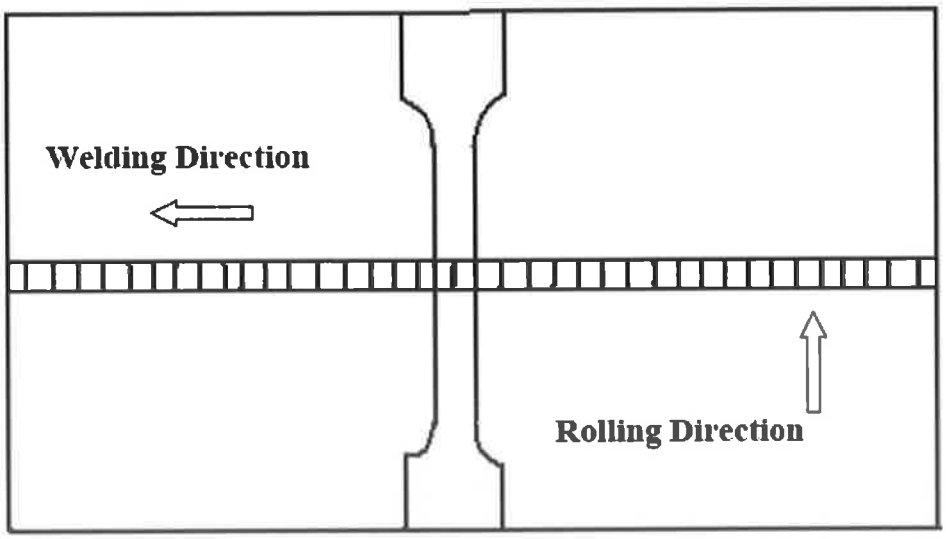

Fig. 4.20: Schematic diagrams of welding direction and testing specimen orientation.

Fig. 4.21: Photograph shows the different tensile specimens.

4.6.2 Impact strength testing

Charpy impact strength subsize specimens were cut from each welded samples according to ASTM E23-02[a] [169]. In the case of the AISI1045 materials the impact specimen has the subsize dimensions of 55 x 10 x 5 mm and were produced by machining, whereas, the impact strength specimens for the AISI304 materials has subsize dimensions of 55 x 10 x 3 mm and were cut from each welded sample by means of laser cutting. The impact strength samples were tested at room temperature using a MAT21 universal pendulum impact tester shown in Fig. 4.22. The average of at least three results of impact strength was calculated for each sample for all materials where the impact strength was considered as a response. The experimental calculated averages were tabulated for further analysis.

Fig. 4.22: Photograph of the standard ASTM universal pendulum impact tester.

4.7 Metallographic Characterization and Microhardness Measurements

4.7.1 Sample preparation

Transverse sections were cut from all samples after laser welding using a cutter with a coolant liquid. The specimens were mounted in Bakelite using a Buehler Simplimet 2000 Mounting Press. A hot-compression mounting procedure was followed to provide a hard mass, which allows fixing of the specimens during the following operations. Grinding was carried out for all specimens using the Buehler type Motopol 2000 grinding and polishing wheel. The procedure involved starting grinding with coarser abrasive silicon carbide paper of 240 grain/cm² and finishing with the finest paper of 800 grain/cm² for 4 min. The details are given in Table 4.3. Polishing was carried out in three stages using diamond suspensions with different grain sizes, as described also in Table 4.3. After polishing, the specimens were cleaned thoroughly by cool running water followed by acetone, and then dried. The AISI1045 specimens were etched using Nital (5% HNO_3 + 95 % ethanol) for 10 seconds to reveal the bead geometry and microstructure [171]. The AISI304 specimens were etched using etching solution consists of 20 ml Ethanol 96% + 20 ml Hydrochloric acid 32% + 1 g Copper 2 chloride to expose bead geometry and microstructure. Finally, the dissimilar weldments were etched using both etching solution mentioned above to reveal bead geometry and microstructure.

Table 4.3: Grinding and polishing stages.

Stage No.	Abrasive	Grain size	Time min	Speed rpm	Lubricant
1	Silicon carbide paper	240 grain/cm²	4	150	water
2	Silicon carbide paper	600 grain/cm²	4	150	water
3	Silicon carbide paper	800 grain/cm²	4	150	water
4	diamond suspension	6 μm	5	250	wet before
5	diamond suspension	3 μm	5	250	wet before
6	diamond suspension	0.05 μm	5	250	wet before

4.7.2 Specimen characterization

4.7.2.1 Microstructure

The microstructures of selected laser welded samples were examined by means of optical microscopy equipped with a video camera, shown in Fig. 4.23. In this work two objective lenses were used with magnifications of 8X and 80X with an eye lens of 16X.

Fig. 4.23: Optical microscopy.

4.7.2.2 Microhardness measurement

Microhardness measurements were carried out at room temperature with a PMT-3 microhardness tester, shown in Fig. 4.24, and equipped with a diamond Vickers indenter. A load of 0.1 kg was applied for fifteen seconds and the size of the

indentation was measured using a light microscope supplied as part of the microhardness tester. The Vickers hardness number is based on the force divided by the surface area of the indentation, as can be seen in Eq. 4.6 [169]. Five measurements were made at different locations for each weld transverse specimen namely: welded zone, HAZ and base metal, and then the average of these five measurements was calculated for each location.

$$HV = 1.8544 \times \frac{P}{d^2} \tag{4.6}$$

Where:

P: load in kgf.

d: indentation length in mm.

Fig. 4.24: Microhardness tester.

4.8 Operating Cost Calculation

Laser welding operating costs can be estimated as welding per hour or welding per unit length for a particular laser welding operation. The welding system used in this work utilized CO_2 using a static volume of laser gases of approximately 7.5 litres every 72 hours. For this welding system with 1.5 kW maximum output power the operating costs generally falling into the categories listed in Table 4.4 [172]. The

operating cost calculation does not account for unscheduled breakdown or maintenance, such as breakdown in the table motion controller or PC hard disc replacement. The total approximated operating cost per hour as a function of the output power can be estimated by 4.954 + 1.158*P. The total approximated operating cost per unit length of the weld is given by Eq. 4.7 assuming 85% utilization. Eq. 4.7 was used to calculate the joint cost per meter for all samples for each material and the results were tabulated for further analysis.

Table 4.4: Operating costs break down.

Element of cost	**Calculations**	**Welding cost €/h**
Laser electrical power	(20.88 kVA)(0.8 pf)(€ 0.104/kWh)*(P/1.5)	1.158*P
Chiller electrical power	(11.52 kVA)(0.8 pf)(€ 0.104/kWh)	0.958
Motion controller power	(4.8 kVA)(0.8 pf)(€ 0.104/kWh)	0.399
Exhaust system power	(0.9 kWh)(€ 0.104/kWh)	0.094
Laser gas LASPUR208	{(€ 989.79/ bottle)/(1500litre/bottle)}x 7.5litre/72h	0.069
Gas bottle rental	(€ 181.37/720h)	0.252
Chiller additives	(€ 284.80/year)/(8760 h/year)	0.033
Shielding gas (Argon)	(5litre/min)(60min/h)(€8.62 x10^{-3}/Liter)	2.586
Nozzle tip	(€ 5.60/200h)	0.028
Exhaust system filters	(€ 5/100h)	0.05
Focus lens	(€184.51/lens)/(1000h)	0.185
Maintenance labour (with overhead)	(12 h/2000h operation)(€50/h)	0.30
Total approximated operating cost per hour		4.954+1.158*P €/h

$$\text{Welding cost[Euro/m]} = \frac{4.954 + 1.158 \times P}{(0.85) \times S[\text{cm/min}][60\text{min/h}][\text{m/100cm}]} = \frac{4.954 + 1.158 \times P}{0.51 \times S} \quad (4.7)$$

Where

P: used output power in kW.

S: Welding speed in cm/min.

CHAPTER V

RESULTS AND DISCUSSION

5- RESULTS AND DISCUSSION

In this chapter, the experimental designs used, the range of each process parameter and experimental layout are presented for each material. This chapter also shows the results for all the materials investigated in this work, in terms of ANOVA analysis of each response, and the validation experiments. The effects of process parameters on each response are described and discussed. Further, the results of the microstructure are illustrated and discussed to distinguish the effect of the process parameters on the mechanical properties.

5.1 Medium Carbon Steel AISI1045

For this material, the experiment was designed based on a three level Box-Behnken design with full replication due to the fact that the number of unwelded plates available was limited and it was not possible to run CCD for this material. Trial samples of butt-welding were performed by varying one of the process variables to determine the working range of each variable. Absence of visible welding defects and at least half depth penetration were the criteria used to choose the working ranges. Table 5.1 shows the laser input variables and experimental design levels used for this material. The experiment was carried out according to the design matrix shown in Table 5.2 in a random order to avoid any systematic error using a CW 1.5 kW CO_2 Rofin laser. Argon gas was used as shielding gas with constant flow rate of 5 ℓ/min. For this material, seven mathematical models were developed successfully to predict the following responses: heat input, depth of penetration (DP), width of FZ (W), width of HAZ (W_{HAZ}), impact strength, notched tensile strength (NTS) and joint operating cost. The procedures described earlier in Chapter 4 were followed to determine and record these responses. The averages of at least three measurements for each response are presented in Table 5.3. Full experimental measured data for all responses can be seen in Appendix B. The heat input was calculated using Heat input = (P/S)*η. Where: η is the welding efficiency which is assumed to be 80 % [173].

Table 5.1: Process variables and experimental design levels used.

Variables	Code	Unit	Limits coded/actual		
			-1	0	+1
Laser power	P	kW	1.2	1.3125	1.425
Welding speed	S	cm/min	30	50	70
Focus point position	F	mm	-2.5	-1.25	0

Table 5.2: Design matrix in actual values.

Exp. No.	Run order	P	S	F	Exp. No.	Run order	P	S	F
1	1	1.2	30	-1.25	10	7	1.3125	70	-2.5
2	8	1.425	30	-1.25	11	9	1.3125	30	0
3	13	1.2	70	-1.25	12	6	1.3125	70	0
4	14	1.425	70	-1.25	13	11	1.3125	50	-1.25
5	4	1.2	50	-2.5	14	17	1.3125	50	-1.25
6	16	1.425	50	-2.5	15	2	1.3125	50	-1.25
7	10	1.2	50	0	16	15	1.3125	50	-1.25
8	3	1.425	50	0	17	12	1.3125	50	-1.25
9	5	1.3125	30	-2.5	-	-	-	-	-

Table 5.3: Experimentally measured responses.

Exp. No.	Av. W [mm]	Av. DP [mm]	Av. W_{HAZ} [mm]	Heat input [J/cm]	Av. Impact Energy [J]	Av. NTS [MPa]	Joint cost [€/m]
1	2.358	3.572	0.561	1920	57	400	0.4146
2	2.805	4.322	0.872	2280	77	452	0.4316
3	1.342	2.705	0.392	823	32	220	0.1777
4	1.852	3.651	0.384	977	50	269	0.1850
5	2.761	2.655	0.453	1152	35	201	0.2488
6	3.381	3.888	0.569	1368	55	240	0.2590
7	2.087	3.813	0.511	1152	53	331	0.2488
8	2.572	4.539	0.574	1368	68	390	0.2590
9	3.681	3.905	0.625	2100	49	361	0.4231
10	1.982	2.367	0.375	900	25	110	0.1813
11	2.423	4.987	0.762	2100	58	408	0.4231
12	1.649	3.824	0.413	900	33	279	0.1813
13	2.625	3.712	0.531	1260	40	334	0.2539
14	2.282	3.872	0.562	1260	38	333	0.2539
15	2.567	3.586	0.466	1260	42	339	0.2539
16	2.413	3.505	0.478	1260	39	331	0.2539
17	2.293	3.626	0.506	1260	41	337	0.2539

5.1.1 Development of weld bead profile parameters models

As a result of analyzing the measured responses by the design expert software, the fit summary output indicates that the linear model is statistically significant for the penetration model; therefore, it will be used for further analysis. For the other responses the quadratic models are statistically recommended for further analysis as they have the maximum predicted and adjusted R^2 [156]. The test for significance of the regression models, the test for significance on individual model coefficients and the lack of fit test were performed using the same statistical package for all responses. By selecting the step-wise regression method, the insignificant model terms can be automatically eliminated. The resulting ANOVA tables (Tables 5.4 to 5.7) for the reduced quadratic models outline the analysis of variance of each response and show the significant model terms. The same tables show also the other adequacy measures R^2, Adjusted R^2 and Predicted R^2. The entire adequacy measures are close to 1, which is in reasonable agreement and indicates adequate models [154, 156]. The Adequate Precision compares the range of the predicted value at the design points to the Average Prediction Error. In all cases the value of Adequate Precision are dramatically greater than 4. An Adequate Precision Ratio above 4 indicates adequate model discrimination [156].

For the heat input model, the Analysis of Variance indicates that the main effect are laser power (P), welding speed (S), the second order effect of welding speed (S^2). The two levels of interaction of laser welding and welding speed (PS) are the most significant model terms associated with heat input. Secondly for the penetration model, the ANOVA analysis indicates that there is a linear relationship between the main effects of the three parameters, which is in agreement with findings of Radaj and El-Batahgy [4, 139]. Also, in case of the welded zone width model, the main effect of laser power (P), welding speed (S), focused position (F), the second order effect of welding speed (S^2), the second order effect of the focused position (F^2) and the two level interaction of welding speed and focus point position (SF) are significant model terms. However, the main effect of welding speed (S) and the main effect of focus point position (F) are the most significant factors associated with the welded zone width. Finally, for the HAZ width model it is evident from the results that the main effect of laser power (P), welding speed (S), focus point position

(F) and the two level interaction of the laser power and welding speed (PS) are significant model terms. However, the main effect of welding speed (S) is the most important factor influencing the HAZ width. The final mathematical models in terms of coded factors as determined by design expert software are shown in Eqs. 5.1 to 5.4. The final empirical models in terms of actual factors are shown in Eqs. 5.5 to 5.8:

Table 5.4: ANOVA table for heat input reduced quadratic model.

Source	Sum of Squares	DF	Mean Square	F Value	Prob > F	
Model	3246465	4	811616	11507	< 0.0001	Significant
P	111932.1	1	111932	1587	< 0.0001	
S	2880000	1	2880000	40833	< 0.0001	
S^2	243952.9	1	243952	3459	< 0.0001	
P*S	10579.56	1	10579	150	< 0.0001	
Residual	846.3732	12	70.53			
Cor Total	3247311	16				
$R^2 = 0.9997$			Pred $R^2 = 0.9989$			

Table 5.5: ANOVA table for penetration reduced linear model.

Source	Sum of Squares	DF	Mean Square	F Value	Prob > F	
Model	6.279	3	2.093	51.399	< 0.0001	Significant
P	1.670	1	1.670	41.007	< 0.0001	
S	2.246	1	2.246	55.158	< 0.0001	
F	2.363	1	2.363	58.031	< 0.0001	
Residual	0.529	13	0.041			
Lack of Fit	0.451	9	0.050	2.560	0.190	Not Significant
Pure Error	0.078	4	0.020			
Cor Total	6.809	16				
$R^2 = 0.922$			Pred $R^2 = 0.849$			
Adj $R^2 = 0.904$			Adeq Precision= 21.931			

Table 5.6: ANOVA table for WZ width reduced quadratic model.

Source	Sum of Squares	DF	Mean Square	F Value	Prob > F	
Model	5.140	6	0.857	58.732	< 0.0001	Significant
P	0.531	1	0.531	36.440	0.0001	
S	2.466	1	2.466	169.105	< 0.0001	
F	1.181	1	1.181	80.985	< 0.0001	
S^2	0.361	1	0.361	24.750	0.001	
F^2	0.386	1	0.386	26.448	0.0004	
S*F	0.214	1	0.214	14.666	0.003	
Residual	0.146	10	0.015			
Lack of Fit	0.048	6	0.008	0.330	0.891	Not significant
Pure Error	0.098	4	0.024			
Cor Total	5.286	16				
$R^2 = 0.972$			Pred $R^2 = 0.922$			
Adj $R^2 = 0.956$			Adeq Precision = 29.498			

Table 5.7: ANOVA table for HAZ width reduced quadratic model.

Source	Sum of Squares	DF	Mean Square	F Value	Prob > F	
Model	0.259	4	0.065	42.631	< 0.0001	Significant
P	0.029	1	0.029	19.138	0.0009	
S	0.197	1	0.197	129.953	< 0.0001	
F	0.007	1	0.007	4.666	0.0517	
P*S	0.025	1	0.025	16.766	0.0015	
Residual	0.018	12	0.002			
Lack of Fit	0.012	8	0.002	0.990	0.5436	Not significant
Pure Error	0.006	4	0.002			
Cor Total	0.277	16				
$R^2 = 0.934$			Pred $R^2 = 0.861$			
Adj $R^2 = 0.912$			Adeq Precision = 22.899			

$$\text{Heat input} = 1260 + 118.29P - 600S + 240S^2 - 51.43PS \quad (5.1)$$

$$DP = 3.68 + 0.46\,P - 0.53S + 0.54F \quad (5.2)$$

$$W = 2.42 + 0.26P - 0.56S - 0.38F - 0.31S^2 + 0.30F^2 + 0.23SF \quad (5.3)$$

$$W_{HAZ} = 0.53 + 0.06P - 0.16S + 0.03F - 0.08PS \quad (5.4)$$

$$\text{Heat input} = 1380 + 2194.28\,P - 60\,S + 0.6\,S^2 - 22.86\,PS \quad (5.5)$$

$$DP = 0.22 + 4.06\,P - 0.03\,S + 0.43\,F \quad (5.6)$$

$$W = -1.790 + 2.291\ P + 0.061\ S - 0.286\ F - 0.0008\ S^2 + 0.193\ F^2 + 0.009\ SF \quad (5.7)$$

$$W_{HAZ} = -2.075 + 2.308\ P + 0.039\ S + 0.024\ F - 0.035\ PS \quad (5.8)$$

Example 1: Evaluate the value of HAZ width at the se welding condition: P = 1.2 kW, S = 35 cm/min and F = -0.25 mm. By substituting in Eq. 5.8 the following can be obtained;

$$W_{HAZ} = -2.075 + 2.308\ (1.2) + 0.039\ (35) + 0.024\ (-0.25) - 0.035\ (1.2*35) = 0.5836 \text{ mm}$$

5.1.1.1 Validation of the models.

Fig 5.1a-d shows the relationship between the actual and predicted values of heat input, DP, W and W_{HAZ}, respectively. This figure indicates that the developed models are adequate because the residuals in prediction of each response are small, as the residuals tend to be close to the diagonal line. To verify the adequacy of the developed models further, three confirmation experiments were carried out using new randomly selected test conditions, each within the experiment range defined earlier. Using the point prediction option in the software, the heat input, DP, W and W_{HAZ} of the validation experiments were predicted using the previous developed models and compared with the actual measured responses of these confirmation experiments. Table 5.8 summarises the experiment conditions, actual experimental values, the predicted values and the percentages of error in prediction. It is evident that the models can adequately describe the responses within the ranges considered as the maximum error percent in prediction is -6.11 % which is in good agreement.

Table 5.8: Confirmation experiments for weld-bead parameters.

Exp. No.	P	S	F		Heat input	DP	W	W_{HAZ}
1	1.35	50	-1.25	Actual	1296	4.012	2.428	0.573
				Predicted	1299.43	3.83	2.505	0.551
				Error %	-0.264	4.75	-3.07	3.99
2	1.31	30	-1.25	Actual	2100	4.407	2.703	0.714
				Predicted	2100	4.21	2.666	0.688
				Error %	0	4.68	1.39	3.78
3	1.31	50	0	Actual	1260	3.962	2.398	0.579
				Predicted	1260	4.22	2.337	0.561
				Error %	0	-6.11	2.61	3.21

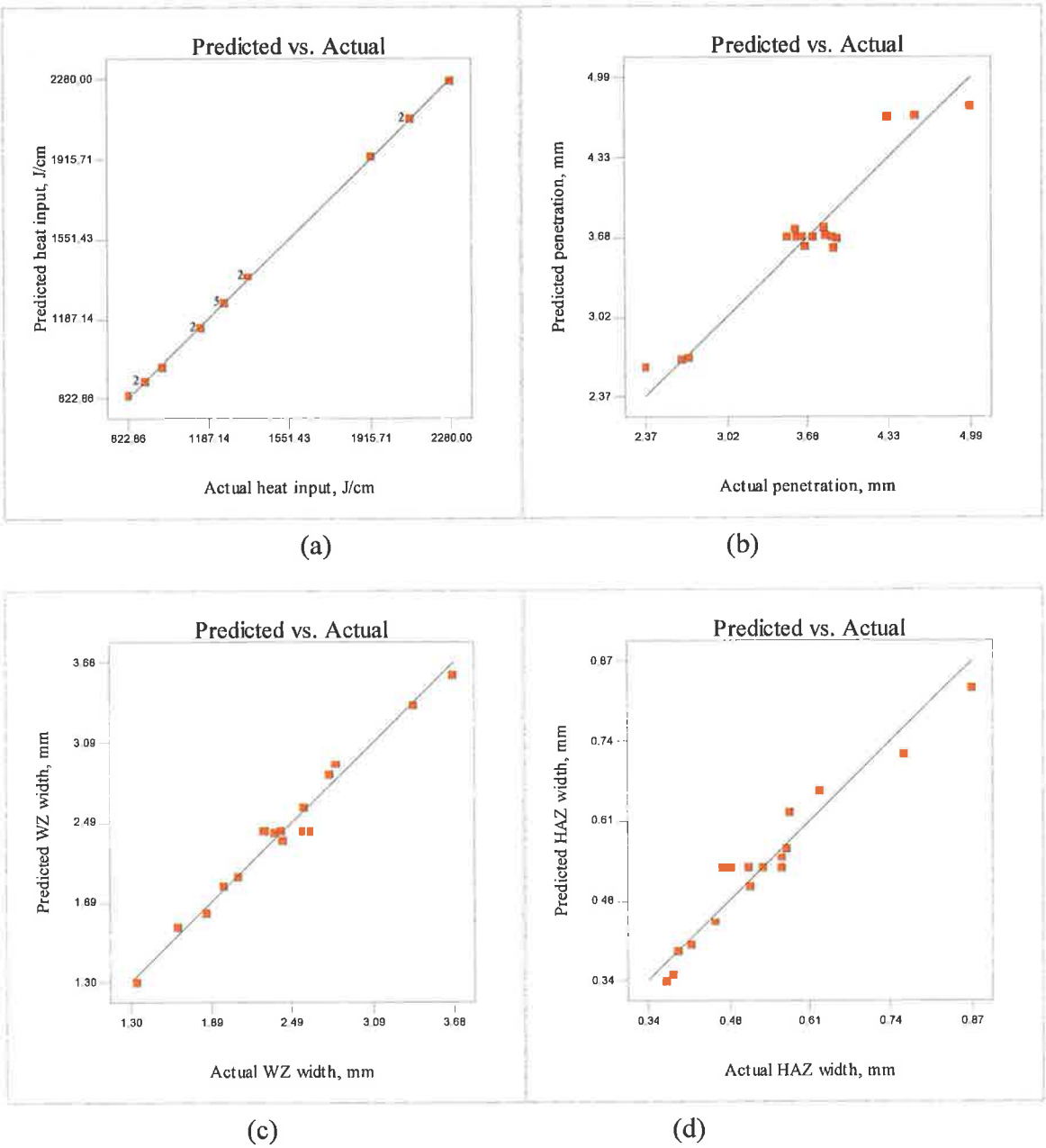

Fig. 5.1: Scatter diagram for, (a) Heat input, (b) Penetration, (c) Width of fusion zone and (d) width of HAZ.

5.1.1.2 Effect of process factors on weld-bead parameters

The laser welding input parameters determine the shape of laser weld-bead, due to the fact that a combination of these parameters control the heat input [4]. For a good weld quality the combination of the output power, welding speed, focal position and shielding gas should be correctly selected. Below is a general discussion of the effect of process variables on the weld-bead parameters.

a) Heat input

The heat input is directly related to laser power, welding speed and welding efficiency, as stated earlier. The reason for predicting the heat input is to develop a model that will include it into the optimisation step at a later stage, because of the software limitations. Fig. 5.2 shows a contours graph of the effect of welding speed and laser power on the heat input. From this graph it is evident that the heat input increases as the (P) increases and the (S) decreases.

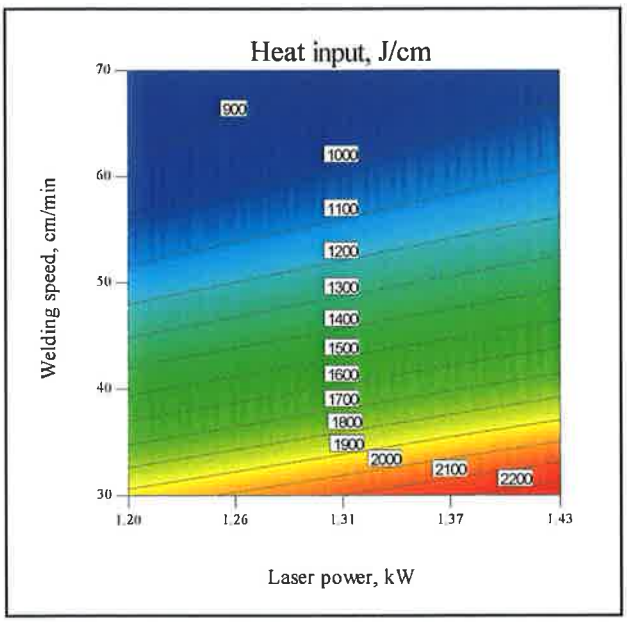

Fig. 5.2: Contours graph shows the effect of P and S on the heat input.

b) Penetration

From the results it is clear that the three parameters are significantly affecting the penetration (DP). These effects are due to the following points: an increase in (P) leads to an increase in the heat input, therefore, more molten metal and consequently more penetration will be achieved. However, the idea is reversed in the case of welding speed (S) effect, because the welding speed is inversely proportional to the heat input. Using a focused beam results in increased power density, which means the heat will localize in a small metal portion resulting in an increase in the power density leading to better penetration. To achieve maximum (DP) the laser power has to be maximum with a focused beam (i.e. F = 0), while (S) has to be minimum. Figs. 5.3-5.4 are contours graphs showing the effect of the process parameters on the weld penetration. Fig. 5.5 is a perturbation plot showing the effect of all parameters on the

penetration. The perturbation plot allows the effect of all the factors at a particular point in the design space to be compared. This type of display does not show the effect of interactions. The lines represent the behaviours of each factor while holding the others in a constant ratio (centre point by default). In the case of more than one factor this type of display could be used to find those factors that most affect the response.

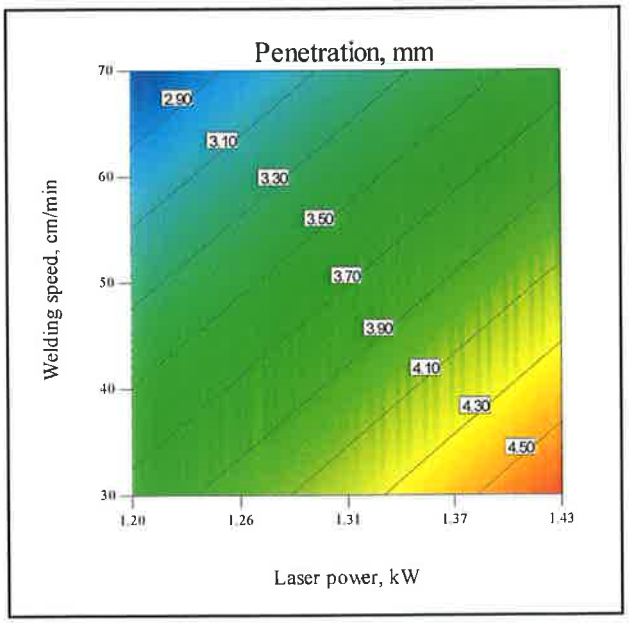

Fig. 5.3: Contour graph shows the effect of P and S on penetration at F = -1.25 mm.

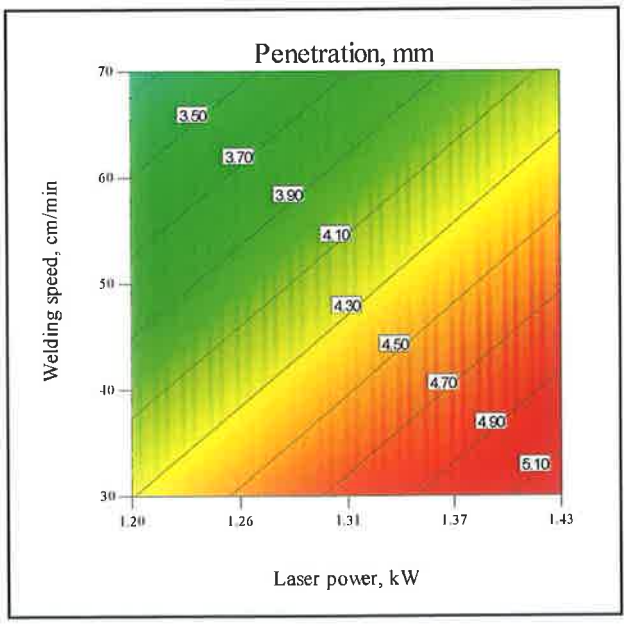

Fig. 5.4: Contour graph shows the effect of P and S on penetration at F = 0 mm.

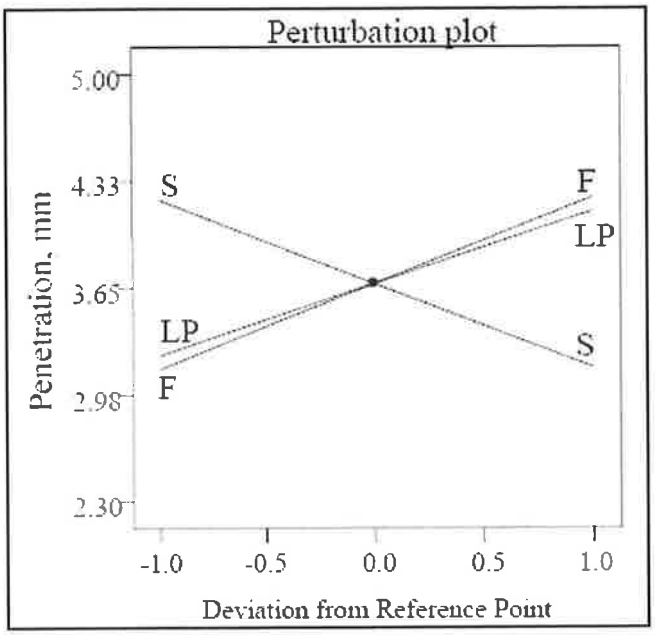

Fig. 5.5: Perturbation plot shows the effect of all parameters on the penetration.

c) Width of fusion zone

The results indicate that the welding speed (S) and focus point position (F) are the most important factors affecting the welded zone width (W). An increase in welding speed (S) leads to a decrease in (W). This is because when (S) is increased the laser beam along the welding line moves at high speed. Therefore, the heat input decreases leading to a reduced volume of the base metal being melted, consequently, the width of the welded zone decreases. Moreover, a defocused beam, which means a wide laser beam, results in spreading the laser power over a wide area. Therefore, wide area of the base metal will melt leading to an increase in (W) or vice versa. The results demonstrate also that the laser power (P) contributes to secondary effects in the bead width. An increase in (P) results in a slight increase in the (W), because of the increase in the power density. Figs. 5.6 -5.7 are contour graphs showing the effect of welding speed and focal point position on the WZ width at laser power values of 1.31 and 1.43 kW respectively.

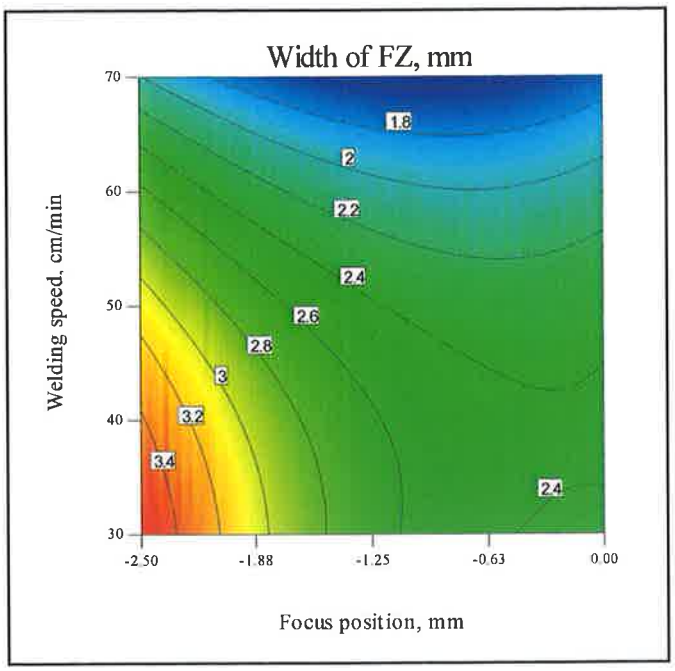

Fig. 5.6: Contours graph shows the effect S and F on W at P = 1.31 kW.

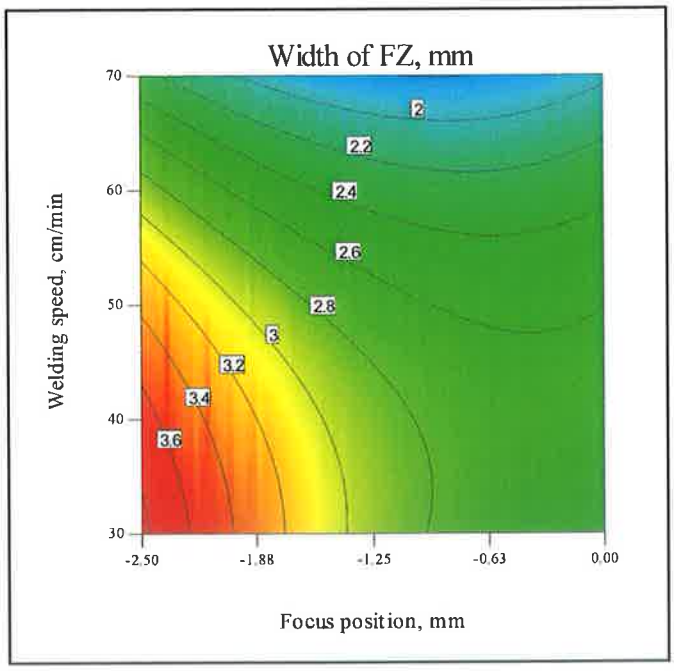

Fig. 5.7: Contours graph shows the effect S and F on W at P = 1.43 kW.

d) Heat affected zone width

The main factor influencing the Width of HAZ (W_{HAZ}) is the welding speed, as the results indicate. This is due to the fact that at low (S) the heat input will be greater. This heat will conduct from the fusion zone to the bulk metal through HAZ

making it wider and coarser. The results show also that the other two factors and the two level interaction of the (PS) are contributing secondary effects on the Width of HAZ (W_{HAZ}). Fig. 5.8 is a contours graph that shows the effect of welding speed and laser power on the HAZ width at a focal point position of -1.25 mm.

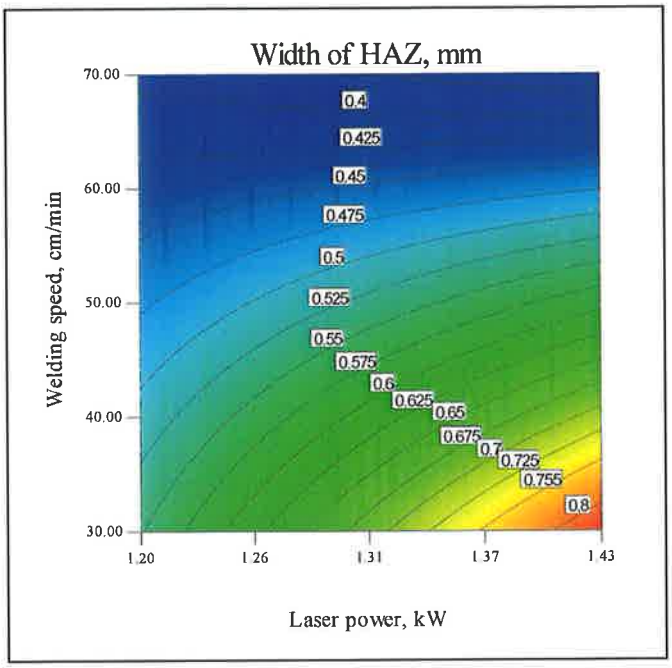

Fig. 5.8: Contours graph shows the effect of welding speed and laser power on the HAZ width at F = -1.25 mm.

5.1.2 Development of impact and notched tensile strength models

As a result of analyzing the measured responses using the Design Expert software, the fit summary selects the highest order polynomial where the additional terms are significant and the model is not aliased. Choosing the step-wise regression method leads to elimination of the insignificant model terms automatically. Table 5.9 and Table 5.10 present the ANOVA results for the impact strength and NTS respectively and show the significant model terms. The same tables show also the other adequacy measures R^2, Adjusted R^2 and Predicted R^2. All the adequacy measures are close to 1, which is in reasonable agreement and indicates adequate models [155, 156]. The Adequate Precision in both cases is greater than 4. An Adequate Precision ratio of greater than 4 indicates adequate model discrimination [156]. The result of the Analysis of Variance for the impact strength model shows that the main effect of the three laser welding parameters and the quadratic effect of

the laser power are significant model terms. However, the welding speed and the laser power are the factors which most affect the impact strength. For the notched tensile strength model, the results indicate that the main effect of the three factors, the quadratic effect of the focus point position and the interaction effect of the welding speed and the focus point position are significant model terms. However, the welding speed and the focus point position are the factors most associated with the notched tensile strength. The final models in terms of coded factors are shown in Eqs. 5.9-5.10. While, the final models in terms of actual factors are presented in Eqs. 5.11-5.12.

Table 5.9: ANOVA analysis for impact strength reduced model.

Source	Sum of Squares	DF	Mean squares	F Value	Prob > F	
Model	2925.27	4	731.318	172.592	< 0.0001	Significant
P	666.13	1	666.125	157.206	< 0.0001	
S	1275.13	1	1275.125	300.931	< 0.0001	
F	288.00	1	288.000	67.968	< 0.0001	
P^2	696.02	1	696.020	164.262	< 0.0001	
Residual	50.85	12	4.237			
Lack of Fit	40.85	8	5.106	2.042	0.2559	Not significant
Pure Error	10.00	4	2.5			
Cor Total	2976.12	16				
R^2= 0.983				Adj. R^2= 0.977		
Pred. R^2= 0.962				Adeq. Precision = 47.65		

Table 5.10: ANOVA analysis for notched tensile strength reduced model.

Source	Sum of Squares	DF	Mean squares	F Value	Prob > F	
Model	117005.7	5	23401.14	370.511	< 0.0001	Significant
P	4950.1	1	4950.13	78.375	< 0.0001	
S	69006.1	1	69006.13	1092.576	< 0.0001	
F	30752.0	1	30752.00	486.897	< 0.0001	
F^2	8576.5	1	8576.47	135.792	< 0.0001	
SF	3721.0	1	3721.00	58.915	< 0.0001	
Residual	694.8	11	63.16			
Lack of Fit	654.0	7	93.42	9.159	0.0246	Significant
Pure Error	40.8	4	10.20			
Cor Total	117700.5	16				
R^2= 0.994				Adj. R^2= 0.991		
Pred. R^2= 0.975				Adeq. Precision = 73.734		

$$\text{Impact Strength} = 40.56 + 9.13P - 12.63S + 6.0F + 12.82P^2 \quad (5.9)$$

$$\text{NTS} = 335 + 24.88P - 92.88S + 62\,F - 45\,F^2 + 30.5\,SF \quad (5.10)$$

$$\text{Impact Strength} = 1716.53 - 2577.74P - 0.6313S + 4.8F + 1012.89P^2 \quad (5.11)$$

$$\text{NTS} = 217.73 + 221.11P - 3.12S - 83.4F - 28.80F^2 + 1.22SF \quad (5.12)$$

5.1.2.1 Validation of the models

Fig. 5.9 shows the actual response versus predicted response for the impact strength and notched tensile strength. Both models are adequate because the residuals distribution have a tendency to be close to the diagonal line. Furthermore, three extra confirmation experiments were carried out using randomly selected test conditions that had not been used before but were within the factor range of the current work. Table 5.11 shows the actual, predicted values for these confirmation experiments and the percentage of error in prediction for both responses. Therefore, it can be said that the models can adequately describe the two responses within the limits of the factors being investigated in this study.

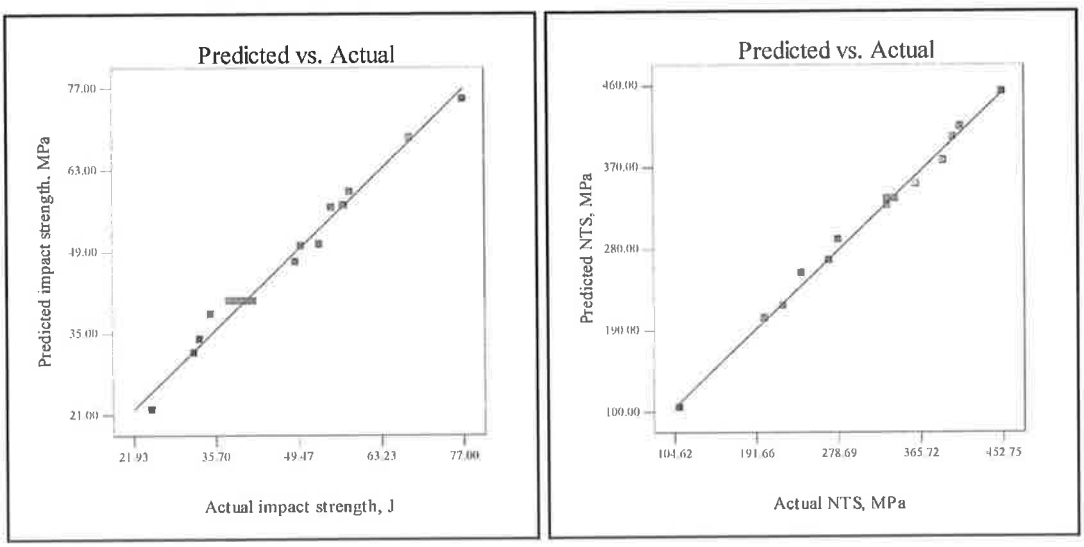

(a) (b)

Fig. 5.9: Scatter diagram for (a) impact strength model and (b) NTS model.

Table 5.11: Confirmation experiments for impact strength and NTS.

Exp. No.	Laser power	Welding speed	Focused position		Impact Strength	NTS
1	1.35	50	-1.25	Actual	42	309
				Predicted	45	343
				Error %	- 6.67	- 9.91
2	1.31	30	-1.25	Actual	56	415
				Predicted	53	427
				Error %	5.66	- 2.81
3	1.31	50	0	Actual	50	363
				Predicted	46	351
				Error %	- 8.70	3.42

5.1.2.2 Effect of process factors on impact strength and NTS

The welded joint performance is interrelated to the welding procedure and the serving conditions. It is well known that the welded components become very tough as the serving temperature decreases; this would result in reduced impact strength of the welded joint. It is obvious from refs. [10, 11] that, using different laser welding procedures would result in different thermal histories of the weldment, which may cause variant microstructure resulting in different mechanical properties of the weldment. Impact strength and notched tensile strength are among the most important mechanical properties of the welded joints. Therefore, predicting the mechanical properties, in particular the impact strength of the laser welded joints at room temperature and the notched tensile strength, is essential to improve the performance of welded joint.

a) Welding speed

The results indicate that the welding speed is the most significant factor associated with both responses as shown in Fig. 5.10 and Fig. 5.11. The slower the welding speed the higher the impact strength and NTS. It is evident from the perturbation plots shown in Fig. 5.12 and Fig. 5.13 that reducing the welding speed from its highest value to lowest value would cause both responses to increase by 89.3 % and 76.85 % respectively. This is due to the fact that when the welding speed decreases, more heat is introduced into the fusion zone. Consequently, there is greater penetration resulting in an excellent joint. On the other hand, if the welding

speed is too high, there is insufficient penetration, which results in a badly welded joint with poor mechanical properties.

b) Laser power

It is evident from the results that the laser power also has a strong effect on the impact strength of the laser-welded joint as shown in Fig. 5.10. It is obvious from the perturbation plots shown in Fig. 5.12 that increasing the laser power from its lowest value to highest value would result in increasing the impact strength by 43.2%. This is due to the fact that using high laser power results in an increase in the power density, at a given focus point position, leading to greater penetration. For the second response the laser power slightly affects the NTS as shown in Fig. 5.11. It is obvious from the perturbation plots shown in Fig. 5.12 that increasing the laser power from its lowest value to highest value would result in increasing the NTS by 16.13 %.

c) Focus point position

The results indicate that the focus point position slightly affects the first response and strongly affects the second response, as shown in Fig. 5.10 and Fig. 5.11 respectively. It is clear from the perturbation plots shown in Fig. 5.12 and Fig. 5.13 that changing the focused position from its lowest value to the highest value (i.e. F = 0) would result in an increase in both responses by 34.3% and 54.63 % respectively. Generally speaking, using a focused laser beam means that the laser power will be localised onto a small area resulting in an increase in the power density leading to better penetration and sound welds.

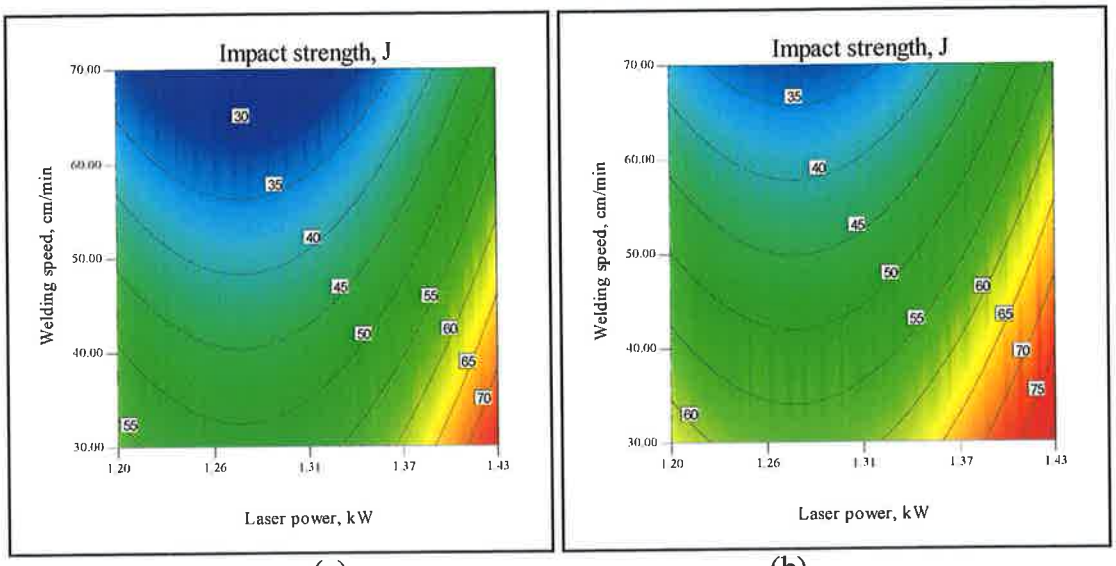

(a) (b)

Fig. 5.10: Contours graph shows the effect of S and P on the impact strength at (a) F = -1.25 mm and (b) F = 0 mm.

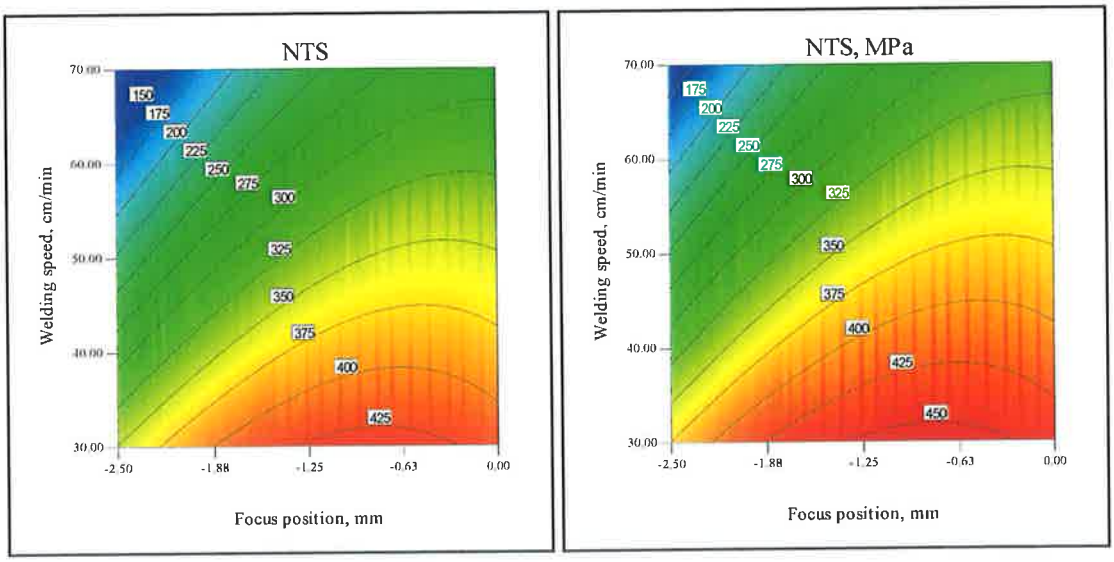

(a) (b)

Fig. 5.11: Contours graph shows the effect of S and F on the NTS at (a) P = 1.31 kW and (b) P = 1.43 kW.

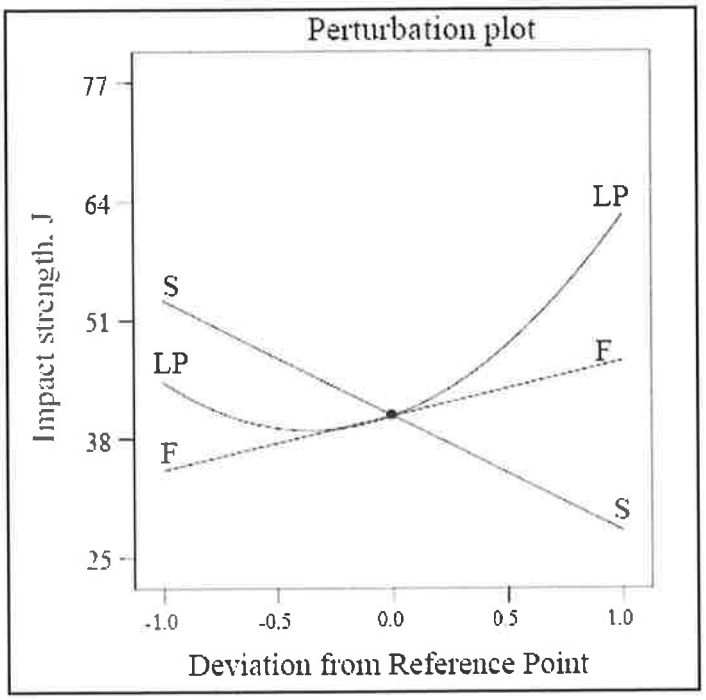

Fig. 5.12: Perturbation plot showing the effect of all parameters on impact strength.

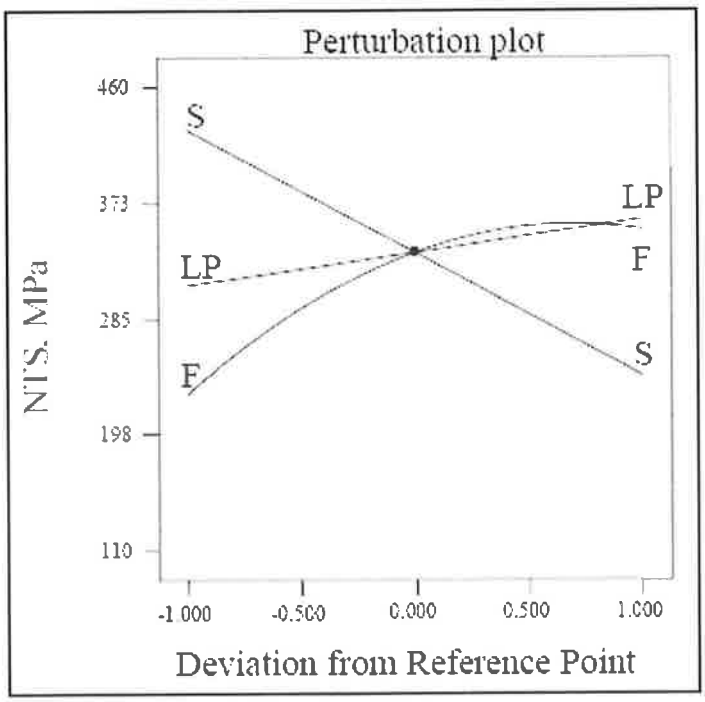

Fig. 5.13: Perturbation plot showing the effect of all parameters on NTS.

5.1.3 Developing the operating cost model

The welding operating costs per meter have been calculated using Eq. 4.7. In this work a mathematical model was developed to minimize the welding operating cost. The same procedure was followed to develop and check the model adequacy. Table 5.12 shows the Analysis of Variance for the reduced quadratic model, summarizes the Analysis of Variance for the cost model and shows the significant model terms as well as the adequacy measures. All the adequacy measures are in reasonable agreement and indicate significance relationships. Accordingly, the model can be used for further analysis. The cost model is presented in Eq. 5.13 in terms of coded factors. The reason for predicting the joint operating cost is for optimization purpose.

$$\text{Joint operating cost} = 0.25 + 5.595\times10^{-3}\,P - 0.12S - 2.433\times10^{-3}\,PS + 0.048S^2 \quad (5.13)$$

Table 5.12: ANOVA analysis for the operating cost model.

Source	Sum of Squares	DF	Mean squares	F Value	Prob > F	
Model	0.127101	4	0.031775	201334.1	< 0.0001	Significant
P	0.00025	1	0.00025	1587	< 0.0001	
S	0.116923	1	0.116923	740845.6	< 0.0001	
PS	2.37E-05	1	2.37E-05	150	< 0.0001	
S^2	0.009904	1	0.009904	62753.98	< 0.0001	
Residual	1.89E-06	12	1.58E-07			
Cor Total	0.127103	16				
$R^2 = 1.000$				Adj. $R^2 = 1.000$		
Pred. $R^2 = 0.9999$				Adeq. Precision = 1174.19		

5.1.4 Microstructure and microhardness investigation

Fig. 5.14 (a) reveals the microstructure of the base metal with equiaxial grains. It is clear that the microstructure of the base metal consists of two phases; ferrite (white) and pearlite (back), which is a mixture of ferrite and cementite (Fe_3C). The average microhardness of the base metal is about 119 HV. The microstructure of the HAZ of sample number 3 is shown in Fig. 5.14 (b); it is obvious that the grains are longer and bigger with an average microhardness of 110 Hv. Fig. 5.15 reveals the microstructure of the weld zone of different samples with a range of heat inputs of

823, 1152, 1260 and 2100 J/cm respectively. It is evident that as the heat input increases the microstructure of the weld area becomes coarser (i.e. grains size become bigger) due to the fact that the greater the amount of heat, the faster the grain growth and bigger the grains. Also, changing the amount of second phase (i.e. reducing the amount of pearlite as the heat input increases) in a predominantly ferrite matrix has a clear effect on the strength of the steel, especially the yield strength, as the surrounding ferrite is more ductile, as stated in [174]. Therefore, as the amount of the second phase is increased and becomes finer, as in Fig. 5.15(a), it is expected to have higher strength. This was also found by [60, 175]. Fig. 5.16 shows the effect of the heat input on the average microhardness of the weld zone. It is clear that as the heat input increases the microhardness decreases. This could be attributed to two factors; the increase in the grain size which takes places as the heat input increases and the coarser second phase due to the relative slow cooling rate. Therefore, those samples that had less heat input, and consequently a faster cooling rate due to the volume of the molten metal being less would have finer pearlite and higher microhardness. This result is in agreement with [175]

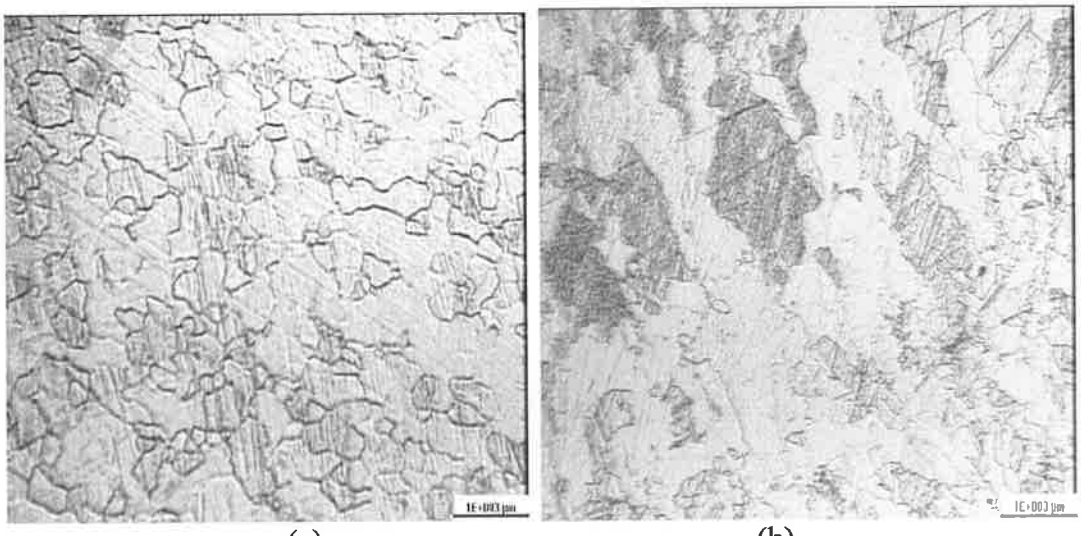

(a) (b)

Fig. 5.14: Micrograph showing the microstructure of (a) Base metal and (b) HAZ of sample no. 3, etched in 5% Nital for 10 seconds.

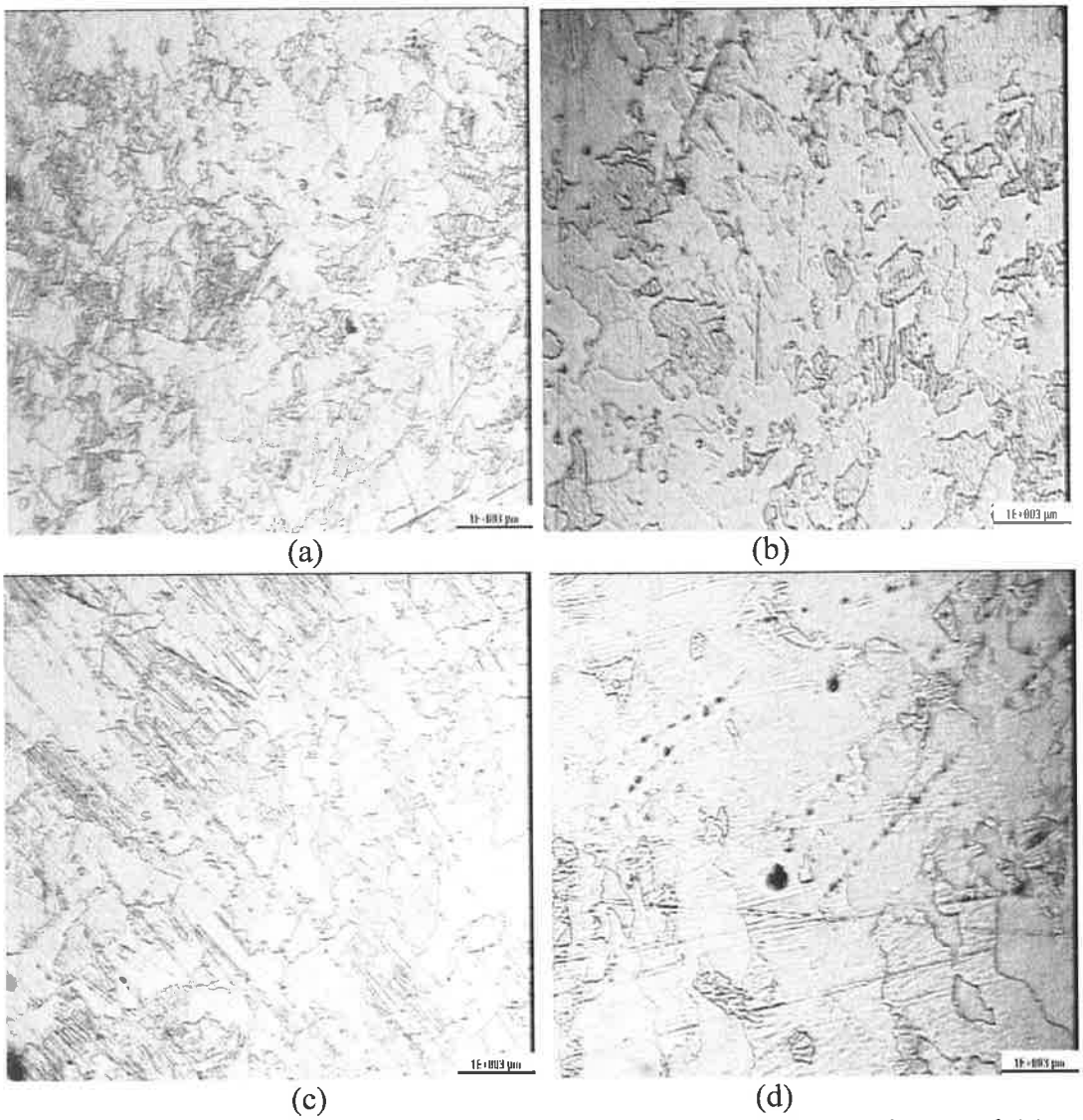

Fig. 5.15: Micrograph revealing the microstructure of medium carbon steel (a) sample No. 3, (b) sample No. 7, (c) sample No. 13 and (d) sample No. 11, etched in 5% Nital for 10 seconds.

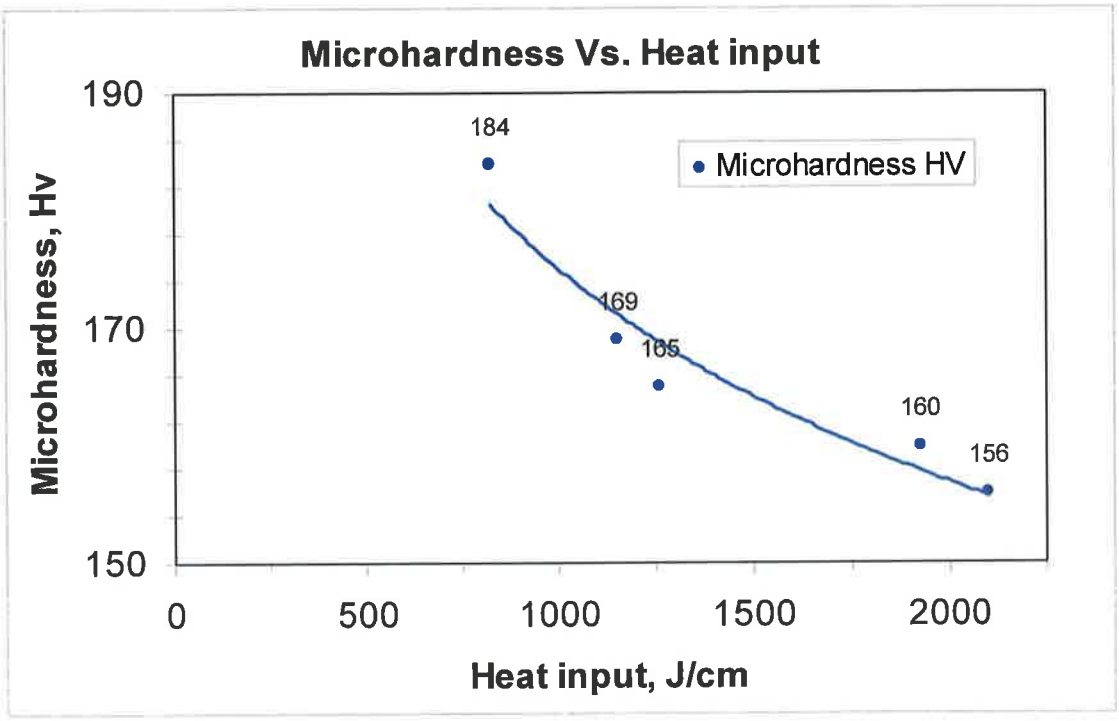

Fig. 5.16: Microhardness Vs. Heat Input for medium carbon steel.

5.2 Stainless Steel AISI304 3 mm

For this material the experiment was designed based on a three factors five levels CCD with full replication [154]. Trial Samples were prepared by changing one variable at a time to define the working ranges of the variables under investigation. Absence of obvious welding defects and full depth of penetration were the criteria used for selection of the working ranges. Table 5.13 shows the process variables, their standardized limits and coded values. The welding operation was carried out in the DCU workshop according to the experimental layout shown in Table 5.14, in a random order to avoid any systematic error in the experiment. Argon gas was used as shielding gas at constant flow rate of 5 l/min. During the laser welding operation the plates were clamped rigidly to avoid any deformation caused by the thermal loading, which may affect the results. No special heat treatments were carried out either before or after the laser welding. However, the plate's edges were prepared to ensure the full contact of the two plates along the weld line during the butt-welding. For this material, twenty eight mathematical models were developed successfully to predict the following responses: twenty one models to predict the residual stress distribution

through the depth and at three locations along the X-axes, nominal heat input (NH), front width of FZ (W), back width (BW), impact strength, tensile strength, weld pool area (A) and joint operating cost. The procedures described earlier in chapter 4 were followed to determine and record these responses. With the exception of residual stress, the averages of at least three measurements for each response are presented in Table 5.15 and Table 5.16. Appendix C presents the full experimental measured data for all responses.

Table 5.13: Independent variable and experimental design levels.

Variable	Notation	Unit	Standardized levels				
			-1.682	-1	0	1	1.682
Laser power	P	[kW]	1.03	1.1	1.2	1.3	1.37
Welding speed	S	[cm/min]	26.48	35	47.5	60	68.52
Focus point position	F	[mm]	-1	-0.8	-0.5	-0.2	0

Table 5.14: Experimental layout.

No	Run order	P	S	F	No	Run order	P	S	F
1	14	1.1	35	-0.8	11	2	1.2	26.48	-0.5
2	19	1.3	35	-0.8	12	18	1.2	68.52	-0.5
3	16	1.1	60	-0.8	13	7	1.2	47.5	-1
4	9	1.3	60	-0.8	14	3	1.2	47.5	0
5	20	1.1	35	-0.2	15	17	1.2	47.5	-0.5
6	13	1.3	35	-0.2	16	15	1.2	47.5	-0.5
7	10	1.1	60	-0.2	17	1	1.2	47.5	-0.5
8	12	1.3	60	-0.2	18	11	1.2	47.5	-0.5
9	4	1.03	47.5	-0.5	19	5	1.2	47.5	-0.5
10	6	1.37	47.5	-0.5	20	8	1.2	47.5	-0.5

Table 5.15: Experimental measured responses.

Std	Tensile strength, MPa	Impact strength, J	Nominal heat input J/cm	Front width, mm	Back width, mm	Weld pool area, mm^2	operating cost Euro/m
1	666	37	1886	3.203	2.004	7.245	0.3489
2	614	43	2229	3.418	2.100	9.154	0.3619
3	643	35	1100	2.667	0.610	4.950	0.2035
4	632	38	1300	2.873	0.895	5.798	0.2111
5	652	43	1886	3.206	1.680	9.020	0.3489
6	640	47	2229	3.490	1.884	9.510	0.3619
7	536	39	1100	2.789	0.625	4.709	0.2035
8	621	42	1300	2.907	0.817	5.631	0.2111
9	546	27	1303	2.759	0.494	5.204	0.2537
10	529	41	1728	3.377	0.953	6.150	0.2700
11	666	45	2719	3.704	2.854	10.027	0.4694
12	637	37	1051	2.375	0.792	6.992	0.1816
13	658	41	1516	3.496	1.135	6.250	0.2619
14	629	45	1516	2.318	1.640	7.003	0.2619
15	692	41	1516	3.428	1.145	6.345	0.2619
16	658	43	1516	2.974	1.096	6.576	0.2619
17	630	43	1516	3.066	1.109	6.749	0.2619
18	638	44	1516	2.982	1.145	6.622	0.2619
19	672	43	1516	3.079	1.094	6.664	0.2619
20	671	45	1516	3.021	1.145	6.556	0.2619

Table 5.16: Actual residual stress in HAZ, 10 mm and 20 mm from weld centre line.

Std	Residual stress [MPa]																			
	HAZ							10 mm from weld centreline							20 mm from weld centreline						
	σ_{11}	σ_{12}	σ_{13}	σ_{14}	σ_{15}	σ_{16}	σ_{17}	σ_{21}	σ_{22}	σ_{23}	σ_{24}	σ_{25}	σ_{26}	σ_{27}	σ_{31}	σ_{32}	σ_{33}	σ_{34}	σ_{35}	σ_{36}	σ_{37}
1	190	143	126	103	98	95	95	95	60	49	39	35	32	32	30	24	19	17	16	15	14
2	215	157	136	101	101	97	98	108	76	63	53	45	42	41	34	27	21	20	18	18	19
3	146	108	103	82	83	79	78	61	35	28	24	23	21	20	22	19	15	13	13	13	13
4	174	131	120	90	87	87	87	83	50	43	33	32	30	29	24	21	18	16	16	16	16
5	262	182	152	114	104	100	98	95	64	53	47	36	34	34	38	28	22	19	18	16	15
6	282	198	151	114	109	105	101	110	76	68	56	48	46	46	39	29	24	22	21	19	20
7	146	123	112	95	87	85	80	63	41	34	26	25	25	25	26	19	17	16	16	15	15
8	172	138	124	99	95	92	90	83	56	50	39	34	33	33	25	22	21	19	18	17	16
9	180	143	120	114	99	90	89	59	34	27	23	20	20	21	26	22	15	15	15	14	13
10	228	157	133	101	96	92	95	79	55	47	41	35	34	34	36	26	22	21	19	18	19
11	309	209	156	110	109	106	104	120	81	69	59	49	46	46	41	29	24	23	21	20	21
12	142	127	120	84	84	78	78	59	39	32	28	27	27	27	22	17	15	14	14	14	16
13	165	121	117	94	95	93	91	69	48	42	32	27	26	25	26	23	21	16	16	15	15
14	181	141	134	101	101	101	95	79	65	51	45	34	33	31	30	26	26	23	22	20	20
15	195	141	122	97	92	87	85	47	46	39	39	34	31	31	25	21	16	15	14	14	15
16	172	134	122	95	89	87	85	52	46	39	31	31	29	29	30	25	19	15	14	14	15
17	172	138	123	94	93	91	88	47	40	37	30	30	29	29	26	23	16	16	16	15	15
18	172	135	121	96	92	84	85	61	50	40	29	26	25	25	25	23	18	15	14	14	14
19	175	141	129	95	94	90	86	49	42	29	23	22	21	20	25	21	17	15	15	15	15
20	172	131	122	94	91	90	87	59	50	42	31	31	29	30	24	21	17	16	15	15	14

5.2.1 Development of weld-bead parameters models

The same steps and adequacy tests, which were outlined earlier, were followed and performed at this point. Tables 5.17 - 5.20 presenting the resulting ANOVA tables and the other adequacy measures for nominal heat input, and the weld-bead parameters models considered here. For the heat input model, the Analysis of Variance indicates that the main effect of the laser power (P), welding speed (S), the second order effect of welding speed (S^2) and the two levels of interaction of laser welding and welding speed (PS) are the most significant model terms associated with heat input. For the front width model, the ANOVA analysis indicates that there is a linear relationship between the main effects of the three parameters. Also, in case of back width of the fusion zone the ANOVA indicates that the main effects along with the quadratic effects of the three factors are significant model terms. For the fusion zone area, the ANOVA shows that the main effect and the quadratic effect of the laser power and welding speed are significant model terms, however, welding speed is the most effective factor. The final mathematical models for the laser four responses in terms of coded factors as determined by the Design-Expert are shown in Eqs. 5.14 - 5.17. While, the final mathematical models in terms of actual factors are presented in Eqs. 5.18 – 5.21.

Table 5.17: ANOVA table for nominal heat input reduced quadratic model.

Source	Sum of Squares	DF	Mean squares	F Value	Prob > F	
Model	3332446	4	0.03178	201334	< 0.0001	Significant
P	237591.6	1	0.00025	1587	< 0.0001	
S	2846217	1	0.11692	740846	< 0.0001	
PS	10214.29	1	2.37E-05	150	< 0.0001	
S^2	238423.2	1	0.0099	62754	< 0.0001	
Residual	16750.94	15	1.58E-07			
Cor Total	3349197	19				
$R^2 = 0.9950$				Adj. $R^2 = 0.9937$		
Pred. $R^2 = 0.9802$				Adeq. Precision = 92.98		

Table 5.18: ANOVA table for front-width reduced quadratic model.

Source	Sum of Squares	DF	Mean squares	F Value	Prob > F	
Model	1.8430	3	0.614	12.859	0.0002	Significant
P	0.2541	1	0.254	5.319	0.0348	
S	1.3648	1	1.365	28.569	< 0.0001	
F	0.2240	1	0.224	4.689	0.0458	
Residual	0.7644	16	0.048			
Lack of Fit	0.6199	11	0.056	1.951	0.2383	Not significant
Pure Error	0.1444	5	0.029			
Cor Total	2.6073	19				
$R^2 = 0.7068$				Adj. $R^2 = 0.6519$		
Pred. $R^2 = 0.5040$				Adeq. Precision = 11.880		

Table 5.19: ANOVA table for back-width reduced quadratic model.

Source	Sum of Squares	DF	Mean squares	F Value	Prob > F	
Model	6.4784	6	1.080	64.847	< 0.0001	Significant
P	0.1751	1	0.175	10.518	0.0064	
S	4.9072	1	4.907	294.722	< 0.0001	
F	0.0045	1	0.004	0.269	0.6126	
P^2	0.2831	1	0.283	17.000	0.0012	
S^2	0.8905	1	0.891	53.485	< 0.0001	
F^2	0.1290	1	0.129	7.748	0.0155	
Residual	0.2165	13	0.017			
Lack of Fit	0.2132	8	0.027	41.085	0.0004	Significant
Pure Error	0.0032	5	0.001			
Cor Total	6.6948	19				
$R^2 = 0.9677$				Adj. $R^2 = 0.9527$		
Pred. $R^2 = 0.8665$				Adeq. Precision = 30.104		

Table 5.20: ANOVA table for fusion zone area reduced quadratic model.

Source	Sum of Squares	DF	Mean squares	F Value	Prob > F	
Model	37.656	4	9.414	30.811	< 0.0001	significant
P	2.430	1	2.430	7.953	0.0129	
S	26.278	1	26.278	86.005	< 0.0001	
P^2	1.438	1	1.438	4.708	0.0465	
S^2	6.868	1	6.868	22.479	0.0003	
Residual	4.583	15	0.306			
Lack of Fit	4.490	10	0.449	24.112	0.0013	significant
Pure Error	0.093	5	0.019			
Cor Total	42.239	19				
$R^2 = 0.8915$				Adj. $R^2 = 0.8626$		
Pred. $R^2 = 0.6823$				Adeq. Precision = 21.255		

$$\text{Nominal Heat Input} = 1510.78 + 131.90\ P - 456.52\ S - 35.73\ PS + 127.47\ S^2 \quad (5.14)$$

$$\text{Front Width} = 3.06 + 0.14\ P - 0.32\ S - 0.13\ F \quad (5.15)$$

$$\text{Back width} = 1.12 + 0.11\,P - 0.60\,S + 0.018\,F - 0.14\,P^2 + 0.25\,S^2 + 0.095\,F^2 \quad (5.16)$$

$$\text{Weld Pool Area} = 6.60 + 0.42\,P - 1.39\,S - 0.31\,P^2 + 0.69\,S^2 \quad (5.17)$$

$$\text{Nominal Heat Input} = 1873.99 + 2676.81\,P - 79.72\,S - 28.59\,PS + 0.82\,S^2 \quad (5.18)$$

$$\text{Front Width} = 2.408 + 1.364\,P - 0.0253\,S - 0.427\,F \quad (5.19)$$

$$\text{Back width} = -14.257 + 34.768\,P - 0.1991\,S + 1.112\,F - 14.015\,P^2 + 1.59094\,E\text{-}003\,S^2 + 1.05125\,F^2 \quad (5.20)$$

$$\text{Weld Pool Area} = -28.538 + 79.668\,P - 0.529\,S - 31.437\,P^2 + 4.39647\,E\text{-}003\,S^2 \quad (5.21)$$

5.2.1.1 Validation of the weld bead models

The validity of the models developed can be drawn also from Fig. 5.17 a-d, which present the relationship between the measured and predicted values of the nominal heat input, W, BW and A. These scatter diagrams indicate that the above mathematical models show a good agreement between the measured and estimated values of the above mentioned responses. In order to verify the model developed, three confirmation welding experiments were carried out using new test conditions selected from the optimal results shown in chapter 6, Tables 6.5 and 6.6. These optimal conditions are within the experimental range of this experiment. A comparison between the experimentally recorded and the predicted responses calculated by the models developed were made for all weld-bead responses. The results of this comparison are presented in Table 5.21. It is clear that the models can effectively explain the responses within the factors domain as the maximum error in prediction is -8.245 %, which indicates good harmony.

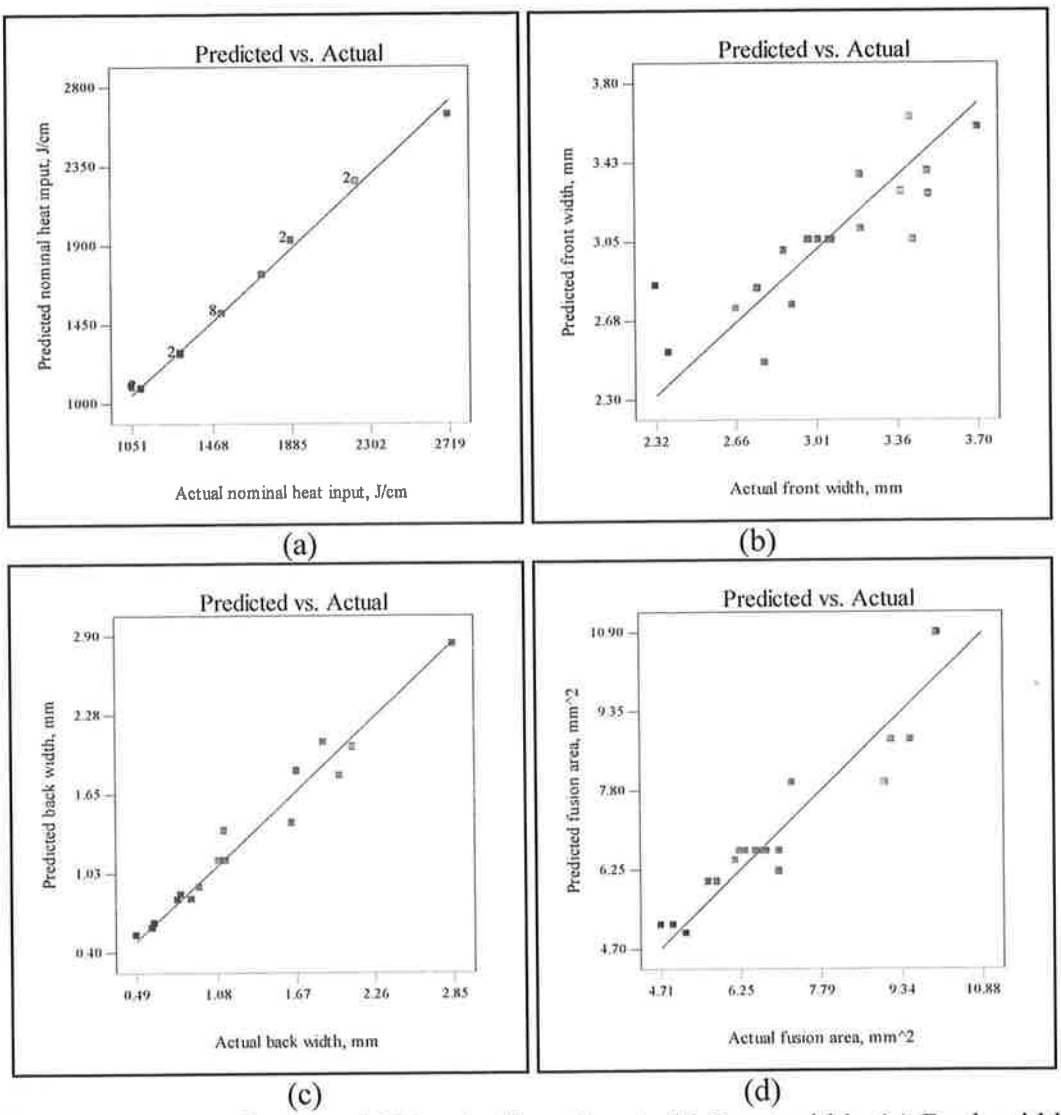

Fig. 5.17: Scatter diagram, (a) Nominal heat input, (b) Front width, (c) Back width and (d) Area of fusion zone.

Table 5.21: Confirmation experiments for weld-bead parameters for 3 mm AISI304.

Exp. No.	P	S	F		W	BW	A
1	1.2	35	-0.2	Actual	3.125	2.027	8.955
				Predicted	3.244	2.083	8.677
				Error %	-3.69	-2.70	3.20
2	1.22	60	-0.8	Actual	2.696	0.871	5.496
				Predicted	2.896	0.865	5.975
				Error %	-6.91	0.75	-8.01
3	1.21	38.85	-0.2	Actual	3.240	1.632	7.681
				Predicted	3.161	1.779	7.931
				Error %	2.51	-8.245	-3.15

5.2.1.2 Effect of process factors on weld-bead parameters of AISI304

The adequate mathematical models developed can be now employed to investigate the main and interaction effect of the process parameters on the different responses.

a) Heat input

It is evident from Fig. 5.18 that there is a proportional relationship between the heat input and the laser power, while the relationship is inversely proportional between the welding speed and the heat input. As stated earlier, the reason for predicting the heat input is for optimization purpose.

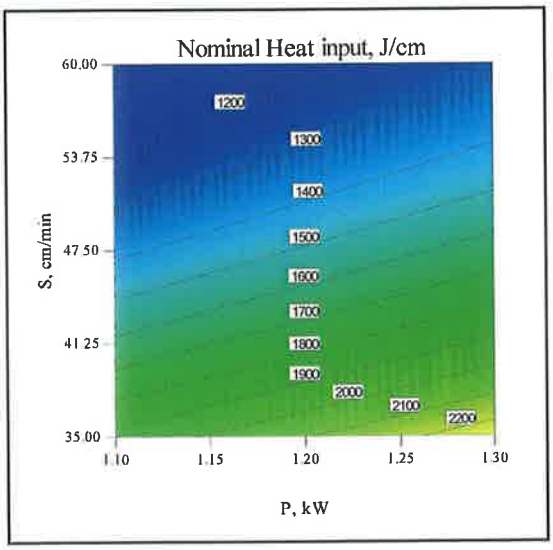

Fig. 5.18: Contours graph shows the effect of P and S on the nominal heat input.

b) Front width

The results indicate that the three parameters have a linear effect on the front width as shown in the perturbation plot in Fig. 5.19. It is clear from Fig. 5.19 that when both the welding speed and the focal position increase the front width decreases. This is due to the fact that as the welding speed increases the heat input decreases, resulting in less molten material which tends to increase the front width. In the case of focal point position the front width increases as the defocused beam is used, due to the fact that applying a defocused beam will result in a wider laser beam. This means that a wider surface area will be exposed to the laser beam which would increase the front width. As the laser power increases the front width increases because of the increase in the heat input. These results were in good agreement with those of Manonmani [74].

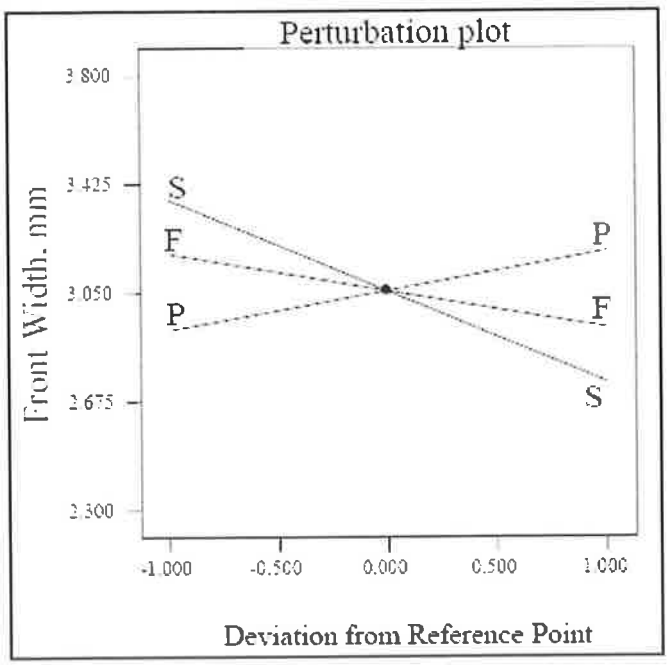

Fig. 5.19: Perturbation plot shows the effect of all parameters on front width.

c) Back width

At low welding speed the diffusion of the heat into the base metal is easy, as stated in [74], hence more heat will make its way into the bulk metal forcing the back width to expand. Also, the results demonstrate that the laser power and the focal position slightly affect the back width, however, both have a positive effect on the

back width. The effect of the process parameters on the back width is presented graphically in Fig. 5.20. In contrast between the effect of focal position on the front and back widths, a key point that can be raised is that the focal position effect is reversed herein, since the back width increases as the focal position increases. This is due to the fact that as the laser beam becomes focused (i.e. F=0) most of the laser power will penetrate and result in less front width at the same time as expanding the back width.

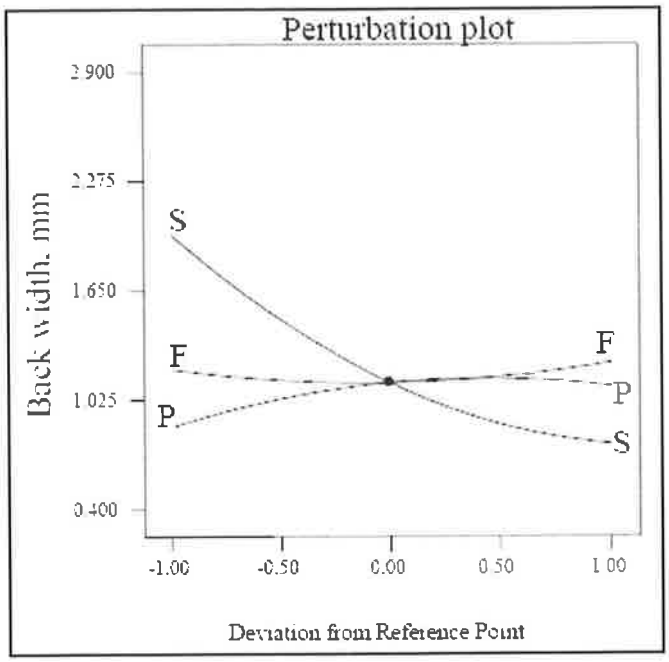

Fig. 5.20: Perturbation plot shows the effect of all parameters on back width.

d) Area of fusion zone

It is evident from the result that both the laser power and welding speed significantly influence the weld pool area in the same manner as they affect both front and back widths, because the weld pool area is a function of both width beads. Although the focal point position is affecting both front and back widths, it has no significant effect on the weld pool area as the results indicate. This is due to the fact that the focal position affects both beads but in totally different ways, as mentioned above. In other words, any reduction in the front width which would be achieved by applying a defocused beam will be faced by an increase in the back width or vice versa. Hence, the overall influence of the focal point position on the weld bead area

will be null. The relationship between the laser power and the welding speed is shown in Fig. 5.21.

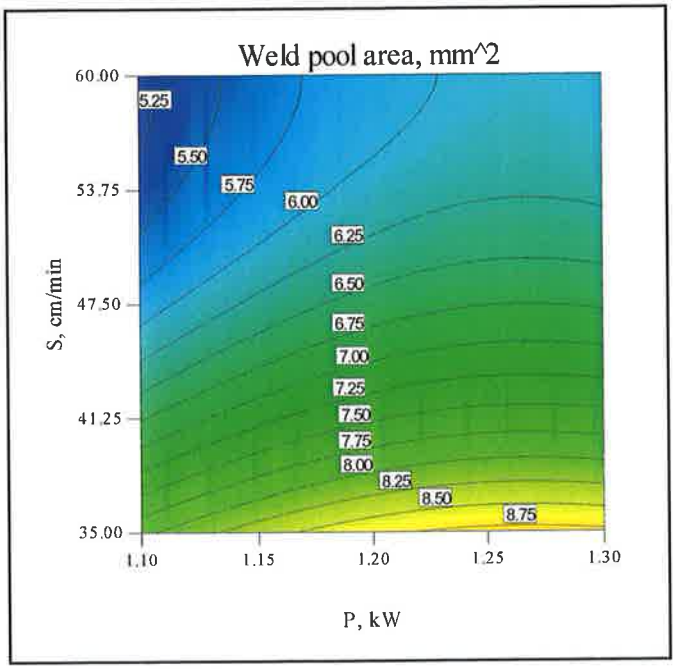

Fig. 5.21: Contours graph shows the effect of S and P on the weld pool area.

5.2.2 Development of residual stress distribution models

For this experiment, twenty-one mathematical models were developed to relate the residual stress distribution to the process input parameters namely, laser power, welding speed and focal point position. The maximum residual stress 'responses' will be abbreviated as σiz. Where i = 1, 2 and 3 refers to the hole number (i.e. i =1 means the first hole near HAZ, i = 2 the second hole 10 mm from the weld centre line and i = 3 the third hole 20 mm from the weld centre line). z = 1, 2 … 7 refers to the increment number in each hole as can be seen in Fig. 5.22. Based on the above description the general second order polynomial shown in Eq. 3.21 will be presented as in Eq. 5.22. For example σ_{11} refers to the maximum residual stress in the HAZ at a depth of 0.127 mm. Another example σ_{27} refers to the maximum residual stress at 10 mm from the weld centre line and at a depth of 2.052 mm from the surface and σ_{35} refers to the maximum residual stress in the third hole, 20 mm from the weld centre line and at a depth of 1.016 mm from the surface and so on. Fig. 5.23 is a photograph shows the locations of the three holes, the strain gauge type and installation.

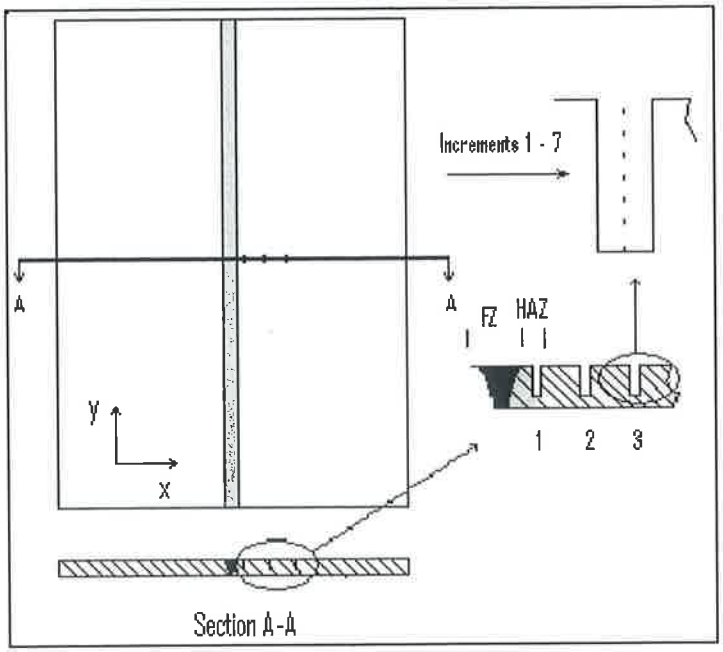

Fig. 5.22: Location of three holes and the increments in each hole, not to scale.

$$\sigma_{iz} = b_0 + b_1 P + b_2 S + b_3 F + b_{11} P^2 + b_{22} S^2 + b_{33} F^2 + b_{12} PS + b_{13} PF + b_{23} SF \quad (5.22)$$

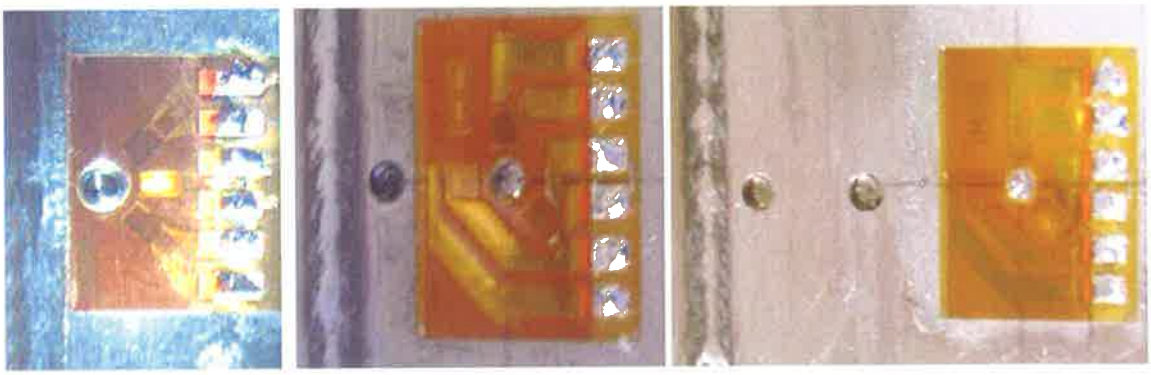

Fig. 5.23: Strain gauge rosette type and installation, photos not to scale.

As mentioned earlier the lack-of-fit test, the sequential F-test for the significance of both the regression models and the individual model terms were performed using Design-Expert statistical software. Selecting the stepwise regression method allows elimination of the insignificant model terms automatically. The Analyses of Variance for the reduced quadratic models for all the responses were abstracted and presented in Table 5.22 (which contains the most important

information from the 21 ANOVA tables). For all models the 'Prob. > F' value does not exceed 0.05, which indicates that the models are statistically significant. Also the terms in these models have a significant effect on the responses being investigated. For the lack of fit, the Prob. > F values were greater than 0.05, which indicate an insignificant lack of fit, except for σ_{14}, where lack of fit is significant at both levels of significance 0.05 and 0.01. It is noted that for σ_{36} and σ_{37} the lack of fit is insignificant at $\alpha = 0.01$.

Table 5.23 shows the other adequacy measure R^2 (i.e. a measure of the amount of variation around the mean explained by the model). The results show that all values of R^2 are close to 1. These values are in reasonable agreement and indicate adequate models. Table 5.23 also shows the Adjusted R^2 and the Predicted R^2, both should be within 0.20 of each other [156]. It is observed that more than 90% of the results were within 0.2 differences. In addition the adequate precision ratios are greater than 4 in all cases, as presented in Table 5.23, which indicates adequate model discrimination. Table 5.24 presents the significant coefficients for all responses as calculated by the Design-Expert package in terms of actual process variables.

Table 5.22: ANOVA results for the twenty one reduced models.

Response No.	Model			Lack of fit			Pure error	
	S. S.	D. F.	Prob.>F	S. S.	D. F.	Prob.>F	S. S.	D. F.
σ_{11}	37406.84	6	< 0.0001	1028.8	8	0.3370	425.33	5
σ_{12}	11720.12	7	< 0.0001	280.35	7	0.1692	81.33	5
σ_{13}	3289.62	7	< 0.0001	64.10	7	0.4880	42.83	5
σ_{14}	1372.42	4	< 0.0001	173.3	10	0.0059*	6.83	5
σ_{15}	935.86	5	< 0.0001	88.26	9	0.1006	14.83	5
σ_{16}	1006.03	4	< 0.0001	64.09	10	0.5762	34.83	5
σ_{17}	999.01	7	< 0.0001	14.74	7	0.3941	8.00	5
σ_{21}	8873.00	6	< 0.0001	327.30	8	0.4839	187.50	5
σ_{22}	3468.81	5	< 0.0001	80.06	9	0.8053	83.33	5
σ_{23}	2739.79	5	< 0.0001	56.68	9	0.9419	103.33	5
σ_{24}	2111.09	5	< 0.0001	32.21	9	0.9947	131.50	5
σ_{25}	1087.32	4	< 0.0001	45.88	10	0.9705	92.00	5
σ_{26}	941.50	4	< 0.0001	33.72	10	0.9702	67.33	5
σ_{27}	936.60	4	< 0.0001	22.87	10	0.9963	85.33	5
σ_{31}	583.63	5	< 0.0001	41.74	9	0.5230	22.83	5
σ_{32}	191.74	3	< 0.0001	15.13	11	0.8327	13.33	5
σ_{33}	191.83	5	< 0.0001	9.88	9	0.6355	6.83	5
σ_{34}	166.97	6	< 0.0001	9.89	8	0.0539	1.33	5
σ_{35}	118.51	6	< 0.0001	7.10	8	0.3918	3.33	5
σ_{36}	73.16	5	< 0.0001	9.89	9	0.0320**	1.50	5
σ_{37}	98.16	6	< 0.0001	12.50	8	0.0337**	1.33	5

* Significant lack of fit.
** Insignificant lack of fit at $\alpha = 0.01$

Table 5.23: Adequacy measures for each model developed.

Response No.	R^2	Adj.R^2	Pred.R^2	Adeq. Precision
σ_{11}	0.963	0.945	0.894	25.009
σ_{12}	0.970	0.953	0.878	26.742
σ_{13}	0.969	0.950	0.895	27.877
σ_{14}	0.884	0.853	0.667	17.693
σ_{15}	0.901	0.865	0.708	18.037
σ_{16}	0.910	0.887	0.855	21.155
σ_{17}	0.978	0.965	0.917	28.493
σ_{21}	0.945	0.920	0.816	18.555
σ_{22}	0.955	0.939	0.891	25.858
σ_{23}	0.945	0.925	0.885	23.509
σ_{24}	0.928	0.902	0.883	20.712
σ_{25}	0.887	0.857	0.818	19.749
σ_{26}	0.903	0.877	0.848	21.457
σ_{27}	0.896	0.869	0.850	20.847
σ_{31}	0.900	0.865	0.769	17.056
σ_{32}	0.871	0.847	0.825	19.482
σ_{33}	0.920	0.891	0.821	18.070
σ_{34}	0.937	0.909	0.738	19.445
σ_{35}	0.919	0.882	0.716	16.187
σ_{36}	0.865	0.817	0.588	14.634
σ_{37}	0.877	0.820	0.559	15.215

Table 5.24: Model terms coefficients in terms of actual variable.

No.	b_0	b_1	b_2	b_3	b_{11}	b_{22}	b_{33}	b_{12}	b_{13}	b_{23}
σ_{11}	1872.53	-2064.14	-16.00	263.26	914.89	0.11	N.S.	N.S.	N.S.	-4.7
σ_{12}	939.93	-914.67	-9.19	95.75	409.04	0.07	-29.19	N.S.	N.S.	-1.93
σ_{13}	371.05	-84.5	-6.67	144.5	N.S.	0.03	N.S.	2.00	-66.67	-0.93
σ_{14}	721.54	-971.38	-0.64	14.10	401.13	N.S.	N.S.	N.S.	N.S.	N.S.
σ_{15}	322.6	-331.71	-0.60	26.64	142.78	N.S.	17.83	N.S.	N.S.	N.S.
σ_{16}	107.54	18.57	-0.59	39.27	N.S.	N.S.	30.13	N.S.	N.S.	N.S.
σ_{17}	446.72	-469.76	-3.03	28.33	180.71	0.009	24.01	1.3	N.S.	N.S.
σ_{21}	1355.3	-1741.18	-10.30	108.85	757.11	0.095	103.77	N.S.	N.S.	N.S.
σ_{22}	109.68	68.33	-4.43	60.44	N.S.	0.036	49.56	N.S.	N.S.	N.S.
σ_{23}	84.98	68.56	-3.99	51.22	N.S.	0.033	42.16	N.S.	N.S.	N.S.
σ_{24}	81.91	55.12	-3.63	43.29	N.S.	0.031	33.31	N.S.	N.S.	N.S.
σ_{25}	51.39	47.76	-2.71	4.83	N.S.	0.023	N.S.	N.S.	N.S.	N.S.
σ_{26}	47.84	45.80	-2.56	6.05	N.S.	0.022	N.S.	N.S.	N.S.	N.S.
σ_{27}	50.77	43.83	-2.58	6.37	N.S.	0.022	N.S.	N.S.	N.S.	N.S.
σ_{31}	289.93	-372.45	-1.54	6.04	162.15	0.012	N.S.	N.S.	N.S.	N.S.
σ_{32}	24.08	11.52	-0.276	2.940	N.S.	N.S.	N.S.	N.S.	N.S.	N.S.
σ_{33}	21.95	16.67	-0.525	26.82	N.S.	0.004	22.08	N.S.	N.S.	N.S.
σ_{34}	124.68	-153.43	-0.708	19.06	70.67	0.006	13.74	N.S.	N.S.	N.S.
σ_{35}	111.14	-133.81	-0.605	19.52	60.86	0.005	14.61	N.S.	N.S.	N.S.
σ_{36}	17.65	12.98	-0.507	12.68	N.S.	0.004	9.41	N.S.	N.S.	N.S.
σ_{37}	-17.79	46.14	0.001	10.48	N.S.	0.007	7.45	-0.6	N.S.	N.S.

N.S. Not Significant

5.2.2.1 How to use the models developed

The developed models can be used to predict the maximum residual stress by following the flowchart shown in Fig. 5.24. The following are two examples to describe how to predict the residual stress:

Example: 1

1. Prediction of σ_{11} which means prediction of maximum residual stress in the HAZ at a depth of 0.127 mm.
2. The model for example 1 can be expressed as follows:
   $\sigma_{11} = 1872.53 - 2064.14P - 16S + 263.26F + 914.89P^2 + 0.11S^2 - 4.7SF$.
3. Considering the following process input parameters:
   P = 1.25 kW, S = 40 cm/min and F = -0.2 mm.
4. By substituting the process input parameters values into the built model the predicted residual stress rounded to the nearest MPa is σ_{11} = 238 MPa.

Example 2:

1. Prediction of σ_{35}, which means prediction of maximum residual stress at 20 mm from the weld centre line and at a depth of 1.016 mm from the surface.
2. The model for example 2 is as follows:
   $\sigma_{35} = 111.14 - 133.81P - 0.605S + 19.52F + 60.86P^2 + 0.005S^2 + 14.61F^2$.
3. Considering the following process input parameters:
   P = 1.1 kW, S = 35 cm/min and F = - 0.8 mm.
4. By substituting the process input parameters values into the built model the predicted residual stress rounded to the nearest MPa is σ_{35} = 16 MPa.

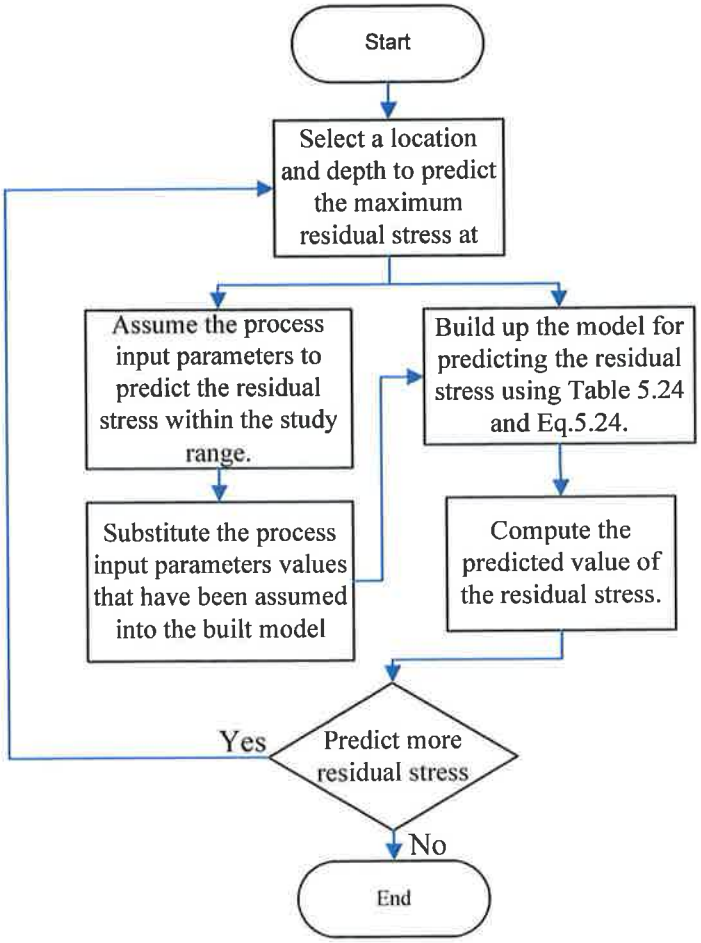

Fig. 5.24: Flowchart shows the steps of building and using the developed models.

5.2.2.2 Validation of the models

In order to verify the adequacy of the models developed, the predicted value and actual experimental measured value after rounding to the nearest MPa are in reasonable agreement as presented earlier in Tables 5.25, 5.26 and 5.27. Two confirmation tests were performed using new test conditions obtained from the optimal solutions shown in chapter 6, Table 6.5 and 6.6. These optimal conditions are: for the first test P= 1.2 kW, S=35cm/min and F= -0.2 mm and for the second test P=1.22 kW, S = 60 cm/min and F= -0.8 mm. A comparison between the experimentally recorded and the predicted responses calculated by the models developed were made for all residual stress. These results are presented in Tables 5.28 and 5.29. It is clear that the models successfully explained the responses within

the variables field, as the maximum average error in prediction is 7.347 %, which indicates good agreement. Based on the above results the models developed are adequate and can be used to predict the responses within the factors field.

Table 5.25: Actual and predicted residual stress on HAZ.

Sample No.	Residual stress [MPa]													
	σ_{11}		σ_{12}		σ_{13}		σ_{14}		σ_{15}		σ_{16}		σ_{17}	
	Act.	Pred.	Act.	Pred.	Act.	Pred.	Act.	Pred.	Act.	Pred.	Act.	Pred.	Act.	Pred.
1	190	201	143	148	126	127	103	105	98	100	95	95	95	97
2	215	228	157	161	136	135	101	103	101	102	97	99	98	98
3	146	150	108	116	103	105	82	89	83	85	79	80	78	79
4	174	176	131	129	120	123	90	87	87	87	87	84	87	87
5	262	261	182	182	152	150	114	113	104	105	100	101	98	99
6	282	287	198	196	151	150	114	111	109	107	105	104	101	101
7	146	139	123	121	112	114	95	97	87	90	85	86	80	81
8	172	165	138	135	124	124	99	95	95	92	92	90	90	90
9	180	179	143	137	120	117	114	109	99	95	90	86	89	87
10	228	223	157	160	133	131	101	106	96	99	92	93	95	95
11	309	295	209	205	156	158	110	109	109	105	106	102	104	103
12	142	149	127	127	120	117	84	82	84	80	78	77	78	78
13	165	155	121	113	117	114	94	89	95	93	93	93	91	90
14	181	195	141	146	134	134	101	103	101	102	101	102	95	94
15	195	175	141	137	122	124	97	96	92	93	87	90	85	86
16	172	175	134	137	122	124	95	96	89	93	87	90	85	86
17	172	175	138	137	123	124	94	96	93	93	91	90	88	86
18	172	175	135	137	121	124	96	96	92	93	84	90	85	86
19	175	175	141	137	129	124	95	96	94	93	90	90	86	86
20	172	175	131	137	122	124	94	96	91	93	90	90	87	86

Table 5.26: Actual and predicted residual stress at 10 mm from weld-centre line.

Sample No.	Residual stress [MPa]													
	σ_{21}		σ_{22}		σ_{23}		σ_{24}		σ_{25}		σ_{26}		σ_{27}	
	Act.	Pred.	Act.	Pred.	Act.	Pred.	Act.	Pred.	Act.	Pred.	Act.	Pred.	Act.	Pred.
1	95	91	60	58	49	48	39	40	35	33	32	31	32	31
2	108	106	76	72	63	61	53	51	45	43	42	40	41	40
3	61	59	35	34	28	27	24	21	23	21	21	20	20	20
4	83	74	50	47	43	41	33	32	32	30	30	29	29	28
5	95	94	64	64	53	53	47	46	36	36	34	35	34	35
6	110	109	76	78	68	67	56	57	48	46	46	44	46	44
7	63	62	41	40	34	33	26	27	25	24	25	23	25	23
8	83	77	56	54	50	46	39	38	34	33	33	33	33	32
9	59	61	34	34	27	26	23	22	20	22	20	21	21	21
10	79	86	55	57	47	49	41	40	35	38	34	36	34	35
11	120	121	81	82	69	70	59	60	49	51	46	48	46	48
12	59	67	39	42	32	35	28	29	27	29	27	29	27	28
13	69	76	48	53	42	44	32	35	27	27	26	25	25	25
14	79	81	65	64	51	53	45	45	34	32	33	31	31	31
15	47	52	46	46	39	38	39	31	34	30	31	28	31	28
16	52	52	46	46	39	38	31	31	31	30	29	28	29	28
17	47	52	40	46	37	38	30	31	30	30	29	28	29	28
18	61	52	50	46	40	38	29	31	26	30	25	28	25	28
19	49	52	42	46	29	38	23	31	22	30	21	28	20	28
20	59	52	50	46	42	38	31	31	31	30	29	28	30	28

Table 5.27: Actual and predicted residual stress at 20 mm from weld-centre line.

Sample No.	Residual stress [MPa]													
	σ_{21}		σ_{22}		σ_{23}		σ_{24}		σ_{25}		σ_{26}		σ_{27}	
	Act.	Pred.	Act.	Pred.	Act.	Pred.	Act.	Pred.	Act.	Pred.	Act.	Pred.	Act.	Pred.
1	30	32	24	25	19	19	17	17	16	16	15	15	14	14
2	34	35	27	27	21	22	20	20	18	19	18	18	19	19
3	22	21	19	18	15	15	13	13	13	13	13	13	13	13
4	24	24	21	20	18	18	16	16	16	16	16	15	16	15
5	38	35	28	26	22	22	19	20	18	19	16	17	15	16
6	39	39	29	29	24	25	22	24	21	22	19	20	20	21
7	26	24	19	20	17	18	16	16	16	16	15	15	15	15
8	25	28	22	22	21	21	19	19	18	19	17	17	16	17
9	26	28	22	21	15	15	15	15	15	14	14	13	13	12
10	36	34	26	25	22	20	21	20	19	18	18	17	19	18
11	41	41	29	29	24	23	23	21	21	20	20	19	21	20
12	22	22	17	17	15	15	14	14	14	14	14	15	16	16
13	26	23	23	22	21	21	16	16	16	16	15	16	15	15
14	30	29	26	25	26	25	23	22	22	21	20	19	20	18
15	25	26	21	23	16	17	15	15	14	15	14	15	15	15
16	30	26	25	23	19	17	15	15	14	15	14	15	15	15
17	26	26	23	23	16	17	16	15	16	15	15	15	15	15
18	25	26	23	23	18	17	15	15	14	15	14	15	14	15
19	25	26	21	23	17	17	15	15	15	15	15	15	15	15
20	24	26	21	23	17	17	16	15	15	15	15	15	14	15

Table 5.28: Results of first confirmation test for residual stress distribution.

Principal stress component	Predicted	Actual	Error %	Absolute Error %
σ_{11}	264.53	258.96	2.151	2.151
σ_{12}	185.0493	179.71	2.971	2.971
σ_{13}	150.366	134.8	11.547	11.547
σ_{14}	108.1758	99.37	8.862	8.862
σ_{15}	104.5987	93.52	11.846	11.846
σ_{16}	102.4548	89.3	14.731	14.731
σ_{17}	98.33588	88.57	11.026	11.026
σ_{21}	94.0686	100.31	-6.222	6.222
σ_{22}	71.24169	67.72	5.200	5.200
σ_{23}	59.94241	57.12	4.941	4.941
σ_{24}	51.01742	44.19	15.450	15.450
σ_{25}	41.16821	40.49	1.675	1.675
σ_{26}	39.19869	39.19	0.022	0.022
σ_{27}	39.12739	38.02	2.913	2.913
σ_{31}	35.53533	33.44	6.266	6.266
σ_{32}	27.63679	27.74	-0.372	0.372
σ_{33}	23.5901	22.33	5.643	5.643
σ_{34}	21.21767	19.58	8.364	8.364
σ_{35}	19.86617	21.92	-9.370	9.370
σ_{36}	18.56415	21.1	-12.018	12.018
σ_{37}	18.64774	21.36	-12.698	12.698
			Average = 7.347	

Table 5.29: Results of second confirmation test for residual stress distribution.

Principal stress component	Predicted	Actual	Error %	Absolute Error %
σ_{11}	155.2579	159.32	-2.550	2.550
σ_{12}	119.3407	117.55	1.523	1.523
σ_{13}	114.7693	108.65	5.632	5.632
σ_{14}	83.59935	79.92	4.604	4.604
σ_{15}	84.49299	79.44	6.361	6.361
σ_{16}	82.35112	76.22	8.044	8.044
σ_{17}	81.42624	75.06	8.482	8.482
σ_{21}	59.54988	61.07	-2.489	2.489
σ_{22}	41.28458	40.93	0.866	0.866
σ_{23}	34.65391	33.99	1.953	1.953
σ_{24}	27.25862	27.57	-1.129	1.129
σ_{25}	26.00943	26.81	-2.986	2.986
σ_{26}	24.75915	26.28	-5.787	5.787
σ_{27}	24.32872	26.31	-7.531	7.531
σ_{31}	20.9742	21.86	-4.052	4.052
σ_{32}	19.07837	20.06	-4.893	4.893
σ_{33}	16.50114	17.78	-7.193	7.193
σ_{34}	13.93109	15.58	-10.584	10.584
σ_{35}	13.864	15.22	-8.909	8.909
σ_{36}	14.22737	14.06	1.190	1.190
σ_{37}	14.52886	14.8	-1.832	1.832
			Average = 4.695	

5.2.2.3 Effect of process parameters on the residual stress distribution

It was demonstrated that all the three parameters have a significant effect on the magnitude and distribution of the residual stress. However, the results show that the most significant factor is the welding speed. The relationships between the residual stresses and the welding speed are almost inversely proportional for all responses. The maximum residual stress increases as the welding speed decreases. This is due to the increase in heat input when the welding speed is decreased, which tends to raise the temperature of the fusion zone thereby resulting in more distortion. It is also evident that high laser power leads to an increase in heat input, which finally results in increasing the residual stress magnitude. As the laser beam is focused (in this experiment F = -0.2 mm) the laser power will be distributed onto a smaller area and

consequently an increase in the power density would take place which leads to an increase in temperature around the fusion zone, resulting in a higher residual stress magnitude. One of the RSM advantages over one factor at a time experimental procedure is its ability to specify the interaction effect between any two factors. Fig. 5.25 shows a contours graph of the interaction effect between the welding speed and the focal point position on σ_{11} at a constant laser power of 1.3 kW. It is clear from this figure that the maximum residual stress of about 287 MPa occurs in the HAZ at a depth of 0.127 mm when using F = - 0.2 mm and welding speed of 35 cm/min. Fig. 5.26 shows a contours graph of the interaction effect between the welding speed and the focal point position on σ_{12} at a constant laser power of 1.3 kW. It is evident from this figure that the relationship is curvilinear, also the maximum residual stress of 195 MPa occurs at the lowest welding speed with F = -0.2 mm. The cube plot displays the relationship between three significant factors, especially when there are interactions between them as in the case of σ_{13}. This type of figure presents the predicted values of the responses from the model for the combinations of the -1 and +1 levels of the three factors. Fig. 5.27 presents the effect of the three factors on the residual stress (i.e. σ_{13}) by using a cube plot to represent this effect. It is noted that the process input parameters can be selected where the residual stress would be minimum or maximum.

The perturbation plot would help to compare the effect of all the factors at a particular point in the design space. Fig. 5.28 shows a comparison between the effects of laser power, welding speed and focal point position on the maximum principal stress σ_{17}. It is evident from this figure that in the case of welding speed steep curvatures indicate that the responses are too sensitive to this factor. While the steep slopes in the case of laser power and focal point position indicate that the responses are relatively slightly sensitive to this factor. From Fig. 5.28 it is evident that by increasing the welding speed from 35 to 60 cm/min the residual stress (i.e. σ_{17}) would be decreased by 15.79%. Decreasing the laser power from 1.37 to 1.1 kW would result in decreasing σ_{17} by 5.56%. Finally, by using a defocused laser beam of -0.8 mm in place of -0.2 mm this would reduce σ_{17} by 3.33%.

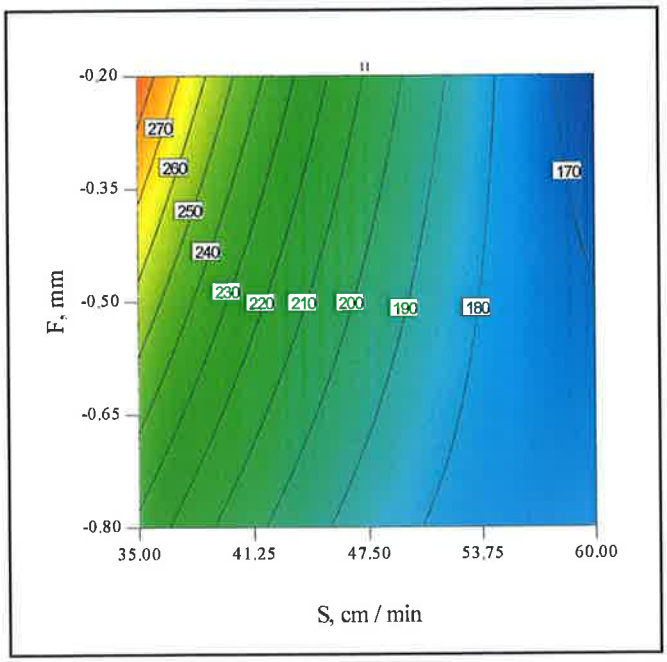

Fig. 5.25: Contours graph shows the effect of S and F on σ_{11} at P = 1.3 kW.

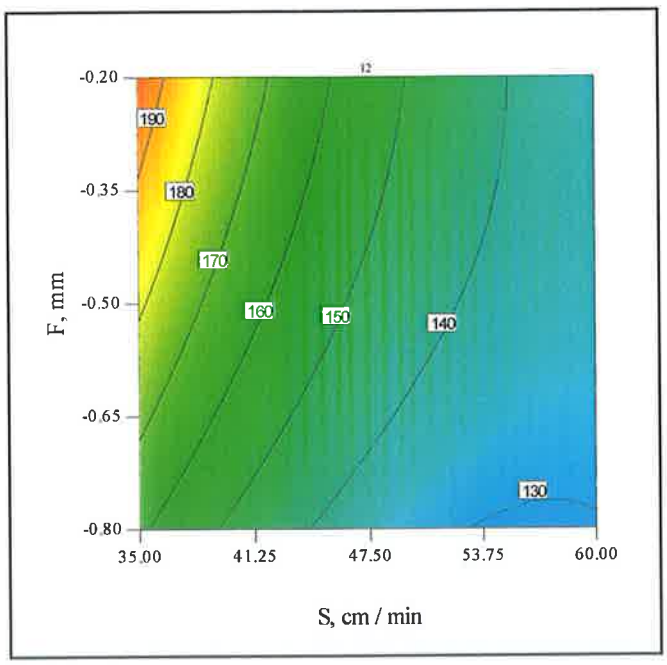

Fig. 5.26: Contours graph shows the effect of S and F on σ_{12} at P = 1.3 kW.

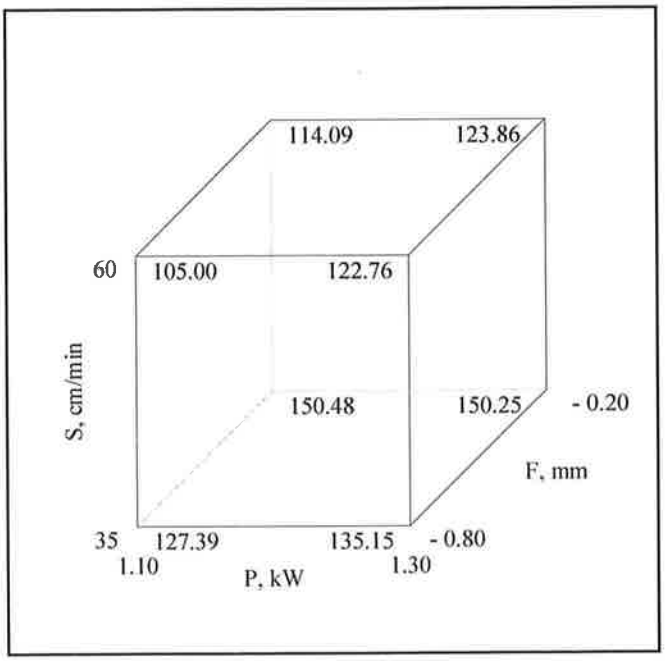

Fig. 5.27: Cube graph shows the effect of the three parameters on σ_{13}.

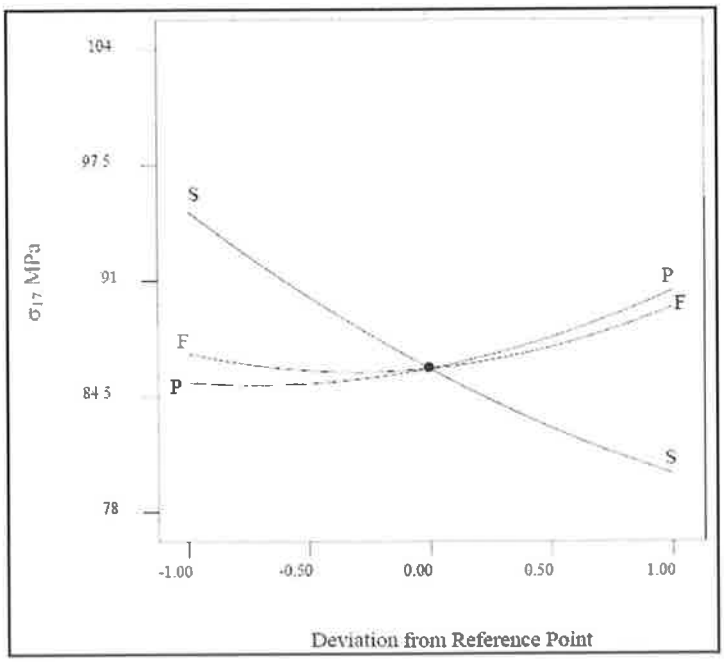

Fig. 5.28: Perturbation plot shows the effect of all the parameters on σ_{17}.

On balance, the most hazardous welding combination at which the welding process is considered unsafe is slow welding speed, high laser power and focused laser beam, because these settings would pre-stress the welds with undesirable tensile stress which would result in a decrease in the weld tensile strength and reduce its fatigue life. These results are in agreement with those of [4, 10 and 148]. In particular, the maximum residual component in the HAZ at a depth of 0.127 mm should be monitored because if this component is minimised the other components would be minimised as well. For the time being the recommended welding conditions at which the welding technique could be considered safe and sound are laser power between (1.15 and 1.22 kW), welding speed between (55 and 60 cm/min) and focal point position of -0.8 mm. Therefore, an overall optimisation should be performed for this investigation which would account for the minimisation of the unwanted residual stress, maximisation of the weld quality and minimisation of the joint operating costs.

5.2.3 Development of the impact, tensile strength and joint cost models

The fit summary tab in the Design-Expert software suggests the highest order polynomial where the additional terms are significant and the model is not aliased. Selecting the step-wise regression method eliminates the insignificant model terms automatically. The sequential F-test for significance of both the regression models and the individual models terms along with the lack of fit test were carried out using Design- Expert V7 software. The ANOVA for the reduced quadratic models summarizes the analysis of each response and shows the significant model terms. Tables 5.30 to 5.32 show the ANOVA results for the tensile strength, impact strength and operating cost respectively. The same tables show also the other adequacy measures R^2, Adjusted R^2 and Predicted R^2. All the adequacy measures are in logical agreement and indicate significant relationships. The adequate precision ratios in all cases are greater than 4 which indicate adequate models discrimination. The Analysis of Variance result for the tensile strength model shows that the main effect of the three laser welding parameters and the quadratic effect of the laser power along with the interaction effect of the three parameters are significant model terms, nevertheless the main effect of laser power was added to support hierarchy.

However, the welding speed and the laser power are the factors most affecting the tensile strength. For the impact strength model the results indicate that the main effect of the three factors and the quadratic effect of the laser power are significant model terms. However, the laser power is the factor most associated with the impact strength. In the welding operation cost model, the Analysis of Variance results demonstrated that the main effect of the laser power and welding speed along with the quadratic effect of the welding speed are the significant model terms. As mentioned earlier, the welding cost per meter can be calculated using Eq. 4.7. In this work, a mathematical model was developed to estimate the cost for optimization purposes. According to the obtained results the developed models are statistically accurate and can be used for further analysis. The final models in terms of coded and actual factors are shown below Eqs. 5.23 to5.28.

Table 5.30: ANOVA analysis for the tensile strength model.

Source	Sum of Squares	DF	Mean squares	F Value	Prob > F	
Model	34184.45	7	4883.492	12.435	0.0001	Significant
P	21.32	1	21.317	0.054	0.8197	
S	2621.85	1	2621.851	6.676	0.0239	
F	1788.57	1	1788.575	4.554	0.0542	
PS	2400.60	1	2400.603	6.113	0.0294	
PF	2306.09	1	2306.085	5.872	0.0321	
SF	2102.52	1	2102.521	5.354	0.0392	
P^2	22943.49	1	22943.493	58.421	< 0.0001	
Residual	4712.75	12	392.729			
Lack of Fit	1964.24	7	280.606	0.510	0.7976	Not significant
Pure Error	2748.50	5	549.701			
Cor Total	38897.19	19				
R-Squared = 0.879				Adj. R-Squared = 0.808		
Pred. R-Squared = 0.643				Adeq. Precision = 10.963		

Table 5.31: ANOVA analysis for the impact strength model.

Source	Sum of Squares	DF	Mean squares	F Value	Prob > F	
Model	339.11	4	84.776	29.003	< 0.0001	Significant
P	107.51	1	107.511	36.781	< 0.0001	
S	61.13	1	61.130	20.914	0.0004	
F	44.77	1	44.771	15.317	0.0014	
P^2	125.69	1	125.693	43.002	< 0.0001	
Residual	43.84	15	2.923			
Lack of Fit	35.90	10	3.590	2.259	0.1906	Not significant
Pure Error	7.94	5	1.589			
Cor Total	382.95	19				
R-Squared = 0.886				Adj. R-Squared = 0.855		
Pred. R-Squared = 0.702				Adeq. Precision = 19.655		

Table 5.32: ANOVA analysis for the operating cost model.

Source	Sum of Squares	DF	Mean squares	F Value	Prob > F	
Model	0.092253	3	0.030751	995.25	< 0.0001	Significant
P	0.000343	1	0.000343	11.09	0.0042	
S	0.084825	1	0.084825	2745.4	< 0.0001	
S^2	0.007084	1	0.007084	229.3	< 0.0001	
Residual	0.000494	16	3.09E-05			
Cor Total	0.092747	19				
R-Squared = 0.995				Adj. R-Squared = 0.994		
Pred. R-Squared = 0.981				Adeq. Precision = 106.64		

$$\text{Tensile Strength} = 658.41 - 1.25\,P - 13.86\,S - 11.44\,F + 17.32\,PS + 16.98\,PF - 16.21\,SF - 39.54\,P^2 \quad (5.23)$$

$$\text{Impact Strength} = 42.88 + 2.81\,P - 2.12\,S + 1.81\,F - 2.93\,P^2 \quad (5.24)$$

$$\text{Joint cost per meter} = 0.26 + 0.01P - 0.08\,S + 0.02\,S^2 \quad (5.25)$$

$$\text{Tensile Strength} = -4433.90 + 9102.06\,P - 19.9\,S - 511.93\,F + 13.86\,PS + 565.94\,PF - 4.32\,SF - 3954.10\,P^2 \quad (5.26)$$

$$\text{Impact Strength} = -401.17 + 730.46\,P - 0.17\,S + 6.04\,F - 292.67\,P^2 \quad (5.27)$$

$$\text{Operating cost per meter} = 0.8177 + 0.0501P - 0.0197\,S + 0.00014\,S^2 \quad (5.28)$$

5.2.3.1 Validation of the models developed

Fig. 5.29 a-b presents the relationship between the measured and predicted values of the tensile strength and impact strength. These scatter diagrams indicate that the above mathematical models exhibit a good agreement between the measured

and estimated values of the above mentioned responses. In order to further verify the developed model, three confirmation welding experiments were carried out using new test conditions selected from the optimal results shown in chapter 6, Table 6.5 and 6.6. These optimal conditions are within the experimental range of this experiment. A comparison between the experimentally recorded and the predicted responses calculated by the models developed were made for all weld-bead responses. The results of this comparison are presented in Table 5.33. It is clear that the models can effectively explain the responses within the factors domain, as the maximum error in prediction is about -7 %, which indicates good agreement.

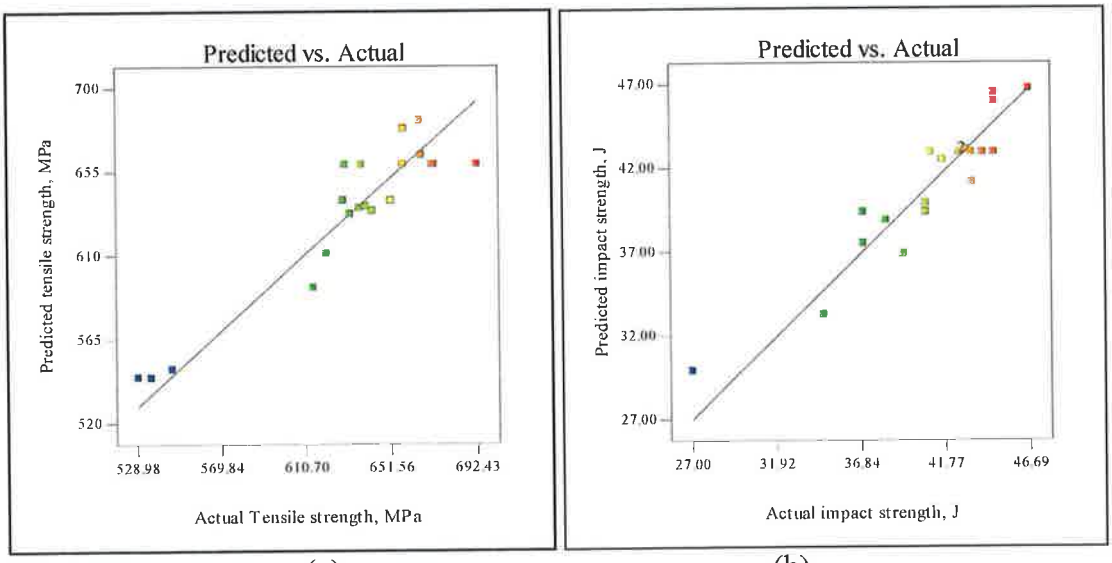

(a) (b)

Fig. 5.29: Scatter diagram (a) Tensile strength and (b) impact strength.

Table 5.33: Confirmation experiments for mechanical properties for 3 mm AISI304.

Exp. No.	P	S	F		Tensile strength, MPa	Impact strength, J	Joint cost, €/m
1	1.2	35	-0.2	Actual	681	46	0.3554
				Predicted	677	47	0.3618
				Error %	0.509	-1.757	-1.700
2	1.22	60	-0.8	Actual	627	40	0.2081
				Predicted	670	39	0.2052
				Error %	-6.987	2.315	1.4049
3	1.21	38.85	-0.2	Actual	710	47	0.3207
				Predicted	668	46	0.3266
				Error %	5.994	1.955	-1.8314

5.2.3.2 Effect of Process Parameters on the mechanical properties

In the subsequent headings, whenever an interaction effect or a comparison between any two input parameters is being discussed the third parameter would be at its centre level.

a) Tensile strength

It is evident from the results that all the process input parameters have a significant effect on tensile strength of a laser butt joint made of AISI304. However, Fig. 5.30 is a perturbation plot which illustrates the effect of the laser welding parameters on the tensile strength and Fig. 5.31 is a contours graph showing the interaction effect between the laser power and focal point position on the tensile strength.

It is evident from Fig. 5.30 that both the welding speed and the focal point position have a slightly negative effect on the tensile strength. While, in the case of the laser power the results demonstrate that increasing the laser power until it reaches its centre value would result in improved tensile strength, and the tensile strength then starts to drop as the laser power tends to increase above the centre limit. Such behaviour could be attributable to one of the following reasons. Firstly, is that the size of the HAZ would affect the weld joint mechanical properties. The HAZ would be wider when applying high laser power, according to El-Batahgy [139] which causes the tensile strength to drop. Secondly, it could be due to the fact that the austenitic stainless steel has low thermal conductivity [150], the heat will be localized and as the laser beam is moved, the localized heat is likely to take more time to conduct through the bulk metal which would allow the grains to grow in the weld zone and in the HAZ, this would result in reducing the tensile strength as stated in [139]. Generally, as the results indicate neither too high laser power nor too low are recommended to weld with.

In terms of interaction effect between laser power and welding speed, it is evident that by using slow welding speeds and high laser power all weld bead parameters, such as penetration and weld bead width, tend to increase, as mentioned in [131]. The settings that reduce the joint tensile strength can be attributed to the following points: 1) When using high laser power and slow welding speed

undesirable tensile residual stresses would result as discussed in [4, 10]. This would speed up the fracture as the joint is pre-stressed. 2) The increment in the heat input would be reflected in a wider HAZ and grain growth of the HAZ area is likely to happen and this would reduce the joint tensile strength as discussed earlier. On the other hand, welding with low laser power and high welding speed would also reduce the tensile strength of the welded joint due to a lack of full joining on a micro scale, especially at the back of the welded joint, i.e. the weld which does not encompass all the joint line is likely to occur because of inadequate back bead width. Therefore, based on the obtained results, applying either high laser power with low welding speed or low laser power with high welding speed is not recommended. Fig. 5.32 shows contours plot of the interaction effect between the laser power and the welding speed at a focus point position of -0.5 mm.

In relation to the interaction effect between the welding speed and focus point position, the results indicate that using either a focused or defocused laser bead with a slow welding speed has no significant effect on the tensile strength. On the other hand, the result indicates that by applying high welding speeds, the focus position should be set at its lowest limit of -0.8 mm to obtain slightly better tensile strength. This is because using a focused beam along with high welding speed would result in a poor joint and its consequences were discussed earlier. Fig. 5.33 is contours plot illustrating the interaction between the welding speed and focus position at a laser power of 1.2 kW.

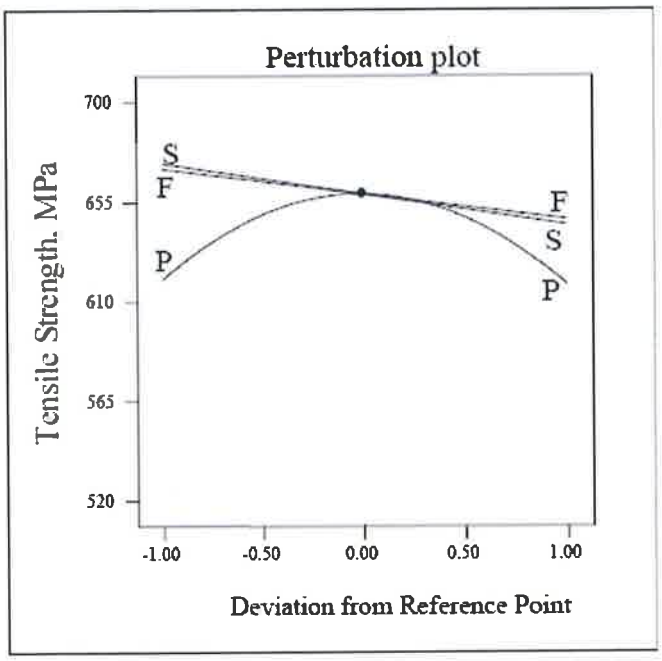

Fig. 5.30: Perturbation plot showing the effect of all factors on the tensile strength.

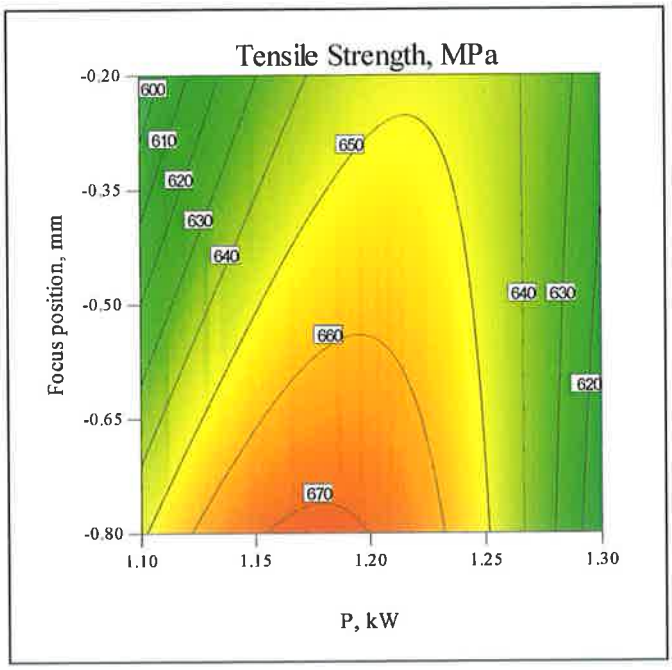

Fig. 5.31: Contours plot showing the effect of P and F on the tensile strength at S = 47.5 cm/min.

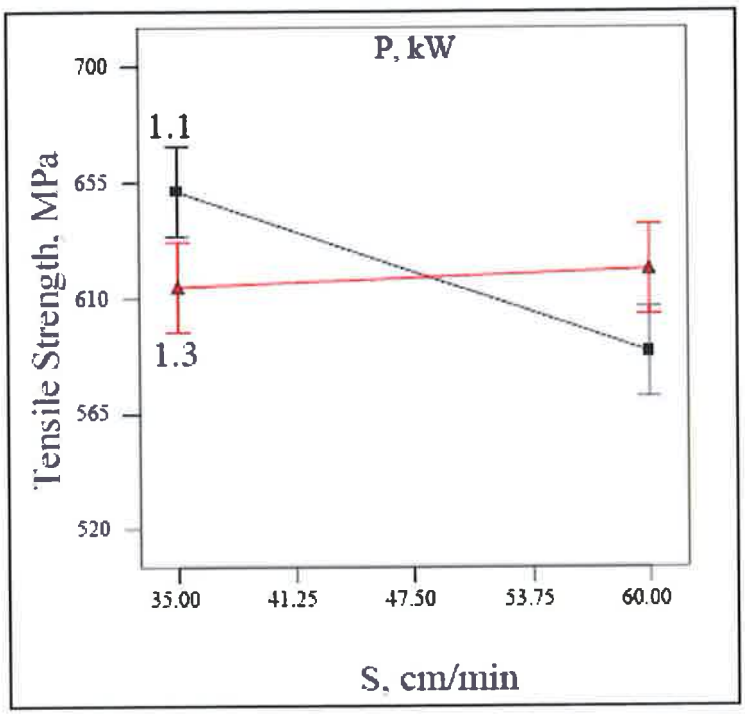

Fig. 5.32: Interaction effect between S and P on the tensile strength at F = - 0.5 mm.

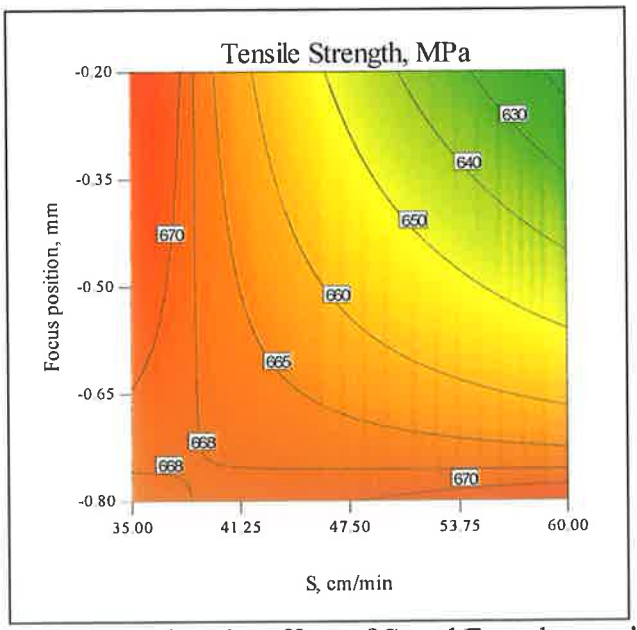

Fig. 5.33: Contours plot showing the effect of S and F on the tensile strength at P = 1.2 kW.

b) Impact strength

In the welding field, toughness is normally expressed as impact toughness, due to the fact that it is usually determined using the Charpy impact notch test. For that

reason, the relationship between the laser welding input parameters and impact strength of the welds must be highlighted. The result demonstrates that all the input parameters have a significant effect on the impact strength of the welded joint. No significant interaction effect was found in the case of the impact strength model. Fig. 5.34 shows a perturbation plot to compare the effect of different welding factors at a particular point (midpoint by default) in the design space. From this figure, it can be noticed that the impact strength increases as the laser power increases, as the high temperature achieved would lead to an annealing of the weld pool and the HAZ which would enhance their toughness. The result demonstrated that using a focused laser beam would improve the impact strength due to the improvement in toughness. Finally, the impact strength decreases as the welding speed increases due to the relatively smaller weld pool size obtained as a result of the high cooling rate which reduces the welds toughness and make them more brittle. Fig. 5.35 shows the effect of the laser power and welding speed on the impact strength at a focus position of -0.5 mm. Generally speaking the results indicate that as the tensile strength increases, the impact strength would be reduced. This is important in the optimization of the welding process.

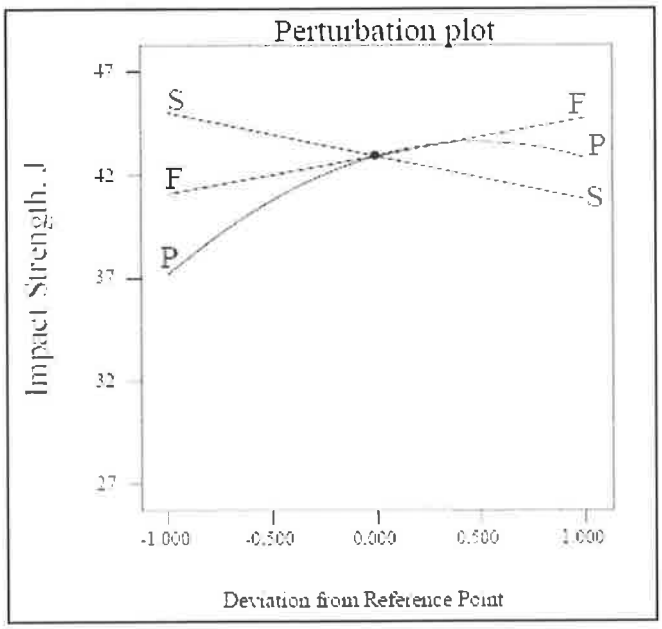

Fig. 5.34: Perturbation plot showing the effect of all factors on the impact strength.

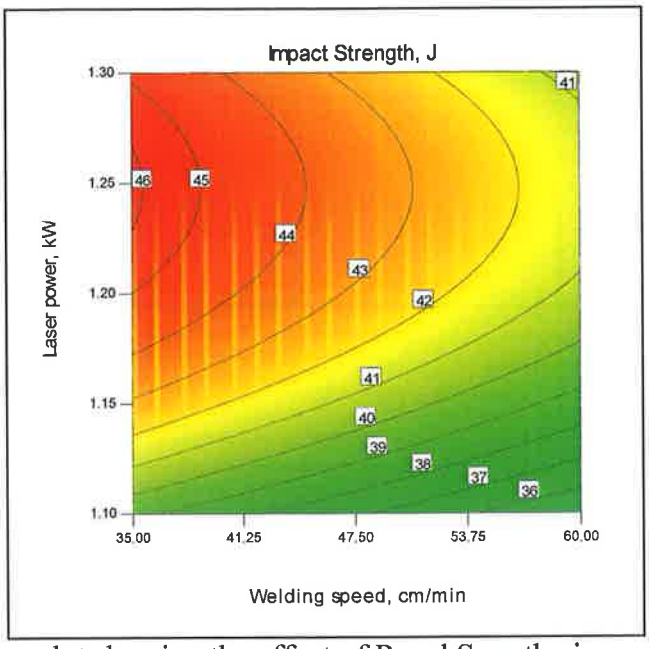

Fig. 5.35: Contours plot showing the effect of P and S on the impact strength at F = -0.5 mm.

5.2.4 Microstructure and microhardness investigation of AISI304 3 mm

The microstructure of a weld zone is clearly different from that of base metal zone of similar composition. This difference is related to different thermal and mechanical histories of both zones upon welding [10, 11]. As mentioned earlier in chapter 1, the secondary aims of this study are to characterize the microstructures and microhardness distribution of the laser welded joints by means of light microscopy and Vickers microhardness. Seven specimens were selected based on the heat input. Table 5.34 presents the welding conditions at which these seven specimens were welded.

Equiaxial austenite grains were observed in the heat-affected zone for all welding conditions as shown in Fig. 5.36. The microstructure of the weld fusion zones under various laser beam-welding parameters is shown in Fig. 5.37. In the course of this work the main obstacle was the etching of the weld metal. The etching solution used was 20 ml Ethanol 96% + 20 ml Hydrochloric acid 32% + 1 g Copper 2 chloride. The results show that the microstructure of the fusion zone was independent of the laser beam welding parameters, while the size and orientation of

the solidification structures were related to laser welding parameters which was in agreement with [139, 148]. It was found that the microstructure became coarser as the heat input of the laser beam welding increased as shown in Fig. 5.37 sample number 5. This was in agreement with [175]. The solidified structure of the weld made with a heat input of up to 1515 J/cm exhibited a distinct orientation as shown in Fig. 5.37 sample number 2. Based on the optical metallographic results, it could be assumed that the weld metal of the laser beam welding within the conditions of concern in this work consisted of single-phase structure of columnar dendrites. Microhardness measurements of the laser welds indicated that both the fusion zone and HAZ had a slightly higher hardness (Hv 201 ± 7) than the base metal (182 ± 3). Generally, the smaller the fusion zone the higher the microhardness because a higher cooling rate results in a finer microstructure. This result is in good agreement with El-Batahgy and Tasy et al. [139, 148]. Unlike carbon and alloy steels, AISI304 would not form a hardened structure after laser welding or heat treatment.

Table 5.34: Laser beam welding condition used in this investigation.

Specimen No.	1	2	3	4	5	6	7
P, (W)	1030	1200	1382	1200	1200	1200	1200
S, (cm/min)	47.5	47.5	47.5	68.52	26.5	47.5	47.5
F, (mm)	-0.50	-0.50	-0.50	-0.50	-0.50	-1	0
Heat input, (J/cm)	1301	1516	1746	1051	2717	1516	1516

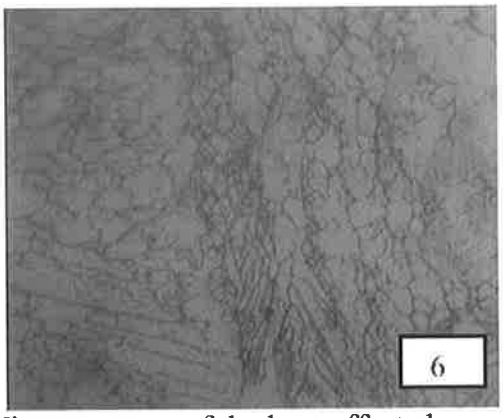

Fig. 5.36: Microstructure of the heat-affected zone, Mag. 80X.

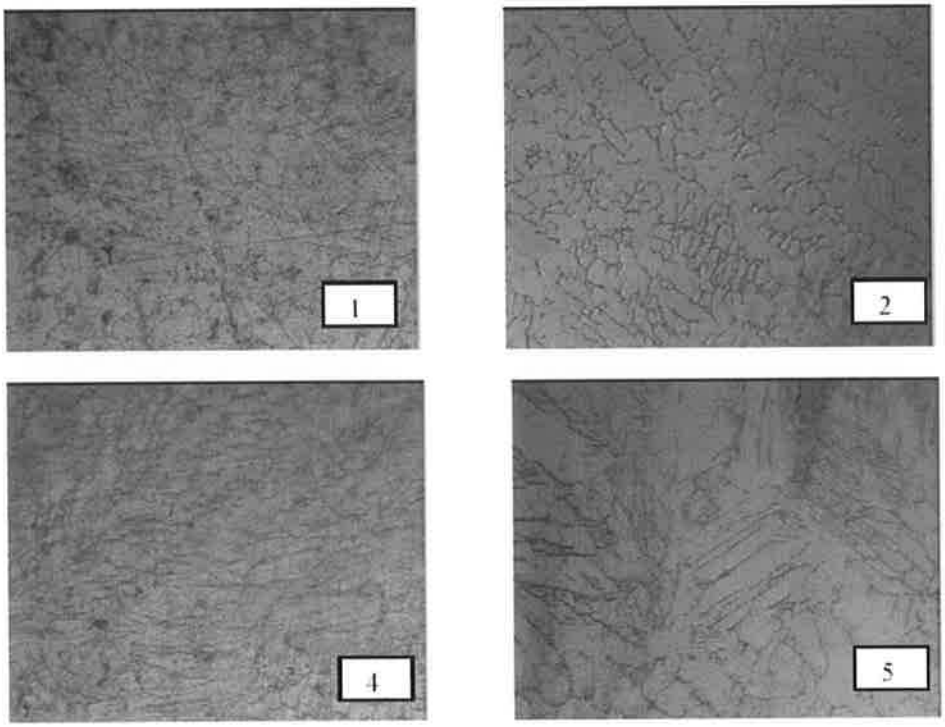

Fig. 5.37: Microstructure of the weld fusion zone at different laser welding conditions, Mag. 80X.

5.3 Stainless Steel AISI304 1 mm

The lap seam joint is one of the most common laser welded sheet metal joints because it offers the most versatility from a design standpoint in respect to ease of manufacture under production conditions. Fortunately, it is also the most simple to weld by laser from a process application point of view; it does not present laser beam to joint alignment problems and joint preparation and location are normally easy to achieve [4]. Tensile-shear strength in a lap joint of thin sheet metals is an important mechanical property to describe the performance of the welded joint.

The experiment was designed based on a three factors five levels central composite rotatable design with full replication [176]. Laser power, travel speed and focus point position are the laser welding input variables. In order to find the range of the process input parameters, trial weld runs were carried out by varying one of the process parameters at a time. Absence of obvious welding defects, a smooth and

uniform welded surface with a sound face and root bead as well as full penetration weld were the criteria used for choosing the working ranges. Table 5.35 shows the process variables and the coded and actual values. Statistical software Design-Expert V7 was used to code the variables and to establish the design matrix shown in Table 5.39.

Stainless steel of standard AISI304 in the form of plates with dimension of 180 mm x 80 mm x 1 mm were lap joined as shown in Fig. 4.2b, using 1.5 kW CW CO_2 Rofin laser and ZnSe focusing lens with a focal length of 127 mm. Argon gas was used as a shielding gas with a constant flow rate of 5 l/min. During the laser welding operation, the plates were clamped rigidly to avoid any distortion. The welding operation was accomplished according to the design matrix Table 5.36 and in a random order to avoid any systematic error in the experiment. For this experiment, six mathematical models were developed successfully to establish the functional relationship between process input parameters and the following responses: NH, W, BW, half penetration width (HW) and joint operating cost. The techniques listed in chapter 4 were applied to measure each response. The average of at least three successful readings was calculated for each response and then presented in Tables 5.37. Appendix D presents the full experimental measured data for all responses.

Table 5.35: Independent variable and experimental design levels used.

Variable	Notation	Unit	Limits				
			-1.682	-1	0	1	1.682
Laser Power	P	[kW]	1.03	1.1	1.23	1.35	1.44
Welding Speed	S	[cm/min]	50	70	100	130	150
Focal Position	F	[mm]	-1.5	-1.2	-0.75	-0.3	0

Table 5.36: Design layout for lap joint experiment.

Std	Run order	P	S	F	Std	Run order	P	S	F
1	16	1.1	70	-1.2	11	5	1.25	50	-0.75
2	1	1.35	70	-1.2	12	18	1.25	150	-0.75
3	10	1.1	130	-1.2	13	3	1.25	100	-1.5
4	17	1.35	130	-1.2	14	9	1.25	100	0
5	20	1.1	70	-0.3	15	2	1.25	100	-0.75
6	8	1.35	70	-0.3	16	15	1.25	100	-0.75
7	11	1.1	130	-0.3	17	13	1.25	100	-0.75
8	6	1.35	130	-0.3	18	12	1.25	100	-0.75
9	7	1.01	100	-0.75	19	14	1.25	100	-0.75
10	19	1.44	100	-0.75	20	4	1.25	100	-0.75

Table 5.37: Average of experimentally measured responses for AISI304 1 mm.

Std	Failure load, kN	Heat input, J/cm	W, mm	BW, mm	HW, mm	Joint operating cost, €/m
1	9.082	943	2.196	0.989	1.693	0.174
2	8.777	1157	2.067	1.046	1.584	0.183
3	7.825	508	1.818	0.599	0.951	0.094
4	7.595	623	1.743	0.568	0.849	0.098
5	8.819	943	1.950	0.697	1.363	0.174
6	8.632	1157	1.938	1.177	1.455	0.183
7	7.471	508	1.620	0.619	0.818	0.094
8	7.353	623	1.647	0.725	0.795	0.098
9	8.308	609	2.106	0.715	1.319	0.120
10	7.894	861	1.729	0.820	1.107	0.130
11	8.991	1483	2.188	1.399	1.840	0.252
12	6.869	489	1.667	0.598	0.712	0.083
13	8.303	735	1.970	0.781	1.360	0.125
14	8.040	735	1.721	0.738	1.010	0.125
15	7.942	735	1.998	0.730	1.283	0.125
16	8.273	735	1.989	0.724	1.181	0.125
17	8.407	735	2.001	0.750	1.191	0.125
18	7.812	735	1.992	0.723	1.148	0.125
19	8.087	735	2.001	0.712	1.173	0.125
20	7.917	735	1.998	0.713	1.181	0.125

5.3.1 Development of weld bead profile parameters models

The same steps and adequacy tests, as described in chapter 3, were also followed and performed at this point. Tables 5.38 - 5.41 presents the resulting ANOVA tables and the adequacy measures for the nominal heat input, W, BW and HW. The same tables present the adequacy measures; all the measures are close to 1 and indicate that there is an adequate functional relationship. However, in some cases the lack of fit is significant; this would not affect the adequacy of these models once the other measures are perfect.

For the heat input model, the Analysis of Variance indicates that the main effect of the laser power (P), welding speed (S), the second order effect of welding speed (S^2) and the two level of interaction of laser welding and welding speed (PS) are the most significant model terms associated with heat input. For the front width bead model, the main effect and the quadratic effect of the three parameters are significant models terms. For the back width bead model the results indicate that the main and interaction effect of the three parameters as well as the quadratic effect of the welding speed are significant model terms. For the half penetration width the ANOVA revealed that there is a linear relationship between these responses and the process parameters. Eqs. 5.29 -5.32 are the adequate models in terms of coded factors while, Eqs. 5.33-5.36 are the same models but in terms of actual factors. In the case of the weld pool, the model developed was not a good model since it accounts for only the main effect of the welding speed. Also, the adequacy measure was not close to 1, with a scattered relationship between the actual and predicted values in the scatter diagram. For that reason it was omitted from this study.

Table 5.38: ANOVA analysis for the nominal heat input model.

Source	Sum of Squares	DF	Mean squares	F Value	Prob > F	
Model	1154490	4	288622.609	401.364	< 0.0001	Significant
P	85979	1	85978.746	119.564	< 0.0001	
S	955177	1	955177.129	1328.288	< 0.0001	
PS	4891	1	4890.714	6.801	0.0198	
S^2	108444	1	108443.846	150.804	< 0.0001	
Residual	10787	15	719.104			
Lack of Fit	10787	10	1078.656			
Cor Total	1165277	19				
R-Squared = 0.991				Adj. R-Squared = 0.988		
Pred. R-Squared = 0.964				Adeq. Precision = 68.693		

Table 5.39: ANOVA analysis for the front width bead model.

Source	Sum of Squares	DF	Mean squares	F Value	Prob > F	
Model	0.5540	6	0.092	33.762	< 0.0001	Significant
P	0.0496	1	0.050	18.137	0.0009	
S	0.3543	1	0.354	129.560	< 0.0001	
F	0.0869	1	0.087	31.776	< 0.0001	
P^2	0.0142	1	0.014	5.210	0.0399	
S^2	0.0114	1	0.011	4.169	0.0620	
F^2	0.0473	1	0.047	17.297	0.0011	
Residual	0.0356	13	0.003			
Lack of Fit	0.0354	8	0.004	171.768	< 0.0001	Significant
Pure Error	0.0001	5	0.000			
Cor Total	0.5895	19				
R-Squared = 0.940				Adj. R-Squared = 0.912		
Pred. R-Squared = 0.756				Adeq. Precision = 19.731		

Table 5.40: ANOVA analysis for the back width bead model.

Source	Sum of Squares	DF	Mean squares	F Value	Prob > F	
Model	0.7864	7	0.112	34.339	< 0.0001	Significant
P	0.0457	1	0.046	13.971	0.0028	
S	0.5514	1	0.551	168.558	< 0.0001	
F	0.0002	1	0.000	0.066	0.8020	
PS	0.0266	1	0.027	8.120	0.0146	
PF	0.0392	1	0.039	11.968	0.0047	
SF	0.0143	1	0.014	4.357	0.0589	
S^2	0.1091	1	0.109	33.336	< 0.0001	
Residual	0.0393	12	0.003			
Lack of Fit	0.0383	7	0.005	28.033	0.0010	Significant
Pure Error	0.0010	5	0.0001951			
Cor Total	0.8256285	19				
R-Squared = 0.953				Adj. R-Squared = 0.925		
Pred. R-Squared = 0.712				Adeq. Precision = 22.239		

Table 5.41: ANOVA analysis for the half penetration width bead model.

Source	Sum of Squares	DF	Mean squares	F Value	Prob > F	
Model	1.6645	3	0.555	160.138	< 0.0001	Significant
P	0.0183	1	0.018	5.269	0.0356	
S	1.5350	1	1.535	443.026	< 0.0001	
F	0.1113	1	0.111	32.120	< 0.0001	
Residual	0.0554	16	0.003			
Lack of Fit	0.0446	11	0.004	1.881	0.2515	Not significant
Pure Error	0.0108	5	0.002			
Cor Total	1.7199	19				
R-Squared = 0.968				Adj. R-Squared = 0.962		
Pred. R-Squared = 0.945				Adeq. Precision = 42.838		

$$\text{Nominal heat input}=730.48 + 79.35\,P - 264.46\,S - 24.73PS + 85.96\,S^2 \quad (5.29)$$

$$\text{Front width}= 2.00 - 0.060\,P - 0.16\,S - 0.080\,F - 0.031P^2 - 0.028\,S^2 - 0.058\,F^2 \quad (5.30)$$

$$\text{Back width}= 0.73 + 0.058\,P - 0.20\,S - 3.98\times10^{-3}\,F - 0.058\,PS + 0.070\,PF + 0.042\,SF + 0.086\,S^2 \quad (5.31)$$

$$\text{Half penetration width}= 1.20 - 0.037\,P - 0.34\,S - 0.091\,F \quad (5.32)$$

$$\text{Nominal heat input}= 981.91 + 1294.10\,P - 19.84\,S - 6.59\,PS + 0.0955\,S^2 \quad (5.33)$$

$$\text{Front width}= -0.502 + 4.447\,P + 8.79\times10^{-4}\,S - 0.608\,F - 2.012\,P^2 - 3.12\times10^{-5}\,S^2 - 0.290\,F^2 \quad (5.34)$$

$$\text{Back width}= -1.473 + 2.932\,P - 4.69\times10^{-3}\,S - 1.845\,F - 0.0154\,PS + 1.244\,PF + 3.13\times10^{-3}\,SF + 9.58\times10^{-5}\,S^2 \quad (5.35)$$

$$\text{Half penetration width}= 2.525 - 0.292\,P - 0.0112\,S - 0.201\,F \quad (5.36)$$

5.3.1.1 Validation of the bead geometry models

In order to check the models developed for their adequacy, scatter diagrams shown in Figs 5.38a-d were drawn for the four responses. From these figures it is notable that the predicted and actual responses values are in a good agreement, because of the linear tendency in all the scatter points. To further verify the developed models, three confirmation weld runs with welding setting chosen randomly from the numerical optimization results shown in Tables 6.8 and 6.9 were carried out. The predicted, actual and percentage of error in prediction for each conformity experiment for the four responses are summarized in Table 5.42. It is evident that the models developed are quite accurate as the maximum error in prediction, about 8.84%, is in good agreement and they can be used to predict the responses within the factors ranges.

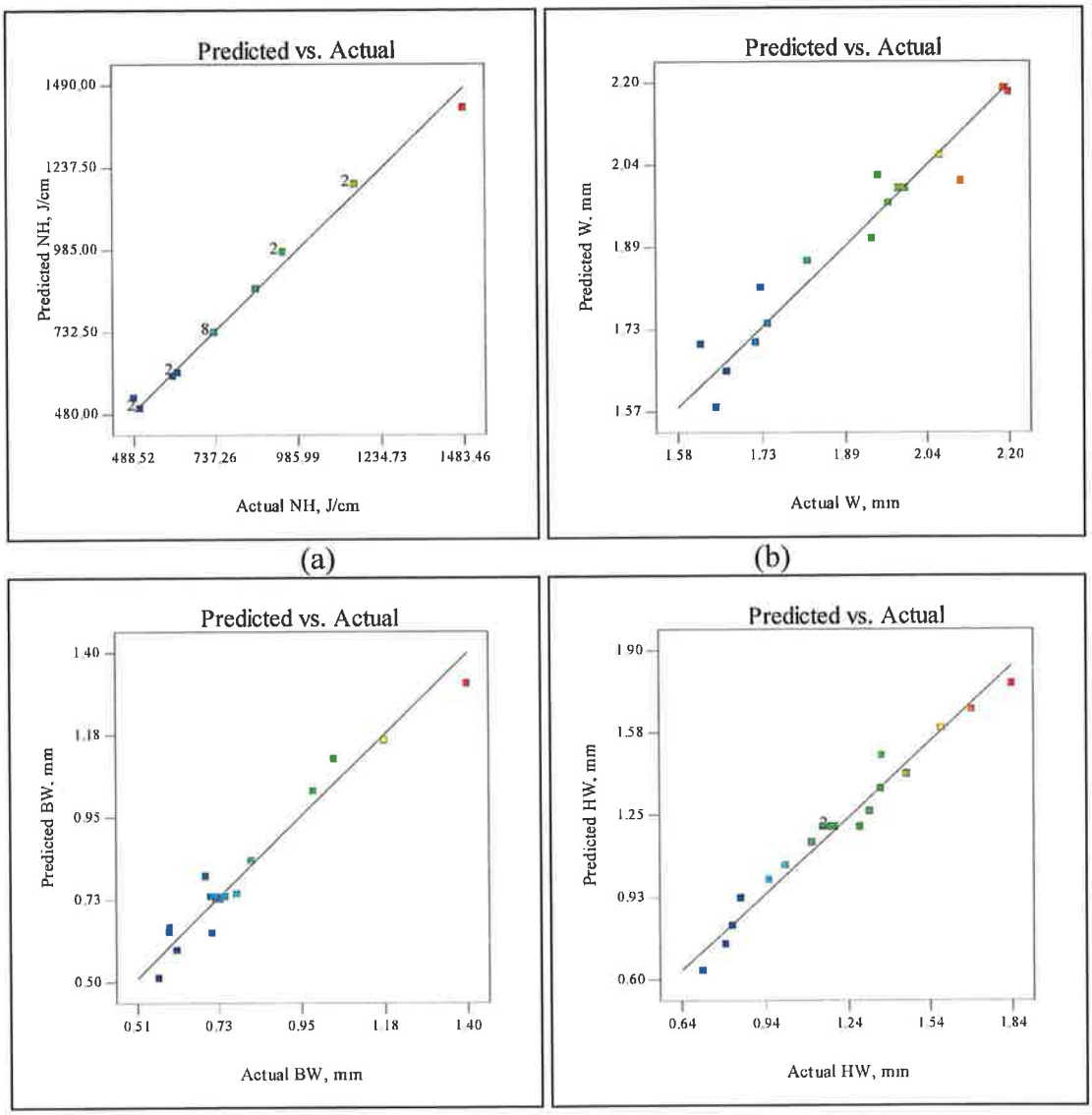

Fig. 5.38: Scatter diagram, (a) Nominal heat input, (b) front width, (c) back width and (d) half penetration width.

Table 5.42: Confirmation experiments for bead geometry for 1 mm AISI304.

Exp. No.	P	S	F		NH, J/cm	W, mm	BW, mm	HW, mm
1	1.1	97.43	-1.2	Actual	678	2.185	0.839	1.404
				Predicted	672.30	2.061	0.765	1.357
				Error %	0.841	5.660	8.838	3.405
2	1.1	111.8	-1.2	Actual	590	2.086	0.717	1.282
				Predicted	560.66	1.980	0.689	1.196
				Error %	4.974	5.066	3.948	6.738
3	1.1	113.5	-1.2	Actual	581	1.939	0.704	1.211
				Predicted	570.13	1.97	0.682	1.177
				Error %	1.870	-1.559	3.129	2.813

5.3.1.2 Effect of process parameters on weld-beads geometry

At this stage the models developed are ready to use to establish the effect of the process factors on the bead profiles parameters.

a) Nominal heat input

In the same way, it is evident from Fig. 5.39 that as the laser power increases the nominal heat input increases, while the relationship between the welding speed and the heat input is in reverse.

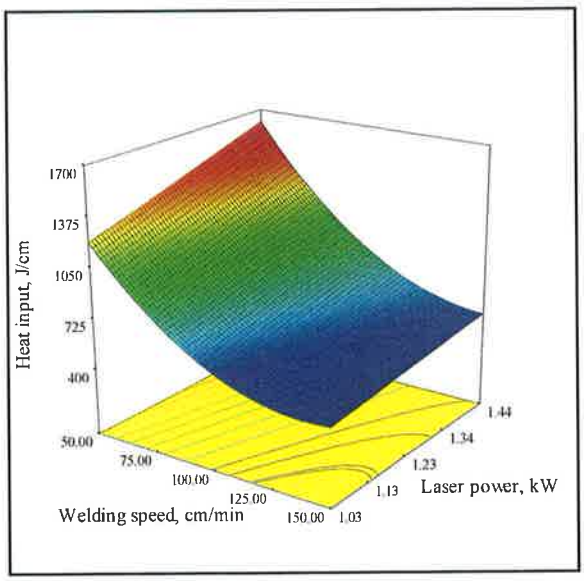

Fig. 5.39: 3D plot showing the effect of P and S on the nominal heat input.

b) Front width

It is clear from Figs. 5.40 and 5.41 that when all process factors increase, the front width decreases. This could be related to the following facts. Firstly, as the welding speed increases the heat input decreases resulting in less molten material which leads to a decrease in the front width. This was also found by [10]. Secondly, the front width increases as the defocused beam is used, due to the fact that applying a defocused beam will result in a wider laser beam which means a wider surface area will be irradiated with the laser beam. As a result of this the front width increases as stated in [4, 74]. The fact that in this case, increasing the laser power causes the front width to decrease, could be attributed to the fact that as the laser power increases the keyholing becomes more efficient and allows the laser power to penetrate much

further into the bulk material. This could help to achieve better back-beads. This is in agreement with the results of [74].

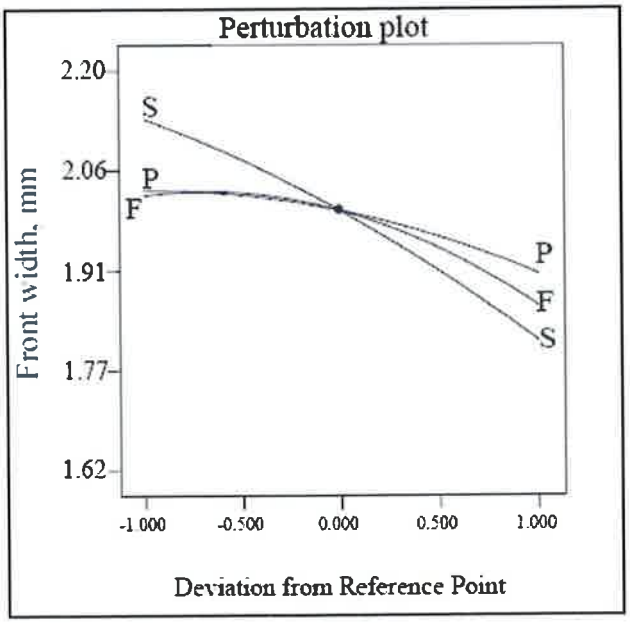

Fig. 5.40: Perturbation plot showing the effect of all factors on the front width.

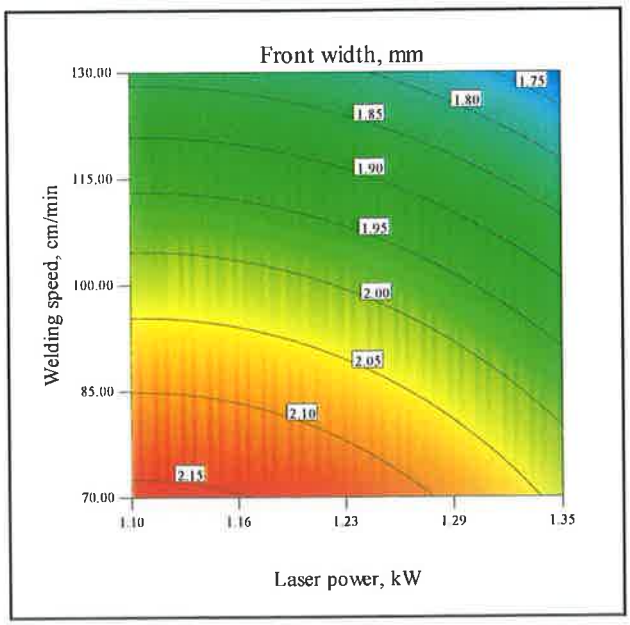

Fig. 5.41: Contours graph showing the effect of P and S on the W.

c) Back width

From Fig. 5.42 it is clear that the focus position has no significant effect on the back-width. On the other hand, the two other factors have opposite effects. The

welding speed has the same effect as the front width. But, as the laser power effect increases the back-width increases in a linear manner. This is due to the key-holing effect mentioned in the previous paragraph and how the heat diffusion becomes much easier as a result of increasing the laser power.

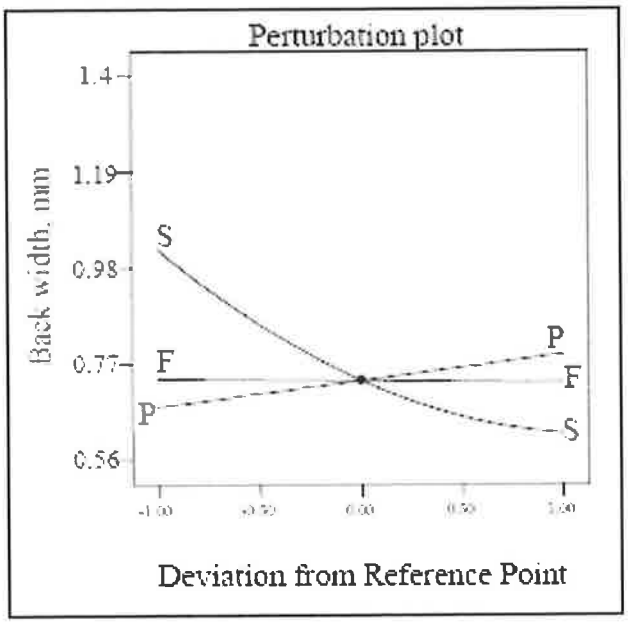

Fig. 5.42: Perturbation plot showing the effect of all factors on the back width of the lap joint.

d) Half penetration width

This bead geometry parameter is very important in the lap seam joining and it is better to increase this bead in such a way to ensure the maximum shear area, and consequently the failure load would be enhanced or vice versa. Fig. 5.43 demonstrates that all the three factors have a significant negative effect on this bead parameter but in varying degrees. Firstly, it is evident that the welding speed is the most important factor affecting the half penetration width, and as it increases the HW decreases remarkably. The reason for such behaviour was described earlier. On the other hand, the other two factors have a slightly negative effect also.

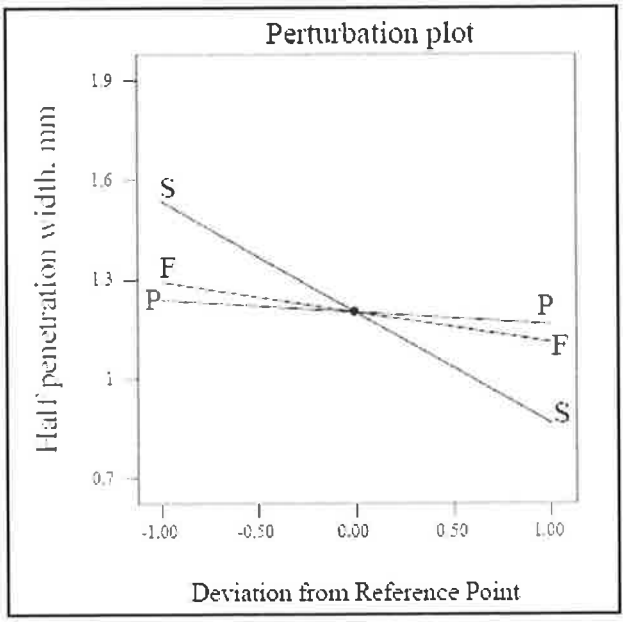

Fig. 5.43: Perturbation plot showing the effect of all factors on the half penetration width of the lap joint.

5.3.2 Development of the failure load and operating cost models

In order to evaluate the effect of process parameters on the failure load 'response', the relationship between process parameters and the response has been developed by using statistical analysis. The regression analysis, Analysis of Variance 'ANOVA', lack of fit test and other adequacy measures were performed. Table 5.43 and Table 5.44 summarizes the ANOVA results for the failure load model and the operating cost model, other adequacy measures R^2, Adjusted R^2 and Predicted R^2 are also presented. These measures are close to 1, which shows that the models is in reasonable agreement and indicates adequate models. Moreover, the adequate precision is greater than 4, which further support the models adequacy. For the failure load model the ANOVA result indicates that the main effects of the three factors are significant model terms. However, the welding speed has the greatest effect on the failure load of the lap joint. For the operating cost model the ANOVA result demonstrates that the main effect of the laser power, welding speed and the quadratic effect of welding speed are significant model terms. The mathematical models in terms of coded data are shown in Eqs. 5.37-5.38 and in terms of actual data are shown in Eqs. 5.39-5.40.

Table 5.43 ANOVA and adequacy measures for failure load model.

Source	Sum of Squares	DF	Mean Square	F Value	Prob > F	
Model	5.785	3	1.928	73.657	< 0.0001	Significant
P	0.173	1	0.173	6.596	0.0206	
S	5.459	1	5.459	208.502	< 0.0001	
F	0.154	1	0.154	5.872	0.0276	
Residual	0.419	16	0.026			
Lack of Fit	0.158	11	0.014	0.274	0.9658	Not significant
Pure Error	0.261	5	0.052			
Cor Total	6.204	19				
R-Squared = 0.932				Pred R-Squared = 0.908		
Adj R-Squared = 0.920				Adeq Precision = 29.388		

Table 5.44 ANOVA and adequacy measures for operating cost model.

Source	Sum of Squares	DF	Mean Square	F Value	Prob > F	
Model	0.03086	3	0.010	524.647	< 0.0001	Significant
P	0.00012	1	0.000	6.279	0.0234	
S	0.02761	1	0.028	1407.827	< 0.0001	
S^2	0.00313	1	0.003	159.834	< 0.0001	
Residual	0.00031	16	0.000			
Lack of Fit	0.00031	11	0.000			
Cor Total	0.03118	19				
R-Squared = 0.990				Pred R-Squared = 0.988		
Adj R-Squared = 0.963				Adeq Precision = 76.364		

$$\text{Failure load} = 8.12 - 0.112\,P - 0.632\,S - 0.106\,F \quad (5.37)$$

$$\text{Joint operating cost} = 0.12 + 3.003 \times 10^{-3}\,P - 0.045\,S + 0.015\,S^2 \quad (5.38)$$

$$\text{Failure load} = 11.152 - 0.9\,P - 0.0211\,S - 0.237\,F \quad (5.39)$$

$$\text{Joint operating cost} = 0.407 + 0.024\,P - 4.7463 \times 10^{-3}\,S + 1.6238 \times 10^{-5}\,S^2 \quad (5.40)$$

5.3.2.1 Validation of the models

Scatter diagrams shown in Fig. 5.44 a-c were drawn to present the relationship between the actual and predicted responses. It is clear from this figure that the residuals are close to forming a straight line which demonstrates that the models are adequate. In order to check the models adequacy further, three confirmation weld

runs were carried out using welding conditions taken from Tables 6.8 and 6.9. The results for the confirmation tests were summarized in Table 5.45. It is evident from Table 5.47 that the models are adequate because the maximum error is about 4.853% and it is possible to employ them in the optimization section.

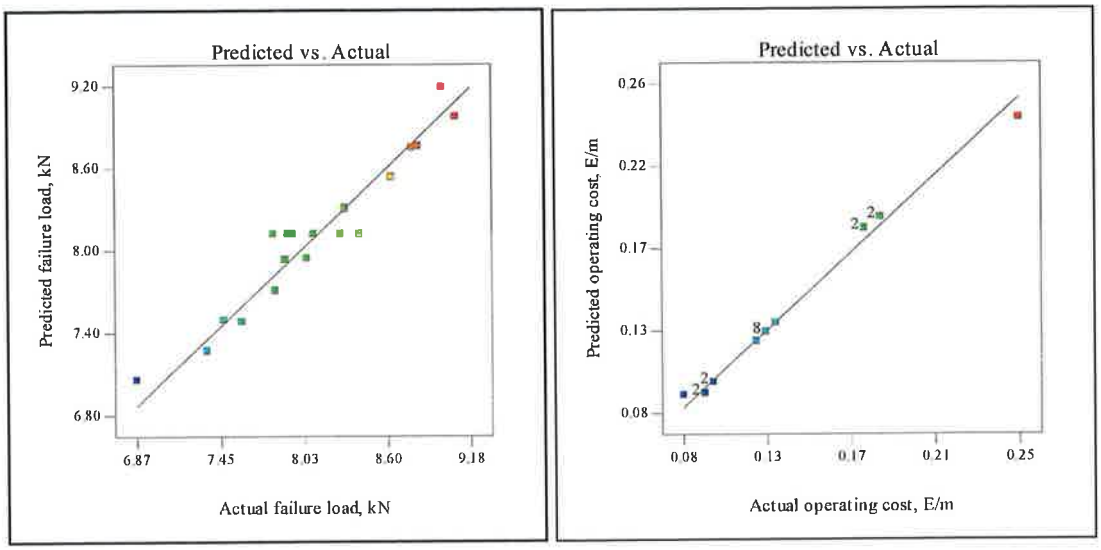

(a) (b)

Fig. 5.44: Scatter diagram for (a) failure load and (b) operating cost.

Table 5.45: Confirmation tests for failure load and operating cost for1 mm AISI304.

Exp. No.	P	S	F		Failure load, kN	Operating cost €/m
1	1.1	97.43	-1.2	Actual	8.294	0.1254
				Predicted	8.393	0.1251
				Error %	-1.188	0.239
2	1.1	111.8	-1.2	Actual	8.002	0.1092
				Predicted	8.054	0.1039
				Error %	-0.657	4.853
3	1.1	113.5	-1.2	Actual	7.925	0.1076
				Predicted	8.090	0.1058
				Error %	-2.079	1.713

5.3.2.2 Effect of process parameters on the failure load

It is clear from Fig. 5.45 that as the welding speed decreases the failure load increases, this is due to the fact that as the welding speed decreases the heat input increases resulting in a greater molten volume and the weld pool becomes bigger or vice versa as discussed in [4, 74]. Therefore, the joint fracture resistance would be enhanced. Also, it is notable from the same figure that the failure load slightly decreases as the laser power increases, due to the increase of power density, as discussed by Dawes and Radaj [4,10]. If the power density exceeded a certain level and is absorbed locally as in our case, 'keyhole welding', the temperature of the weld pool reaches the evaporation point of the base metal and some molten metal would evaporate, simultaneously a depression would form onto the top surface of the joint, 'undercuts', which reduce the joint strength. Fig. 5.46 shows that using a defocused laser beam would slightly increase the joint strength, due to the fact that the welding with defocused beam results in the spreading out the laser beam onto a wider area, which produces a wider weld pool and consequently increases the weld longitudinal cross-section area (i.e. shear area) which requires more load to break the joint. Although according to Huang et al. [131], using a defocused laser beam tends to reduce the penetration. But in this work all the welding settings give full penetration as a setting criteria used to choose the working range of each factor. The results prove that using slow welding speed, low laser power and a defocused laser beam would produce an overlap joint with higher strength, but this may affect other mechanical properties such as fatigue life. Since, slow welding speed would increase the unwanted residual stress which may reduce the fatigue strength of the weld joint as mentioned by Radaj and Tsay [10,148]. Therefore, this work should be extended to study the behaviour of other mechanical properties and microstructural characterization of this type of joint to present the optimal welding conditions that would improve the servicing life of the welded joint.

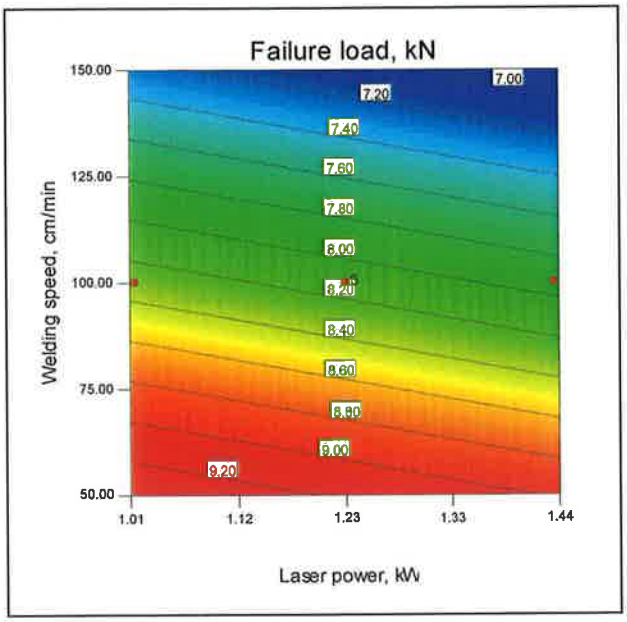

Fig. 5.45: Contours graph showing the effect of S and P on the failure load at F = -0.75 mm.

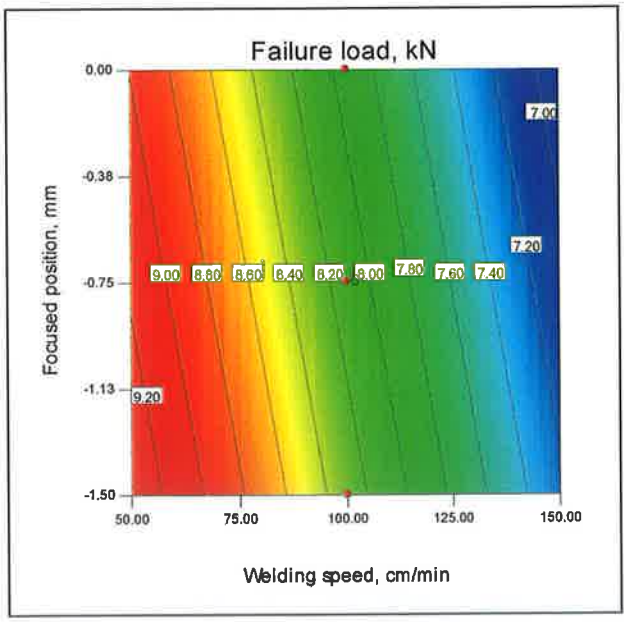

Fig. 5.46: Contours graph showing the effect of S and F on the failure load at P=1.25 kW.

5.3.3 Microstructure and microhardness investigation

The microstructure of the base metal consists of fine austenite as shown in Fig. 5.47a. While, the microstructure of the HAZ reveals columnar dendrites as shown in Fig. 5.47 b and c this results is in agreement with the results of El-Batahgy [134, 139], but disagreed with Tsay [148] who observed annealed twins in the HAZ. For the weld area the microstructure of the samples with low heat inputs of 489 and 609 J/cm exhibit fine dendritic grains as shown in Fig. 5.48 a and b. This is due to the faster cooling rate or solidification rate which was achieved as the welding speed increases. These results were in agreement with those of Nath et al. and El-Batahgy [134, 139]. While, as the heat input starts to increase to 861 and 1483 J/cm the dendritic grain become clearer as they become bigger as shown in Fig. 5.48 c and d. Also, it was found that the microhardness measurements of the laser welds indicated that FZ had a slightly higher hardness (230 ± 7 Hv) than the base metal, while the HAZ had a slightly lower hardness of (203 ± 3 Hv) than the base metal.

During laser welding an extremely localized heat input could be achieved which resulting in high cooling rates as stated above, due to this, a formulation of non-equilibrium microstructure, such as delta ferrite, could occur as stated in [146, 147 and 150]. In the course of this work to detect such non-equilibrium microstructures sophisticated equipment such as SEM and X-ray diffraction are required, since the microstructure investigation is not the main aim then there is no need to do so.

Based on the above result and discussion it could be assumed that the weld microstructure consists of single phase of columnar dendrites.

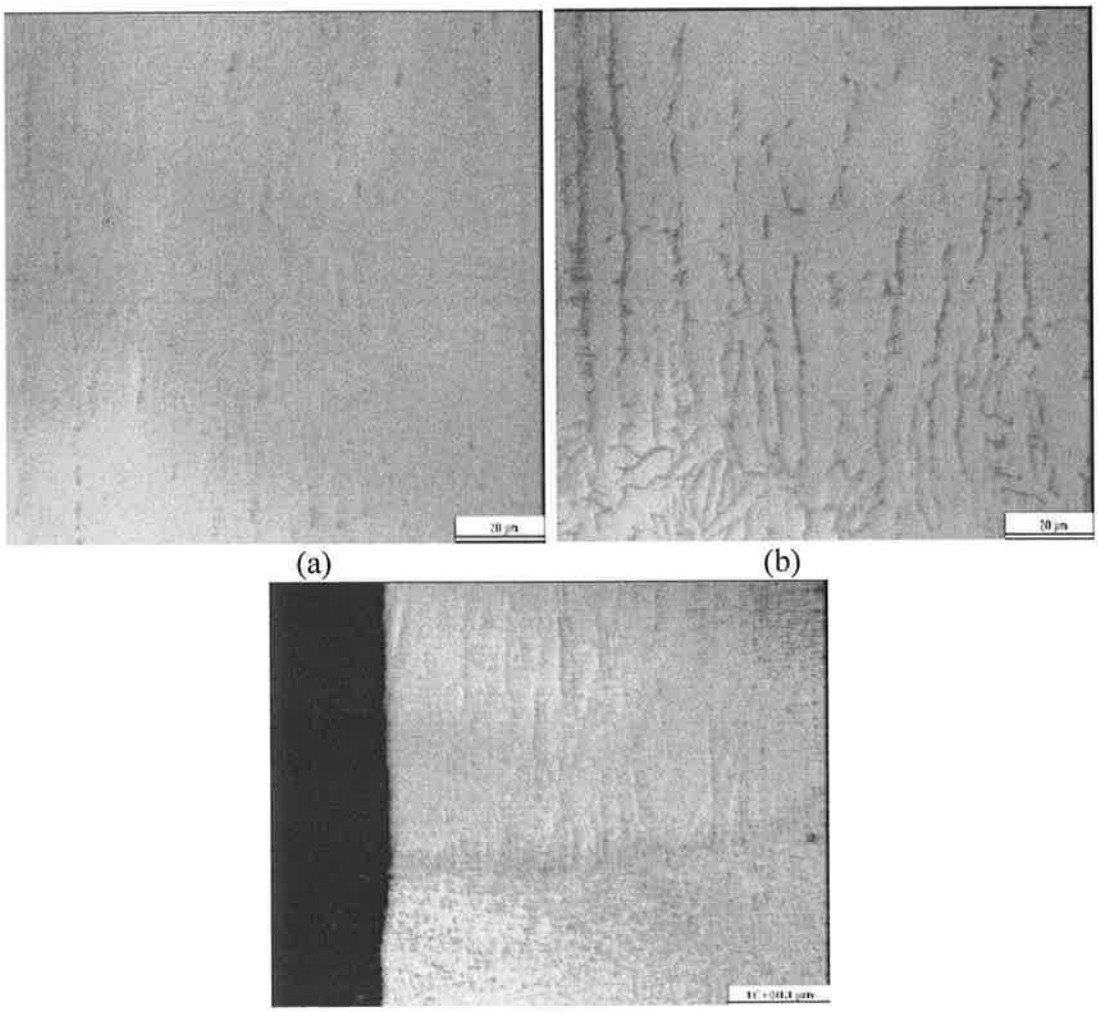

Fig. 5.47: Microstructure of the (a) base metal, (b) HAZ and (c) base metal, HAZ and weld pool at low magnification.

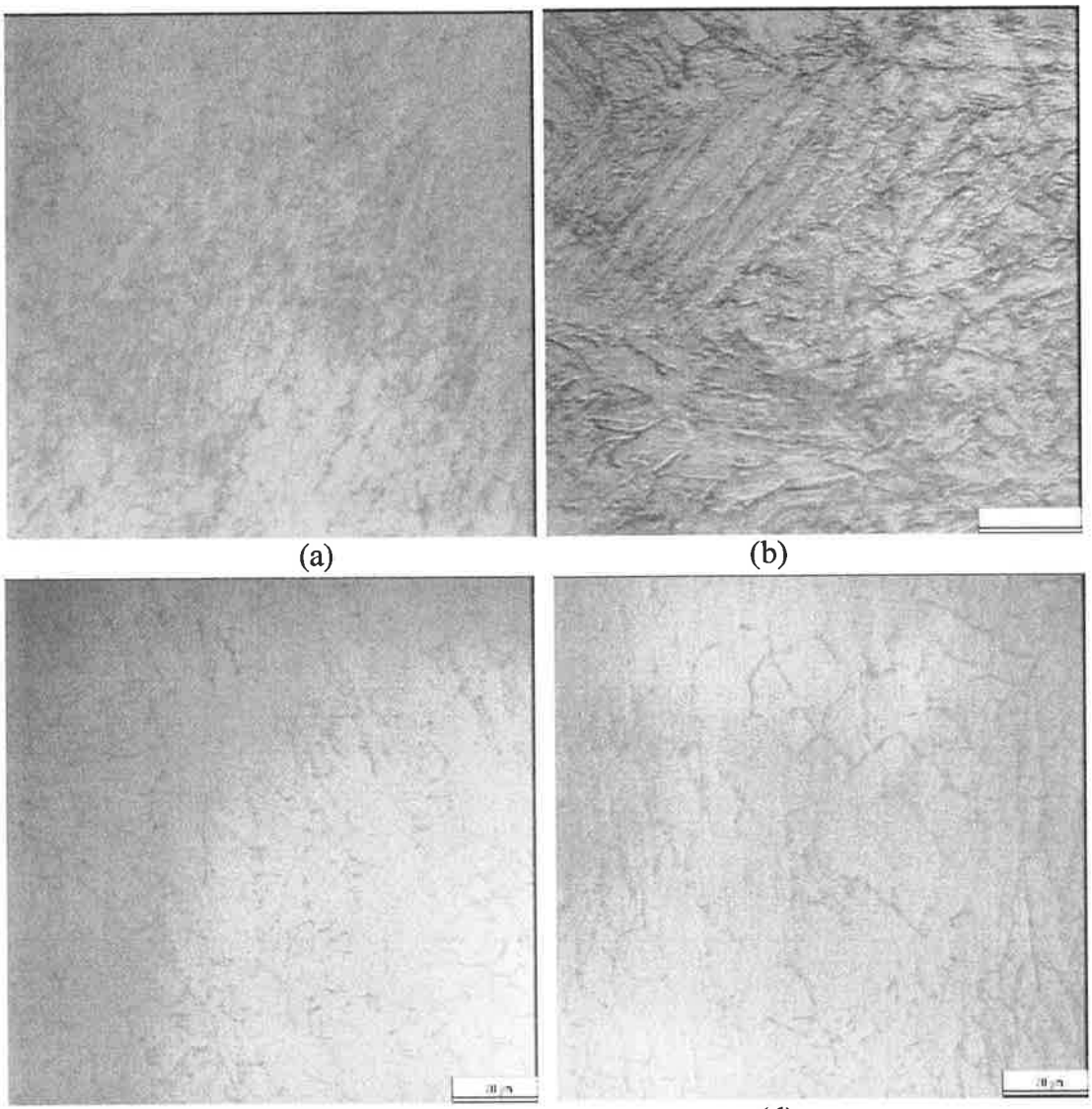

Fig. 5.48: Micrographs revealing the microstructure of AISI304 1 mm lab joint (a) sample No. 12, (b) sample No. 9, (c) sample No. 10 and (d) sample No. 11.

5.4 Dissimilar Welding of AISI304 and AISI1016

For this material the experiment was designed based on a three factors five levels CCD with full replication [155]. Pilot experiments were carried out using OVAT to identify the factors ranges. Lack of visible welding defects and full depth of penetration were the criteria for selecting the ranges. Table 5.46 presents the process factors, their limits and coded values. The welding operation was performed according to the design matrix shown in Table 5.47, in a random order. Argon gas was used as shielding gas at constant flow rate of 5 l/min. Throughout the laser welding the plates were clamped rigidly to avoid any deformation taking place due to the thermal loading. No special heat treatments were carried out either before or after the laser welding. For this material, twenty empirical models were developed successfully to predict the following responses: fourteen models to predict the residual stress distribution close to the HAZ and through the depth of each material, nominal heat input (NH), front width of FZ (W), back width (BW), weld pool area (A), impact strength and joint operating cost. The procedures explained earlier in chapter 4 were followed to determine and record these responses. Averages of at least three measurements for each response were presented in Table 5.48 and Table 5.49. Appendix E presents a full experimentally measured data for all responses.

Table 5.46: Independent variable and experimental design levels.

Variable	Notation	Unit	Standardized/actual levels				
			-1.682	-1	0	1	1.682
Laser power	P	[kW]	1.06	1.13	1.24	1.35	1.42
Welding speed	S	[cm/min]	24.77	35	50	65	75.23
Focus point position	F	[mm]	-1	-0.8	-0.5	-0.2	0

Table 5.47: Dissimilar welding experimental layout.

No	Run order	P	S	F	No	Run order	P	S	F
1	20	1.13	35	-0.8	11	6	1.24	24.77	-0.5
2	9	1.35	35	-0.8	12	12	1.24	75.23	-0.5
3	4	1.13	65	-0.8	13	14	1.24	50	-1
4	8	1.35	65	-0.8	14	18	1.24	50	0
5	3	1.13	35	-0.2	15	2	1.24	50	-0.5
6	5	1.35	35	-0.2	16	10	1.24	50	-0.5
7	11	1.13	65	-0.2	17	19	1.24	50	-0.5
8	16	1.35	65	-0.2	18	15	1.24	50	-0.5
9	1	1.06	50	-0.5	19	17	1.24	50	-0.5
10	13	1.42	50	-0.5	20	7	1.24	50	-0.5

Table 5.48: Experimentally measured responses for the dissimilar welding.

Std	NH, J/cm	Impact strength, J	W, mm	BW, mm	A, mm^2	operating cost €/m
1	1937	30.67	2.239	1.010	4.392	0.3508
2	2314	39.33	2.648	1.253	6.760	0.3651
3	1043	20.67	1.372	0.535	3.833	0.1889
4	1246	26.67	1.795	0.630	4.639	0.1966
5	1937	33.33	2.161	1.630	6.896	0.3508
6	2314	40.00	2.469	2.147	7.616	0.3651
7	1043	24.00	1.299	0.577	3.623	0.1889
8	1246	29.67	1.613	0.491	4.354	0.1966
9	1266	30.00	1.596	0.617	4.230	0.2422
10	1710	40.00	2.177	1.353	5.727	0.2590
11	3003	32.33	3.407	2.740	9.343	0.5058
12	989	20.00	1.118	0.598	5.342	0.1666
13	1488	24.67	1.775	0.808	4.349	0.2506
14	1488	34.00	1.425	0.824	4.513	0.2506
15	1488	31.00	1.787	0.701	4.542	0.2506
16	1488	29.00	1.572	0.734	5.067	0.2506
17	1488	27.33	1.779	0.657	5.191	0.2506
18	1488	32.33	1.781	0.758	5.038	0.2506
19	1488	29.67	1.755	0.822	5.147	0.2506
20	1488	28.67	1.722	0.790	5.558	0.2506

Table 5.49: Actual residual stress in HAZ, in AISI304 side and AISI1016 side.

Actual residual stress, MPa														
Std	AISI304							AISI1016						
	σ_1	σ_2	σ_3	σ_4	σ_5	σ_6	σ_7	σ_8	σ_9	σ_{10}	σ_{11}	σ_{12}	σ_{13}	σ_{14}
1	254	159	125	99	94	92	87	270	195	140	105	105	101	93
2	287	187	138	103	97	95	91	295	203	143	107	108	106	98
3	150	116	93	72	72	69	65	171	129	113	91	90	89	87
4	187	146	110	88	86	80	79	245	151	131	94	92	92	89
5	259	188	139	98	95	90	89	276	199	149	115	108	103	97
6	293	192	141	105	99	94	90	310	213	151	115	111	104	100
7	174	146	122	94	93	93	89	191	155	130	99	95	94	90
8	206	153	114	93	91	88	87	252	183	135	101	99	95	92
9	190	139	109	89	88	86	84	202	145	116	100	94	91	87
10	256	171	124	93	90	87	87	260	177	129	104	100	95	92
11	341	223	164	113	112	108	104	352	237	170	115	110	101	99
12	183	145	122	87	86	84	81	199	153	128	91	89	86	83
13	177	129	112	93	90	86	84	193	146	122	96	95	94	88
14	196	157	130	102	101	97	91	214	162	132	107	99	98	93
15	183	153	143	106	103	94	93	213	171	143	105	98	94	90
16	181	153	145	108	103	94	93	217	169	138	102	95	91	88
17	187	152	143	105	100	95	92	221	173	122	100	91	88	88
18	183	153	143	105	101	96	92	218	168	142	104	98	92	89
19	181	150	140	104	100	96	93	215	174	136	102	97	90	89
20	183	153	143	103	102	97	92	210	174	141	104	97	91	90

5.4.1 Development of weld-bead parameters models

The same steps and adequacy tests, which were outlined earlier, were followed and performed for this material too. Tables 5.50 - 5.53 summarize the resulting ANOVA tables and the other adequacy measures for nominal heat input, front width, back width and weld pool area models for the dissimilar welding. For the heat input model, the Analysis of Variance indicates that the main effect of the laser power (P), welding speed (S), the second order effect of welding speed (S^2) and the two level interaction of laser welding and welding speed (PS) are the most significant model terms associated with heat input. For the front width model, the ANOVA analysis indicates that the main effects of the three parameters and the quadratic effect of welding speed (S^2) are significant model terms. While, for back width bead the ANOVA indicates that the main effects of the three factors, the

interaction effect between the (SF) and the quadratic effects of welding speed (S^2) are significant model terms. For the weld pool area, the ANOVA shows that the main effect of the three factors, the interaction effect between welding speed and focal position (SF) and the quadratic effect of the welding speed (S^2) and focal position (F^2) are significant model terms. The final mathematical models for the last four responses in terms of coded factors as determined by Design-Expert are shown in Eqs. 5.41 - 5.44. The final mathematical models in terms of actual factors are presented in Eqs. 5.45 – 5.48

Table 5.50: ANOVA analysis for the heat input model.

Source	Sum of Squares	DF	Mean squares	F Value	Prob > F	
Model	4640790	4	1160198	395	< 0.0001	Significant
P	266328	1	266328	91	< 0.0001	
S	3914850	1	3914850	1334	< 0.0001	
PS	15149	1	15149	5	0.0382	
S^2	444463	1	444463	151	< 0.0001	
Residual	44027	15	2935			
Cor Total	4684817	19				
R-Squared = 0.991				Adj. R-Squared = 0.988		
Pred. R-Squared = 0.963				Adeq. Precision =68.30		

Table 5.51: ANOVA analysis for the front width model.

Source	Sum of Squares	DF	Mean squares	F Value	Prob > F	
Model	4.944	4	1.236	54.709	< 0.0001	Significant
P	0.433	1	0.433	19.153	0.0005	
S	3.890	1	3.890	172.184	< 0.0001	
F	0.089	1	0.089	3.927	0.0661	
S^2	0.533	1	0.533	23.573	0.0002	
Residual	0.339	15	0.023			
Lack of Fit	0.305	10	0.031	4.508	0.0551	Not significant
Pure Error	0.034	5	0.007			
Cor Total	5.283	19				
R-Squared = 0.936				Adj. R-Squared = 0.919		
Pred. R-Squared = 0.799				Adeq. Precision =27.12		

Table 5.52: ANOVA analysis for the back width model.

Source	Sum of Squares	DF	Mean squares	F Value	Prob > F	
Model	6.037	5	1.207	36.475	< 0.0001	Significant
P	0.295	1	0.295	8.915	0.0098	
S	4.018	1	4.018	121.365	< 0.0001	
F	0.153	1	0.153	4.614	0.0497	
SF	0.324	1	0.324	9.788	0.0074	
S^2	1.248	1	1.248	37.696	< 0.0001	
Residual	0.463	14	0.033			
Lack of Fit	0.446	9	0.050	13.812	0.0050	Significant
Pure Error	0.018	5	0.004			
Cor Total	6.501	19				
R-Squared = 0.929				Adj. R-Squared = 0.903		
Pred. R-Squared = 0.806				Adeq. Precision =22.38		

Table 5.53: ANOVA analysis for the weld pool area model.

Source	Sum of Squares	DF	Mean squares	F Value	Prob > F	
Model	34.685	6	5.781	30.378	< 0.0001	Significant
P	3.736	1	3.736	19.634	0.0007	
S	18.613	1	18.613	97.808	< 0.0001	
F	0.723	1	0.723	3.799	0.0732	
SF	1.857	1	1.857	9.758	0.0081	
S^2	7.834	1	7.834	41.167	< 0.0001	
F^2	1.272	1	1.272	6.686	0.0226	
Residual	2.474	13	0.190			
Lack of Fit	1.938	8	0.242	2.260	0.1921	Not significant
Pure Error	0.536	5	0.107			
Cor Total	37.159	19				
R-Squared = 0.933				Adj. R-Squared = 0.903		
Pred. R-Squared = 0.797				Adeq. Precision =21.48		

$$NH=1478.84 + 139.65\ P - 535.40\ S - 43.52\ PS + 174.03\ S^2 \quad (5.41)$$

$$W= 1.74 + 0.18\ P - 0.53\ S - 0.081\ F + 0.19\ S^2 \quad (5.42)$$

$$BW= 0.78 + 0.15\ P - 0.54\ S + 0.11\ F - 0.20\ SF + 0.29\ S^2 \quad (5.43)$$

$$A= 5.01 + 0.52\ P - 1.17\ S + 0.23\ F - 0.48\ SF + 0.73\ S^2 - 0.30\ F^2 \quad (5.44)$$

$$NH= 1987.87 + 2588.20\ P - 80.34\ S - 26.37\ PS + 0.77\ S^2 \quad (5.45)$$

$$W= 3.50 + 1.62\ P - 0.12\ S - 0.269\ F + 0.00085\ S^2 \quad (5.46)$$

$$BW = 5.47 + 1.34\,P - 0.19S + 2.59\,F - 0.045\,SF + 0.0013\,S^2 \quad (5.47)$$

$$A = 13.39 + 4.75\,P - 0.46\,S + 2.84\,F - 0.11\,SF + 0.0033\,S^2 - 3.29\,F^2 \quad (5.48)$$

5.4.1.1 Validation of the developed models

Fig. 5.49 a-d shows these scatter diagrams for the last four responses. These diagrams point out that the above mathematical models demonstrate a good agreement between the measured and estimated values of these responses. In order to verify the model developed further, three confirmation welding experiments were carried out using new test conditions selected from the optimal results shown in chapter 6, Tables 6.11 - 6.13. These optimal conditions are within the experimental range of this experiment. Table 5.54 presents the comparison results between the experimentally measured responses and the ones predicted using the models developed. It is clear that the models can explain the responses within the factors region, as the maximum error in prediction is about 16.451 % which indicates a fair agreement.

Table 5.54: Confirmation tests for weld bead parameters for dissimilar welding.

Exp. No.	P	S	F		NH, J/cm	W, mm	BW, mm	A, mm^2
1	1.35	45.87	-0.2	Actual	1766	2.245	1.214	6.456
				Predicted	1791	2.00	1.264	5.976
				Error %	-1.416	10.913	-4.119	7.440
2	1.13	49.39	-0.2	Actual	1373	1.664	0.857	4.702
				Predicted	1360	1.508	0.774	4.489
				Error %	0.947	9.393	9.706	4.530
3	1.14	65	-0.8	Actual	1052	1.374	0.594	4.161
				Predicted	1030	1.320	0.496	4.056
				Error %	2.091	3.953	16.451	2.523

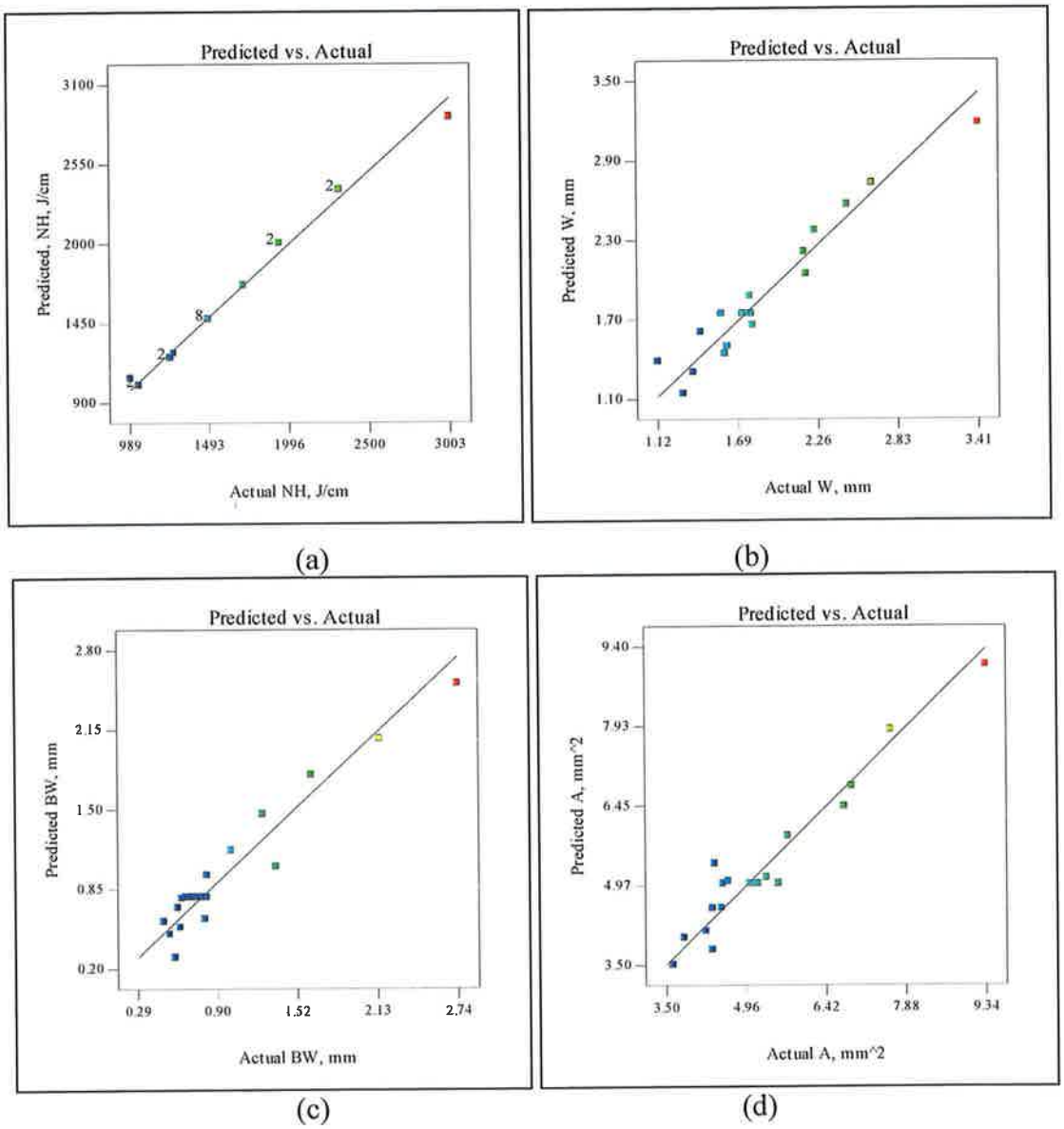

Fig. 5.49: Scatter diagrams for (a) Nominal heat input, (b) front width, (c) back width and (d) weld pool area.

5.4.1.2 Effect of process parameters on the weld bead parameters

The models developed can be used at this stage to investigate the effect of the process parameters on the weld bead parameters.

a) Heat input

It is clear from Fig. 5.50 that as the laser power increases the heat input increases too and the relationship is linear, but as the welding speed increases the heat input sharply decreases with a curvilinear relationship.

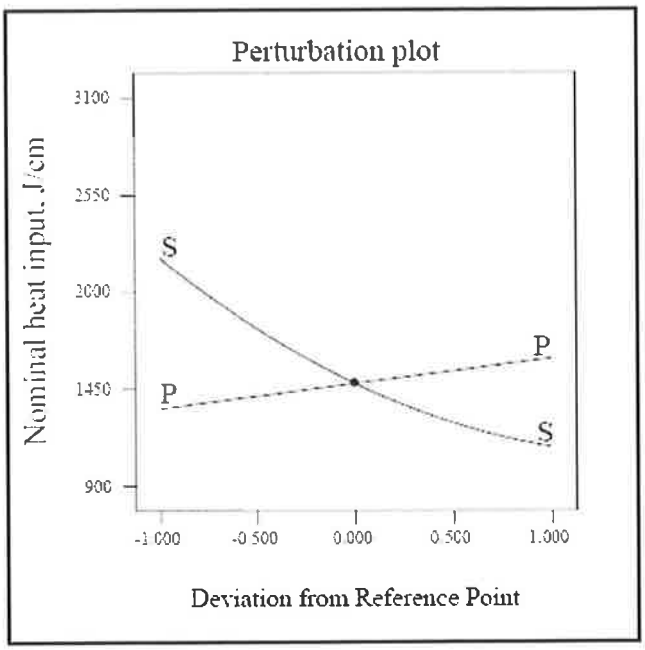

Fig. 5.50: Perturbation diagram showing the effect of P and S on NH.

b) Front width

The results indicate that the welding speed is the most important factor affecting this weld bead parameter. The laser power and the focus position also have a significant effect. Fig. 5.51 show the interaction effect between the welding speed and the laser power at F = -0.5 mm. By decreasing the S from its highest value to its smallest value the front width increases by 74.43%. This can be attributed to the fact that using a slower welding speed tends to increase the heat input which results in more material being melted. By increasing the laser power from its lowest value to the highest one the bead width would increase by 22.29%

and this can be attributed to the same reason as the increase in the laser power results in more heat input. While, for the focal point position defocusing the laser bead from -0.2 to -0.8 mm would result in a 9.64% increase in the front width. This is due to the fact that a wider laser beam would spread the laser power over a wider area and thus cause the front width to increase.

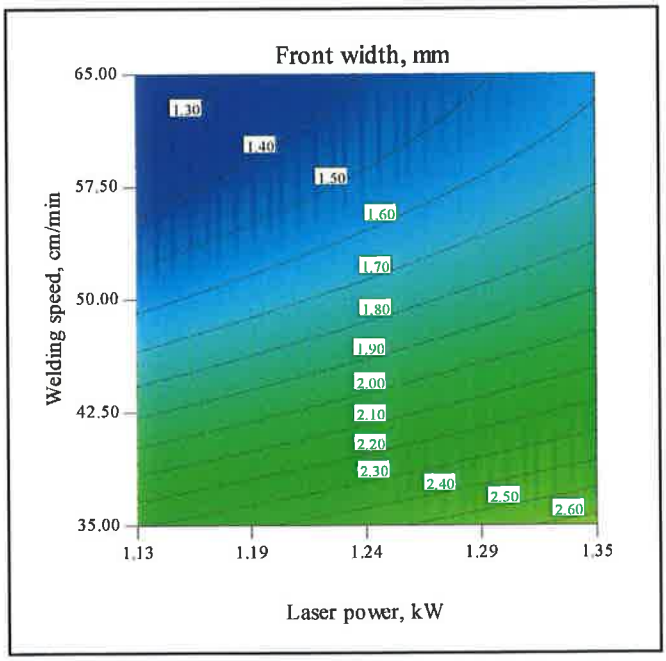

Fig. 5.51: Contours graph showing the effect of P and S on W at F = -0.5 mm.

c) Back width

The results demonstrated that the process parameters affect the back width with the same trend that these parameters exhibited on the front width, with small variations. Accordingly, when decreasing the welding speed from its maximum value to its minimum value this bead would increase by 203%. In the case of increasing the laser power from its minimum value to the maximum value the back width would increase by 46.1%. While by defocusing the laser beam the back width would decrease by 23.75%. However, Fig. 5.52 is a perturbation plot which shows the effect of process parameters on the back-width.

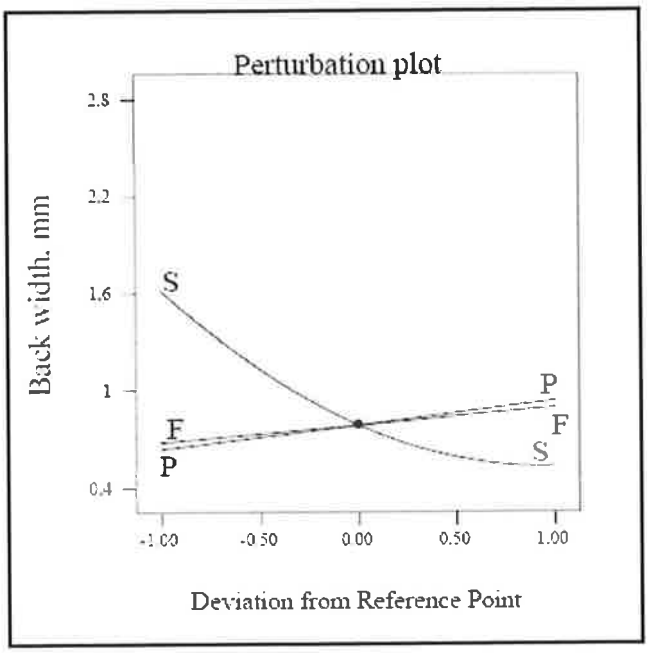

Fig. 5.52: Perturbation diagram showing the effect of all factors on the back width.

d) Weld pool area

The weld pool area is a function of all the process parameters as the results indicated. It increases by decreasing both the laser power and welding speed and decreases by defocusing the laser beam as shown in Fig. 5.53 and Fig. 5.54 below. From the model developed it is evident that by lowering the welding speed from its highest value to its lowest one the weld pool area would increase by 51%. And by increasing the laser power in the same manner the weld area would increase by 23.32%. While, using defocused laser beam instead of a focused one this would result in a reduction in the weld pool area of 9.31%.

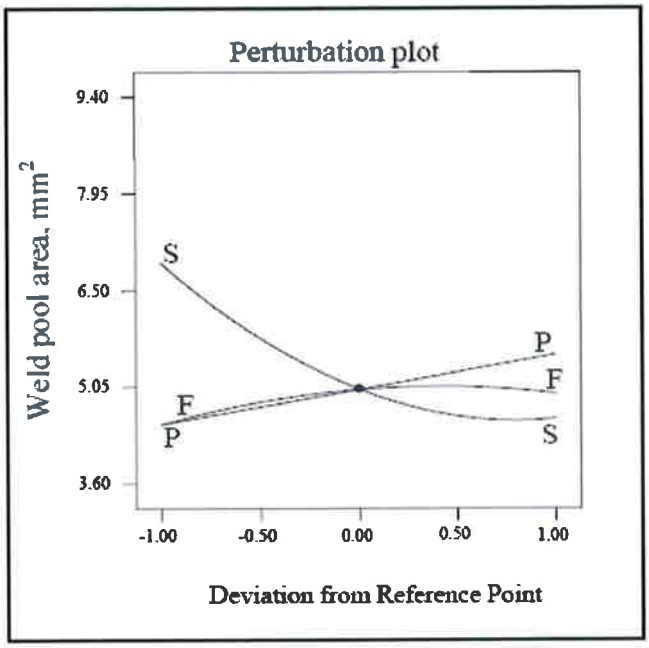

Fig. 5.53: Perturbation diagram showing the effect of all factors on the weld pool area.

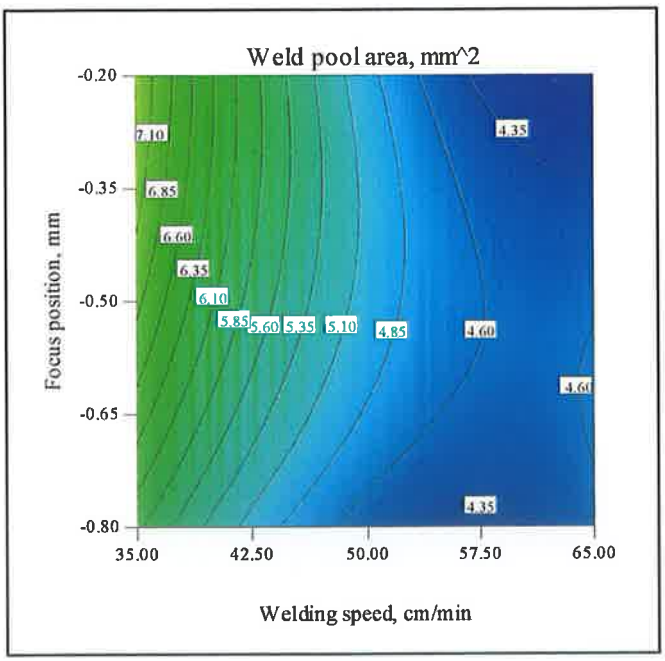

Fig. 5.54: Contours graph showing the effect of F and S on A at P = 1.24 kW.

5.4.2 Development of the residual stress distribution models

For this dissimilar welding experiment, fourteen models were developed effectively to relate the residual stress distribution to the laser welding process parameters. The Analysis of Variance demonstrated that all the laser welding process parameters investigated in this work have a significant effect on the residual stress distribution. For this dissimilar welding experiment the residual stress was measured at two locations one on each side and as close as possible to the weld seam to ensure the holes are located in the HAZ. The residual stress were abbreviated as follows: from σ_1 to σ_7 will represent the distribution over the depth of the principal stresses on the stainless steel side, while from σ_8 to σ_{14} will represent the distribution over the depth of residual stress on the low carbon steel side. The same statistical tests which were carried out previously were also performed. In this case there is no point in presenting 14 ANOVA tables, only the most important information from these tables is summarized and presented in Table 5.55. For all models the 'Prob. > F' value does not exceed 0.05, which indicates that the models are adequate. Also, the terms in these models have a significant effect on the responses being investigated. For the lack of fit, the Prob. > F values were greater than 0.05, which indicates an insignificant lack of fit, except for σ_5 and σ_7 where the lack of fit is significant at both levels of significance 0.05 and 0.01. It is noted that for σ_6, σ_8, and σ_9 the lack of fit is insignificant at $\alpha = 0.01$.

Table 5.56 presents the adequacy measure R^2. The results show that all values of R^2 are close to 1. These values are in good agreement and indicate adequate models. Table 5.56 also shows the adjusted R^2 and the Predicted R^2, both should be within 0.20 of each other [156]. It is observed that more than 64% of the results were within 0.2 differences. Besides that the adequate precision ratios are greater than 4 in all cases as presented in Table 5.56, which indicate an adequate model. Table 5.57 presents the significant coefficients for all responses as calculated by the software in terms of the actual parameters.

Table 5.55: ANOVA results for the fourteen models for dissimilar welding.

Response No.	Model			Lack of fit			Pure error	
	S. S.	D. F.	Prob.>F	S. S.	D. F.	Prob.>F	S. S.	D. F.
σ_1	48587	7	< 0.0001	34.36	7	0.5041	23.78	5
σ_2	10850	7	< 0.0001	32.53	7	0.1102	7.29	5
σ_3	5331	7	< 0.0001	72.82	7	0.0673	12.45	5
σ_4	1583	7	< 0.0001	95.29	7	0.0613	15.51	5
σ_5	1235	6	< 0.0001	174.12	8	0.0051**	7.87	5
σ_6	1111	7	< 0.0001	89.5	7	0.0117*	6.57	5
σ_7	944	7	< 0.0001	111	7	0.0006**	2.33	5
σ_8	38543	6	< 0.0001	1116	8	0.0127*	75.4	5
σ_9	12038	6	< 0.0001	441.5	8	0.0146*	31.65	5
σ_{10}	2618	5	< 0.0001	278	9	0.8154	295	5
σ_{11}	910	3	< 0.0001	12.2	11	0.9327	15.91	5
σ_{12}	697	3	< 0.0001	103	11	0.3295	30.24	5
σ_{13}	535	6	< 0.0001	60	8	0.2008	17.04	5
σ_{14}	325	6	< 0.0001	34.32	8	0.0583	4.82	5

* Not Sig. at $\alpha = 0.01$ and ** Sig. at both values of α.

Table 5.56: Adequacy measures for each model developed for dissimilar welding.

Response No.	R^2	Adj.R^2	Pred.R^2	Adeq. Precision
σ_1	0.9998	0.9981	0.9960	136.76
σ_2	0.9963	0.9942	0.9849	90.38
σ_3	0.9843	0.9751	0.9311	40.67
σ_4	0.9346	0.8964	0.7925	17.33
σ_5	0.8716	0.8123	0.5822	14.64
σ_6	0.9204	0.8739	0.6427	18.33
σ_7	0.8928	0.8303	0.4995	15.93
σ_8	0.9700	0.9562	0.8883	31.84
σ_9	0.9622	0.9447	0.8843	30.73
σ_{10}	0.8199	0.7556	0.6784	14.33
σ_{11}	0.9700	0.9644	0.9573	40.64
σ_{12}	0.8395	0.8094	0.7631	17.59
σ_{13}	0.8743	0.8163	0.5737	12.18
σ_{14}	0.8924	0.8428	0.5669	14.02

Table 5.57: Model terms coefficients in terms of actual values for dissimilar welding.

No.	b_0	b_1	b_2	b_3	b_{11}	b_{22}	b_{33}	b_{12}	b_{13}	b_{23}
σ_1	2229.53	-2723.4	-15.15	-7.5617	1164.7	0.125	14.07	0	0	0.867
σ_2	479	-196.93	-6.36	213.66	76.75	0.049	-35.435	0	-177.8	0
σ_3	-1067.4	2014.5	-0.625	69.5	-826	0	-91.85	0	-132.8	0.460
σ_4	-627	1124.3	0.838	-63.06	-444.7	-0.009	-34.53	0	0	0.780
σ_5	-538.9	1023	-0.104	-49.22	-406.8	0	-29.56	0	0	0.631
σ_6	-368.26	758.51	0.101	10.24	-313.6	0	-23.01	0	-57.67	0.997
σ_7	-282.2	616.45	0.0655	25.62	-256.65	0	-25.18	0	-68.27	0.866
σ_8	1811	-1818.9	-20.51	20.16	696.4	0.107	5.73	0	0	0
σ_9	230	84.16	-5.55	-82.70	0	0.045	-47.90	0	0	1.176
σ_{10}	-318.4	860.1	-3.067	13.26	-333.3	0.024	0	0	0	0
σ_{11}	122.71	8.431	-0.477	12.70	0	0	0	0	0	0
σ_{12}	107.22	13.63	-0.450	6.00	0	0	0	0	0	0
σ_{13}	299.28	-274.52	-1.046	31.759	114.50	0.007	27.92	0	0	0
σ_{14}	211	-154.4	-0.872	16.26	67.1	0.006	11.36	0	0	0

5.4.2.1 Validation of the residual stress models for dissimilar welding

To confirm the adequacy of the models developed, the predicted values and actual experimental measured values rounded to the nearest MPa were presented in Tables 5.58 and 5.59. It is evident that all the actual and predicted responses are in good agreement. To check the models developed in mid-points, two conformation tests were performed using new welding settings. These optimal conditions are: for the first test P= 1.352 kW, S= 45.87 cm/min and F= -0.2 mm and for the second test P= 1.14 kW, S= 65 cm/min and F= -0.8 mm. The results of these confirmation tests are listed in Tables 5.60 and 5.61. It is clear that the models successfully explained the responses within the variables field, as the maximum absolute average error in prediction for both test and sides is 7.341%, which indicates good agreement. Accordingly the models developed are adequate and can be used to predict the responses within the factors field.

Table 5.58: Actual and predicted residual stress on HAZ for AISI304 side.

Sample No.	Residual stress [MPa]													
	σ_1		σ_2		σ_3		σ_4		σ_5		σ_6		σ_7	
	Act.	Pred.	Act.	Pred.	Act.	Pred.	Act.	Pred.	Act.	Pred.	Act.	Pred.	Act.	Pred.
1	254	252	159	159	125	125	99	100	94	97	92	93	87	89
2	287	289	187	189	138	141	103	105	97	100	95	99	91	96
3	150	151	116	116	93	95	72	78	72	79	69	72	65	70
4	187	187	146	146	110	111	88	83	86	82	80	78	79	78
5	259	258	188	188	139	142	98	99	95	98	90	95	89	92
6	293	294	192	195	141	140	105	104	99	101	94	93	90	90
7	174	172	146	145	122	120	94	92	93	91	93	92	89	89
8	206	208	153	151	114	119	93	96	91	94	88	90	87	87
9	190	192	139	140	109	108	89	86	88	84	86	83	84	80
10	256	253	171	170	124	120	93	94	90	89	87	86	87	85
11	341	341	223	220	164	164	113	112	112	111	108	105	104	101
12	183	183	145	147	122	121	87	87	86	90	84	85	81	82
13	177	175	129	129	112	109	93	91	90	87	86	83	84	80
14	196	197	157	158	130	129	102	102	101	99	97	95	91	91
15	183	183	153	152	143	142	106	105	103	100	94	95	93	92
16	181	183	153	152	145	142	108	105	103	100	94	95	93	92
17	187	183	152	152	143	142	105	105	100	100	95	95	92	92
18	183	183	153	152	143	142	105	105	101	100	96	95	92	92
19	181	183	150	152	140	142	104	105	100	100	96	95	93	92
20	183	183	153	152	143	142	103	105	102	100	97	95	92	92

Table 5.59: Actual and predicted residual stress on HAZ for AISI1016 Side.

Sample No.	Residual stress [MPa]													
	σ_8		σ_9		σ_{10}		σ_{11}		σ_{12}		σ_{13}		σ_{14}	
	Act.	Pred.	Act.	Pred.	Act.	Pred.	Act.	Pred.	Act.	Pred.	Act.	Pred.	Act.	Pred.
1	270	269	195	189	140	139	105	105	105	102	101	100	93	93
2	295	292	203	207	143	146	107	107	108	105	106	102	98	96
3	171	169	129	130	113	118	91	91	90	89	89	89	87	85
4	245	231	151	148	131	125	94	93	92	92	92	91	89	88
5	276	281	199	193	149	147	115	113	108	106	103	102	97	96
6	310	305	213	211	151	154	115	115	111	109	104	104	100	99
7	191	181	155	155	130	126	99	99	95	92	94	92	90	88
8	252	243	183	173	135	133	101	101	99	95	95	94	92	91
9	202	202	145	154	116	117	100	101	94	96	91	93	87	89
10	260	274	177	185	129	130	104	105	100	101	95	97	92	93
11	352	350	237	239	170	167	115	115	110	110	101	104	99	100
12	199	215	153	158	128	132	91	91	89	87	86	87	83	86
13	193	204	146	146	122	128	96	97	95	96	94	96	88	89
14	214	224	162	170	132	141	107	109	99	102	98	100	93	94
15	213	214	171	170	143	135	105	103	98	99	94	91	90	89
16	217	214	169	170	138	135	102	103	95	99	91	91	88	89
17	221	214	173	170	122	135	100	103	91	99	88	91	88	89
18	218	214	168	170	142	135	104	103	98	99	92	91	89	89
19	215	214	174	170	136	135	102	103	97	99	90	91	89	89
20	210	214	174	170	141	135	104	103	97	99	91	91	90	89

Table 5.60: The first confirmation test for residual stress of dissimilar welding.

Principal stress component	Predicted	Actual	Error %	Absolute Error %
σ_1	236.84	229.23	3.21	3.21
σ_2	168.58	159.17	5.58	5.58
σ_3	132.26	125.31	5.25	5.25
σ_4	103.07	97.4	5.50	5.50
σ_5	98.87	93.61	5.32	5.32
σ_6	92.29	88.29	4.34	4.34
σ_7	89.31	84.63	5.24	5.24
σ_8	259.98	266.26	-2.41	2.41
σ_9	188.02	198.29	-5.46	5.46
σ_{10}	141.67	134.31	5.20	5.20
σ_{11}	109.65	101.9	7.07	7.07
σ_{12}	103.78	99.35	4.27	4.27
σ_{13}	98.80	94.75	4.10	4.10
σ_{14}	94.72	90.85	4.08	4.08
				Average =4.789

Table 5.61: The second confirmation test for residual stress of dissimilar welding.

Principal stress component	Predicted	Actual	Error %	Absolute Error %
σ_1	149.87	157.33	-4.98	4.98
σ_2	117.09	109.97	6.08	6.08
σ_3	97.93	88.14	10.00	10.00
σ_4	79.40	74.34	6.37	6.37
σ_5	79.54	73.62	7.45	7.45
σ_6	73.28	72.84	0.60	0.60
σ_7	70.95	72.76	-2.55	2.55
σ_8	170.72	199.83	-17.05	17.05
σ_9	130.60	139.49	-6.81	6.81
σ_{10}	118.92	102.92	13.46	13.46
σ_{11}	91.13	81.8	10.24	10.24
σ_{12}	88.71	81.71	7.89	7.89
σ_{13}	89.10	84.53	5.12	5.12
σ_{14}	85.14	81.59	4.18	4.18
				Average= 7.341

5.4.2.2 Effect of process parameters on residual stress distribution

As the results indicate, the main effect of all the parameters and most of the quadratic effects are significant terms in all models. It is notable that in all cases the interaction effect between the laser power and welding speed are not significant. In this case the same trend in the parameters effect which was observed in the case of 3 mm AISI304 similar welding has been noticed here too. This parameters effect can be seen in Figs. 5.55 and 5.56. These figures are perturbation plots of the maximum principal stress at the surface of both sides, i.e. σ_1 and σ_8. These kinds of plots help to show how the process parameters are affecting the responses. From these two figures it is demonstrated that as the laser welding process parameters are increased, from their lowest limit to their highest limit, the residual stress component σ_1 and σ_8 would be influenced as follow:

parameter	σ_1	σ_8
S	-36.43%	-28.78%
P	20.11%	21.39%
F	7.3%	5.77%

* The minas sign means that the response decreased.

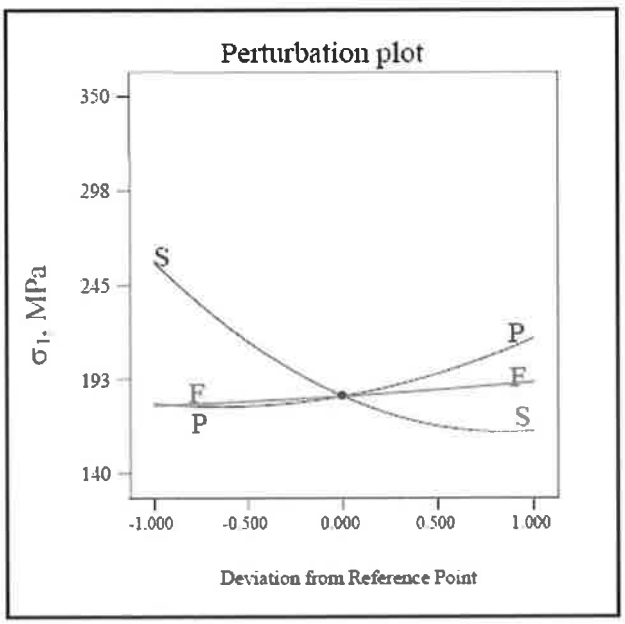

Fig. 5.55: Perturbation plot showing the effect of all parameters on σ_1.

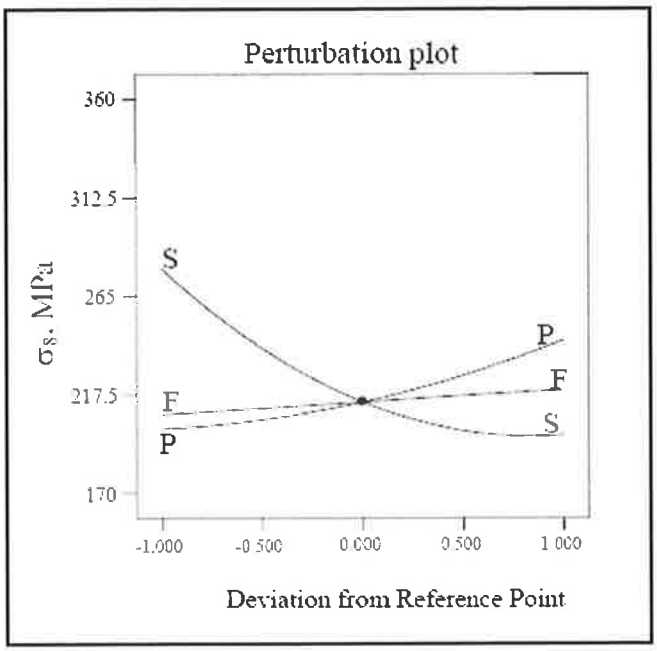

Fig. 5.56: Perturbation plot showing the effect of all parameters on σ_8.

Generally speaking, the rest of the maximum residual stresses at different depths are more or less affected by the process parameters in the same manner as has been seen in the similar welding of 3 mm AISI304. Again, the most risky welding condition at which the welded part is considered unsafe is that which pre-stressed the welded joint with unwanted tensile stress, which would reduce the serving life of the welded component. The most risky condition is slow welding speed which tends to increase the unwanted residual stress sharply. Again, by monitoring the surface residual stress component of both sides this would help to produce a welded joint with the desired properties. If the minimization of the residual stress is the most desired option, then the safe welding condition would be as follows: welding speed of about 65 cm/min, laser power of about 1.14 kW and focal position of about -0.8 mm. However, these conditions which are meant to be safe from a residual stress point of view, could not be considered safe if, for example, the impact strength needs to be of a certain figure. Therefore, a general optimization model should be run to determine the welding conditions which satisfy all the requirements for all responses of interest.

5.4.3 Development of the impact strength and joint operating cost models

The same procedures of statistical testing were performed for these two responses as well. The ANOVA results indicate that for the impact strength model the main effect of the three parameters and the quadratic effect of laser power and welding speed are significant model terms. While for the operating cost model the analysis shows that the main effect of laser power along with the main effect and the quadratic effect of the welding speed are significant model terms. In addition to that, the entire adequacy measures are in reasonable agreement for both models. However, Tables 5.62 and 6.63 summarizes the ANOVA and shows the entire adequacy measures. The final models in terms of coded and actual factors are shown in Eqs. 5.51 to 5.54 for both responses. It was not possible to develop a model to predict the tensile strength for the dissimilar welded joint, due to the fact that all the obtained welded joints had tensile strengths higher than the soft metal (AISI304). Fig. 5.57 is a photograph showing how the fracture always occurs in the stainless steel side of all the tensile test specimens. This agreed with the result obtained by Murti el al. [102].

Table 5.62: ANOVA analysis for the impact strength model of dissimilar welding.

Source	Sum of Squares	DF	Mean squares	F Value	Prob > F	
Model	561.34	5	112.268	41.985	< 0.0001	Significant
P	140.59	1	140.590	52.576	< 0.0001	
S	291.32	1	291.320	108.944	< 0.0001	
F	47.10	1	47.105	17.616	0.0009	
P^2	56.08	1	56.075	20.970	0.0004	
S^2	19.59	1	19.592	7.327	0.0170	
Residual	37.44	14	2.674			
Lack of Fit	21.66	9	2.407	0.763	0.6596	Not significant
Pure Error	15.78	5	3.156			
Cor Total	598.78	19				
R-Squared = 0.9375				Adj. R-Squared = 0.9151		
Pred. R-Squared = 0.8569				Adeq. Precision = 24.56		

Table 5.63: ANOVA analysis for the operating cost model of dissimilar welding.

Source	Sum of Squares	DF	Mean squares	F Value	Prob > F	
Model	0.1240	3	0.04134	526.970	< 0.0001	Significant
P	0.0004	1	0.00038	4.862	0.0424	
S	0.1110	1	0.11102	1415.359	< 0.0001	
S^2	0.0126	1	0.01260	160.690	< 0.0001	
Residual	0.0013	16	0.00008			
Lack of Fit	0.0013	11	0.00011			
Cor Total	0.1253	19				
R-Squared = 0.9375				Adj. R-Squared = 0.9151		
Pred. R-Squared = 0.8569				Adeq. Precision = 76.57		

$$\text{Impact strength} = 29.62 + 3.21\,P - 4.62\,S + 1.86\,F + 1.96\,P^2 - 1.16\,S^2 \quad (5.51)$$

$$\text{Joint operating cost} = 0.25 + 0.0053\,P - 0.090\,S + 0.029\,S^2 \quad (5.52)$$

$$\text{Impact strength} = 248.48 - 373.13\,P + 0.208\,S + 6.19\,F + 162.21\,P^2 - 0.005S^2 \quad (5.53)$$

$$\text{Joint operating cost} = 0.816 + 0.048\,P - 0.019\,S + 0.00013\,S^2 \quad (5.54)$$

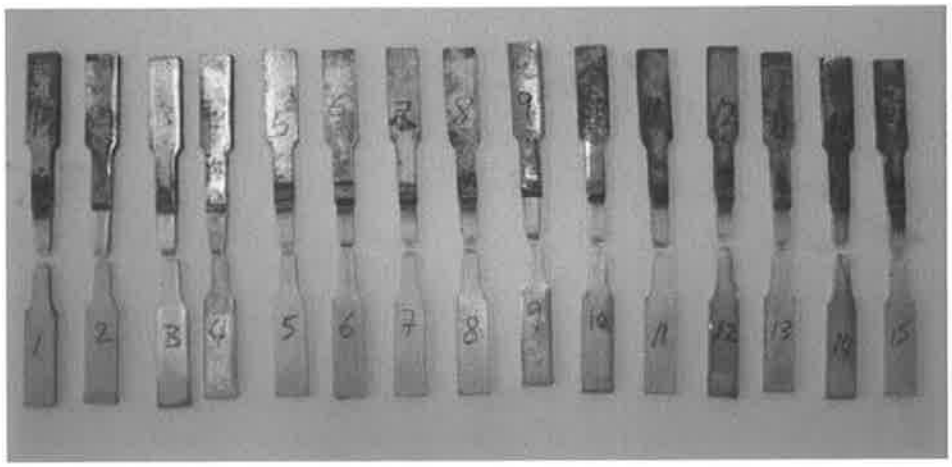

Fig. 5.57: Tensile strength specimens for dissimilar welding after testing.

5.4.2.1 Validation of the models developed

The mathematical models are valid to describe both the impact strength and operating cost as shown in Fig. 5.58 a-b. These figures indicate that in the above mathematical models there is a good agreement between the measured and estimated values of the above mentioned responses. In order to further verify the model developed, three confirmation welding experiments were carried out using new test conditions, selected from the optimal results shown in chapter 6, Tables 6.11, 6.12 and 6.13. These optimal conditions are within the experimental domain of this experiment. A comparison between the experimentally recorded and the predicted responses calculated by the models developed were made for both responses. The results of this comparison are presented in Table 5.64. It is obvious that the models can successfully describe the responses within the factors domain, as the maximum error predicted is 8.696 %, which indicates good agreement.

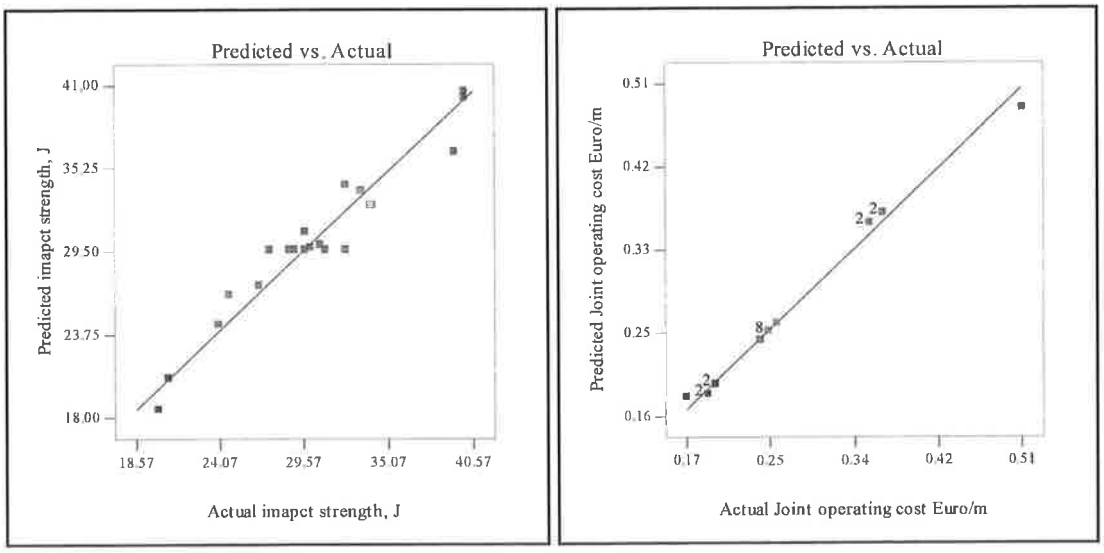

(a) (b)

Fig. 5.58: Scatter diagram for (a) Impact strength and (b) operating cost.

Table 5.64: Confirmation tests for impact strength and operating cost models.

Exp. No.	P	S	F		Impact strength, J	Operating cost, €/m
1	1.35	45.87	-0.2	Actual	40	0.2786
				Predicted	38	0.2814
				Error %	4.202	-1.005
2	1.13	49.39	-0.2	Actual	33	0.2486
				Predicted	30	0.2475
				Error %	8.163	0.442
3	1.14	65	-0.8	Actual	23	0.1893
				Predicted	21	0.1834
				Error %	8.696	3.117

5.4.2.2 Effect of process parameters on the impact strength and joint cost

In this typical dissimilar welding experiment a relatively hard metal is welded to a softer one. The low carbon steel has a tensile strength and impact strength of 840 MPa and 20 J respectively and for the stainless steel they are 712 MPa and 49 J respectively. For this reason it is important to produce a laser welded joint with mechanical properties better than those of both base metals. It is clear from the result that all the considered laser process parameters have a significant effect on the impact strength of dissimilar welds. Also, in this experiment no interaction effect has been found. Fig. 5.59 is a perturbation plot presenting how the process parameters affect the impact strength of the welds. From this figure it is evident that as the welding speed increases the impact strength decreases, due to the fact that welding with a high welding speed induces less heat into the metal which would make the weld zone harder and more brittle due to the high cooling rate achieved. If the laser power increases and a focused laser beam is being used, a slight improvement in the impact strength would occur. Since as the laser power increases and the laser beam is focused this would increase the power density which would result in more heat input and raise the weld pool temperature. Fig. 5.60 is a contours graph showing the effect of laser power and welding speed on the impact strength of the dissimilar joint.

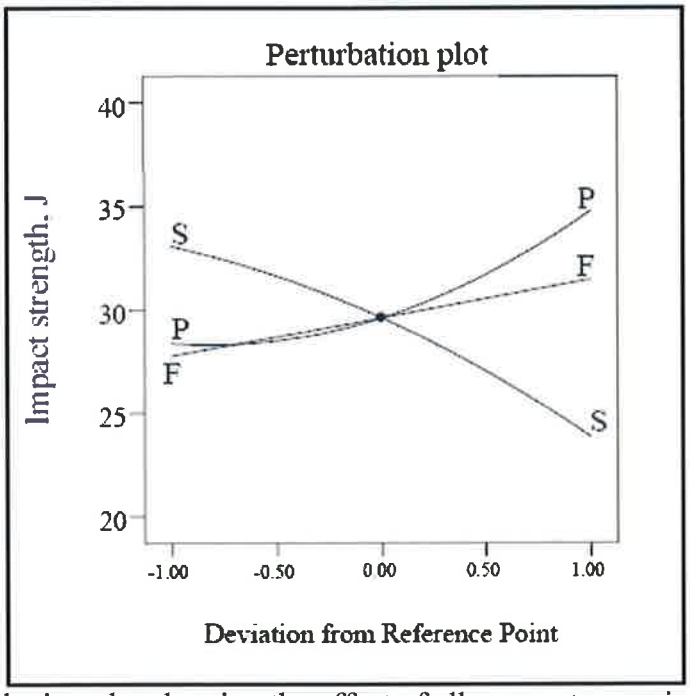

Fig. 5.59: Perturbation plot showing the effect of all parameters on impact strength of dissimilar welding.

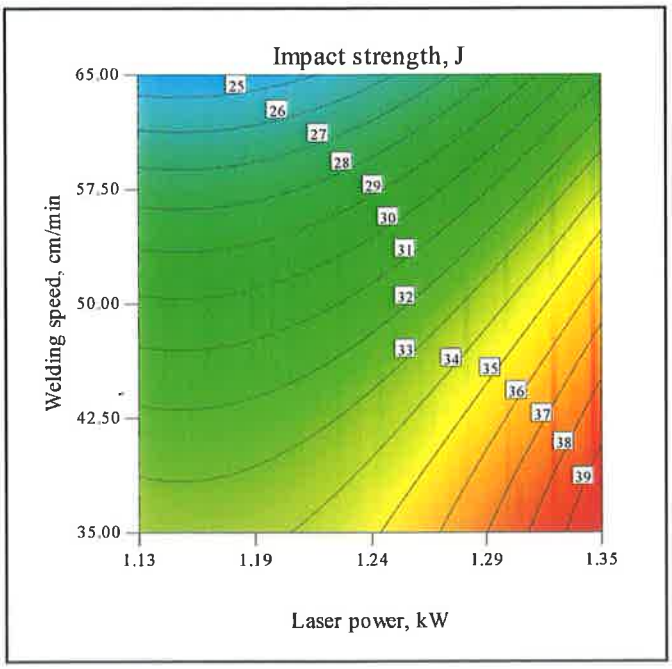

Fig. 5.60: Contours graph showing the effect of S and P on impact strength at F = -0.2 mm.

5.4.3 Microstructure and microhardness study for dissimilar welding

The base metal microstructure of the AISI304 consists of a single phase of equiaxial grains while the microstructure of the base metal of AISI1016 consists of a two phase structure of ferrite and pearlite as shown in Fig. 5.61 a and b. The average microhardness of both AISI304 and AISI1016 are 241 and 276 Hv respectively. Fig. 5.61 c and d shows the microstructure of the interface between the WZ, HAZ and BM for both sides of the joint. It is clear that the microstructure of the HAZ on the stainless steel side exhibits coarse columnar dendrites, while a mixture of coarse pearlite and ferrite was observed on the other side of the joint. It is evident from Fig. 5.62 a-c that the microstructure of the dissimilar weldment consists of equiaxial grains and the grain size becomes coarser as the heat input increases. Fig. 5.63 shows the distribution of the microhardness along the surface of the dissimilar weld for three samples with different heat inputs. It is evident from this figure that the highest microhardness is achieved for the weldment near the AISI1016 side in sample no.12 which has the minimum heat input. Also, the microhardness of the fusion zone is always higher than that of the HAZ or even the base metal in all samples, and it is always higher in the AISI1016 side in all samples due to the fact that this alloy contains small percentage of carbon which tends to form a relatively hard phase (i.e. pearlite).

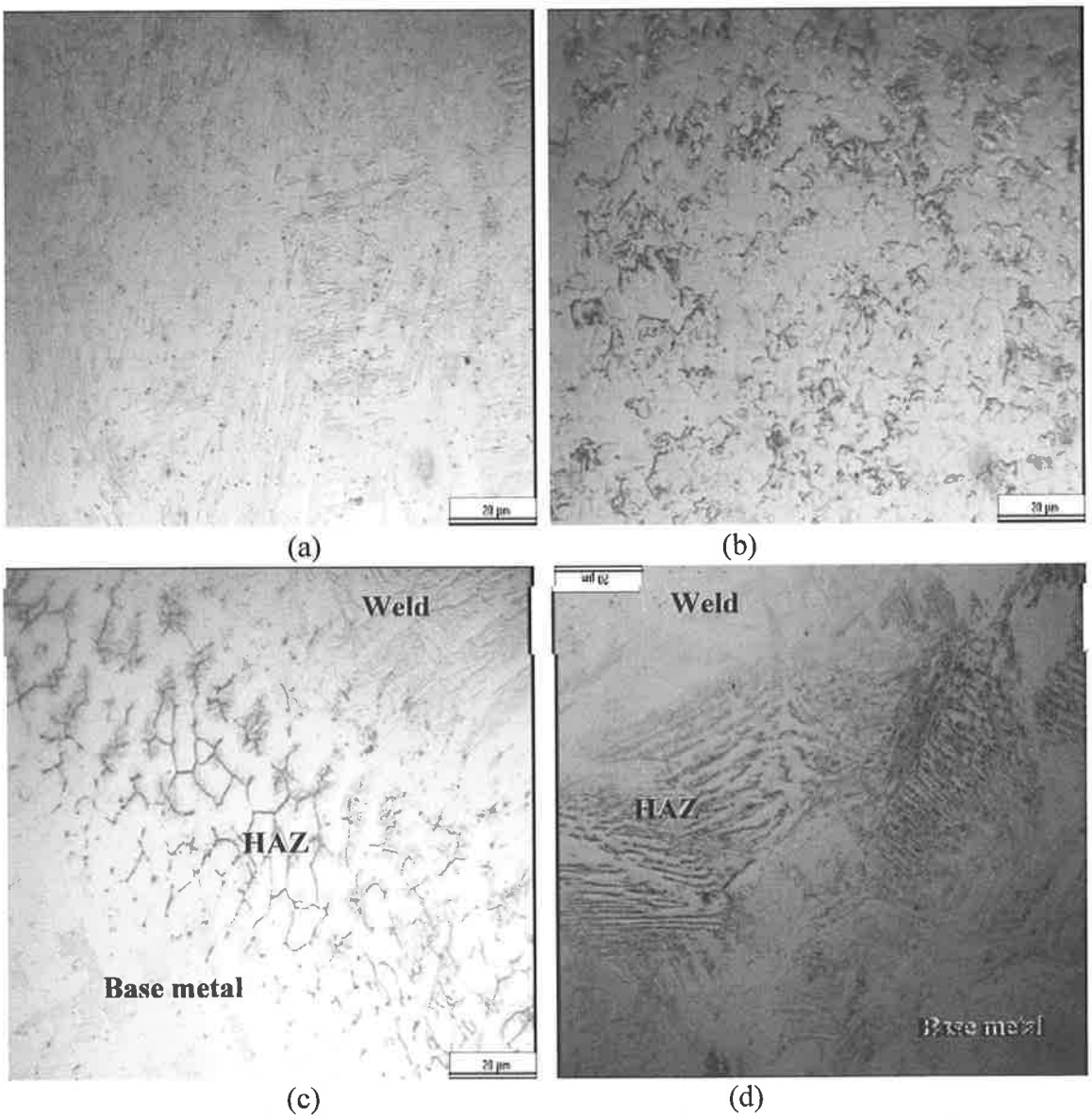

Fig. 5.61: Micrographs showing the microstructure of (a) base metal of AISI304, (b) base metal of AISI1016, (c) weld, HAZ and base metal of AISI304 side and (d) weld, HAZ and base metal of AISI1016 side.

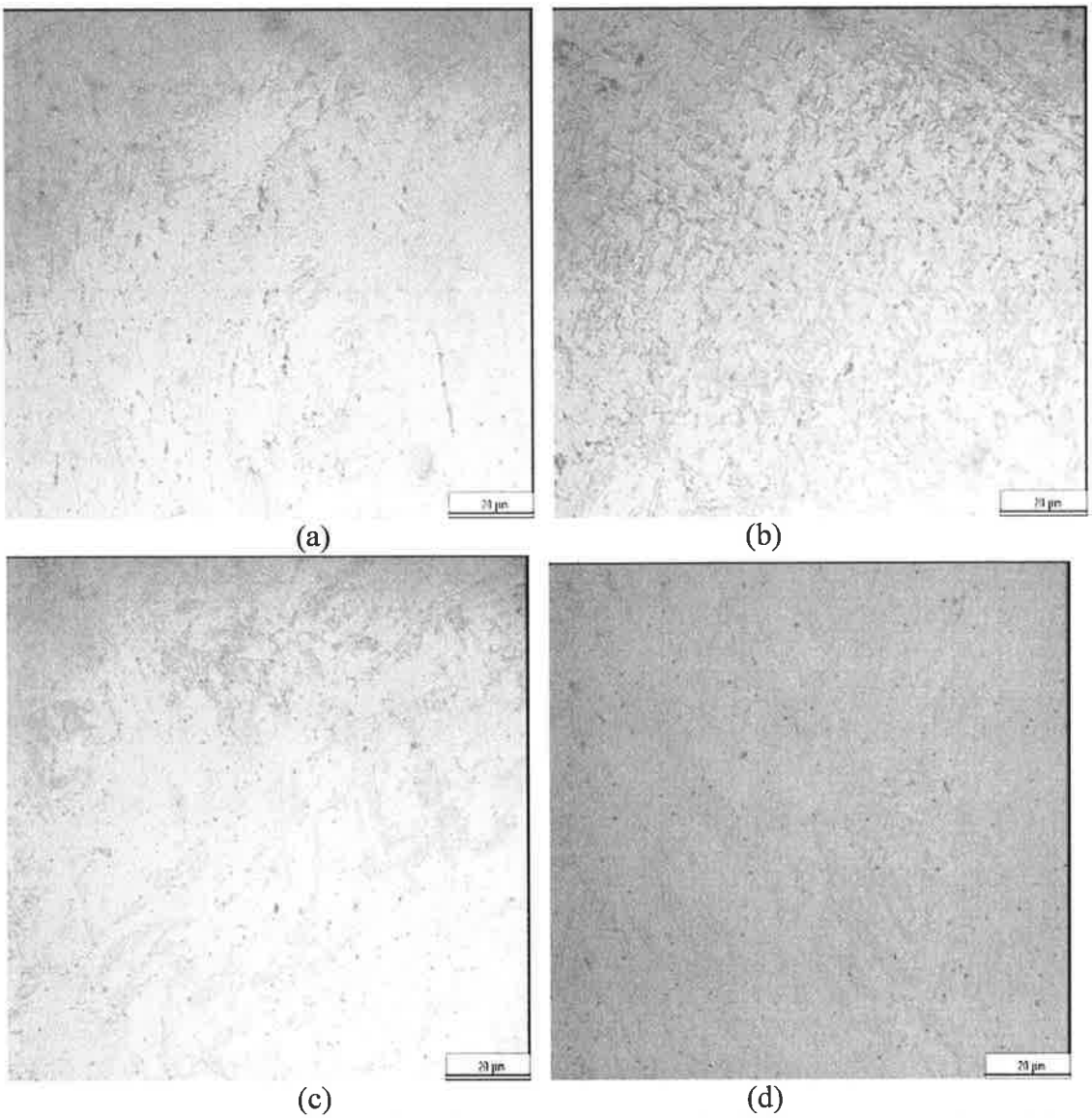

Fig. 5.62: Micrographs revealing the microstructure of AISI304 1 mm lab joint (a) sample No. 12, (b) sample No. 9, (c) sample No. 15 and (d) sample No. 11.

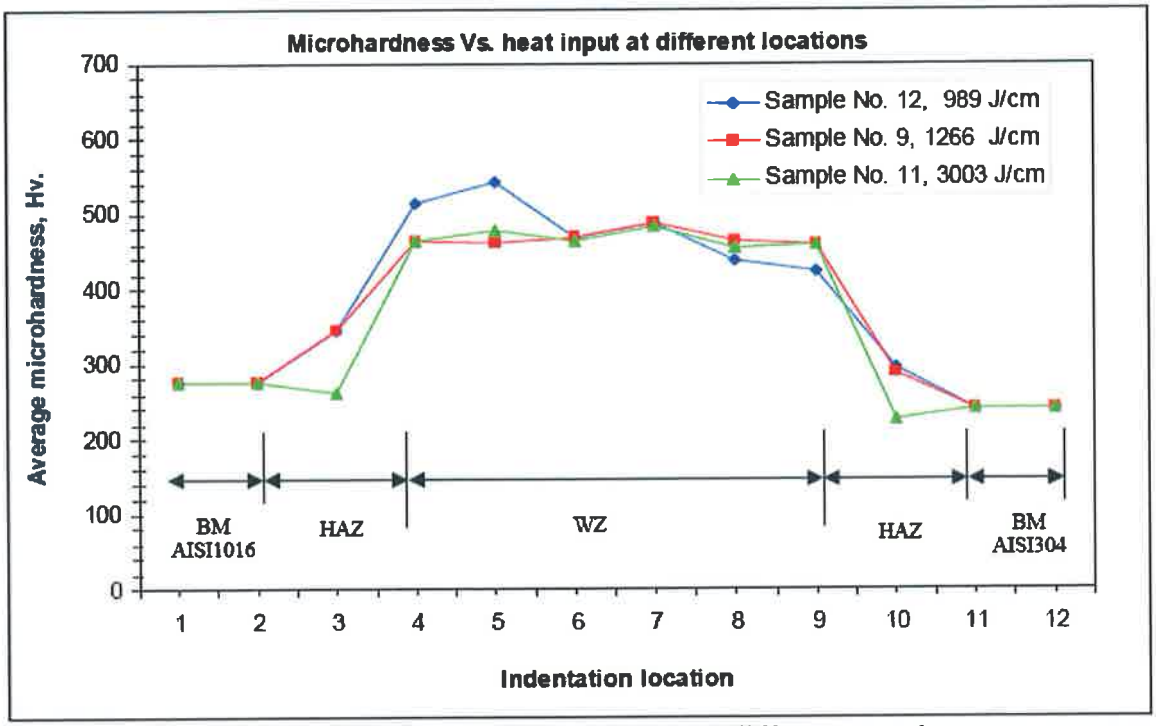

Fig. 5.63: Microhardness Vs. Heat Input for different samples.

CHAPTER VI

OPTIMIZATION

6. OPTIMIZATION

6.1 Medium Carbon Steel AISI1045

6.1.1 Numerical Optimization

In the numerical optimization of this material, two criteria were implemented as presented in Table 6.1. The difference between the two criteria is the achieved depth of penetration, which was set to 5 mm in the first criterion and 2.5 mm in the second criterion. However, constraining the penetration to 2.5 mm in the second criterion means that a doubled-sided butt joint is required in order to achieve a sound weldment. Also, the impact and NTS strength have to be omitted, because their values would represent the mechanical properties of half penetration, which will not reflect the true mechanical properties after the application of double sided butt joint. Table 6.2 presents the optimal welding condition at which the full penetration would be achieved. However, to meet the first criterion the laser power has to be set to its highest level with welding speed ranged between 35.3 and 36.74 cm/min, while the laser beam has to be set to F = 0 mm. Implementing these welding conditions would result in excellent mechanical properties of the welds, as presented in Table 6.2. However, some responses such as Width of FZ and Width of HAZ would be higher due to the high heat input which resulted from using a high laser power and low speed. Also, operating cost of about € 0.37/m could be achieved. This represents a reduction of 14.3 % when compared with the previous maximum operating cost of €0.4316/m.

The optimal welding conditions that meet the requirements of the second criterion are shown in Table 6.3. It is clear that in order to produce the optimal weld the laser power has to be set at the lowest level, the welding speed set between 67.1 and 69.95 cm/min and the focus point position set between -1.87 to -1.69 mm. These welding conditions would result in a partial penetration and they could yield the desired mechanical properties if double sided butt jointing is carried out. Furthermore, by applying the optimal welding conditions that comply with the second criterion, the weld bead width of FZ and HAZ would be minimized by 43.2 % and 50.1 % respectively. Although the heat was introduced twice, with an average total heat input for the two passes of 1679 J/cm, it is still less than the average heat input of 1934 J/cm which resulted from the first optimization criterion. This

reduction in the heat input would result in less distortion and greater improvement of the weld quality. As the welding speed was doubled, the welding operating cost would be significantly reduced; the weld joint operating cost per meter could be minimized by 16.6 % as compared to the maximum operating cost of €0.4316/m. In contrast between the two optimization criteria, it is clear that the difference between the operation costs of both criteria is about 2 % in favour of the second criterion.

6.1.2 Graphical Optimization

In the graphical optimization, the range of each response has been selected from the numerical optimization results. The ranges obtained from the two criteria which were proposed in the numerical optimization were brought into the graphical optimization as well. In the first criterion, the responses can be described as follows: heat input of (1740 - 1950 J/cm), penetration of (4.89 - 5 mm), Width of FZ of (2.5 – 2.7 mm), width of HAZ of (0.6 - 0.8 mm), impact strength of (70 - 77 J), NTS of (400 - 438 MPa) and operating cost of (0.33 - 0.39 €/m). While for the second criterion the responses values are: heat input of (840 - 930 J/cm), penetration of (2.5 - 3 mm), Width of FZ of (1.4 – 2.1 mm), width of HAZ of (0.3 - 0.43 mm) and operating cost of (0.17 - 0.2 €/m/side). Figs. 6.1 and 6.2 show the green area which is the region that meets the first and the second criterion respectively.

Table 6.1: Optimization criteria and importance for 5 mm AISI1045.

Name	First criteria	Second criteria	Importance
Laser power	Minimize	Minimize	4
Welding speed	Maximize	Maximize	4
Focused position	Is in range	Is in range	3
Heat input	Minimize	Minimize	5
Penetration	Is target = 5*	Is target = 2.5**	5
Width	Minimize	Minimize	1
Width HAZ	Minimize	Minimize	1
Impact strength	Maximize	Maximize	3
NTS	Maximize	Maximize	3
Joint cost	Minimize	Minimize	5

* The range has been changed to (4.99-5.1) and ** the range was (2.49-2.51)

Table 6.2: Optimal solutions for the first criterion for 5 mm AISI1045.

No	LP	S	F	Heat input	P	W	W_{HAZ}	Impact strength	NTS	Joint cost	D
1	1.41	36.26	0	1924.9	5.00	2.6476	0.7734	74	417	0.3664	0.3807
2	1.41	36.11	0	1930.7	5.00	2.6448	0.7740	74	418	0.3677	0.3805
3	1.42	36.53	0	1914.2	5.00	2.6530	0.7720	74	417	0.3639	0.3801
4	1.41	35.81	0	1942.9	5.00	2.6385	0.7755	73	418	0.3705	0.3792
5	1.42	36.74	0	1905.9	5.00	2.6570	0.7710	75	417	0.3621	0.3785
6	1.41	35.64	0	1949.8	5.00	2.6350	0.7762	73	418	0.3720	0.3780
7	1.41	35.9	-0.01	1940.5	5.00	2.6426	0.7759	74	419	0.3696	0.3767
8	1.41	36.04	-0.01	1935.3	5.00	2.6457	0.7754	74	419	0.3684	0.3765
9	1.41	35.3	0	1963.6	5.00	2.6278	0.7777	73	419	0.3752	0.3748
10	1.41	36.1	0	1933.0	5.00	2.6472	0.7754	74	418	0.3679	0.3738

Table 6.3: Optimal solutions for the second criterion for 5 mm AISI1045.

No.	LP	S	F	Heat input	P	W	W_{HAZ}	Joint cost	D
1	1.2	68.78	-1.76	838.3	2.50	1.4877	0.3864	0.1797	0.6568
2	1.2	69.05	-1.75	837.0	2.50	1.4657	0.3857	0.1793	0.6568
3	1.2	68.49	-1.78	839.8	2.50	1.5113	0.3871	0.1801	0.6568
4	1.2	69.42	-1.73	835.5	2.50	1.4359	0.3848	0.1789	0.6567
5	1.2	69.68	-1.71	834.4	2.50	1.4149	0.3842	0.1785	0.6565
6	1.2	67.83	-1.82	843.5	2.50	1.5659	0.3887	0.1811	0.6565
7	1.2	68.08	-1.81	842.1	2.50	1.5456	0.3880	0.1807	0.6565
8	1.2	67.67	-1.83	844.5	2.50	1.5796	0.3891	0.1814	0.6564
9	1.2	69.95	-1.69	833.4	2.50	1.3930	0.3836	0.1782	0.6563
10	1.2	67.1	-1.87	848.2	2.50	1.6265	0.3904	0.1823	0.6559

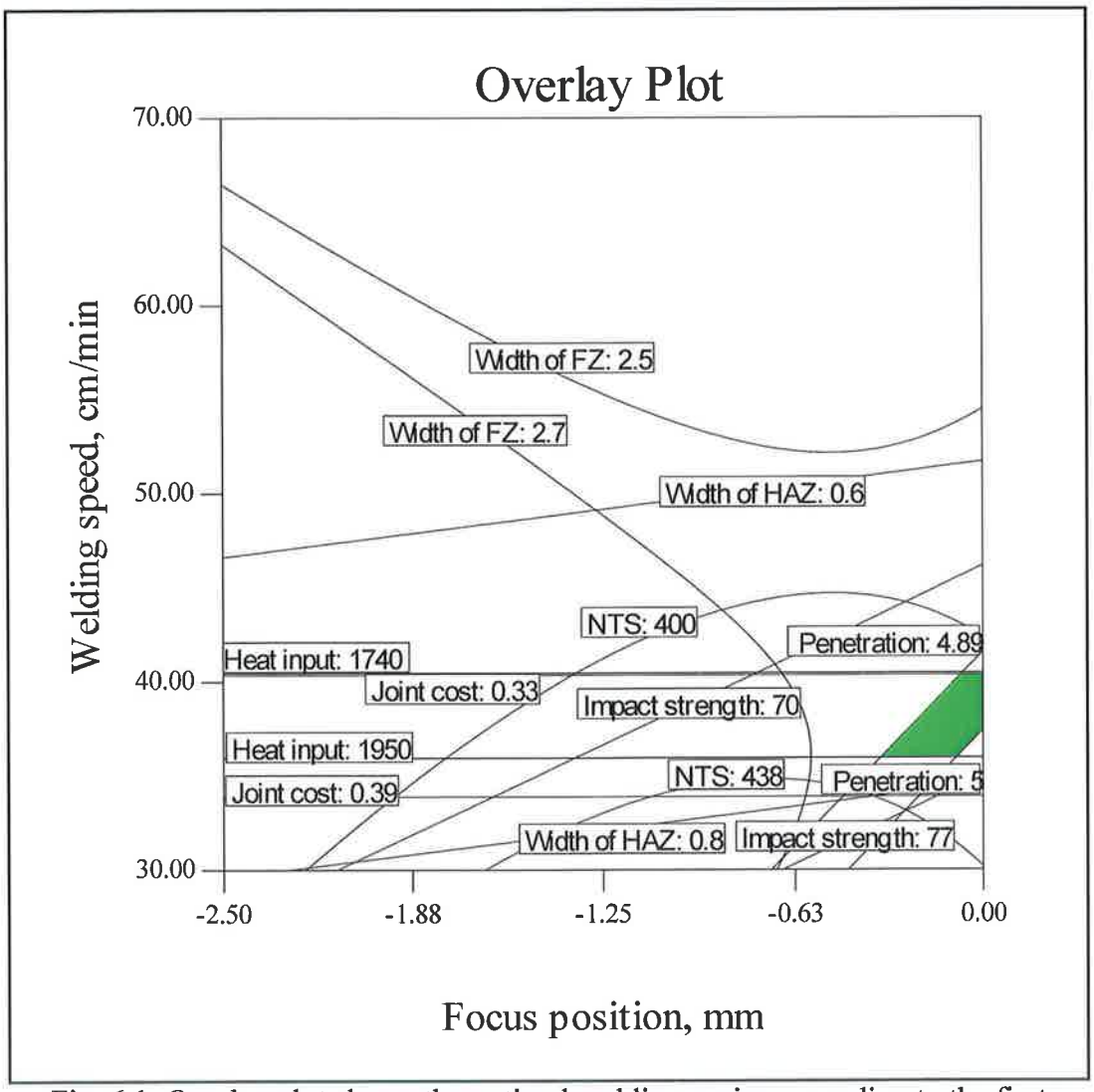

Fig. 6.1: Overlay plot shows the optimal welding region according to the first criterion in the graphical optimization at p= 1.42 kW for 5 mm AISI1045.

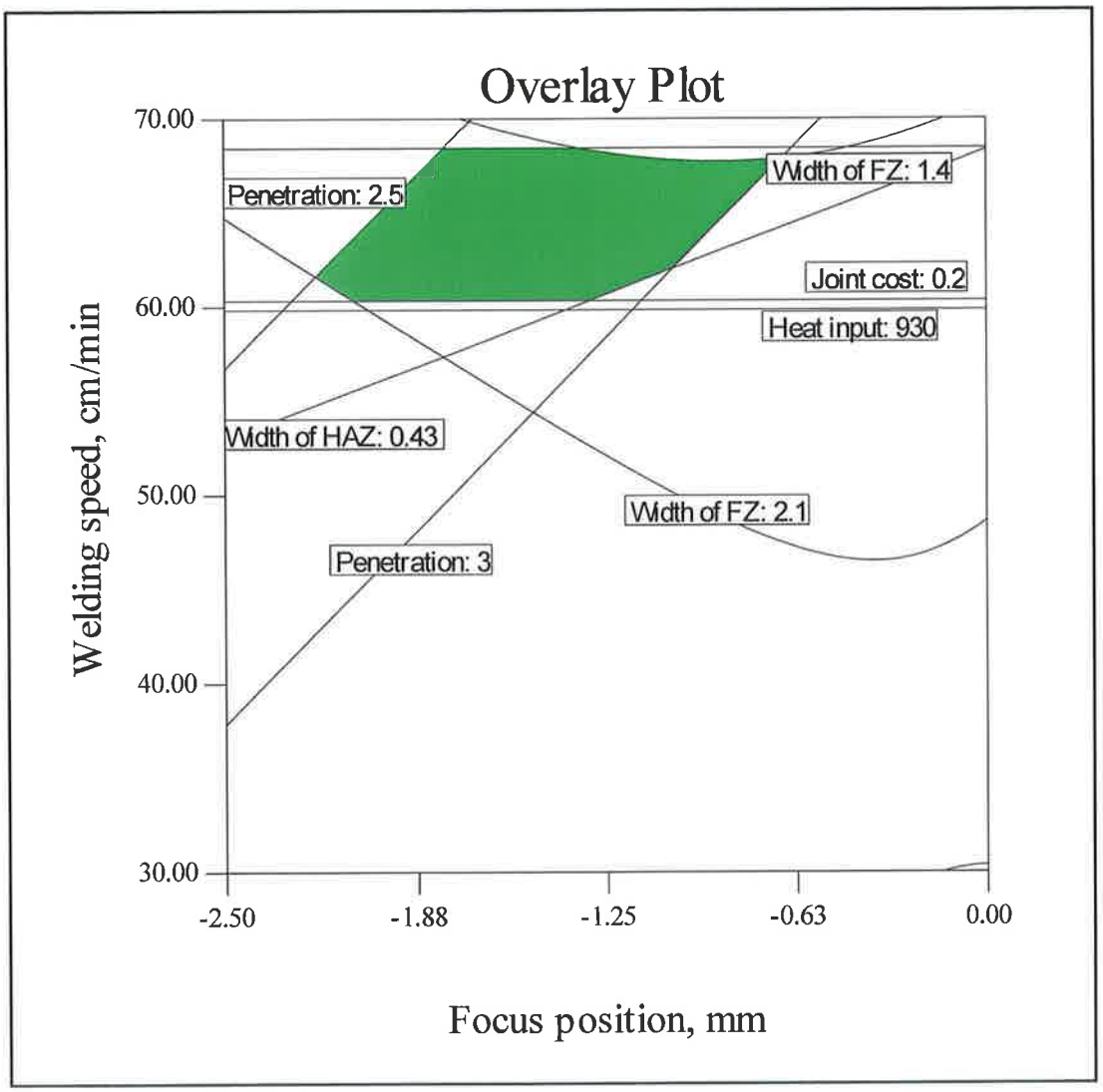

Fig. 6.2: Overlay plot shows the optimal welding region according to the second criterion in the graphical optimization at p = 1.2 kW for 5 mm AISI1045.

6.2 Stainless Steel AISI304 3 mm

6.2.1 Numerical optimization

The issue of linking between the strength and toughness must be addressed as any increase in the strength is usually reflected as deterioration in toughness. As a consequence both strength and toughness are usually studied together. On balance, and based on the discussion in the previous chapter it is required to run an optimization technique to find out the optimal welding condition at which the desirable mechanical properties of the welded joint can be achieved. In fact, once the models have been developed and checked for adequacy, the optimization criteria can be set to find out the optimum welding conditions. In this investigation two criteria were implemented to produce sound weldment at relatively low operating cost. The first criterion is to reach maximum tensile strength and impact strength with no limitation on either the process parameters or the responses. While, in the second criterion, the goal was to reach maximum tensile and impact strength at relatively low operating cost by using maximum welding speed and minimum heat input. Table 6.4 summarizes these two criteria and Tables 6.5 and 6.6 present the optimal solution based on the two optimization criteria as determined by Design-Expert software.

The optimization results clearly demonstrate that, whatever the optimization criteria, the laser power has to be around its centre limit of 1.2 kW to achieve the maximum tensile and impact strength. This result supports the discussion made in the previous chapter on the effect of laser power on the responses. Table 6.5 presents the optimal welding conditions according to the first criterion which would lead to maximum tensile and impact strength of about 677 MPa and 47 J respectively at high joint operating cost of about € 0.36 per meter. But if the joint cost is to be reduced much further by approximately 43.3 %, and acceptable tensile and impact strengths are to be maintained, then the welding speed has to be maximized to its highest value and a focus position of -0.8 mm has to be used instead of -0.2 mm. In this case, the tensile and impact strength would be about 670 MPa and 39 J respectively as can be seen in Table 6.6.

Table 6.4 Optimization criteria used for 3 mm AISI304.

Parameter or Response	Limits		Importance	First criterion	Second criterion
	Lower	Upper			
Laser power	1.1	1.3	3	is in range	is in range
Welding speed	35	60	3	is in range	maximize
Focus position	-0.8	-0.2	3	is in range	is in range
σ_{11}	142	309	5	is in range	minimize
Tensile Strength	529	692	5	maximize	maximize
Impact Strength	27	46.67	5	maximize	maximize
Joint cost per meter	0.1816	0.4694	3	is in range	minimize
Nominal Heat input	1051	2719	3	is in range	is in range
Front Width	2.318	3.704	3	is in range	is in range
Back width	0.494	2.854	3	is in range	is in range
Weld pool area	4.709	10.027	3	is in range	is in range

6.2.2 Graphical optimization

It is obvious that the graphical optimization allows visual selection of the optimum welding conditions according to certain criterion. Graphical optimization results in plots called overlay plots. These plots are extremely practical for quick technical use at the workshop to choose the values of the welding parameters to achieve certain response values for this type of material. The green/shaded areas on the overlay plots Fig. 6.3 and 6.4 are the regions that meet the proposed criteria.

Table 6.5: Optimal solution as obtained by Design-Expert based on the first criterion for 3 mm AISI304.

No.	P	S	F	σ_{11}	Tensile strength	Impact strength	Cost	Heat input	W	BW	A	Desirability
1	1.2	35	-0.2	264.53	677.052	46.750	0.3618	2095	3.245	2.083	8.677	0.952
2	1.2	35	-0.2	264.18	677.05	46.73	0.3617	2090	3.241	2.080	8.666	0.952
3	1.2	35	-0.2	264.46	677.04	46.79	0.3618	2094	3.244	2.082	8.675	0.952
4	1.2	35	-0.2	264.03	677.04	46.69	0.3616	2088	3.239	2.078	8.660	0.952
5	1.2	35	-0.2	264.57	677.03	46.82	0.3618	2095	3.245	2.083	8.679	0.952
6	1.2	35	-0.2	264.04	677.01	46.75	0.3617	2092	3.244	2.079	8.671	0.952
7	1.2	35	-0.2	263.80	677.00	46.69	0.3616	2089	3.241	2.077	8.663	0.952
8	1.2	35	-0.2	264.78	676.99	46.86	0.3619	2098	3.247	2.085	8.685	0.952
9	1.2	35.02	-0.2	263.80	676.98	46.67	0.3614	2086	3.238	2.076	8.653	0.952
10	1.21	38.85	-0.2	282.67	667.482	46.500	0.3267	1903	3.161	1.779	7.931	0.917

Table 6.6: Optimal solution as obtained by Design-Expert based on the second criterion for 3 mm AISI304.

No.	P	S	F	σ_{11}	Tensile strength	Impact strength	Cost	Heat input	W	BW	A	Desirability
1	1.21	60	-0.76	154.92	668.43	39.47	0.2048	1194	2.870	0.840	5.950	0.837
2	1.21	60	-0.78	155.09	669.78	39.37	0.2048	1193	2.875	0.847	5.947	0.837
3	1.21	60	-0.77	155.01	669.28	39.40	0.2048	1193	2.873	0.845	5.948	0.837
4	1.21	60	-0.78	155.11	670.10	39.34	0.2047	1192	2.876	0.849	5.946	0.837
5	1.21	60	-0.79	155.16	670.43	39.31	0.2047	1192	2.878	0.851	5.946	0.837
6	1.21	60	-0.78	155.24	670.13	39.35	0.2048	1193	2.878	0.850	5.949	0.837
7	1.21	60	-0.79	155.26	670.61	39.31	0.2047	1193	2.879	0.853	5.947	0.837
8	1.21	60	-0.77	154.84	668.62	39.45	0.2048	1193	2.869	0.840	5.947	0.837
9	1.21	60	-0.78	154.94	669.84	39.35	0.2047	1192	2.874	0.846	5.944	0.837
10	1.22	60	-0.8	155.26	670.433	39.401	0.2052	1201	2.896	0.865	5.975	0.814

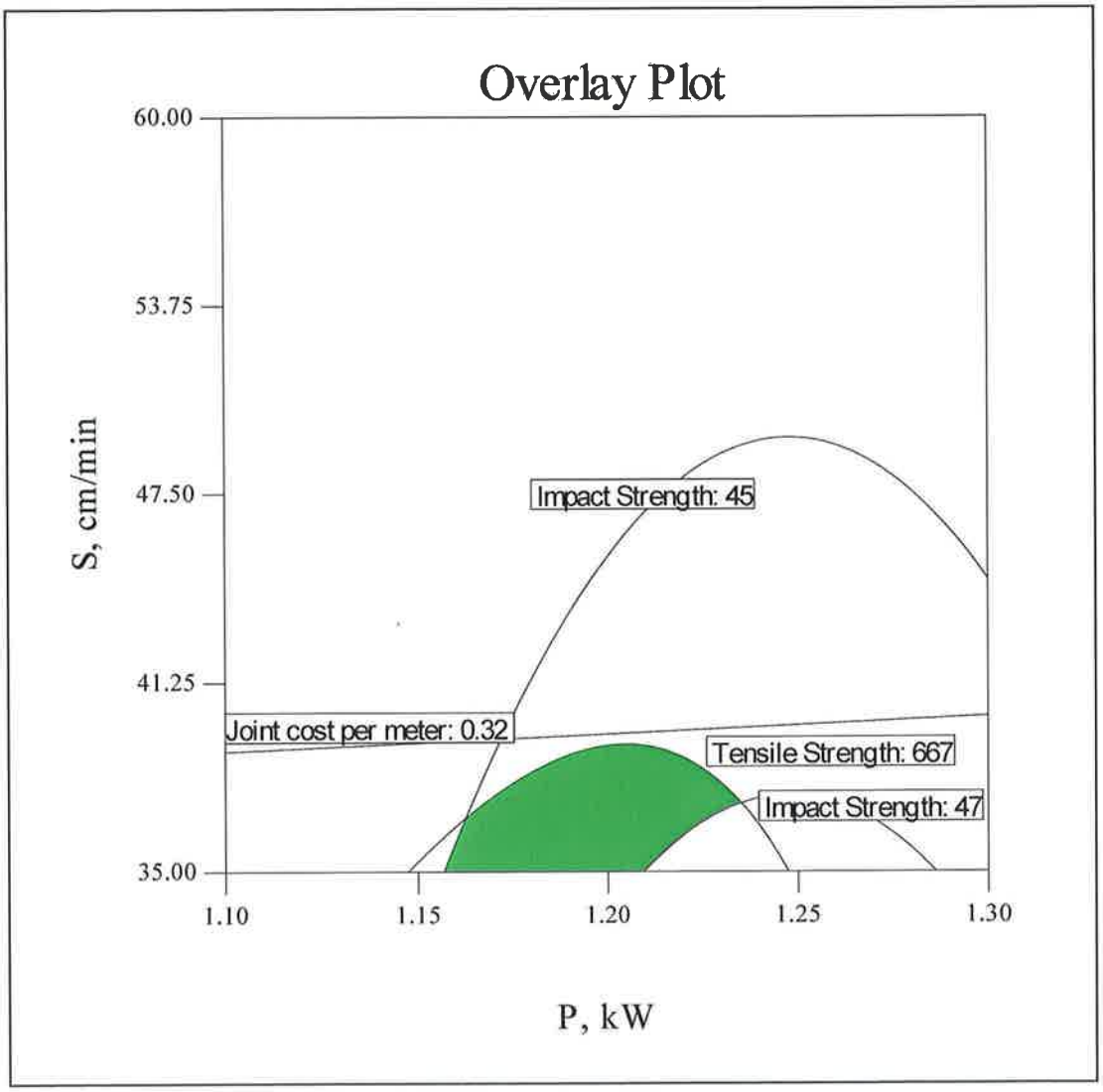

Fig. 6.3: Overlay plot shows the region of optimal welding condition based on the first criterion at F = -0.2 mm for 3 mm AISI304.

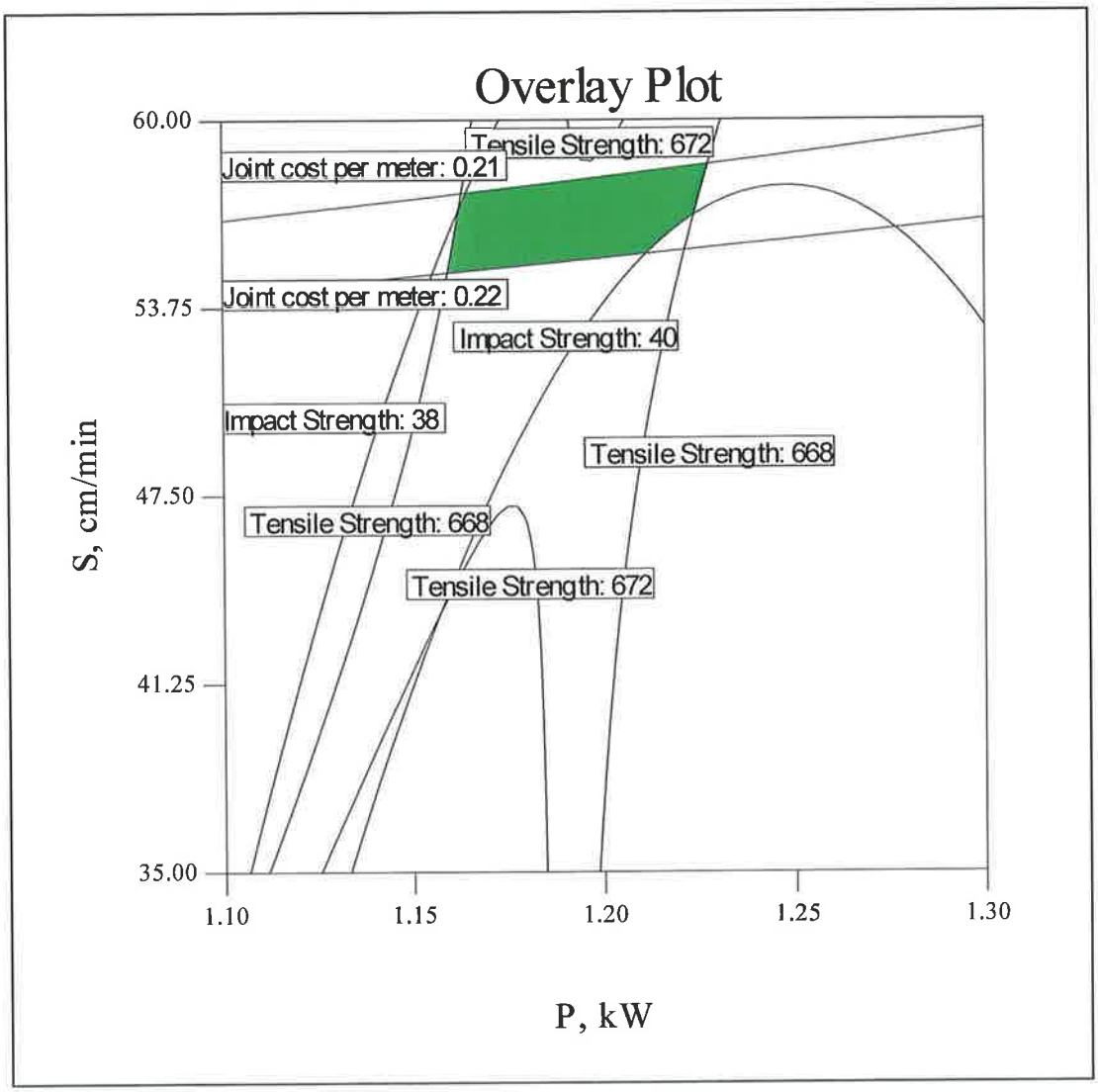

Fig. 6.4: Overlay plot shows the region of optimal welding condition based on the second criterion at F = -0.8 mm for 3 mm AISI304.

6.3 Stainless Steel AISI304 1 mm

6.3.1 Numerical optimization

Lap seam joint is an important joint configuration and it has quite a lot of applications in many industry [11]. For this joint configuration two different optimization criteria were implemented to achieve sound welds at a competitive cost as summarized in Table 6.7. The first optimization criterion is set to reach maximum failure load by maximizing half penetration width and minimizing both the heat input and joint cost. Whilst, in the second optimization criterion the aim was to produce a cost effective lap joint with the highest possible failure load by maximizing both welding speed and half penetration width and minimizing the following: laser power, heat input and joint operating cost. The optimization result of both criteria revealed that a laser power of 1.1 kW and focus point position of -1.2 mm. A welding speed ranged between 95.5 and 98.5 cm/min is optimal. Table 6.8 shows the optimal welding conditions based on the first criterion. It is demonstrated from the first optimization criterion that a failure load of about 8.434 kN would be achieved at an operating cost of €0.1282/m. If these optimal settings were used, a slight loss in the failure load of 6.2% would occur followed by a significant drop in the operating cost of about 49.1%, as compared with the previous operating cost of €0.2520/m which lead to a failure load of about 8.991 kN. In order to achieve a greater reduction in the operating cost the second optimization criterion was introduced which necessitates the welding speed to be increased to between 110.42 and 113.52 cm/min. It is evident from the result of this criterion that a failure load of about 8.119 kN would be reached at an operating cost of €0.1073/m. In this case the percentage of the reduction in the failure load of around 9.7% would take place followed by a significant reduction in the operating cost of about 57.4% as compared with the same setting. In comparison between the two optimization criteria, it is clear that by using the second criterion the percentage of reduction in the failure load would be around 3.73% with a further saving in the operating cost of about 16.30%.

6.3.2 Graphical optimization

As mentioned earlier the range of each response has been chosen from the numerical optimization results in Tables 6.8 and 6.9. Figs. 6.5 and 6.6 show green areas which are the regions that comply with the first and second criteria respectively.

Table 6.7 Optimization criteria used for 1 mm AISI304.

Parameter or Response	Limits		Importance	First criterion	Second criterion
	Lower	Upper			
Laser power	1.1	1.35	3	is in range	minimize
Welding speed	70	130	3	is in range	maximize
Focus position	-1.2	-0.3	3	is in range	is in range
Failure load, kN	6.869	9.082	5	maximize	maximize
Heat input	489	1483	3	minimize	minimize
Front width	1.620	2.196	3	is in range	is in range
Back width	0.568	1.399	3	is in range	is in range
Half penetration width	0.712	1.84	3	maximize	maximize
Joint operating cost	0.0831	0.2522	3	minimize	minimize

Table 6.8: Optimal solution as obtained by Design-Expert based on the first criterion for lap-joint.

No.	P, kW	S, cm/min	F, mm	Failure load, kN	NH, J/cm	W, mm	BW, mm	HW, mm	Joint operating cost, €/m	Desirability
1	1.1	97.43	-1.2	8.393	672.300	2.061	0.765	1.357	0.1251	0.6683
2	1.1	97.67	-1.2	8.388	670.254	2.060	0.763	1.354	0.1248	0.6683
3	1.1	97.15	-1.2	8.399	674.712	2.063	0.767	1.360	0.1256	0.6682
4	1.1	96.84	-1.2	8.405	677.296	2.064	0.769	1.363	0.1261	0.6682
5	1.1	98.19	-1.2	8.377	665.935	2.057	0.760	1.348	0.1240	0.6682
6	1.1	98.5	-1.2	8.370	663.323	2.056	0.758	1.345	0.1235	0.6682
7	1.1	96.44	-1.2	8.414	680.814	2.066	0.772	1.368	0.1267	0.6681
8	1.1	97.96	-1.2	8.381	667.790	2.059	0.761	1.350	0.1243	0.6680
9	1.1	95.94	-1.2	8.424	685.184	2.069	0.775	1.373	0.1275	0.6680
10	1.1	95.5	-1.2	8.434	689.000	2.071	0.778	1.378	0.1282	0.6679

Table 6.9: Optimal solution as obtained by Design-Expert based on the second criterion for lap-joint.

No.	P, kW	S, cm/min	F, mm	Failure load, kN	NH, J/cm	W, mm	BW, mm	HW, mm	Joint operating cost, €/m	Desirability
1	1.1	111.81	-1.2	8.090	570.093	1.980	0.689	1.196	0.1057	0.6926
2	1.1	111.45	-1.2	8.097	572.161	1.982	0.690	1.200	0.1062	0.6926
3	1.1	112.22	-1.2	8.081	567.721	1.977	0.687	1.191	0.1053	0.6926
4	1.1	111.21	-1.2	8.102	573.537	1.984	0.691	1.203	0.1064	0.6926
5	1.1	112.79	-1.2	8.069	564.534	1.974	0.685	1.185	0.1047	0.6925
6	1.1	110.66	-1.2	8.114	576.776	1.987	0.693	1.209	0.1070	0.6925
7	1.1	110.42	-1.2	8.119	578.255	1.988	0.694	1.211	0.1073	0.6924
8	1.1	113.52	-1.2	8.054	560.544	1.969	0.682	1.177	0.1039	0.6923
9	1.1	111.95	-1.2	8.086	569.295	1.980	0.687	1.193	0.1056	0.6923
10	1.1	111.4	-1.19	8.097	572.439	1.983	0.690	1.199	0.1062	0.6922

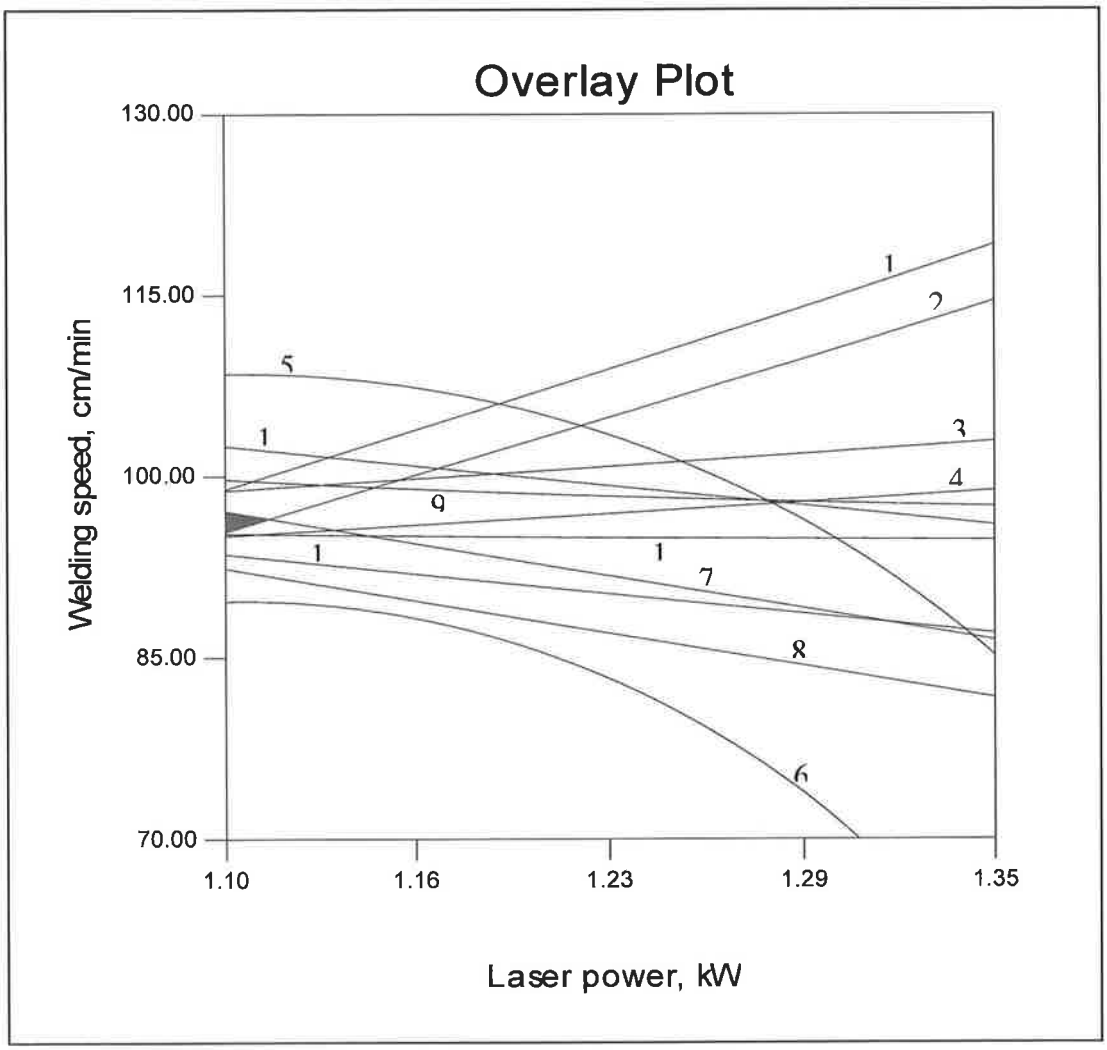

Fig. 6.5: Overlay plot shows the region of optimal welding condition based on the first criterion at F = -1.2 mm for 1 mm AISI304. Below is a Key for Fig. 6.5:

1- Heat input of 660 J/cm.
2- Heat input of 690 J/cm.
3- Joint cost of 0.1230 €/m.
4- Joint cost of 0.129 €/m.
5- Front width of 2.0 mm.
6- Front width of 2.10mm.
7- Failure load of 8.40 kN.
8- Failure load of 8.50 kN.
9- Back width of 0.750 mm.
10- Back width of 0.780 mm.
11- Half penetration width of 1.30 mm.
12- Half penetration width of 1.40 mm.

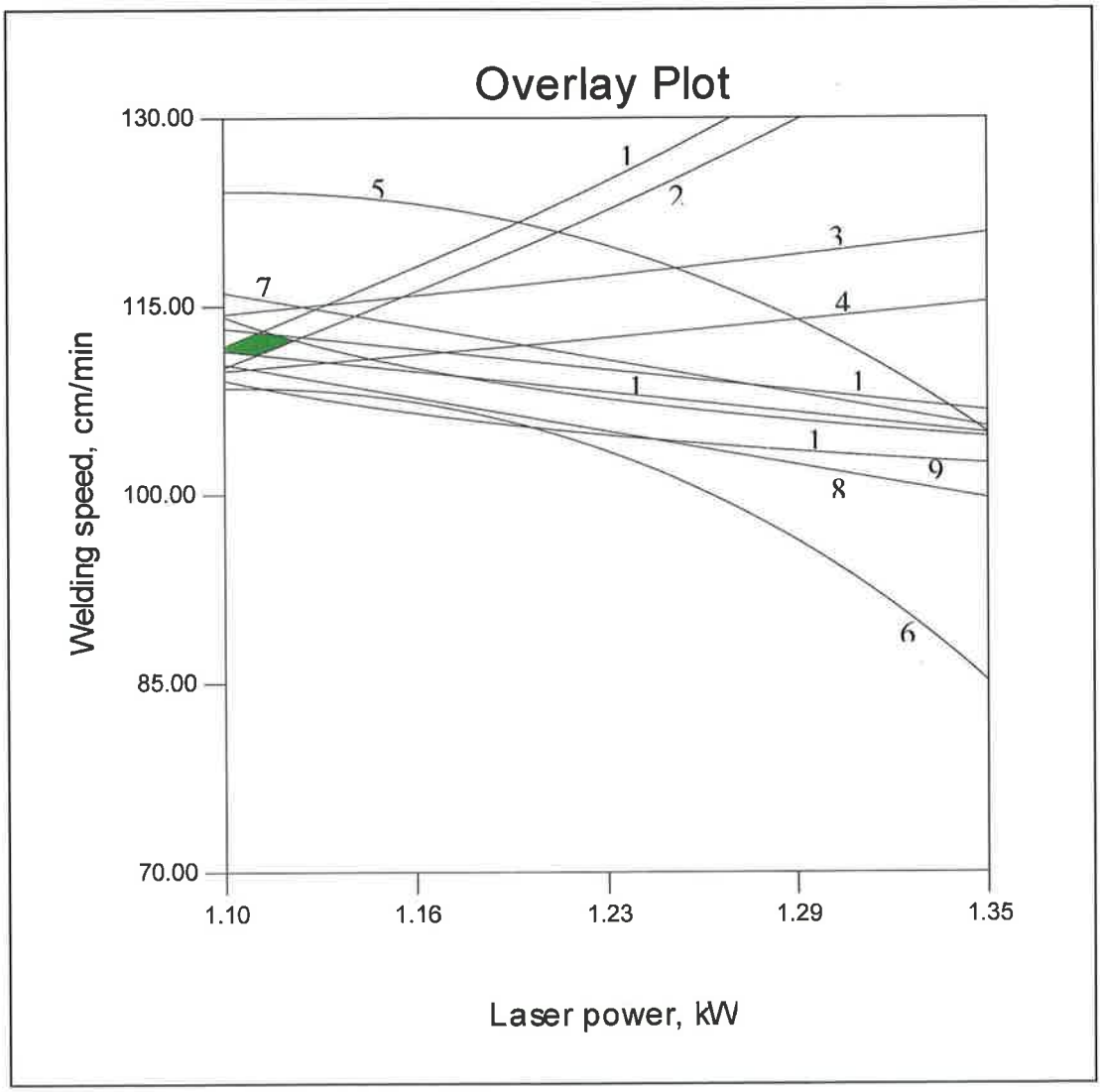

Fig. 6.6: Overlay plot shows the region of optimal welding condition based on the second criterion at F = -1.2 mm for 1 mm AISI304. Below is a key for Fig. 6.6:

1- Heat input of 570 J/cm.
2- Heat input of 580 J/cm.
3- Joint cost of 0.1030 €/m.
4- Joint cost of 0.1080 €/m.
5- Front width of 1.9 mm.
6- Front width of 2.0mm.
7- Failure load of 8.0 kN.
8- Failure load of 8.120 kN.
9- Back width of 0.70 mm.
10- Back width of 0.710 mm.
11- Half penetration width of 1.180 mm.
12- Half penetration width of 1.20 mm.

6.4 Dissimilar Welding of 3 mm AISI304 and AISI1016.

6.4.1 Numerical optimization

Welding of dissimilar metals is one of the challenging jobs facing modern manufacturers, due to the differences in the thermal conductivity and melting temperatures of these materials. Dissimilar welding is commonly used in the power generation, chemical, petrochemical, nuclear and electronics industries for the purpose of tailoring component properties or weight reduction. In the present case, the objective is to enhance the joint impact strength of dissimilar joints of AISI1016 hard metal, which has a low impact strength of 20 J, to a relatively soft metal AISI304, which has an impact strength of 49 J. In this experiment three optimization criteria were implemented to define the operating conditions at which sound and cost effective weldments could be achieved. The first criterion is to maintain maximum joint impact strength with maximum back width and minimize the weld bead and operating cost. In the second optimization criterion the goal was to produce joints with maximum impact strength but some restrictions were put on the process parameters. In the third optimization criterion the objective was to produce welds with minimum residual stress and low operating cost. Table 6.10 summaries these optimization criteria. Tables 6.11 to 6.13 present the optimal welding conditions as determined by the software based on the models developed and on each optimization criteria. For the first criterion, the optimization results reveal that both the laser power and the focal position should be set at 1.35 kW and -0.2 mm respectively, and the welding speed should be between 45 and 46.77 cm/min to meet the requirement of this criterion. It is clear from Table 5.48 in the previous chapter that an impact strength of about 39 J could be obtained at a relatively higher operating cost of about 0.3651 €/m, but by using the optimal welding setting shown in Table 6.11 an impact strength of about 38 J would be achieved at an operating cost of 0.2876 €/m. Therefore, the operating cost was successfully reduced by 21.2% and the impact strength was slightly reduced by 2.6%. Also, the bead geometry parameters were significantly improved. For the second criterion, the optimization results indicate that both the laser power and the focal position should be set at 1.13 kW and -0.2 mm respectively, and the welding speed should be between 49 and 50 cm/min to comply with the second criterion conditions. Again, it is clear from Table 5.48 that an impact

strength of about 31 J could be obtained at a relatively high operating cost of about 0.3508 €/m, however by using the optimal welding setting shown in Table 6.11 an impact strength of about 31 J would be achieved at an operating cost of 0.2500 €/m. Consequently, the operating cost was effectively reduced by 28.7%. Also, the residual stress and the bead geometry parameters were significantly enhanced. Finally, to meet the conditions set in the third criterion, the optimization results demonstrate that the laser power, welding speed and the focal position has to be set at 1.14 kW, 65 cm/min and -0.8 mm respectively. Although the residual stresses have been reduced significantly, the joint impact strength failed at about 21 J, which makes the joint too brittle.

6.4.2 Graphical optimization for dissimilar welding

Again in this case the range of each response has been selected based on the results of the numerical optimization as presented in Tables 6.11 to 6.13. The overlay plots shown in Figs. 6.7 to 6.9 reveal the green regions that comply with each criterion.

Table 6.10 Optimization criteria used for dissimilar welding.

Parameter or Response	Limits		Importance	First criterion	Second criterion	Third criterion
	Lower	Upper				
Laser power	1.13	1.35	3	is in range	minimize	is in range
Welding speed	35	65	3	is in range	maximize	is in range
Focused position	-0.8	-0.2	3	is in range	is in range	is in range
σ_1	149.8	340.9	5	none	minimize	minimize
σ_8	171.4	351.8	5	none	minimize	minimize
Heat input	989	3003	3	none	minimize	none
Impact strength	20	40	5	maximize	maximize	none
operating cost	0.1666	0.5058	3	minimize	minimize	minimize
Front width	1.118	3.407	3	minimize	minimize	none
Back width	0.491	2.740	3	maximize	maximize	none
Weld pool area	3.623	9.343	3	minimize	minimize	none

Table 6.11: Optimal solution based on the first criterion for dissimilar welding.

No.	P	S	F	Impact strength, J	Joint cost, €/m	W, mm	BW, mm	A, mm^2	D
1	1.35	45.87	-0.2	37.83	0.2814	2.003	1.264	5.976	0.6219
2	1.35	45.71	-0.2	37.87	0.2825	2.010	1.274	5.999	0.6219
3	1.35	45.44	-0.2	37.95	0.2845	2.022	1.291	6.036	0.6218
4	1.35	45.31	-0.2	37.98	0.2854	2.027	1.298	6.054	0.6218
5	1.35	45.16	-0.2	38.02	0.2865	2.034	1.308	6.075	0.6216
6	1.35	45.01	-0.2	38.06	0.2876	2.040	1.317	6.096	0.6215
7	1.35	46.77	-0.2	37.59	0.2751	1.965	1.211	5.855	0.6214
8	1.35	45.41	-0.2	37.94	0.2847	2.024	1.291	6.042	0.6213
9	1.35	46.55	-0.2	37.63	0.2766	1.975	1.223	5.886	0.6212
10	1.35	45.75	-0.2	37.77	0.2822	2.006	1.270	5.986	0.6212

Table 6.12: Optimal solution based on the second criterion for dissimilar welding.

No.	P	S	F	σ_1, MPa	σ_8, MPa	NH, j/cm	Impact strength, j	joint cost, €/m	W, mm	BW, mm	A, mm^2	D
1	1.13	49.39	-0.2	188	209	1359	30.42	0.2475	1.508	0.774	4.488	0.6330
2	1.13	49.52	-0.2	188	209	1355	30.38	0.2466	1.503	0.767	4.473	0.6330
3	1.13	49.29	-0.2	189	209	1363	30.45	0.2481	1.512	0.779	4.501	0.6330
4	1.13	49.16	-0.2	189	210	1367	30.49	0.2489	1.516	0.786	4.515	0.6330
5	1.13	49.67	-0.2	187	208	1350	30.33	0.2457	1.498	0.760	4.457	0.6330
6	1.13	48.99	-0.2	190	210	1373	30.54	0.2500	1.523	0.795	4.535	0.6328
7	1.13	49.98	-0.2	187	207	1340	30.24	0.2439	1.486	0.744	4.422	0.6326
8	1.13	49.01	-0.2	189	210	1372	30.51	0.2498	1.523	0.792	4.536	0.6325
9	1.13	49.34	-0.2	188	209	1366	30.41	0.2480	1.515	0.781	4.511	0.6324
10	1.13	49.57	-0.2	187	209	1360	30.34	0.2466	1.509	0.772	4.492	0.6322

Table 6.13: Optimal solution based on the third criterion for dissimilar welding.

No.	P	S	F	σ_1, MPa	σ_8, MPa	Impact strength, J	joint cost, €/m	D
1	1.14	65	-0.8	150	171	20.7	0.1834	0.9848
2	1.14	65	-0.8	150	171	20.7	0.1835	0.9848
3	1.14	65	-0.8	150	171	20.7	0.1835	0.9848
4	1.14	64.99	-0.8	150	171	20.7	0.1835	0.9847
5	1.14	65	-0.79	150	171	20.7	0.1836	0.9847
6	1.14	65	-0.8	150	171	20.7	0.1836	0.9847
7	1.14	65	-0.8	150	171	20.7	0.1836	0.9847
8	1.14	65	-0.8	150	171	20.7	0.1833	0.9846
9	1.14	64.84	-0.8	150	171	20.8	0.1837	0.9845
10	1.14	65	-0.8	150	171	20.7	0.1834	0.9845

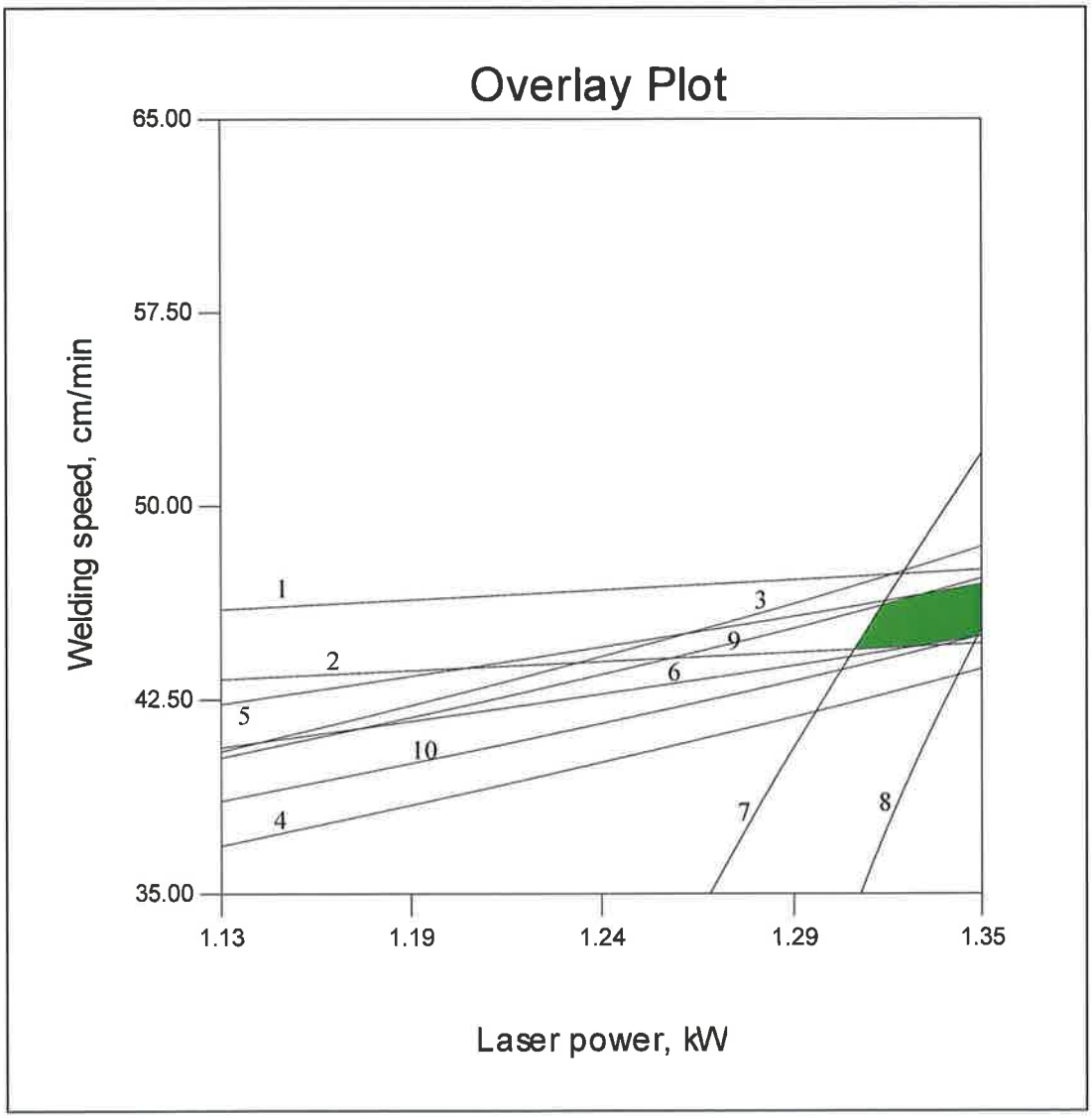

Fig. 6.7: Overlay plot shows the region of optimal welding condition based on the first criterion at F = -0.2 mm for dissimilar welding. Below is a key for Fig. 6.7:

1- Joint cost of 0.2700 €/m.
2- Joint cost of 0.2900 €/m.
3- Front width of 1.9 mm.
4- Front width of 2.10mm.
5- Back width of 1.20 mm.
6- Back width of 1.320 mm.
7- Impact strength of 36 J.
8- Impact strength of 38 J.
9- Weld-pool area of 5.80 mm^2.
10- weld-pool area of 6.10 mm^2.

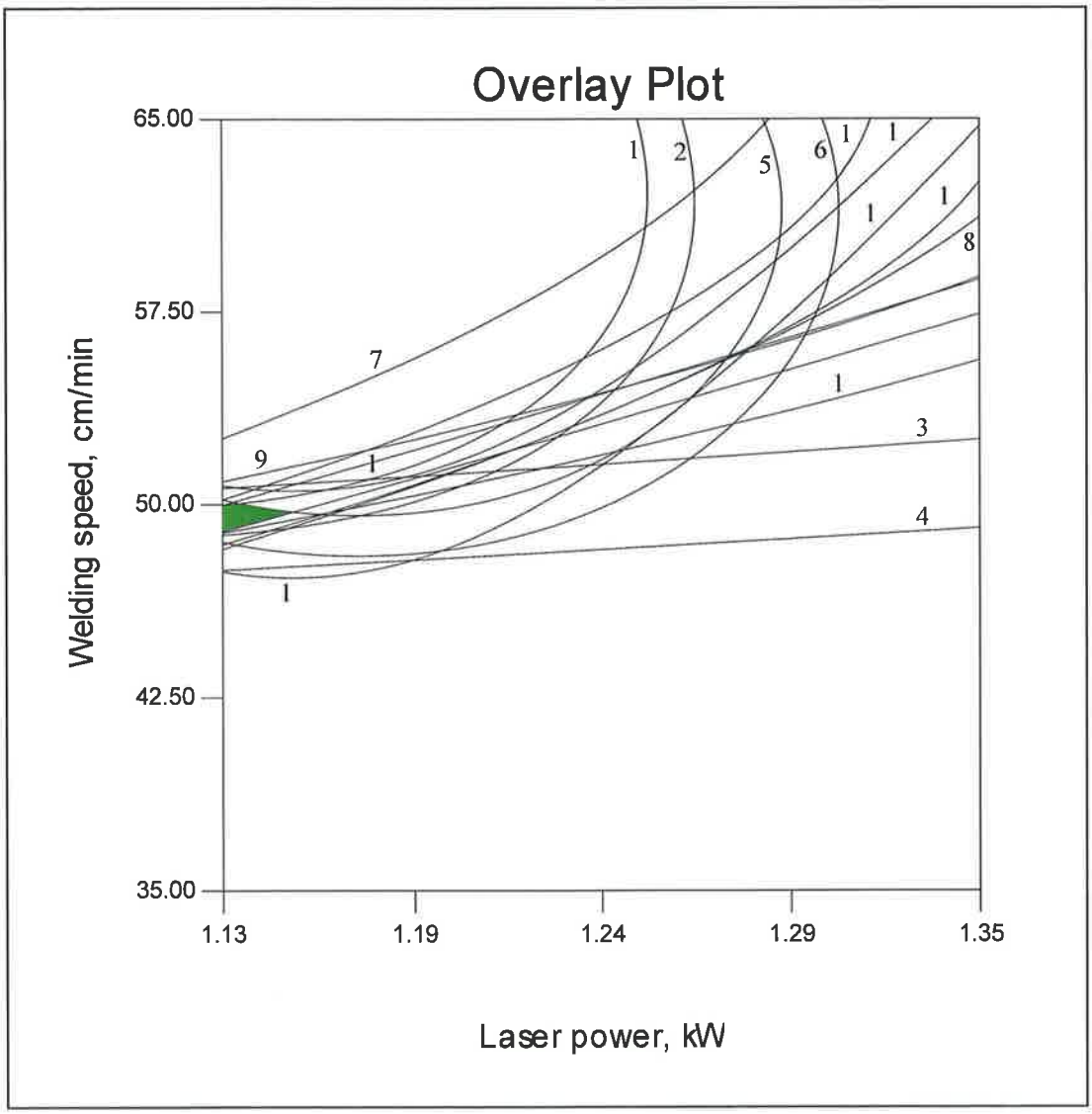

Fig. 6.8: Overlay plot shows the region of optimal welding condition based on the second criterion at F = -0.2 mm for dissimilar welding. Below is a key for Fig. 6.8:

1- σ_8 of 207 MPa.
2- σ_8 of 207 MPa.
3- Joint cost of 0.240 €/m.
4- Joint cost of 0.260 €/m.
5- σ_1 of 186 MPa.
6- σ_1 of 191 MPa.
7- Front width of 1.40 mm.
8- Front width of 1.550 mm.
9- Back width of 0.70 mm.
10- Back width of 0.80 mm.
11- Impact strength of 30 J.
12- Impact strength of 31 J.
13- Heat input of 1340 J/cm.
14- Heat input of 1375 J/cm.
9- Weld-pool area of 4.40 mm^2.
10- weld-pool area of 4.60 mm^2.

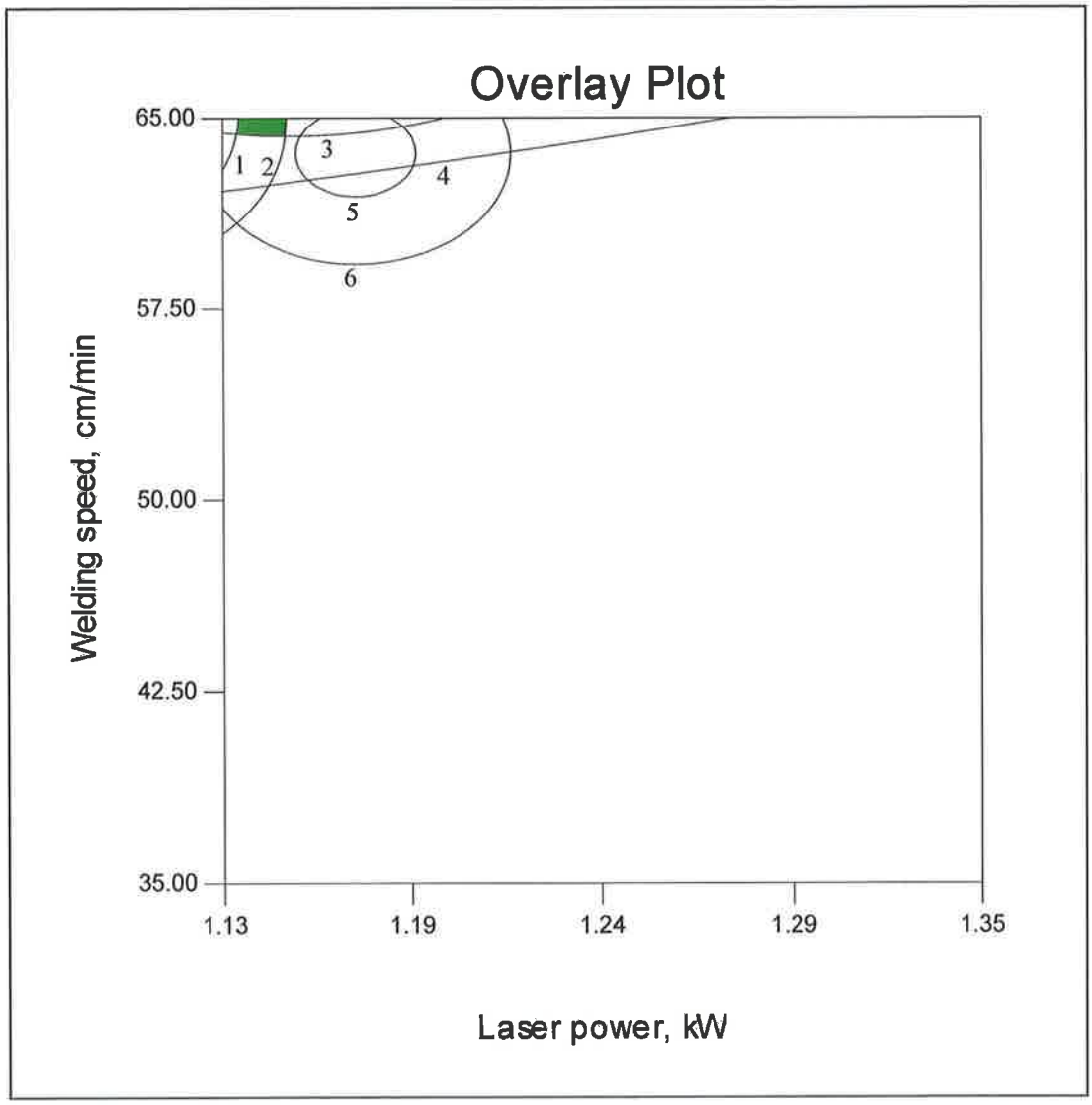

Fig. 6.9: Overlay plot shows the region of optimal welding condition based on the third criterion at F = -0.8 mm for dissimilar welding. Below is a key for Fig. 6.9:

1- σ_8 of 170 MPa.
2- σ_8 of 172 MPa.
3- Joint cost of 0.180 €/m.
4- Joint cost of 0.190 €/m.
5- σ_1 of 149 MPa.
6- σ_1 of 151 MPa.

CHAPTER VII

CONCLUSIONS AND RECOMMENDATIONS FOR FUTURE WORK

7. CONCLUSIONS AND RECOMMENDATIONS FOR FUTURE WORK

7.1 Conclusions

The following conclusions were drawn from the results obtained and are applicable only for the materials investigated in this work: The developed mathematical models and the optimal solutions are valid in the welding parameters ranges that were used for developing the mathematical models. Extrapolation over those limits would limit the applicability of the found solution.

7.1.1 General conclusions

1. There is a high level of interest in the adaptation of RSM and ANNs to predict responses and optimize the welding processes.
2. The RSM designs used in this study can be employed easily to develop mathematical models to predict the weld-bead geometry parameters, residual stress and mechanical properties, if the correct ranges for all the process parameters are carefully selected to ensure regular behaviour of all responses within the experiment domain (i.e. linear or at least low order polynomial).
3. RSM provides benefits in the applications where immediate predictions are needed and computationally intensive predictions are too slow. This technique allows the selection of the optimal combinations, and prevents loss of materials. Also, it has the advantage that the contribution of each factor to a particular response can be determined along with the effect of factor interaction on a given response.
4. The CO_2 laser welding process was successfully optimized using RSM and the desirability optimization approach. In the course of this work 62 mathematical models were effectively developed.
5. The laser welding parameters affect the solidified structure size and orientation. Higher heat input leads to coarser microstructure. There was no significant change in the microhardness of either fusion zone or HAZ, for any of the welded joints except for AISI1045 and dissimilar welding where the microhardness value decreases as the heat input increases.

6. The overlay plots were drawn for all criteria for all materials to allow a visual representation of the optimal welding conditions. This type of plotting would assist the technicians and machine operator to find out the optimal setting quickly.

7.1.2 AISI1045 5 mm butt joint

1. The heat input plays an important role in the weld-bead parameters dimension. S has a negative effect on all the responses investigated, whereas; P has a positive effect. While, as F goes into the metal (i.e. F<0) the penetration significantly reduces and the HAZ width slightly reduces, but WZ width increases.
2. Full depth penetration achievement has a strong effect on the other bead parameters investigated.
3. The main factor affecting the impact strength and tensile strength is S. Also, P and F have strong effect on the impact strength and NTS respectively.
4. From the optimization results it was demonstrated that the full depth penetration can be achieved by using P =1.41 kW, S = 36 cm/min and F = 0, and the operating cost would be minimized by 14.7%. While, for partial depth penetration the optimal conditions are P= 1.2 kW, S ranged between 67.1 and 69.95 cm/min and F spanned between -1.69 and -1.87 mm. In this case the operating cost for the double sided butt joint would be minimised by 16.6% and the total heat input would be minimised by 13.2%.

7.1.3 AISI304 3 mm butt joint

1. All the responses investigated decrease as S increases, also, these responses increase as P and F increase, except for the tensile strength, which increases until P reaches its centre limit and then it starts to decrease, and F has a negative effect on the tensile strength.
2. The interactions of the process input parameters exhibited secondary contributions to the residual stress distribution and the interaction between P and S exhibited significant contributions to the tensile strength.

3. Extracted optimal welding ranges at which the process could be considered safe have been determined to produce welds with minimum residual stress, while maintaining good mechanical properties. These ranges are:

    a) P of about 1.2 kW, S ranged between 35 and 38.85 cm/min and F = -0.2 mm. There is a high joint operating cost of about € 0.36 per meter if these conditions are being used.

    b) P = 1.2 kW, S = 60 cm/min and F = -0.8 mm, if the joint cost is to be reduced by 43.3 % and acceptable mechanical properties are maintained.

7.1.4 AISI304 1 mm lap joint

1. Any increase in effect S, would cause a reduction in all responses. Also, any increase in P would cause a reduction in all responses but the back width will slightly increase. Any increase in F will lead to a minor reduction in the failure load and a reduction in all the weld-bead parameters but the back width would slightly increase.
2. The optimal setting for P and the F position are 1.1 kW and -1.2 mm respectively.
3. A minor reduction in the failure load of 6.2% would occur along with a significant drop in the operating cost of about 49.1% when S ranged between 95.5 and 98.5 cm/min is used. While, using S ranged between 110.42 and 113.52 cm/min would result in a slight reduction in the failure load of about 9.7% with a significant reduction in the operating cost of about 57.4%.

7.1.5 Dissimilar welding 3 mm butt joint

1. All the investigated responses decrease as the S increases, but these responses increase as both P and F increase.
2. The joint tensile strength was always higher than those of the softer of the two materials that formed the joint.
3. The optimal settings that maximise the impact strength are: P of 1.35 kW, F of -0.2 mm and S ranging between 45 and 46.77 cm/min, with a reduction in

the joint cost of about 21.2%. However, if maximising the impact strength is desired with some restrictions on the process parameters, the optimal setting is: P of 1.13 kW, F of -0.2 mm and S ranging between 49 and 50 cm/min, with a reduction in the joint cost of about 28.7%. While, if the minimisation of the residual stress is desired the optimal welding settings are: P of 1.14 kW, F of -1.8 mm and S of 65 cm/min.

7.2 Recommendations for Future Work

1. Programme all the developed models to be fed to a robotic controller in a production system for automatic control of welding conditions.
2. Extend this investigation and study more mechanical properties, such as impact strength at different temperatures and fatigue life etc., to give a complete picture of these commonly used materials.
3. Apply this technique to other widely used materials, ferrous or nonferrous, in order to provide a comprehensive database on them.
4. Apply this technique to optimize other dissimilar welding and different joint configurations.
5. Apply this technique to optimize other welding processes, such as underwater laser welding.
6. Investigate the interaction between the two materials in the dissimilar welding and possibility of any enrichment with carbon in the stainless steel side as it affects the corrosion resistance.
7. Compare the measured data with numerical simulation base techniques.

REFERENCES

[1] A. D. Althouse, C. H. Turnquist, W. A. Bowditch and K. E. Bowditch, Modern welding, The Goodheart-Willcox Co., Inc., USA, 1984.

[2] H. B. Cary, Modern welding technology, Prentice-Hall, Inc. New Jersey, 1979.

[3] Solar Navigator (online) http://www.solarnavigator.net/welding.htm , (accessed on 06.2005).

[4] C. Dawes, Laser Welding, Abington Publishing, New York, NY, 1992.

[5] W. M. Steen, Laser Material processing, Springer, London, 1991.

[6] A. I. Khuri and J. A. Cornell, Response Surfaces Design and Analysis, 2nd Ed, Marcel Dekker, New York, (1996).

[7] E. Macherauch & K. H. Kloos, Origin, Measurement and Evaluation of Residual Stress, Residual Stress in Science and Technology, Edited by E. Macherauch, V. Hank DGM Verlag, 1987, pp. 3-26.

[8] I. C. Noyan and J. B. Cohen, Residual Stress Measurement by Diffraction and Interpretation, Springer-Verlag, 1987, pp. 1-12.

[9] E. Macherauch and H. Wohlfahrt, Different Sources of Residual Stress as a Result of Welding, conf. On Residual stresses in welded construction and their effect, London, UK, 15-17 Nov. 1977, pp. 267-282.

[10] D. Radaj, Heat effect off welding, Springer Verlag, pp. 18-67.

[11] American Welding Society, Welding handbook, Welding technology, 7th edition, Miami, American Welding Society, 1981, ISBN 0-87171-126-5.

[12] J. Lu: Handbook of Measurement of Residual stresses (Society of Experimental Mechanics Inc, the Fairmont press, 1996).

[13] A. G. Olabi and M. S. J. Hashmi: Review of Methods for measuring Residual Stresses in Components (Proceedings of 9th Conf. on Manufacturing Research Sep. 1993).

[14] L. Mordfin, Measurement of residual stress: problems and opportunities, Inter. Conf. on residual stress of designers and metallurgists, 9-10 April 1980, Chicago USA, pp. 189-210.

[15] K. Masubuchi, Analysis of welded structures, 1st Ed., Pergamon press, ISBN: 0080227147, 1980, pp. 114-115.

[16] F.A. Kandil, J. D. Lord et al. , A review of residual stress measurement methods, a guide to technique selection, NPL Report MAT(A)04, Feb. 2001.

[17] J. H. Norton and D. Rosenthal , Stress measurement by x-ray diffraction , proceedings of the society for experimental stress analysis, Vol. 1, n. 2, 1944, pp. 73-76.

[18] J. H. Norton and D. Rosenthal, Application of the x-ray method of stress measurement to problems involving residual stress in metals, proceedings of the society for experimental stress analysis, Vol. 1, n. 2, 1944, pp. 81-90.

[19] M. E. Fitapztrick, A. T. Fry , P. Holdway, F.A. Kandil, J. Shackleton and L. Suominen, Determination of residual stresses by X-ray diffraction, National Physical Laboratory, Guide No. 52, March 2002.

[20] P. Rangaswamy, et al., Comparison of residual strains measured by X-ray and neutron diffraction in a titanium (Ti-6Al-4V) matrix composite, J. of Material Science and engineering A259, 1999, pp. 209-219.

[21] X. Wei and J. He, A study on residual stress distribution measurement of dual phase stainless steel by means of x-ray method, Proceedings of 11th international offshore and polar eng. Conf. Vol. 4, Stavanger, Norway, June 17-22.2001, pp. 314-318.

[22] J. Lu et al., study of residual welding stress using the step-by-step hole drilling and X-ray diffraction method, J. of welding in the world, Vol. 33 n. 2, 1994, pp. 118-128.

[23] M. J. Park, et al., Residual stress measurement on welded specimen by neutron diffraction, J. of Mat. Proc. Tech. Vol. 155-156, 2004, pp. 1171-1177.

[24] H.Y. Lee, K. M. Nikbin and P.O. Dowd, A generic approach for a linear fracture mechanics analysis of components containing residual stress, Inter. J. of Pressure vessels and Piping, Vol. 82, 2005, pp. 797-806.

[25] A. Paradowska, J. W.H. Price, R. Ibrahim and T. Finlayson, A neutron diffraction of residual stress due to welding, J. of Mat. Proce. Tech., Vol. 164-165, 2005, pp. 1099-1105.

[26] P. J. Withers and H. K. D. H. Bhadeshia, Measurement techniques, J. of Materials Science and Technology, Vol. 17, April 2001, pp. 355-365.

[27] J. Mathar, Determination of initial stresses by measuring the deformation around drilled holes, Trans. Of ASME Vol. 56, n 4, 1934, pp. 249-254.

[28] W. Soete and R. Vancrombrugge, An industial method for the determination of residual stresses, Proc. Of SESA, Vol. 8, n. 1, 1950, pp. 181-197.

[29] R. A. Kelsey, Measuring non-uniform residual stresses by the hole drilling method, Proc. Of SESA, Vol. XIV, n. 1, 1956, pp. 181-194.

[30] N. J. Rendler and I. Vigness, hole drilling strain-gauge method of measuring residual stresses, J. of Experimental mechanics, Vol. 6, n. 12, 1966, pp. 577-586.

[31] J. E. Bynum, Modifications to the hole-drilling technique of measuring residual stresses for improved accuracy and reproducibility, J. of Experimental Mechanics, Vol. 21, n. 1, 1981, pp. 21-33.

[32] S. Redner and C. C. Perry, Factors affecting the accuracy of residual stress measurements using the blind-hole drilling method, Proc. Of the 7th Inter. Conf. on Experimental stress analysis, Haifa, 23-27. Augest.1982, pp. 604-616.

[33] A. Ajovalasit, The influence of hole eccentricity on the calibration constants of rosettes used in the hole drilling method, Proc. Of the 7th Inter. Conf. on Experimental stress analysis, Haifa, 23-27. Augest.1982, pp. 591-601.

[34] E. Procter and E. M. Beaney, Recent developments in centre-hole technique for residual-stress measurement, J. of Experimental mechanics, Vol. 6, 1982, pp. 10-15.

[35] M. T. Flaman, brief investigation of induced drilling stresses in the centre-hole method of residual stress measurement, J. of experimental mechanics, Vol. 22, 1982, pp. 26-30.

[36] G. S. Schajer, Application of finite element calculations to residual stresses measurements, J. of Eng. Mat. And Tech. Vol. 103, 1981, pp. 157-163.

[37] M. T. Flaman and B. H. Manning, Determination of residual stress variation with depth by hole drilling method, J. of Experimental Mechanics, Vol. 25, n. 3, 1985, pp. 205-207.

[38] J. M. Boag, M. T. Flaman and J. A. Herring, Considerations of using the hole drilling method for measuring residual stresses in Engineering components,

proc. Of ASM's conf. on residual stress in design, Cincinnati Ohio USA, Edited by W. B. Young, 1987, pp. 1-6.

[39] C. L. Chow and C. H. Cundiff, on residual stress measurements in light truck wheels using the hole drilling method, J. of Experimental Mechanics, Vol. 25, n. 1, 1985, pp. 54-59.

[40] A. M. Nawwar, K. McLachian and J. Shewchuk, A modified hole drilling technique for determination residual stresses in thin plate, Experimental Mechanics Vol. 16, n.6, 1976, pp. 226-232.

[41] M. Bijak-Zochowski, A semidestructive method of measuring residual stresses, VDI-Berichte, 313, 1978, pp. 469-476.

[42] A. Niku-Lari, J. Lu and J. F. Flavenot, measurement of residual-stress distribution by the incremental hole-drilling method, J. of Experimental Mechanics, Vol. 25, No. 2 1985, pp. 175-185.

[43] G. S. Schajer, Measurement of non-uniform residual stresses using the hole-drilling method. Part I- stress calculation procedures, Trans. Of the ASME, Vol. 110, 1988, pp. 338-343.

[44] G. S. Schajer, Measurement of non-uniform residual stresses using the hole-drilling method. Part II-practical application of the integral method, Trans. Of the ASME, Vol. 110, 1988, pp. 344-349.

[45] D. Shaw and H. Y. Chen, A finite-element technique to analyze the data measured by the hole-drilling method, J. of Experimental Mechanics, Vol. **, 1990, pp.120-123.

[46] J. Lu and J. F. Flavenot, Applications of the incremental hole-drilling method for measurement of residual-stress distribution, J. of Experimental Techniques, Vol. 13, No. 11 1989, pp. 18-24.

[47] G. S. Schajer, Strain data averaging for the hole-drilling method, J. of Experimental Techniques, Vol. 15, n. 2, 1991, pp. 25-28.

[48] Y. C. Lin and C. P. Chou, Error induced by local yielding around hole in hole drilling method for measuring residual stress of materials, J. of Materials Sci. and Tech., Vol. 11, 1995, pp. 600-604

[49] M. T. Flaman and J. M. Boag, Comparison of residual stress variation with depth-analysis technique for the hole-drilling method, J. of Experimental Mechanics, Vol. 30, No. 4, Dec. 1990, pp. 352-355.

[50] M. Beghini and L. Bertini, Recent advances in the hole drilling method for residual stress measurement, J. of Mat. Eng. and performance, Vol. 7, n. 2, 1998, pp. 163-172.

[51] B. Zuccarello, Optimal calculation steps for the evaluation of residual stress by the incremental hole-drilling method, J. of Experimental Mechanics, Vol. 39, n. 2, 1999, pp. 117-124.

[52] ASTM E837-01^{el}, Standard test method for determining residual stress by the hole drilling strain gauge method, ASTM standard book, Vol. 03.01, 2003, pp. 694-703.

[53] Technical Note TN-503, Measurement of residual stresses by the hole drilling strain gauge method, on 09.2005. vishay.com/brands/measurements_group/guide/tn/tn503/503index.htm.

[54] P. V. Grant, J. D. Lord and P. S. Whitehead, The Measurement of Residual Stresses By the Incremental Hole Drilling Technique, National Physical Laboratory, 2002, Guide No. 53.

[55] R. Gadow, M. Escribano, M. Buchmann, Residual stress analysis in thermally sprayed layer composites, using the microhole milling and drilling method, Journal of Thermal Spray Technology, v 14, n 1, March, 2005, p 100-108

[56] R. Gadow, M. Escribano, M. Buchmann, Determination of residual stresses in ceramic layer composites, using the microhole drilling method, In Abstracts of 8th European interregional conf. on ceramics, CIEC8, 3-5 September 2002,Lyon.

[57] M. Buchmann and R. Gadow, High speed circular milling method for the determination of residual stresses in coatings and composites, In Proc. of Ceramic Eng. And Sci., Eds. T. Jessen and E. Ustundag, American Ceramic Society, Westerville Ohio, 2000, pp. 109-116.

[58] P. Grant, J. Lord, P. Whitehead and T. Fry, The application of fine increment hole drilling for measuring machining-induced residual stresses, in Proc. Of 4th Inter. Conf. on Advances in Experimental Mechanics IV, University of

Southampton, Trans Tech Publications, Vols 3-4, Switzerland, August 2005, pp. 105-110.

[59] D. Radaj, Heat effects of welding- temperature field, residual stress, Distortion, Springer-Verlag, 1992.

[60] L. P. Connor, Welding Handbook-welding processes, Vol. 2, 8th Ed, American welding Society, 1991.

[61] J. Raveendra and R. S. Parmar, Mathematical models to predict weld bead geometry for flux cored arc welding, J. of Metal construction, Vol. 19, n. 2, January 1987, pp. 31R-35R

[62] V. K. Gupta and R. S. Parmar, Fractional factorial technique to predict dimensions of the weld bead in automatic submerged arc welding, IE(I) Journal-MC, Vol. 70, Nov. 1989, pp.67-75.

[63] L. J. Yang, M. J. Bibby and R. S. Chandel, Linear regression equations for modelling the submerged-arc welding process, J. of Materials Processing Technology, Vol. 39, 1993, pp. 33-42.

[64] N. Murugan, R. S. Parmar and S. K. Sud, Effect of submerged arc welding process variables on dilution and bead geometry in single wire surfacing, J. of Material Processing Technology, Vol. 37, 1993, pp. 767-780.

[65] N. Murugan and R. S. Parmar, effects of MIG process parameters on the geometry of the bead in the automatic surfacing of stainless steel, J. of Materials Processing Technology, Vol. 41, 1994, pp. 381-398.

[66] C. M. D. Starling, P. V. Marques and P. J. Modenesi, Statistical modelling of narrow-gap GTA welding with magnetic arc oscillation, J. of Material Processing Technology, Vol. 51, 1995, pp. 37-49.

[67] N. Murugan and R. S. Parmar, Effect of welding conditions on microstructure and properties of tupe 316L stainless steel submerged arc welding cladding, Welding Journal, AWS, Vol. 76, n. 5, May 1997, pp. 210-s-220-s.

[68] V. Gunaraj and N. Murugan, Application of response surface methodology for predicting weld bead quality in submerged arc welding of pipes, J. of Mat. Processing Tech., Vol. 88, 1999, pp. 266-275.

[69] V. Gunaraj and N. Murugan, Prediction and comparison of the area of the heat-affected zone for the bead-on-plates and bead-on-joint in submerged arc welding of pipes, J. of Mat. Processing Tech., Vol. 95, 1999, pp. 246-261.

[70] E. Koleva, Statistical modelling and computer programs for optimisation of the electron beam welding of stainless steel, J. Vacuum, Vol. 62, 2001, pp. 151-157.

[71] V. Gunarai and N. Murugan, Prediction and optimization of weld bead volume for the submerged arc process-part 1, Welding journal, AWS, October 2000, 286-s – 294-s.

[72] V. Gunarai and N. Murugan, Prediction and optimization of weld bead volume for the submerged arc process-part 2, welding journal, AWS, November 2000, 331-s – 338-s.

[73] Gunaraj and Murugan, Prediction of heat-affected zone characteristics in submerged arc welding of structural steel pipes, welding journal, AWS, January 2002, 94-s – 98-s.

[74] K .Manonmani, N. Murugan and G. Buvanasekaran, Effect of process parameters on the weld bead geometry of laser beam welded stainless steel sheets, Inter. J. for the Joining of Materials, Vol. 17, n. 4, 2005, pp.103-109.

[75] Gunaraj and Murugan, Prediction and control of weld bead geometry and shape relationships in submerged arc welding of pipes, J. of Mat. Processing Tech., Vol. 168, 2005, 478-487.

[76] D. Kim, S. Rhee, and H. Park, Modelling and optimization of a GMA welding process by genetic algorithm and response surface methodology, Int. J. of Prod. Res., Vol. 40, n. 7, 2002, pp. 1699-1711.

[77] E. Koleva, Electro beam weld parameters and thermal efficiency improvement, Vacuum J., Vol. 77, 2005, pp. 413-421

[78] D. S. Correia, C. V. Goncalves, S. S. da Cunha and V. A. Ferraresi, Comparison between genetic algorithms and response surface methodology in GMAW optimization, J. of Mat. Processing Tech., Vol. 160, 2005, pp. 70-76.

[79] E. Koleva and I. Vuchkov, Model-based approach for quality improvement of electro beam welding applications in mass production, J. Vacuum, Vol. 77, 2005, pp. 423-428.

[80] T. Kannan and N. Murugan, Effect of flux cored arc welding process parameters on duplex stainless steel clad quality, J. of Material Processing Technology, Vol. 176, 2006, pp. 230-239.

[81] I. S. Kim, J. S. Son, I. G. Kim and O. S. Kim, A study on relationship between process variable and bead penetration for robotic CO_2 arc welding, J. of Mat. Processing Tech., Vol. 136, 2003, pp. 139-145.

[82] I. S. Kim, K. J. Son, Y. S. Yang and P. K. D. V. Yaragada, Sensitivity analysis for process parameters in GMA welding processes using a factorial design method, Inter. J. of Machine Tools & manufacture, Vol. 43, 2003, pp. 763-769.

[83] D. Kim, M. Kang and S. Rhee, Determination of optimal welding conditions with a controlled random search procedure, Welding journal, AWS, August 2005, 125-s – 130-s.

[84] K. Andersen, G. Cook, G. Karsai nad K. Ramaswmy, Artificial neural network applied to arc welding process modelling and control, IEEE Transactions on Industry Applications, Vol. 26, n. 5, Sep./Oct. 1990, pp. 824-830.

[85] G. Cook, R. J. Barnett, K. Andersen and A. M. Strauss, Weld modelling and control using artificial neural networks, IEEE Transactions on Industry Applications, Vol. 31, n. 6, Nov/Dec. 1995, pp. 1484-1491.

[86] J. M. Vitek, Y. S. Iskander, E. M. Oblow et al., Neural network modeling of pulsed-laser weld pool shapes in aluminum alloy welds, proceedings of 5th Inter. Conf. on Trends in Welding Research, Pine Mountain, GA, June 1-5.1998, ASM Inter., pp.442-448.

[87] S.C. Juang, Y. S. Tarng and H. R. Lii, A comparison between the back-propagation and counter-propagation networks in the modelling of the TIG welding process, J. of Material Processing Technology, Vol. 75, 1998, pp. 54-62.

[88] H. Park and S. Rhee, Estimation od weld bead size in Co_2 laser welding by using multiple regression and neural network, J. of Laser Application, Vol. 11. n. 3, 1999, pp.143-150.

[89] B. Chan, J. Pacey and M. Bibby, Modelling gas metal arc weld geometry using artificial neural network technology, J. of Canadian Metallurgical Quarterly, Vol. 38, n. 1, 1999, pp. 43-51.

[90] Y. S. Tarng, H. L. Tsai and S. S. Yeh, Modeling, Optimization and classification of weld quality in tungsten inert gas welding, Inter. J. of Machine tools & Manufacture, Vol. 39, 1999, pp. 1427-1438.

[91] J. Lee and K. Um, A comparison in a back-bead prediction of gas metal arc welding using multiple regression analysis and artificial neural network, J. of Optics and Lasers in Engineering, Vol. 34, 2000, pp. 149-158.

[92] J. Y. Jeng, T. Mau and S. Leu, Prediction of laser butt joint welding parameters using back propagation and learning vector quantization networks, J. of Mat. Processing Technology, Vol. 99, 2000, pp. 207-218.

[93] D.S. Nagesh and G. L. Datta, Prediction of weld bead geometry and penetration in shielded metal-arc welding using artificial neural networks, J. of Mat. Processing Technology, Vol. 123, 2002, pp.303-312.

[94] G. E. Ridings, R. C. Thomson and G. Thewlis, Prediction of multiwire submerged arc weld bead shape using neural network modelling, J. of Science and Technology of welding and joining, Vol. 7, n. 5, 2002, pp. 265-279.

[95] I. S. Kim, J. S. Son, C. E. Park, C. W. Lee and Y. K. D. V. Prasad, A study on prediction of bead height in robotic arc welding using a neural network, J. of Mat. Processing Technology, Vol. 130-131, 2002, pp. 229-234.

[96] G. Casalion, and F. M. C. Minutolo, A model for evaluation of laser welding efficiency and quality using an artificial neural network and fuzzy logic, J of Engineering Manufacture, Vol. 218, part B, 2004, pp. 1-6.

[97] K. H. Christensen, T. SØrensen and J. K. Kristensen, Gas metal arc welding of butt joint with varying gap width on neural networks, J. of Science and Technology of welding and joining, Vol. 10, n.1, 2005, pp. 32-43.

[98] S. C. Juang and Y. S. Tarng, Process parameters selection for optimizing the weld pool geometry in the tungsten inert gas welding of stainless steel, J. of Mat. Processing Technology, Vol. 122, 2002, 33-37.

[99] H. K. Lee, H. S. Han, K. J. Son and S. B. Hong, Optimization of Nd-YAG laser welding parameters for sealing small titanium tube ends, J. of Materials Science and Engineering, Vol. A415, 2006, pp. 149-155.

[100] K. K. Wang and G. Rasmussen, Optimization of inertia welding process by response surface methodology, J. of Engineering for Industry, Vol. 94, n. 4, 1972, pp. 999-1006.

[101] P. Harris and B. L. Smith, Factorial techniques for weld quality prediction, J. of Metal Construction, November 1983, pp. 661-666.

[102] K. G. K. Murti and S. Sundaresan, Parameter optimization in friction welded dissimilar materials, J. of Metal Construction, Vol. 15, n. 6, June 1983, pp. 331-335.

[103] S. K. Arya and R. S. Parmar, Mathematical models for predicting angular distortion in CO_2-shielded flux cored arc welding, in the proceedings of Inter. Conf. on joining of Metals (JOM-3), Helsingor, Denmark, 1986, pp. 240-245.

[104] H. Yamaguchi, K. Ogawa and K. Sakaguchi, Optimization of friction welding condition of 5056 aluminium alloy, J. of Japan Institute of Light metal, Vol. 41, n. 10, 1991, pp. 716-720.

[105] O. Koichi, Y. Hiroshi, K. Seiichi and S. Kazuhiko, Optimization of friction welding condition for S4 5C carbon steel using a statistical technique, J. of Japan Welding Society, Vol. 24, n. 2, 1993, pp. 47-53.

[106] K. Y. Benyounis, A. H. Bettamer, A. G. Olabi and M. S. J. Hashmi, Prediction the impact strength of spiral-welded pipe joints in Submerged arc welding of low carbon steel, Proceedings of IMC21, Limerick 1-3-Sep. 2004, pp. 200-210.

[107] Y. Zhou, Z. Li, L. Hu, A. Fuji and T. H. North, Mechanical properties of particulate MMC/AISI 304 friction joints, J. of ISIJ Inter., Vol. 35, n. 10, 1995, pp. 1315-1321.

[108] E. S. Ege, O. T. Inal and C. A. Zimmerly, Response surface study on production of explosive-welded aluminium-titanium laminates, J. of Materilas Science, Vol. 33, 1998, pp. 5327-5338.

[109] V. Balasubramanian and B. Guha, Assessment of some factors affecting fatigue endurance of welded cruciform joints using statistical techniques, Inter. J. of Fatigue, Vol. 21, 1999, pp. 873-877.

[110] V. Balasubramanian and B. Guha, Fatigue life prediction of load carrying cruciform joints of pressure vessel steel by statistical tools, J. of Materials and Design, Vol. 25, 2004, pp. 615-623.

[111] T. T. Allen, R. W. Richardson, D. P. Tagliabue and G. P. Maul, Statistical process design for robotic GMA welding of sheet metal, Welding Journal, AWS, May 2002, pp. 69-s – 77-s.

[112] K. Raghukandan, Analysis of the explosive cladding of Cu-low carbon steel plates, J. of Mat. Processing Technology, Vol. 139, 2003, pp. 573-577.

[113] V. V. Murugan and V. Gunaraj, Effects of process parameters on angular distortion of gas metal arc welded structural steel plates, Welding Journal, AWS, Nov. 2005, pp. 165-s – 171-s.

[114] R. Koganti, C. Karas, A. Joaquin, D. Henderson, M. Zaluzec and A. Caliskan. Metal inert gas (MIG) welding process optimization for joining aluminium sheet material using OTC/DAIHEN equipment, Proceedings of IMECE'03, ASME Inter. Mech. Eng. Congress, Washington, D. C. , Nov. 15-21, 2003, pp.409-425.

[115] K. Sampath, Constrains-based modelling Enables successful development of welding electrode specification for critical navy application, Welding journal, AWS, Aug. 2005, pp. 131-s -138-s.

[116] O. E. Canyurt, Estimation of welded joint strength using genetic algorithm approach, Inter. J. of Mechanical Sciences, Vol. 47, 2005, pp. 1249-1261.

[117] T. Pine, M. M. Lee, and T. B. Jones, Factors affecting torsional properties of box sections, J. of Ironmarking and Steelmarking, Vol. 25, n. 3, 1998, pp. 205-209.

[118] G. Casalino, S. J. Hu and W. Hou, Deformation prediction and quality evaluation of the gas metal arc welding butt weld, J. of Engineering Manufacture, Vol. 217 part B, pp. 1-8.

[119] K. Seshank, S. R. K. Rao, Y. Singh and K. P. Rao, Prediction of bead geometry in pulsed current gas tungsten arc welding of aluminium using artificial neural networks, Proceedings of Inter. Conf. on Information and Knowledge Engineering, IKE 03, June 23 - 26, 2003, Las Vegas, Nevada, USA, pp. 149- 153.

[120] L. Li-ming, Z. Mei-li, N. Ji-tai and Z. Zhong-dian, Predicting effects of diffusion welding parameters on welded joint properties by artificial neural

network, J. of Yrans. Nonferrous Metal Society China, Vol. 11, n. 4, Aug. 2001, pp. 475-478.

[121] Z. Sterjovski, D. Nolan, D. Dunne and J. Norrish, Predicting the HAZ hardness of pipeline and tap fitting steels with artificial neural networks, in Proceedings of the 4th Inter. Conf. on pipeline technology, University of Wollongong, NEW, Australia, 2004, pp. 1233-1245.

[122] M. P. Lightfoot, G. J. Bruce, N. A. McPherson and K. Woods, The application of artificial neural networks to weld-induced deformation in ship plate, Welding J., AWS and WRC, February 2005, pp. 23-s – 26-s.

[123] Z. Sterjovski, D. Nolan, K. R. Carpenter, D. P. Dune and J. Norrish, Artificial neural network for modelling the mechanical properties of steels in various applications, J. of Materials Processing Technology, Vol. 170, No. 3, 2005, pp. 336-544.

[124] H. Okuyucu, A. Kurt and E. Arcaklioglu, Artificial neural network application to the friction stir welding of aluminium plates, J. of Materials & Design, Vol. 29, 2007, pp. 78-84.

[125] L. K. Pan, C. C. Wang, Y. C. Hsiso and K. C. Ho, Optimization of Nd-YAG laser welding onto magnesium alloy via Taguchi analysis, J. of Optics & Laser Technology, Vol. 37, 2004, pp. 33-42.

[126] M. Murugananth, S. S. Babu and S. A. David, Optimization of shielded metal arc weld metal composition for charpy toughness, Welding Journal, AWS, Oct. 2004, pp. 267-s-276-s.

[127] Y. Wei, H. K. D. Bhadeshia and T. Sourmail, Mechanical property prediction of commercially pure titanium welds with artificial neural network, J. of Material Science Technology, Vol. 21, n. 3, 2005, pp. 403-407.

[128] E. M. Anawa, A. G. Olabi and M. S. J. Hashmi, Optimization of ferritic/Austenitic laser welded components, presented at AMPT2006 Inter. Conf. July 30 – Aug. 3, 2006, Las Vegas, Nevada, USA, 2006.

[129] E. M. Anawa and A. G. Olabi, Effect of laser welding conditions on toughness of dissimilar welded components, J. of Applied Mechanics and Materials, Vol. 5-6, 2006, 375-380.

[130] A. Mathieu, R. Shabadi, A. Deschamps, M. Suery, S. Mattei, D. Grevey and E. Cicala, Dissimilar material joining using laser (aluminum to steel using zinc-based filler wire), J. of Optics & Laser Technology, Vol. 39, 2007, pp. 652-661.

[131] Q. Huang, J. Hagstrom, H. Skoog and G. Kullberg, Effect of CO_2 laser parameter variations on sheet metal welding, J. of Materials, Vol. 3, n. 3, 1991, pp. 79-88.

[132] J. D. Kim, Parametric evaluation of CO_2 laser beam welding, ASME publication PED, welding and Joining Processes, Vol. 51, 1991, pp. 195-201.

[133] K. W. Carlson, The role of heat input in deep penetration laser welding, Proce. of ICALEO'85, San Francisco, California, USA, Nov. 1985, pp. 49-57.

[134] J. Kroos, U. Gratzke and G. Simon, Towards a self-consistent model of the keyhole in penetration laser welding, J. of Physics D: applied Physics, Vol. 26, 1993, pp. 474-480.

[135] P. E. Denney and A. E. Metzbower, Synchronized laser-video camera system study of high power laser material interactions, Proc. ICALEO 91, San Jose, Nov. 1991, Orlando, FL, Laser institute of America, 1991, pp. 84-93.

[136] A. K. Nath, R. Sridhar, P. Ganesh and R. Kaul, Laser power coupling efficiency in conduction and keyhole welding of austenitic stainless steel, Sãdhahã, Vol. 27, part 3, June 2002, pp. 383-392.

[137] R. V. Duhamel and C. M. Banas, Laser welding of steels and nickel alloys, J. of Laser in Materials Processing, 1983, p. 209.

[138] M. Bass, Laser materials processing, vol. 3, editor by F. F. Y. Wang, north-Holland publishing com. Amsterdam, 1983.

[139] A. M. El-Batahgy, Effect of laser welding parameters on fusion zone shape and solidification structure of austenitic stainless steels, Materials letters, Vol. 32, 1997, pp. 155-163.

[140] G. J. Bruck, J. E. Smith and R. D. O'Brokta, A study of the effect of essential variable on high power laser beam welding of inconel 600, Proce. of ICALEO'85, San Francisco, California, USA, Nov. 1985, pp. 11-18.

[141] E. S. Ng and I. A. Watson, characteristics of CO_2 laser welded high carbon steel gauge plate, J. of Laser applications, Vol. 9, n. 1, 1997, pp. 15-21.

[142] J. Mazumder and W. M. Steen, Welding of Ti-6 Al-4 V by a Continuous Wave CO_2 Laser, J. of Met. Constr., Vol. 12, n. 9, 1980, pp. 423-427.

[143] T. Sibollano, A. Ancona, V. Berardi, E. Schingaro, G. Basile and P. M. Lugara, A study of the shielding gas influence on the laser beam welding of AA2083 aluminum alloys by in-process spectroscopic investigation, Optics and lasers in Engineering, Vol. 44, 2006, pp. 1039-1051.

[144] B. G. Chung, S. Rhee and C. H. Lee, The effect of shielding gas types on CO_2 laser tailored blank weldability of low carbon automotive galvanized steel, J. of Materials Science and Engineering, Vol. A272, 1999, pp. 357-362.

[145] Z. Li and G. Fontana, Autogenous laser welding of stainless steel to free-cutting steel for the manufacture of hydraulic valves, J. of Materials Processing Technology, Vol. 74, 1998, pp. 174-182.

[146] A. Zambon and F. Bonollo, Rapid solidification in laser welding of stainless steels, J. of Materials Science and Engineering, Vol. A178, 1994, pp. 203-207.

[147] R. A. Farrar, The importance of microstructural transformations for welding and the stability of long term service properties, Welding in the World, Vol. 36, 1995, pp. 143-151.

[148] L. W. Tsay, M. C. Young and C. Chen, Fatigue crack growth behaviour of laser-processes 304 stainless steel in air and gaseous hydrogen, J. of Corrosion Science, Vol. 45, 2003, pp. 1985-1997.

[149] E. Bayraktar, J. Moiron and D. Kaplan, Effect of welding conditions on the formability characteristics of thin sheet steels: mechanical and metallurgical effects, J. of Materials Processing Technology, Vol. 175, 2006, pp. 20-26.

[150] U. Dilthey and A. Risch, Laser welding of stainless steels and stainless/low alloy material combinations, J. of Welding in the world, Vol. 36, 1995, pp. 135-142.

[151] S. Katayama and A. Matsunawa, Solidification behaviour and microstructural characteristics of pulsed and continuous laser welded stainless steels, Proc. of ICALEO'85, San Francisco, California, USA, Nov. 1985, pp. 19-25.

[152] J. Antony, Design of experiments for engineers and scientists, Elsevier, 2003.

[153] G. E. P. Box and K. B. Wilson, On the experimental attainment of optimum conditions, J. of the Royal Statistical Society B13, 1951, pp. 1- 45.

[154] D. C. Montgomery, *Design and Analysis of Experiments*. 2nd Edition, John Wiley & Sons, New York, 1984.

[155] A. I. Khuri and J. A. Cornell, *Response Surfaces Design and Analysis*. 2nd Edition, Marcel Dekker, New York, 1996.

[156] Design-Expert software, V7, user's guide, Technical manual, Stat-Ease Inc., Minneapolis, MN, 2005.

[157] Information Technology laboratory, http://www.itl.nist.gov/, (accessed on July, 2006).

[158] http://www.tfhrc.gov/pavement/pubs/03060/images/image033.gif, (accessed on July, 2006).

[159] S. Akhnazarova and V. Kafarov, Experiment optimization in chemistry and chemical engineering, 1st Ed, Mir Publishers, Moscow, 1982.

[160] C. R. Hicks, Fundamental concepts in the design of experiments, 4th Ed., Saunders College Publishing, 1993.

[161] G. E. P. Box and D. W. Behnken, Some new three level designs for the study of quantitative variables, Technometrics, Vol. 2, n., 4, November 1960, pp. 455-475.

[162] M. J. Anderson and P. J. Whitcomb, RSM simplified: optimizing processes using response surface methods for design of experiments, Productivity Press, 2005.

[163] S. Chatterjee and B. Price, Regression analysis by example, 2nd Ed., Wiley and Sons, Inc., 1977, pp. 200-202.

[164] R. H. MYERS AND D.C. Montgomery, Response surface methodology-process and product optimization using designed experiment, John Wiley & Sons, 1995.

[165] Rofin DC 015 Slab laser operating manual, Serial No. 2042/2042, 2002.

[166] Mechtronic Technology in Motion, http://www.mechtronic.co.uk/about.html (Accessed on 10/4/2006).

[167] W. E. Nickola, Practical subsurface residual stress evaluation by the hole drilling method, Proceedings of SEM spring Conference on Experimental Mechanics, New Orleans, LA. June 8-13-1986, pp. 47-57.

[168] C. P. Wu, L. W. Tsay and C. Chen, Notched tensile testing of T-200 maraging steel and its laser welds in hydrogen, J. of Materials Science and Engineering, Vol. A346, 2003, pp. 302-309.

[169] Annual book of ASTM standards, Metals test methods and analytical procedures, ASTM international, Vol. 03.01, 2003.

[170] R. Borrisutthekul, Y. Miyashits and Y. Mutoh, Dissimilar material laser welding between magnesium alloy AZ31B and aluminium alloy A5052-O, J. of Science and Technology of Advanced Materials, Vol. 6, 2005, pp. 199-204.

[171] Metals Handbook, Metallographic and Microstructures, American Society for Metals, Ninth Edition, Vol. 9, (1992).

[172] D. Havrilla and P. Anthony, Laser cutting process fundamentals and troubleshooting guideline, 2nd printing Rofin, 2002, p. 51.

[173] P. W. Fuerschbach, Measurement and Prediction of Energy Transfer Efficiency in Laser Welding, Welding Journal, 1996, Vol. 75, pp. 24s – 34s.

[174] D. R. Askeland, The Science and Engineering of materials, 3rd Edition, Chapman & Hall, 1996, pp. 352-400.

[175] I. Hrivak, Theory of weldability of metals and alloys, Materials Science Monographs 74, Elsevier, 1992.

[176] G. E. P. Box and J. S. Hunter, Multi-factor experimental design for exploring response surface, Ann. of Math. Stat. Vol. 28, 1957, pp. 195-241.

APPENDICES

Appendix A: Sample Excel-file spreadsheet

Data for 304 stainless steel, 3 mm near HAZ laser welding																
Sample 1																
Depth		Measured Strain micro strain		Relieved Strains			Coefficients							Direction	Equiv. Uniform stress to depth Z MPa	
Z mm	Z/D			e3 + e1	e3 - e1	e3 +e1 -2e2									min	max
0.127	0.025	e1	-9	-1.70E-05	1.00E-06	-2.30E-05	a	0.01170	b	0.02808				-43.76	31.29	189.52
		e2	3				A	-3.849E-08	B	-7.275E-08						
		e3	-8				4A	-1.540E-07	4B	-2.910E-07						
0.254	0.050	e1	-17	-3.10E-05	3.00E-06	-3.90E-05	a	0.02756	b	0.06552				-42.80	27.86	143.08
		e2	4				A	-9.068E-08	B	-1.697E-07						
		e3	-14				4A	-3.627E-07	4B	-6.790E-07						
0.508	0.099	e1	-30	-5.60E-05	4.00E-06	-6.60E-05	a	0.05300	b	0.14040				-43.27	34.84	125.73
		e2	5				A	-1.744E-07	B	-3.637E-07						
		e3	-26				4A	-6.975E-07	4B	-1.455E-06						
0.762	0.149	e1	-39	-7.70E-05	1.00E-06	-9.30E-05	a	0.09434	b	0.21645				-44.69	20.55	103.48
		e2	8				A	-3.104E-07	B	-5.608E-07						
		e3	-38				4A	-1.242E-06	4B	-2.243E-06						
1.016	0.198	e1	-44	-8.60E-05	2.00E-06	-1.04E-04	a	0.10812	b	0.26910				-44.45	23.14	97.74
		e2	9				A	-3.557E-07	B	-6.972E-07						
		e3	-42				4A	-1.423E-06	4B	-2.789E-06						
1.27	0.248	e1	-48	-9.50E-05	1.00E-06	-1.15E-04	a	0.12084	b	0.31239				-44.75	24.21	95.26
		e2	10				A	-3.976E-07	B	-8.093E-07						
		e3	-47				4A	-1.590E-06	4B	-3.237E-06						
2.052	0.400	e1	-52	-1.03E-04	1.00E-06	-1.29E-04	a	0.12800	b	0.36300				-44.78	26.85	95.44
		e2	13				A	-4.211E-07	B	-9.404E-07						
		e3	-51				4A	-1.685E-06	4B	-3.762E-06						

Data for 304 stainless steel, 3 mm, 10 mm from welding line, laser welding															
Sample 1															
Depth		Measured Strain micro strain		Relieved Strains			Coefficients							Direction	Equiv. Uniform stress to depth Z MPa	
Z mm	Z/D			e3 + e1	e3 - e1	e3 +e1 -2e2									min	max
0.127	0.025	e1	-2	-1.00E-05	-6.00E-06	2.00E-06	a	0.011	b	0.024				-9.22	43.65	94.51
		e2	-6				A	-3.619E-08	B	-6.218E-08						
		e3	-8				4A	-1.448E-07	4B	-2.487E-07						
0.254	0.050	e1	-3	-1.40E-05	-8.00E-06	8.00E-06	a	0.026	b	0.056				-22.50	21.42	60.41
		e2	-11				A	-8.554E-08	B	-1.451E-07						
		e3	-11				4A	-3.422E-07	4B	-5.803E-07						
0.508	0.099	e1	-5	-2.30E-05	-1.30E-05	1.10E-05	a	0.050	b	0.120				-20.12	21.26	48.65
		e2	-17				A	-1.645E-07	B	-3.109E-07						
		e3	-18				4A	-6.580E-07	4B	-1.244E-06						
0.762	0.149	e1	-8	-3.40E-05	-1.80E-05	1.00E-05	a	0.090	b	0.185				-14.53	17.96	39.45
		e2	-22				A	-2.961E-07	B	-4.793E-07						
		e3	-26				4A	-1.184E-06	4B	-1.917E-06						
1.016	0.198	e1	-8	-3.50E-05	-1.90E-05	1.30E-05	a	0.106	b	0.230				-17.19	15.43	34.75
		e2	-24				A	-3.488E-07	B	-5.959E-07						
		e3	-27				4A	-1.395E-06	4B	-2.383E-06						
1.27	0.248	e1	-9	-3.70E-05	-1.90E-05	1.30E-05	a	0.118	b	0.267				-17.19	15.50	32.15
		e2	-25				A	-3.882E-07	B	-6.917E-07						
		e3	-28				4A	-1.553E-06	4B	-2.767E-06						
2.052	0.400	e1	-8	-3.80E-05	-2.20E-05	1.40E-05	a	0.121	b	0.310				-16.24	15.75	31.98
		e2	-26				A	-3.981E-07	B	-8.031E-07						
		e3	-30				4A	-1.592E-06	4B	-3.212E-06						

Data for 304 stainless steel, 3 mm, 20 mm from welding centre-line, laser welding														
Sample 1														
Depth		Measured Strain micro strain		Relieved Strains			Coefficients					Direction	Equiv. Uniform stress to depth Z MPa	
Z mm	Z/D			e3 + e1	e3 - e1	e3 +e1 -2e2							min	max
0.127	0.025	e1	-3	-1.00E-06	5.00E-06	3.00E-06	a	0.011	b	0.024		15.48	-16.54	30.35
		e2	-2				A	-3.619E-08	B	-6.218E-08				
		e3	2				4A	-1.448E-07	4B	-2.487E-07				
0.254	0.050	e1	-6	-1.00E-06	1.10E-05	5.00E-06	a	0.026	b	0.056		12.22	-17.90	23.74
		e2	-3				A	-8.554E-08	B	-1.451E-07				
		e3	5				4A	-3.422E-07	4B	-5.803E-07				
0.508	0.099	e1	-10	-4.00E-06	1.60E-05	2.00E-06	a	0.050	b	0.120		3.56	-6.89	19.05
		e2	-3				A	-1.645E-07	B	-3.109E-07				
		e3	6				4A	-6.580E-07	4B	-1.244E-06				
0.762	0.149	e1	-14	-8.00E-06	2.00E-05	2.00E-06	a	0.090	b	0.185		2.86	-3.73	17.24
		e2	-5				A	-2.961E-07	B	-4.793E-07				
		e3	6				4A	-1.184E-06	4B	-1.917E-06				
1.016	0.198	e1	-16	-9.00E-06	2.30E-05	-1.00E-06	a	0.106	b	0.230		-1.24	-3.21	16.11
		e2	-4				A	-3.488E-07	B	-5.959E-07				
		e3	7				4A	-1.395E-06	4B	-2.383E-06				
1.27	0.248	e1	-17	-9.00E-06	2.50E-05	1.00E-06	a	0.118	b	0.267		1.15	-3.25	14.84
		e2	-5				A	-3.882E-07	B	-6.917E-07				
		e3	8				4A	-1.553E-06	4B	-2.767E-06				
2.052	0.400	e1	-18	-1.00E-05	2.60E-05	2.00E-06	a	0.121	b	0.310		2.20	-1.84	14.40
		e2	-6				A	-3.981E-07	B	-8.031E-07				
		e3	8				4A	-1.592E-06	4B	-3.212E-06				

Data for dissimilar laser welling of plain carbon + 304 stainless steel, 3 mm near HAZ plain carbon steel side															
Sample 1															
Depth		Measured Strain micro strain		Relieved Strains			Coefficients					Direction	Equiv. Uniform stress to depth Z MPa	
Z mm	Z/D			e3 + e1	e3 - e1	e3 +e1 -2e2							min	max
0.127	0.025	e1	-12	-2.20E-05	2.00E-06	-3.20E-05	a	0.01170	b	0.02808		-43.21	33.27	269.63
		e2	5				A	-3.632E-08	B	-6.783E-08				
		e3	-10				4A	-1.453E-07	4B	-2.713E-07				
0.254	0.050	e1	-22	-3.60E-05	8.00E-06	-5.60E-05	a	0.02756	b	0.06552		-40.93	15.85	194.57
		e2	10				A	-8.554E-08	B	-1.583E-07				
		e3	-14				4A	-3.422E-07	4B	-6.330E-07				
0.508	0.099	e1	-28	-5.20E-05	4.00E-06	-8.20E-05	a	0.05300	b	0.14040		-43.60	18.50	139.55
		e2	15				A	-1.645E-07	B	-3.391E-07				
		e3	-24				4A	-6.580E-07	4B	-1.357E-06				
0.762	0.149	e1	-36	-6.50E-05	7.00E-06	-1.03E-04	a	0.09434	b	0.21645		-43.06	6.13	104.86
		e2	19				A	-2.928E-07	B	-5.228E-07				
		e3	-29				4A	-1.171E-06	4B	-2.091E-06				
1.016	0.198	e1	-40	-7.30E-05	7.00E-06	-1.31E-04	a	0.10812	b	0.26910		-43.47	3.93	104.84
		e2	29				A	-3.356E-07	B	-6.500E-07				
		e3	-33				4A	-1.342E-06	4B	-2.600E-06				
1.27	0.248	e1	-43	-7.90E-05	7.00E-06	-1.47E-04	a	0.12084	b	0.31239		-43.64	3.90	101.42
		e2	34				A	-3.751E-07	B	-7.546E-07				
		e3	-36				4A	-1.500E-06	4B	-3.018E-06				
2.052	0.400	e1	-43	-7.90E-05	7.00E-06	-1.51E-04	a	0.12800	b	0.36300		-43.67	6.61	92.81
		e2	36				A	-3.973E-07	B	-8.768E-07				
		e3	-36				4A	-1.589E-06	4B	-3.507E-06				

Data for dissimilar plain carbon + 304 stainless steel near HAZ on stainless steel side, laser welding															
Sample 1															
Depth		Measured Strain micro strain		Relieved Strains			Coefficients						Direction	Equiv. Uniform stress to depth Z MPa	
Z mm	Z/D			e3 + e1	e3 - e1	e3 +e1 -2e2								min	max
0.127	0.025	e1	-11	-2.00E-05	2.00E-06	-3.60E-05	a	0.01170	b	0.02808			-43.41	5.98	253.80
		e2	8				A	-3.849E-08	B	-7.275E-08					
		e3	-9				4A	-1.540E-07	4B	-2.910E-07					
0.254	0.050	e1	-18	-3.20E-05	4.00E-06	-4.80E-05	a	0.02756	b	0.06552			-42.62	17.28	159.17
		e2	8				A	-9.068E-08	B	-1.697E-07					
		e3	-14				4A	-3.627E-07	4B	-6.790E-07					
0.508	0.099	e1	-27	-5.00E-05	4.00E-06	-7.80E-05	a	0.05300	b	0.14040			-43.53	18.00	125.36
		e2	14				A	-1.744E-07	B	-3.637E-07					
		e3	-23				4A	-6.975E-07	4B	-1.455E-06					
0.762	0.149	e1	-35	-6.50E-05	5.00E-06	-1.05E-04	a	0.09434	b	0.21645			-43.64	5.49	99.22
		e2	20				A	-3.104E-07	B	-5.608E-07					
		e3	-30				4A	-1.242E-06	4B	-2.243E-06					
1.016	0.198	e1	-39	-7.30E-05	5.00E-06	-1.19E-04	a	0.10812	b	0.26910			-43.80	8.59	94.01
		e2	23				A	-3.557E-07	B	-6.972E-07					
		e3	-34				4A	-1.423E-06	4B	-2.789E-06					
1.27	0.248	e1	-44	-8.20E-05	6.00E-06	-1.32E-04	a	0.12084	b	0.31239			-43.70	10.74	92.38
		e2	25				A	-3.976E-07	B	-8.093E-07					
		e3	-38				4A	-1.590E-06	4B	-3.237E-06					
2.052	0.400	e1	-46	-8.50E-05	7.00E-06	-1.39E-04	a	0.12800	b	0.36300			-43.56	13.46	87.46
		e2	27				A	-4.211E-07	B	-9.404E-07					
		e3	-39				4A	-1.685E-06	4B	-3.762E-06					

Appendix B: Practically measured data for AISI1045

Exp. No.	WZ Width [mm]	WZ penetration [mm]	Width of HAZ [mm]	Joint operating cost €/m	Heat input [J/cm]	Three results of Impact strength [J]			Av. Impact Energy [J]	Max. load kN			NTS MPa
1	2.358	3.572	0.561	0.4146	1920	60	56	55	57	7.391	7.071	7.119	400
2	2.805	4.322	0.872	0.4316	2280	75	76	79	77	7.985	8.262	8.149	452
3	1.342	2.705	0.392	0.1777	823	27	33	35	32	4.468	3.757	3.649	220
4	1.852	3.651	0.384	0.1850	977	55	45	51	50	4.794	5.059	4.679	269
5	2.761	2.655	0.453	0.2488	1152	36	36	33	35	3.130	4.136	3.613	201
6	3.381	3.888	0.569	0.2590	1368	55	58	52	55	4.389	4.596	3.977	240
7	2.087	3.813	0.511	0.2488	1152	53	52	55	53	5.323	6.242	6.307	331
8	2.572	4.539	0.574	0.2590	1368	68	71	66	68	6.344	7.680	7.058	390
9	3.681	3.905	0.625	0.4231	2100	50	47	51	49	6.723	6.639	6.137	361
10	1.982	2.367	0.375	0.1813	900	26	27	22	25	1.935	2.112	1.876	110
11	2.423	4.987	0.762	0.4231	2100	56	58	61	58	7.748	6.726	7.570	408
12	1.649	3.824	0.413	0.1813	900	32	35	32	33	4.648	5.266	5.128	279
13	2.625	3.712	0.531	0.2539	1260	41	37	42	40	5.848	6.238	5.940	334
14	2.282	3.872	0.562	0.2539	1260	38	40	37	38	6.525	5.618	5.842	333
15	2.567	3.586	0.466	0.2539	1260	44	39	42	42	6.166	6.252	5.878	339
16	2.413	3.505	0.478	0.2539	1260	36	47	35	39	5.693	6.412	5.762	331
17	2.293	3.626	0.506	0.2539	1260	40	43	39	41	6.348	5.712	6.143	337
18 C_1	2.428	4.012	0.573	0.2556	1296	39	41	45	42	5.348	5.648	5.685	309
19 C_2	2.703	4.407	0.714	0.4229	2100	60	55	54	56	7.885	6.859	7.665	415
20 C_3	2.398	3.962	0.579	0.2538	1260	47	53	49	50	6.842	6.784	5.968	363

Appendix C: Practically measured data for AISI304 3 mm.

Table C-1: Bead geometry for 3 mm butt welding of AISI304

No.	Front Width			Average Front Width, mm	Back width			Average Back width, mm	Weld pool area mm^2			Average area, mm^2
	1	2	3		1	2	3		1	2	3	
1	3.002	3.214	3.393	3.203	2.042	1.935	2.035	2.004	7.109	7.701	6.925	7.245
2	3.409	3.485	3.361	3.418	1.997	2.164	2.138	2.100	9.270	9.053	9.138	9.154
3	2.655	2.668	2.677	2.667	0.613	0.644	0.574	0.610	4.902	5.168	4.780	4.950
4	2.760	2.878	2.980	2.873	0.847	0.925	0.912	0.895	5.801	6.019	5.574	5.798
5	3.188	3.137	3.292	3.206	1.541	1.747	1.751	1.680	9.166	9.117	8.776	9.020
6	3.527	3.464	3.478	3.490	1.748	1.926	1.977	1.884	9.454	9.259	9.817	9.510
7	2.875	2.793	2.699	2.789	0.599	0.718	0.559	0.625	4.662	4.766	4.699	4.709
8	2.950	2.850	2.921	2.907	0.847	0.806	0.798	0.817	5.813	5.657	5.423	5.631
9	2.769	2.781	2.728	2.759	0.478	0.523	0.482	0.494	3.821	5.209	4.590	5.204
10	3.618	3.231	3.283	3.377	1.098	0.801	0.959	0.953	7.484	7.387	7.243	6.150
11	3.615	3.753	3.745	3.704	2.842	2.962	2.757	2.854	11.394	11.367	11.229	10.027
12	2.377	2.455	2.292	2.375	0.735	0.765	0.877	0.792	4.854	4.859	4.723	6.992
13	3.403	3.553	3.531	3.496	1.136	1.126	1.142	1.135	7.055	6.949	6.946	6.250
14	2.342	2.316	2.297	2.318	1.534	1.712	1.675	1.640	6.763	7.004	6.951	7.003
15	3.433	3.440	3.410	3.428	1.193	1.030	1.212	1.145	6.166	6.064	6.208	6.345
16	2.913	3.074	2.936	2.974	1.149	1.130	1.008	1.096	7.143	5.738	6.847	6.576
17	2.907	3.182	3.109	3.066	1.111	1.025	1.192	1.109	6.673	6.926	6.649	6.749
18	2.948	2.897	3.102	2.982	1.089	1.218	1.127	1.145	6.450	6.996	6.421	6.622
19	3.362	2.929	2.946	3.079	1.254	1.052	0.975	1.094	6.175	6.798	7.018	6.664
20	2.982	2.973	3.108	3.021	1.129	1.106	1.201	1.145	6.494	6.372	6.802	6.556

Table C-2: Mechanical properties, heat input & joint cost for 3 mm butt welding of AISI304.

Exp. No.	Heat input [J/cm]	Three results of Impact strength [J]			Av. Impact Energy [J]	Three results of Max load [kN]			Av. Tensile strength [MPa]	Joint cost [€/m]
1	1886	34	38	39	37	12.007	12.121	11.839	666	0.3489
2	2229	42	47	40	43	11.125	11.239	10.811	614	0.3619
3	1100	30	36	38	35	11.664	11.483	11.570	643	0.2035
4	1300	38	39	38	38	11.633	10.905	11.597	632	0.2111
5	1886	44	42	44	43	11.612	12.026	11.562	652	0.3489
6	2229	48	47	45	47	11.772	11.148	11.624	640	0.3619
7	1100	39	38	41	39	9.274	9.658	9.985	536	0.2035
8	1300	42	40	43	42	11.217	11.074	11.243	621	0.2111
9	1303	27	26	28	27	9.852	9.772	9.838	546	0.2537
10	1728	40	42	40	41	9.862	9.048	9.655	529	0.2700
11	2719	46	45	43	45	11.934	12.231	11.782	666	0.4694
12	1051	41	34	36	37	11.543	11.502	11.335	637	0.1816
13	1516	40	42	40	41	11.919	11.832	11.778	658	0.2619
14	1516	40	44	50	45	10.443	11.805	11.711	629	0.2619
15	1516	42	40	41	41	12.624	12.237	12.530	692	0.2619
16	1516	40	46	44	43	11.765	11.658	12.087	658	0.2619
17	1516	44	43	43	43	11.127	11.604	11.275	630	0.2619
18	1516	46	44	42	44	11.859	10.812	11.764	638	0.2619
19	1516	40	43	45	43	12.154	12.147	12.000	672	0.2619
20	1516	43	47	44	45	11.654	12.215	12.382	671	0.2619

Table C-3: practically measured micro-strains for AISI304 near HAZ.

Depth		Measured Strain micro strain	Sample No.																			
Z mm	Z/D		1	2	3	4	5	6	7	8	9	10	11	12	13	14	15	16	17	18	19	20
0.127	0.025	e1	-9	-11	-8	-11	-13	-14	-7	-11	-12	-16	-28	-8	-10	-11	-11	-10	-9	-10	-10	-10
		e2	3	1	1	-5	2	2	1	-4	-3	-5	-12	-1	-2	-4	-2	-1	-1	-1	-2	-1
		e3	-8	-10	-6	-10	-12	-13	-7	-9	-8	-10	-7	-7	-8	-10	-10	-8	-9	-8	-9	-8
0.254	0.050	e1	-17	-19	-13	-17	-21	-22	-15	-20	-21	-22	-41	-15	-16	-20	-18	-17	-17	-17	-18	-17
		e2	4	3	2	-3	3	7	0	-9	-9	-7	-15	0	-2	-8	-1	-2	-2	-3	-1	-3
		e3	-14	-16	-11	-16	-20	-20	-14	-19	-19	-20	-15	-15	-14	-19	-16	-16	-17	-17	-16	-16
0.508	0.099	e1	-30	-31	-24	-28	-34	-36	-27	-36	-34	-36	-55	-29	-29	-39	-29	-29	-30	-31	-32	-29
		e2	5	6	4	1	7	8	3	-15	-13	-10	-17	1	0	-23	2	1	-3	-3	1	2
		e3	-26	-29	-22	-28	-33	-30	-24	-32	-31	-33	-27	-27	-26	-39	-27	-28	-30	-28	-28	-27
0.762	0.149	e1	-39	-39	-34	-35	-43	-43	-39	-51	-54	-47	-59	-33	-41	-52	-39	-37	-39	-42	-37	-37
		e2	8	8	6	4	9	10	5	-29	-14	-12	-18	3	1	-20	3	4	-1	-5	4	3
		e3	-38	-36	-27	-34	-42	-41	-33	-49	-47	-42	-41	-32	-33	-43	-36	-36	-37	-38	-36	-36
1.016	0.198	e1	-44	-45	-41	-40	-46	-48	-39	-56	-52	-52	-66	-41	-48	-59	-44	-41	-46	-47	-43	-44
		e2	9	10	8	5	11	12	7	-31	-12	-13	-18	4	2	-28	4	6	0	-7	5	4
		e3	-42	-43	-32	-39	-45	-47	-38	-54	-49	-47	-48	-35	-40	-55	-40	-39	-42	-44	-42	-39
1.27	0.248	e1	-48	-50	-44	-45	-50	-53	-44	-60	-53	-56	-68	-43	-55	-66	-47	-45	-50	-48	-46	-49
		e2	10	12	9	6	13	14	8	-32	-11	-11	-18	5	2	-27	6	7	1	-8	7	4
		e3	-47	-46	-34	-44	-48	-50	-41	-59	-50	-49	-57	-37	-43	-59	-42	-43	-46	-47	-45	-44
2.052	0.400	e1	-52	-54	-46	-49	-55	-57	-43	-64	-57	-61	-73	-48	-58	-65	-50	-47	-52	-53	-48	-51
		e2	13	14	12	7	16	17	11	-34	-9	-8	-20	5	2	-27	7	10	3	-9	8	6
		e3	-51	-51	-37	-48	-49	-50	-43	-62	-52	-55	-60	-39	-46	-62	-45	-46	-49	-52	-47	-47

Table C-4: practically measured micro-strains for AISI304 10 mm from weld centreline.

Depth		Measured Strain micro strain	sample no.																			
Z mm	Z/D		1	2	3	4	5	6	7	8	9	10	11	12	13	14	15	16	17	18	19	20
0.127	0.025	e1	-2	-3	-2	-7	-7	-9	-3	-7	-4	-7	-11	-5	-6	-7	-4	-4	-4	-2	-2	-2
		e2	-6	-7	-4	-4	-7	-6	-4	-5	-1	-4	-6	-2	-4	-4	-3	-4	-3	-4	-3	-5
		e3	-8	-9	-5	-2	-6	-4	-5	-2	-2	-1	0	-1	-1	-1	-1	-1	-1	-5	-4	-4
0.254	0.050	e1	-3	-5	-2	-10	-12	-15	-7	-10	-6	-11	-17	-7	-9	-13	-9	-9	-8	-3	-3	-3
		e2	-11	-10	-5	-7	-9	-10	-7	-10	-4	-8	-10	-3	-5	-6	-7	-5	-5	-6	-4	-6
		e3	-11	-15	-7	-3	-7	-5	-7	-4	-4	-3	-2	-3	-4	-3	-3	-3	-2	-10	-8	-10
0.508	0.099	e1	-5	-7	-3	-17	-20	-27	-9	-17	-9	-19	-28	-10	-16	-20	-15	-15	-15	-4	-5	-6
		e2	-17	-15	-8	-12	-11	-19	-12	-18	-8	-12	-19	-6	-7	-10	-13	-9	-8	-9	-7	-12
		e3	-18	-25	-11	-4	-8	-7	-11	-9	-8	-4	-4	-8	-5	-5	-4	-5	-3	-16	-11	-16
0.762	0.149	e1	-8	-9	-4	-23	-31	-39	-16	-26	-14	-28	-42	-16	-20	-30	-26	-21	-21	-5	-7	-7
		e2	-22	-33	-13	-14	-17	-26	-15	-21	-9	-17	-26	-8	-7	-13	-21	-13	-11	-12	-9	-16
		e3	-26	-33	-16	-5	-12	-8	-14	-10	-9	-8	-6	-10	-6	-8	-5	-6	-4	-20	-15	-21
1.016	0.198	e1	-8	-10	-4	-27	-29	-40	-18	-27	-14	-29	-42	-19	-21	-28	-27	-25	-25	-5	-7	-7
		e2	-24	-24	-15	-17	-18	-27	-16	-22	-11	-17	-27	-8	-9	-16	-22	-15	-14	-14	-10	-18
		e3	-27	-37	-18	-5	-11	-8	-15	-11	-11	-7	-3	-10	-7	-8	-6	-7	-5	-22	-17	-25
1.27	0.248	e1	-9	-11	-3	-28	-30	-43	-20	-29	-15	-32	-45	-21	-23	-30	-28	-27	-27	-4	-7	-8
		e2	-25	-24	-16	-19	-19	-32	-17	-23	-12	-17	-29	-9	-10	-16	-23	-16	-15	-14	-11	-19
		e3	-28	-39	-19	-4	-12	-8	-16	-12	-13	-5	-2	-11	-7	-8	-7	-7	-5	-24	-19	-27
2.052	0.400	e1	-8	-12	-1	-30	-32	-45	-21	-31	-17	-34	-48	-23	-24	-30	-30	-28	-29	-3	-7	-9
		e2	-26	-27	-17	-20	-20	-34	-18	-25	-13	-21	-31	-9	-13	-17	-24	-17	-19	-16	-12	-20
		e3	-30	-40	-20	-2	-11	-8	-17	-12	-13	-5	-1	-10	-8	-8	-6	-7	-6	-26	-19	-29

Table C-5: practically measured micro-strains for AISI304 20 mm from weld centreline.

Depth		Measured Strain micro strain	sample no.																			
Z mm	Z/D		1	2	3	4	5	6	7	8	9	10	11	12	13	14	15	16	17	18	19	20
0.127	0.025	e1	-3	-3	-1	-2	-3	-1	-2	-2	-2	-3	-3	-1	-1	-1	-2	-3	-2	-2	-2	-2
		e2	-2	-2	-2	-2	-3	-3	-1	-2	-1	-2	-3	-2	-2	-3	0	-1	-2	0	-2	-2
		e3	2	0	-1	1	0	-3	-1	0	-1	-1	-3	-1	-2	-1	0	1	-1	0	0	1
0.254	0.050	e1	-6	-5	-3	-4	-6	-5	-2	-4	-4	-5	-4	-3	-2	-4	-5	-6	-5	-5	-4	-3
		e2	-3	-5	-4	-4	-1	-4	-4	-4	-1	-4	-5	-3	-5	-5	-1	-2	-3	-1	-4	-5
		e3	5	0	-1	1	1	-4	-2	-1	-1	-2	-5	-2	-3	-3	2	2	0	1	1	1
0.508	0.099	e1	-10	-8	-5	-8	-9	-8	-7	-8	-6	-8	-7	-6	-5	-8	-8	-9	-7	-8	-7	-6
		e2	-3	-7	-6	-5	2	-7	-3	-3	-2	-5	-8	-4	-7	-10	-3	-4	-4	-5	-6	-7
		e3	6	-1	-2	2	3	-7	-1	-2	-1	-4	-8	-2	-7	-5	3	3	0	2	1	1
0.762	0.149	e1	-14	-13	-7	-11	-12	-14	-12	-12	-10	-13	-13	-10	-9	-13	-11	-11	-12	-10	-11	-10
		e2	-5	-11	-9	-8	3	-10	-5	-5	-5	-8	-14	-5	-10	-15	-7	-8	-6	-9	-8	-10
		e3	6	-3	-3	0	3	-8	0	-4	-3	-7	-13	-2	-8	-9	3	3	1	3	2	2
1.016	0.198	e1	-16	-15	-9	-13	-13	-16	-14	-13	-12	-15	-15	-12	-11	-15	-13	-13	-14	-12	-13	-13
		e2	-4	-11	-10	-9	6	-10	-7	-4	-7	-10	-15	-6	-11	-16	-8	-9	-8	-10	-9	-10
		e3	7	-3	-4	-2	4	-8	0	-4	-4	-7	-14	-2	-10	-10	4	5	2	5	3	3
1.27	0.248	e1	-17	-16	-11	-15	-13	-16	-15	-14	-13	-16	-16	-13	-12	-16	-14	-15	-15	-14	-15	-15
		e2	-5	-13	-10	-10	6	-10	-8	-4	-9	-13	-16	-7	-12	-17	-10	-10	-10	-11	-10	-11
		e3	8	-3	-4	-2	4	-9	0	-5	-5	-8	-15	-2	-11	-10	5	6	3	6	4	4
2.052	0.400	e1	-18	-18	-11	-16	-13	-18	-16	-15	-13	-17	-17	-16	-13	-17	-17	-17	-17	-16	-16	-16
		e2	-6	-15	-11	-11	10	-11	-8	-5	-9	-14	-16	-7	-12	-17	-11	-12	-11	-11	-12	-12
		e3	8	-4	-5	-2	6	-9	1	-4	-4	-8	-15	-2	-10	-10	5	7	6	7	5	6

Table C-6: Confirmation results for bead geometry.

No.	Front width, mm			Av. Front width	Pred.	Error %	Back width, mm			Av. Back width	Pred.	Error %	Weld pool Area, mm^2			Av. Weld area	Pred.	Error %
C1	3.100	3.064	3.211	3.125	3.24466	-3.688	2.155	1.995	1.930	2.027	2.0829	-2.700	8.666	9.210	8.990	8.955	8.6774	3.203
C2	2.757	2.896	2.434	2.696	2.89584	-6.913	0.944	0.840	0.830	0.871	0.8648	0.751	5.594	5.566	5.329	5.496	5.9749	-8.010
C3	3.371	3.186	3.164	3.240	3.16094	2.512	1.632	1.643	1.621	1.632	1.7786	-8.245	7.900	7.643	7.501	7.681	7.9312	-3.151

Table C-7: Confirmation results for mechanical properties & joint cost.

No.	Tensile strength, MPa			Av. TS.	Pred.	Error %	Impact strength, J			AV. IS	Pred.	Error %	Joint cost E/m	Pred.	Error %
C1	685	676	-	681	677	0.509	46	48	44	46	47	-1.757	0.3554	0.362	-1.7998
C2	626	628	626	627	670	-6.987	42	38	41	40	39	2.315	0.2081	0.205	1.4049
C3	715	710	706	710	668	5.994	46	50	46	47	46	1.955	0.3207	0.3266	-1.8314

Appendix D: Practically measured data for AISI304 1 mm lap joint.

Table D-1: Bead geometry for 1 mm lap joint of AISI304

No.	Front Width			Average Front Width, mm	Back width			Average Back width, mm	Weld pool area mm^2			Average area, mm^2	Half penetration width			Average half penetration width, mm
	1	2	3		1	2	3		1	2	3		1	2	3	
1	2.215	2.072	2.302	2.196	0.832	1.007	1.127	0.989	4.059	4.419	4.182	4.220	1.362	1.783	1.935	1.693
2	1.919	2.255	2.028	2.067	0.876	1.141	1.120	1.046	3.845	4.153	3.903	3.967	1.345	1.778	1.628	1.584
3	1.806	1.848	1.799	1.818	0.588	0.623	0.585	0.599	2.829	2.828	2.700	2.786	0.997	0.959	0.897	0.951
4	1.686	1.723	1.821	1.743	0.564	0.568	0.572	0.568	2.827	2.611	2.307	2.582	0.819	0.827	0.902	0.849
5	1.910	1.978	1.962	1.950	0.630	0.721	0.741	0.697	3.262	3.310	3.472	3.348	1.301	1.427	1.362	1.363
6	1.827	2.082	1.904	1.938	1.196	1.205	1.130	1.177	3.890	4.106	3.794	3.930	1.355	1.536	1.474	1.455
7	1.455	1.704	1.701	1.620	0.584	0.661	0.612	0.619	2.553	2.698	2.709	2.653	0.800	0.863	0.792	0.818
8	1.719	1.600	1.621	1.647	0.688	0.703	0.785	0.725	2.558	2.480	2.467	2.502	0.815	0.757	0.812	0.795
9	2.113	2.039	2.167	2.106	0.715	0.708	0.721	0.715	3.264	3.573	3.522	3.218	1.244	1.395	1.317	1.319
10	1.749	1.722	1.717	1.729	0.819	0.841	0.801	0.820	3.171	2.892	3.167	3.108	1.131	1.092	1.098	1.107
11	2.165	2.180	2.218	2.188	1.440	1.359	1.398	1.399	4.481	4.755	4.279	4.068	1.902	1.797	1.821	1.840
12	1.688	1.825	1.487	1.667	0.628	0.596	0.571	0.598	2.503	2.290	2.296	3.022	0.712	0.690	0.735	0.712
13	1.954	1.985	1.971	1.970	0.773	0.782	0.787	0.781	3.466	3.201	2.901	2.868	1.369	1.363	1.347	1.360
14	1.798	1.693	1.672	1.721	0.676	0.820	0.717	0.738	2.707	3.171	3.383	3.340	1.146	0.968	0.917	1.010
15	2.021	1.812	2.161	1.998	0.718	0.744	0.727	0.730	3.483	3.132	3.290	3.043	1.354	1.171	1.323	1.283
16	1.846	2.203	1.917	1.989	0.715	0.735	0.721	0.724	3.227	3.169	3.302	3.233	1.241	1.174	1.128	1.181
17	1.877	2.107	2.018	2.001	0.786	0.704	0.761	0.750	3.724	3.240	3.164	3.376	1.103	1.297	1.172	1.191
18	1.923	2.071	1.981	1.992	0.701	0.726	0.741	0.723	3.288	3.543	3.127	3.319	1.078	1.162	1.203	1.148
19	2.104	1.948	1.952	2.001	0.676	0.698	0.762	0.712	3.216	3.172	3.104	3.164	1.124	1.247	1.148	1.173
20	1.956	2.140	1.897	1.998	0.711	0.721	0.708	0.713	3.178	3.206	3.171	3.185	1.132	1.210	1.201	1.181

Table D-2: Joint cost, heat input & failure load for 1 mm lap joint of AISI304

Exp. No.	Joint cost €/m	Heat input [J/cm]	Three results of Max load kN			Av. Fracture load, kN
1	0.1744	943	9.246	8.786	9.213	9.082
2	0.1826	1157	8.974	8.859	8.499	8.777
3	0.0939	508	7.96	7.495	8.021	7.825
4	0.0983	623	7.495	7.697	7.592	7.595
5	0.1744	943	8.577	9.047	8.832	8.819
6	0.1826	1157	8.625	8.588	8.682	8.632
7	0.0939	508	7.372	7.471	7.57	7.471
8	0.0983	623	7.208	7.377	7.474	7.353
9	0.1202	609	8.325	8.652	7.946	8.308
10	0.1297	861	8.239	8.22	8.123	8.194
11	0.2522	1483	9.251	8.956	8.765	8.991
12	0.0831	489	7.237	7.068	6.301	6.869
13	0.1250	735	8.161	8.636	8.113	8.303
14	0.1250	735	8.037	8.019	8.064	8.040
15	0.1250	735	7.933	7.756	8.137	7.942
16	0.1250	735	8.647	7.565	8.607	8.273
17	0.1250	735	8.392	8.456	8.373	8.407
18	0.1250	735	8.086	8.228	7.122	7.812
19	0.1250	735	7.855	8.236	8.171	8.087
20	0.1250	735	7.933	7.45	8.368	7.917

Table D-3: Confirmation results for bead geometry.

No.	Front width, mm			Av. Front width	Pred.	Error %	Back width, mm			Av. Back width	Pred.	Error %	width of half penetration, mm			Av. WHP	Pred.	Error %
C1	2.178	2.246	2.131	2.185	2.061	5.660	0.724	0.977	0.816	0.839	0.765	8.838	1.463	1.452	1.298	1.404	1.357	3.405
C2	2.092	2.077	2.088	2.086	1.980	5.066	0.741	0.693	0.717	0.717	0.689	3.948	1.332	1.254	1.261	1.282	1.196	6.738
C3	2.054	1.752	2.012	1.939	1.970	-1.559	0.694	0.707	0.712	0.704	0.682	3.129	1.249	1.151	1.233	1.211	1.177	2.813

Table D-4: Confirmation results for area of WZ.

No.	Area of weld pool/ mm^2			Av. Area	Pred.	Error %
C1	3.412	3.387	3.160	3.320	3.289	0.935
C2	3.060	3.028	3.154	3.081	3.054	0.880
C3	3.092	3.146	2.982	3.073	3.026	1.548

Table D-5: Confirmation results for failure load, heat input & joint cost.

No.	failure load, kN			Av. Failure load	Pred.	Error %	Heat input	Pred.	Error %	Joint cost	Pred.	Error %
C1	8.172	8.440	8.271	8.294	8.393	-1.188	678	672.299	0.841	0.1254	0.1251	0.239
C2	8.064	7.917	8.024	8.002	8.054	-0.657	590	560.656	4.974	0.1092	0.1039	4.853
C3	7.712	8.408	7.656	7.925	8.090	-2.079	581	570.1331	1.870	0.1076	0.1058	1.713

Appendix E: Practically measured data for dissimilar welding

Table E-1: Bead geometry for dissimilar welding.

No.	Front Width			Average Front Width, mm	Back width			Average Back width, mm	Weld pool area mm^2			Average area, mm^2
	1	2	3		1	2	3		1	2	3	
1	2.232	2.267	2.218	2.239	1.215	0.848	0.968	1.010	4.512	4.26	4.404	4.392
2	2.823	2.488	2.632	2.648	1.168	1.278	1.312	1.253	6.252	6.387	7.642	6.760
3	1.342	1.421	1.352	1.372	0.589	0.523	0.493	0.535	3.429	4.486	3.583	3.833
4	1.792	1.754	1.838	1.795	0.711	0.61	0.569	0.630	4.739	4.462	4.716	4.639
5	2.054	2.236	2.193	2.161	1.732	1.846	1.311	1.630	6.876	7.203	6.61	6.896
6	2.399	2.652	2.356	2.469	2.189	2.144	2.108	2.147	7.034	8.191	7.623	7.616
7	1.317	1.313	1.266	1.299	0.568	0.552	0.612	0.577	3.926	3.577	3.367	3.623
8	1.693	1.509	1.638	1.613	0.506	0.527	0.441	0.491	4.363	4.456	4.243	4.354
9	1.641	1.58	1.567	1.596	0.582	0.619	0.649	0.617	4.427	4.279	4.048	4.230
10	2.382	2.165	1.983	2.177	1.356	1.367	1.337	1.353	6.399	6.91	5.845	5.727
11	3.401	3.386	3.435	3.407	2.866	2.651	2.702	2.740	10.48	10.911	10.718	9.343
12	1.201	1.124	1.029	1.118	0.603	0.572	0.62	0.598	2.972	2.702	2.845	5.342
13	1.64	1.825	1.861	1.775	0.806	0.821	0.798	0.808	5.034	4.981	5.094	4.349
14	1.444	1.434	1.396	1.425	0.892	0.85	0.847	0.824	4.32	4.216	4.29	4.513
15	1.635	1.922	1.803	1.787	0.776	0.679	0.691	0.701	4.207	4.481	4.826	4.542
16	1.571	1.618	1.527	1.572	0.732	0.821	0.724	0.734	4.674	6.21	4.316	5.067
17	1.663	1.868	1.807	1.779	0.657	0.661	0.589	0.657	5.104	5.223	5.245	5.191
18	1.728	1.824	1.791	1.781	0.721	0.772	0.765	0.758	4.954	5.174	4.986	5.038
19	1.752	1.755	1.757	1.755	0.738	0.818	0.916	0.822	5.121	5.524	4.795	5.147
20	1.621	1.782	1.764	1.722	0.732	0.82	0.817	0.790	6.078	5.306	5.291	5.558

Table E-2: Joint cost, heat input and impact strength for dissimilar welding.

Exp. No.	Joint cost €/m	Heat input J/cm	Three results of Impact strength [J]			Av. Impact Energy [J]
1	0.3508	1937	30	30	32	31
2	0.3651	2314	40	38	40	39
3	0.1889	1043	20	22	20	21
4	0.1966	1246	26	26	28	27
5	0.3508	1937	32	35	33	33
6	0.3651	2314	38	40	42	40
7	0.1889	1043	22	24	26	24
8	0.1966	1246	28	29	32	30
9	0.2422	1266	30	29	31	30
10	0.2590	1710	41	38	41	40
11	0.5058	3003	31	33	33	32
12	0.1666	989	20	18	22	20
13	0.2506	1488	24	26	24	25
14	0.2506	1488	36	34	32	34
15	0.2506	1488	28	32	33	31
16	0.2506	1488	29	26	32	29
17	0.2506	1488	27	28	27	27
18	0.2506	1488	32	34	31	32
19	0.2506	1488	28	26	35	30
20	0.2506	1488	30	28	28	29

Table E-3: Practically measured micro-strains for dissimilar welding near HAZ at AISI1016 side.

Depth		Measured Strain micro strain	sample no.																			
Z mm	Z/D		1	2	3	4	5	6	7	8	9	10	11	12	13	14	15	16	17	18	19	20
0.127	0.025	e1	-12	-13	-7	-10	-10	-13	-9	-12	-9	-10	-14	-9	-10	-11	-10	-9	-9	-11	-8	-8
		e2	5	7	6	6	13	9	7	4	3	8	9	4	3	3	3	5	7	5	9	7
		e3	-10	-10	-5	-9	-7	-10	-4	-9	-8	-9	-13	-7	-6	-7	-8	-8	-7	-6	-6	-7
0.254	0.050	e1	-22	-21	-11	-15	-15	-23	-16	-20	-16	-16	-22	-15	-15	-18	-18	-17	-18	-18	-16	-16
		e2	10	10	11	8	23	13	9	5	6	12	15	10	9	7	7	8	9	9	11	11
		e3	-14	-17	-10	-13	-13	-15	-12	-17	-12	-15	-20	-12	-11	-13	-15	-15	-14	-13	-15	-15
0.508	0.099	e1	-28	-27	-20	-25	-24	-30	-28	-28	-25	-26	-32	-25	-25	-29	-29	-28	-25	-28	-27	-27
		e2	15	16	17	14	32	18	10	9	7	14	19	15	14	10	10	11	11	15	14	13
		e3	-24	-26	-19	-24	-21	-25	-23	-26	-22	-22	-31	-22	-20	-23	-28	-26	-22	-25	-24	-27
0.762	0.149	e1	-36	-35	-27	-29	-32	-40	-36	-35	-34	-34	-36	-30	-32	-37	-36	-35	-34	-35	-35	-33
		e2	19	19	23	20	38	20	12	11	13	18	23	17	17	16	15	15	17	17	17	18
		e3	-29	-32	-25	-27	-27	-32	-30	-33	-32	-31	-34	-26	-28	-32	-32	-31	-29	-31	-29	-32
1.016	0.198	e1	-40	-40	-32	-30	-35	-46	-40	-40	-37	-39	-41	-35	-37	-40	-39	-39	-36	-38	-37	-37
		e2	29	27	28	29	44	25	15	15	15	24	26	21	21	19	17	18	19	21	22	21
		e3	-33	-37	-29	-32	-31	-35	-34	-37	-36	-33	-39	-29	-33	-35	-36	-33	-32	-34	-34	-35
1.27	0.248	e1	-43	-46	-35	-37	-39	-49	-43	-43	-40	-41	-43	-40	-42	-44	-42	-42	-39	-42	-40	-41
		e2	34	29	33	33	46	27	19	18	22	27	28	21	26	25	21	19	22	22	23	22
		e3	-36	-41	-32	-33	-34	-37	-39	-40	-37	-36	-40	-32	-35	-38	-38	-37	-35	-36	-35	-36
2.052	0.400	e1	-43	-46	-40	-40	-42	-51	-45	-46	-41	-45	-47	-43	-43	-46	-45	-44	-43	-43	-42	-44
		e2	36	30	36	36	47	30	22	21	23	28	31	22	27	26	22	21	24	25	26	24
		e3	-36	-42	-33	-35	-35	-39	-40	-41	-40	-38	-42	-34	-36	-39	-40	-39	-38	-39	-39	-39

Table E-4: Practically measured micro-strains for dissimilar welding near HAZ at AISI304 side.

Depth		Measured Strain micro strain	Sample no.																			
Z mm	Z/D		1	2	3	4	5	6	7	8	9	10	11	12	13	14	15	16	17	18	19	20
0.127	0.025	e1	-11	-15	-7	-9	-13	-15	-8	-9	-9	-12	-20	-8	-8	-9	-9	-10	-9	-8	-10	-9
		e2	8	4	3	4	3	5	5	4	3	4	7	5	4	4	2	3	4	5	3	2
		e3	-9	-11	-6	-7	-11	-11	-6	-9	-8	-11	-9	-7	-7	-8	-8	-6	-7	-7	-6	-8
0.254	0.050	e1	-18	-23	-13	-17	-23	-24	-17	-17	-16	-20	-33	-16	-16	-18	-17	-19	-18	-16	-17	-20
		e2	8	6	5	5	2	6	5	6	4	5	8	6	5	6	3	3	4	6	5	3
		e3	-14	-17	-11	-14	-20	-17	-14	-15	-14	-17	-13	-14	-11	-15	-17	-15	-15	-16	-15	-14
0.508	0.099	e1	-27	-35	-20	-27	-39	-34	-28	-26	-24	-30	-45	-28	-26	-29	-33	-35	-33	-34	-35	-36
		e2	14	6	9	7	-4	7	7	9	8	5	10	7	6	8	4	5	5	7	6	5
		e3	-23	-26	-18	-20	-29	-28	-25	-22	-22	-25	-25	-25	-23	-27	-32	-30	-31	-29	-27	-28
0.762	0.149	e1	-35	-43	-26	-35	-45	-45	-36	-35	-35	-36	-52	-35	-38	-38	-41	-43	-41	-40	-42	-44
		e2	20	9	12	7	-7	9	9	12	11	7	10	8	7	10	4	6	7	8	8	6
		e3	-30	-33	-23	-30	-38	-32	-33	-31	-28	-33	-30	-29	-31	-36	-41	-39	-38	-38	-35	-34
1.016	0.198	e1	-39	-48	-30	-41	-50	-49	-45	-42	-40	-41	-59	-41	-44	-45	-47	-47	-45	-45	-48	-49
		e2	23	10	16	8	-8	10	10	13	12	10	11	9	8	11	4	7	8	9	9	8
		e3	-34	-36	-27	-35	-45	-37	-36	-35	-35	-37	-39	-34	-35	-43	-47	-45	-44	-44	-40	-42
1.27	0.248	e1	-44	-53	-33	-43	-55	-52	-52	-47	-43	-44	-64	-45	-45	-50	-49	-50	-51	-51	-54	-53
		e2	25	11	17	9	-10	11	11	15	13	12	11	9	9	12	5	7	9	10	10	9
		e3	-38	-41	-29	-36	-48	-41	-40	-37	-40	-41	-43	-39	-41	-45	-48	-46	-44	-45	-42	-44
2.052	0.400	e1	-46	-55	-35	-47	-57	-54	-54	-48	-47	-50	-66	-47	-49	-52	-53	-53	-53	-53	-56	-55
		e2	27	12	18	9	-9	12	12	18	14	13	13	11	10	13	6	9	11	12	11	11
		e3	-39	-43	-30	-39	-52	-43	-42	-42	-42	-43	-46	-40	-43	-46	-51	-50	-47	-46	-45	-45

Table E-5: Confirmation results for bead geometry.

No.	Front width, mm			Av. Front width	Pred.	Error %	Back width, mm			Av. Back width	Pred.	Error %	Weld pool Area, mm^2			Av. Weld area	Pred.	Error %
C1	2.104	2.235	2.396	2.245	2.000	10.913	1.144	1.239	1.259	1.214	1.264	-4.119	6.308	6.636	6.425	6.456	5.976	7.440
C2	1.542	1.665	1.786	1.664	1.508	9.393	0.916	0.802	0.854	0.857	0.774	9.706	4.956	4.622	4.528	4.702	4.489	4.530
C3	1.452	1.378	1.293	1.374	1.320	3.953	0.688	0.592	0.501	0.594	0.496	16.451	4.003	4.239	4.241	4.161	4.056	2.523

Table E-6: Confirmation results for impact strength & joint cost.

Impact strength, J			AV. IS	Pred.	Error %	Joint cost E/m	Pred.	Error %
40	40	39	40	38	4.202	0.2786	0.2814	-1.005
33	31	34	33	30	8.163	0.2486	0.2475	0.442
24	22	23	23	21	8.696	0.1893	0.1834	3.117

Appendix F: List of publications

1- Peer-reviewed Journal papers

[1] K. Y. Benyounis, A.G. Olabi and M. S. J Hashmi, Effect of Laser-Welding Parameters on the Heat Input and Weld-Bead Profile, Journal of Materials Processing Technology, Vol. 164-165C, 2005, pp. 971-978.

[2] K. Y. Benyounis, A.G. Olabi and M. S. J Hashmi, Optimizing the laser-welded butt joints of medium carbon steel using RSM, Journal of Materials Processing Technology, Vol. 164-165C, 2005, pp. 979-983.

[3] K. Y. Benyounis, A.G. Olabi and M. S. J Hashmi, Residual Stresses Prediction for CO_2 Laser Butt-Welding of 304-Stainless Steel, Applied Mechanics and Materials, Vol. 3-4, 2005, Trans Tech. Publication, Switzerland, pp.125-130.

[4] A.G. Olabi, K. Y. Benyounis and M. S. J Hashmi, Application of response surface methodology in describing the residual stress distribution in CO_2 laser welding of AISI304 Strain, An International Journal for Experimental Mechanics, Vol. 43, No. 1, 2007, pp. 37-46.

[5] K. Y. Benyounis, A.G. Olabi and M. S. J Hashmi, Mechanical properties and minimum cost scheme of CO_2 laser welding of AISI304, Accepted for publication in Journal of Optics & Laser Technology, 2007.

[6] K. Y. Benyounis and A.G. Olabi, Optimization of different welding process using statistical and numerical approaches- A reference guide, Accepted for publication in Journal of Advances in Engineering Software on 2007.

2- Conference papers

[7] K. Y. Benyounis, A.G. Olabi and M. S. J Hashmi, Estimation of mechanical properties of laser welded joints using RSM, IMC22, Institute of Technology Tallaght, Ireland, 31st August to the 2nd September 2005, pp. 565-571.

[8] K. Y. Benyounis, A.G. Olabi and M. S. J Hashmi, Microstructure and weld-bead geometry investigation of laser beam welding of AISI304, ACMS-IV, 4th International Arab Congress on material science, Tripoli, Libya, 26-28 Sep. 2005, 113-119.

[9] K. Y. Benyounis, A.G. Olabi and M. S. J Hashmi, Effect of Laser welding parameters on the tensile-shear strength of AISI304 sheet, Proc. Of AMPT2006, Las Vegas, USA, 30th Jul – 3rd Aug., 2006.

[10] K. Y. Benyounis, A.G. Olabi and M. S. J Hashmi, Mechanical properties, weld-bead and cost approach for CO_2 laser welding process optimization, 23rd IMC23, Belfast- Northern Ireland, 30th Aug. to 1st Sep., 2006.